Investigations of Daytime Upper Atmospheric Dynamics over Low- and Equatorial-latitudes

A thesis submitted in partial fulfilment of the requirements
for the degree of

Doctor of Philosophy

by

Sunil Kumar
(Roll No. 18330022)

Under the guidance of

Prof. Duggirala Pallamraju
Space and Atmospheric Sciences Division
Physical Research Laboratory, Ahmedabad, India

Department of Physics
Indian Institute of Technology Gandhinagar, India

2023

Dedicated to my family

Declaration

I, Sunil Kumar, declare that this written submission represents my ideas in my own words, and where others' ideas or words have been included, I have adequately cited and referenced the original sources. I also declare that I have adhered to all principles of academic honesty and integrity and have not misrepresented or fabricated or falsified any idea/data/fact/source in my submission. I understand that any violation of the above can cause disciplinary action by the Institute and can also evoke penal action from the sources which have thus not been properly cited or from whom proper permission has not been taken when needed.

Sunil Kumar

(Roll no. 18330022)

Date: 17 July 2023

Certificate

It is certified that the work contained in the thesis entitled ***"Investigations of Daytime Upper Atmospheric Dynamics over Low- and Equatorial-latitudes"*** by Mr. Sunil Kumar (Roll no. 18330022), has been carried out under my supervision and this work has not been submitted elsewhere for any degree, or diploma.

(Prof. Duggirala Pallamraju)
Thesis Supervisor
Space and Atmospheric Sciences Division
Physical Research Laboratory
Unit of Department of Space, Government of India
Ahmedabad-380009, Gujarat, India.

Date: 17 July 2023

Acknowledgments

The thesis period was a great experience in my life at the Physical Research Laboratory (PRL), Ahmedabad. I would like to express my heartfelt gratitude to all those who have supported and blessed me throughout my thesis journey.

First, I would like to express my sincere gratitude to my thesis supervisor, Prof. Duggirala Pallamraju, for his valuable guidance, encouragement, support, and feedback throughout the completion of this thesis work. I consider myself extremely fortunate to have such a supervisor who recognized my potential very well from the beginning. His expertise in the field of the upper atmosphere and optical instrumentation shaped my interest and understanding in this area. I am grateful for his unique perspective in approaching scientific problems and for his valuable suggestions and ideas, which have kept me motivated in my research work. Personally, his hard-working ability, strong mental strength, calm behavior, and composed character always inspired me. I would also like to express my thanks to Bhuvaneswari Ma'am for her warm hospitality and the delicious meals provided at her home, creating a homely atmosphere that made my research journey even more memorable.

I would like to extend my heartfelt appreciation to the members of my Doctoral Studies Committee (DSC), Prof. Dibyendu Chakrabarty, Dr. Amitava Guharay, Dr. Mudit Srivastava for their support, critical questions, and comments which helped me to improve my understanding of the subject. The interactions and discussions I had with them have been immensely beneficial to me. I thank them for going through the thesis and making valuable suggestions. I also would like to thank the members of the academic review committee of PRL for their helpful comments and suggestions as their input has not only contributed to the improvement of my research but has also had a positive impact on my overall growth as a researcher.

I am obliged to the Department of Space, Government of India, for offering the research grant during my tenure. I would like to thank Dr. Anil Bhardwaj, Director of PRL, for providing the necessary facilities for research work, his support regarding the reimbursement of registration fees for various conferences, and for giving permission for the foreign visit. I extend my thanks to Prof. Sudhir K. Jain, Director, IIT, Gandhinagar for providing the administrative help and facilities to carry out the thesis work. I also thank Prof. P. Janardhan, former Dean; Prof. D. Pallamraju, present Dean, Mr. Deekshitulu, former Registrar; Prof. R.D. Deshpande, present Registrar for providing the necessary facilities for my research work. I would like to extend my sincere gratitude to Nishtha Ma'am and the library staff for their dedicated efforts in managing the library, handling book grants, organizing book fairs, and ensuring access to journal subscriptions. I express my heartfelt thanks to Dr. Bhushit Vaishnav, head of academics, for his unwavering support in all academic-related matters. The excellent internet facility and software support provided by the computer center of PRL have been instrumental in facilitating my research work, and I am truly grateful for their services. I would also like to acknowledge all the faculty members of PRL for fostering a conducive research environment. Additionally, I express my appreciation to the administration, canteen, accounts, CMD, and purchase section of PRL for their assistance and provision of facilities in various aspects. Furthermore, I extend my thanks to the academic and administrative personnel of IITGn for their support, as well as their efficient handling of official formalities.

The primary data set for this thesis work is obtained using two MISE one of which is commissioned at Jawaharlal Nehru Technological University, Hyderabad (JNTUH) under the PRL-JNTUH collaboration. In this regard, I thank Vice Chancellor, JNTUH, Prof. A. Reddy, Director, University Foreign Relations, and Dr. T. Vijayalakshmi, Head, Center for Environment, IST, JNTUH for the smooth operation of MISE.

I would like to thank Prof. Claudia Stolle for giving me an opportunity to visit the Leibniz Institute for Atmospheric Physics, Germany (IAP) to carry out the research work under the SCOSTEP visiting scholar program. I am very thankful to the SCOSTEP chairman Prof. Kazuo Shiokawa and SCOSTEP scientific secretary late Prof. Patricia Doherty for selecting me in this program. I am very grateful to my collaborator Dr. Tarique Siddiqui for the very useful scientific discussion and immense help during my visit to IAP. I also thank Dr. Afsheen, Dr. Shivakandan, and Dr. Priyanka for their help. I would like to thank Satyendra for his help during my visit to Germany and for his plan to visit European cities with me. I am sincerely grateful to the Indian Institute of Geomagnetism, Navi Mumbai, especially Dr. Gopi K. Seemala for providing the geomagnetic data.

I am truly grateful to my esteemed colleagues in the Space and Atmospheric Sciences division, including Prof. S. Ramachandran, Prof. L. Sahu, Prof. S. Sharma, Dr. H. Gadhvi, Dr. N. Ojha, Dr. R. P. Singh, Dr. T. A. Rajesh, Dr. K. Venkatesh, Mr. S. Venkataramani, Mr. A. Manke, Mr. M. Bhavsar, Mr. T. K. S. Kumar, Mr. Malaidevan, Ms. Sourita, Dr. Tanzil, Dr. Sumanjit, Dr. Subarna, Sneha di, Anil, Aditya, Rahul, Vishnu, Jacob, Abhishek, Aniket for creating such a wonderful working environment. Their support and expertise have been invaluable to me throughout my research journey. I consider myself fortunate to have seniors such as Fazlul, Deepak, Kuldeep, Sandeep, Suman, Sovan, and Ankit in this division, offering me valuable guidance and mentorship. Interacting with the juniors, including Kshitiz, Bijoy, Gaurav, Kamran, Dharmendra, Kiran, Haritha, Komal, Aakash, and Sandeep, during various division activities has been a pleasure.

I am very thankful to my colleagues in the Optical Aeronomy group for such a friendly atmosphere. I am really thankful to Subir, Pradip, Shashank, Pankaj, Sovan, Chithra, Mohit, Kshitiz, Dupinder, and Narayan for providing long-lasting wonderful moments. The time spent with them playing table tennis, football, and cricket, discussing various aspects, and having lunch and dinner was great. I express my heartfelt gratitude to my *seniors Subir and Sovan for their support and valuable suggestions throughout my research journey. Their guidance and mentorship strongly contributed to the improvement of my understanding of the subject. Engaging in scientific discussions with them and my junior (Kshitiz) has consistently broadened my knowledge.*

I convey my heartfelt thanks to the friends of my batch Akanksha, Anju, Anupam, Arijit, Binal, Dayanand, Deepak, Deepak Rai, Deva, Meghna, Monika, Naba, Namita, Naval, Pranav, Sandeep, Sanjit, Siddharth, Supriya, Vikas, Yash, and Yogesh for spending a wonderful time and for providing memorable moments on various occasions.

I have met wonderful seniors in PRL like, Subir, Sandeep, Surendra, Kaustav, Priyank, Abdur, Harish, Madhu, Sana, Shivani, Shushant, Arvind, Alka, Neeraj, Abhay, Ankit, Partha, Sanwali, Anshika, Himanshu, Satyjeet, Deepak raja and juniors Saumya, Vinit, Birendra, Malika, Shreya, Aakash, Sandeep. Those were some precious moments playing volleyball, cricket, table tennis, badminton, celebrating festivals, etc., I will never forget. I express my heartfelt thanks to my friends Anju, Adesh, Mahendra, Mukesh, Rahish, and Pramod for their constant love and support.

I want to express my sincere gratitude to Anil, Omprakash, Abhishek, and Avinash Sir who developed a love and curiosity for science inside me during school time. I thank my college teachers Jitendra and Satyaveer Sir for their excellent teaching.

The journey would have been incomplete without the constant support and blessings from my parents. Staying away from home was the most difficult part. I am indebted forever to them. I express my gratitude to my sisters and brother (Manisha, Bharti, Bulesh), as well as my cousin brothers (Tarachand, Shreechand), for giving me a delightful childhood and continuing to shower their affection and support to this day.

Sunil Kumar

Abstract

The Earth's upper atmosphere (UA) is composed of neutral species and charged particles and its behavior is influenced by solar forcing, ionospheric electrodynamics, lower atmospheric forcing, space weather effects, among others. This region also experiences a variety of waves, such as, gravity waves (GWs), planetary waves, and tides, all of which primarily originate in the lower atmosphere and travel upwards under favorable conditions. Tidal winds in the dynamo region generate eastward electric field over the magnetic equator during daytime which engenders several processes, such as, the Equatorial Electro Jet (EEJ), the equatorial ionization anomaly, and the equatorial temperature and wind anomaly. These processes, in addition to neutral winds, influence the distribution of plasma and neutral densities over low- and equatorial-latitudes. The daytime UA dynamics is investigated by observing the OI 630.0 nm dayglow emissions which serve as a tracer of the atmospheric behavior over a broad altitudinal region centered at 230 km. The dayglow emissions are obtained by two in-house built spectrographs, MISE (Multi-wavelength Imaging Spectrograph using Echelle grating), that are in operation from Hyderabad (17° N, 78° E, 9° magnetic latitude, MLAT) and Ahmedabad (AHD, 23° N, 73° E, 15° MLAT). MISE has a large field-of-view (FOV), and thus, these two together cover a wide spatial region of 5°-18° MLAT. In addition, other datasets, such as, the EEJ strengths from the Indian and American longitudes, electron density from digisonde located at AHD, and neutral winds from Ionospheric Connection Explorer (ICON) satellite have been used.

The tidal behavior in the equatorial electrodynamics is investigated during the periods of weak and strong Stratospheric Polar Vortices (SPV) in the northern hemisphere. The strength of the SPV can significantly impact the atmospheric circulations, leading to changes in the spectrum of vertically propagating atmospheric waves which drive the changes in the EEJ. We have analyzed geomagnetic tidal variations obtained from Huancayo (12.5° S, 284.7° E, 0.6° MLAT) during 34 northern hemispheric winters. It is known

that during weak SPV conditions, an enhancement is observed in the amplitude of solar and lunar semidiurnal tides in the UA. Whereas, when the SPV is strong, the result from the present study reveals that the amplitudes of these tides decrease. Also, it is revealed that while the response of the geomagnetic semidiurnal lunar tidal variation to SPV conditions is prompt, the response of semidiurnal solar tidal variation to SPV is delayed by approximately 10 days. These results provide observational evidence that the strong SPV conditions do also have pronounced effects on the equatorial ionospheric behavior. In contrast, the reports until now had presented significant effects in the UA only during weak SPV conditions. Also, the effects of the equatorial electrodynamics and meridional winds are investigated using the OI 630.0 nm dayglow emission variability during January-February 2020 in the spatial region of 5°-18° MLAT. It is observed that the poleward meridional wind contributes to an enhancement in the dayglow emission near the magnetic equator, and, to a reduction as one moves away from the equator. Whereas, the effect of the equatorial electric field is found to be nearly equal in the spatial region under consideration. In addition, we have developed a method to estimate the thermospheric neutral winds using three-dimensional GW characteristics. In this method we have obtained the propagation characteristics of GWs in the horizontal (zonal & meridional) and vertical directions using large FOV optical and radio measurements from AHD. These measured three-dimensional GW propagation characteristics are used as inputs into the GW dispersion relation to estimate the thermospheric horizontal winds given the fact that the neutral wind and the gravity wave propagation are inter-twined with each other. These winds, so estimated, are found to corroborate well with those measured independently by Michelson Interferometer for Global High-resolution Thermospheric Imaging (MIGHTI) on-board the ICON satellite.

In summary, this thesis presents new findings on (a) the effect of the lower atmospheric forcing on the UA equatorial electrodynamics processes, particularly during strong SPV conditions; (b) effect of equatorial electric fields and neutral winds on the UA behavior over low-latitudes; and (c) methods to estimate the daytime thermospheric neutral winds, thereby, bringing out new insights into the intriguing nature of the coupling processes in the daytime UA dynamics over low- and equatorial-latitudes.

Contents

List of Tables

List of Figures

Chapter 1

Introduction

1.1 The structure of atmosphere

The Earth's atmosphere refers to the gaseous layer that surrounds our planet, which consists of mainly nitrogen (about 78%) and oxygen (about 21%). Other gases, such as, carbon dioxide, water vapor, and noble gases are present in smaller amounts. The neutral density of the atmosphere decreases exponentially with altitudes. The atmosphere has several important functions, including protecting our planet from harmful solar radiation, regulating the temperature, and providing the air that living organisms can breathe. It is also responsible for weather patterns and climate. The atmosphere is composed of several distinct layers with varying characteristics. Based on mixing, the atmosphere is divided into two regions, namely *homosphere* and *heterosphere*. Homosphere refers to a region below $\sim$100 km in altitude, where the atmospheric gases are well mixed due to turbulence, whereas at altitudes beyond 100 km, i.e., in the heterosphere, atmospheric gases are distributed based on their masses. Therefore, heavier molecules dominate at the lower part of the heterosphere, whereas, lighter atoms dominate at higher altitudes. The boundary between these two layers is called *turbopause*. In the atmosphere, hydrostatic equilibrium is maintained due to the combined effects of pressure gradient force and gravity.

The temperature of the atmosphere varies with altitude due to heating and cooling by different atmospheric constituents. Based on the temperature gradient, the atmosphere is broadly categorized into five different layers: the *troposphere*, *stratosphere*, *mesosphere*,

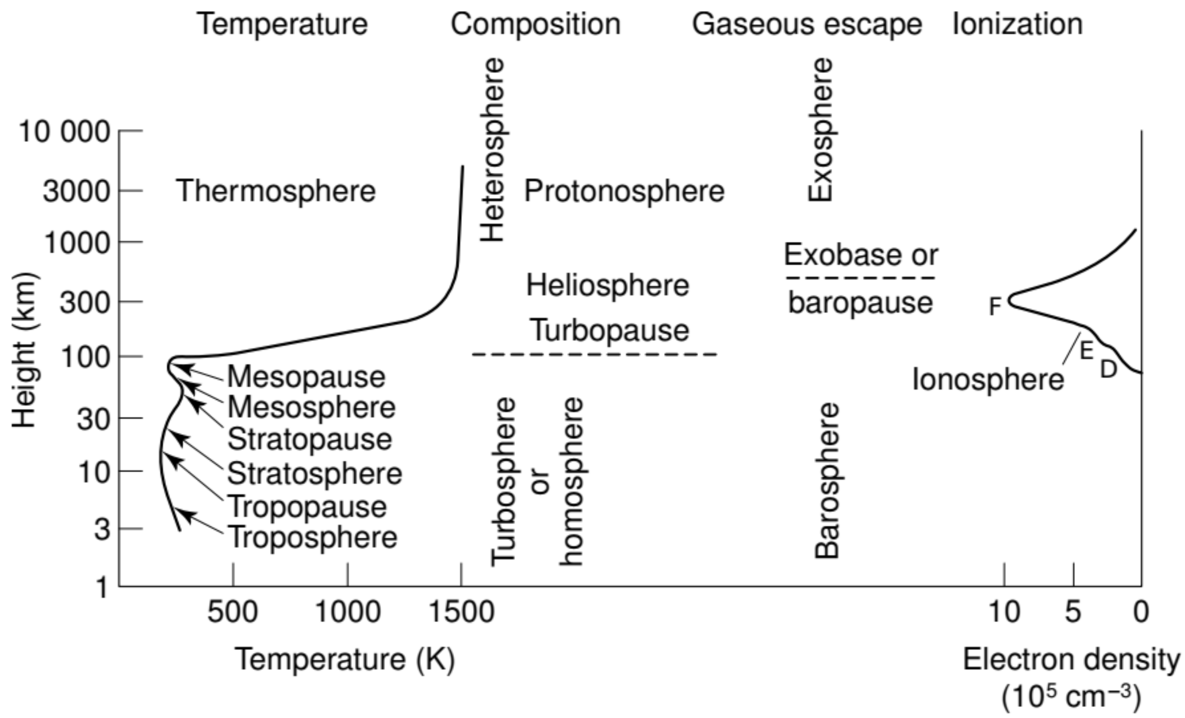

Figure 1.1: The structure of Earth's atmosphere; classification of the different layers based on variations in the temperature, composition, and ionization is shown. (From *Hargreaves* (1992))

thermosphere, and *exosphere* as shown in Figure 1.1. These layers are described in detail in the following sections.

Troposphere: This is the lowest layer of the atmosphere, extending from the Earth's surface to an altitude of about 8-16 km depending on the latitudes. It is characterized by decreasing temperature with increasing altitude. The surface of the Earth gets heated by the incoming solar radiation, which then re-radiates and warms the lower atmosphere, thus the temperature decreases with increasing altitudes in the troposphere. The temperature decreases at a rate of 6.5 $K\ km^{-1}$, which is known as the atmospheric lapse rate. This negative gradient in the temperature supports convective activity in the troposphere. It is the region where weather, as we know, occurs. The boundary between the troposphere and stratosphere is called *tropopause*.

Stratosphere: The stratosphere extends up to around 50 km wherein the temperature gradient is positive. This layer contains the ozone layer, which heats up due to the absorption of solar ultraviolet (UV) radiation, and therefore the temperature increases with altitude in this region. This layer plays an important role in enabling life on Earth as it absorbs UV radiation and stops it from reaching the ground, which is very harmful for living species. The upper boundary of the stratosphere where temperature stops to increase with altitude is called *stratopause*.

Mesosphere: The mesosphere refers to the atmospheric region between 50 to 90 km. In this part of the atmosphere, temperature decreases with altitude which occurs primarily due to the radiative cooling by CO_2. Mesosphere is also associated with the layer where meteors burn up upon entering the Earth's atmosphere. The uppermost part of the mesosphere is called the *mesopause*, which is the coldest region of the Earth's atmosphere.

Thermosphere: The atmosphere between around 90 km to 800 km is known as the thermosphere, which is characterized by the sharp rise in temperatures due to the absorption of high-energy solar radiation by neutral species. As the incoming radiation is solar activity dependent, the temperature of this region shows variations with solar activity. In addition to solar radiation, the breaking of waves contributes to the heat budget as it leads to energy deposition. Over high-latitudes, particle precipitation events and Joule heating by auroral currents drive variability in the thermospheric temperature. Due to the Joule heating by auroral currents, the circulation is generated from high-latitudes to low-latitudes, which can alter the neutral composition over low-latitudes. In addition, the temporal and spatial variation in temperature can generate waves that propagate towards low-latitudes and can affect the temperature and composition.

Exosphere: This is the outermost layer of the atmosphere with an extremely low density of neutrals, and is composed mainly of individual atoms and molecules that are very far apart. The mean free path of constituents is larger than the scale heights, which leads to very few collisions among them.

The troposphere is associated with the *lower atmosphere*, stratosphere and lower part of the mesosphere constitutes the *middle atmosphere*. *Upper atmosphere* (UA) consists of the upper portion of the mesosphere, thermosphere, and exosphere.

So far, we have been discussing the different layers of the Earth's atmosphere based on the mixing of species and variation in neutral temperature. As one goes up in altitude, ionization occurs due to the interaction of neutrals with high-energy solar radiation, and an electrically conductive layer is formed. In a given volume, the number of ions and electrons are the same, and they follow quasi-neutrality. This conductive layer has sufficient plasma density which can affect radio wave propagation and it is known as the ionosphere. Although the plasma density in the ionosphere is 3 orders less than the neutral density, it has a significant impact on the electrical properties of the ionosphere. Ionosphere extends from around 60 km to 1000 km in altitude and it is a part of the upper atmosphere. It plays an important role in various atmospheric and space processes, including radio communications and space weather.

The plasma density of the ionosphere changes with altitude, geographic location, time of the day, seasons, and solar cycles. Since Earth is a magnetized body, the motion of these charged particles is controlled by both the neutral dynamics and magnetic field.

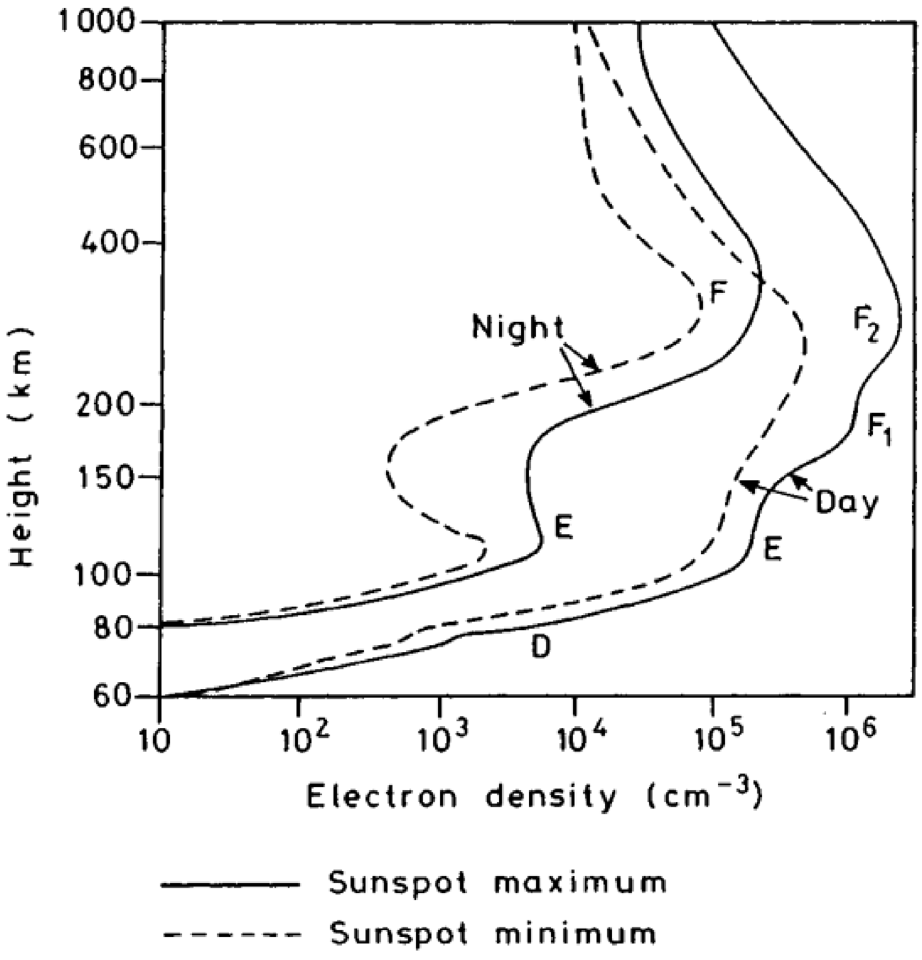

Figure 1.2: A typical electron density variation with heights in the Ionosphere is shown for the day and nighttime corresponding to the solar maxima and minima conditions. (From *Hargreaves* (1992))

In the presence of a magnetic field, ions and electrons gyrate around the magnetic field with frequency $\omega_{i,e} = qB/m_{i,e}$, where q = charge; B = strength of magnetic field; m_e = mass of electrons; and m_i = mass of ions. The ionospheric structure is further classified into several layers based on the production mechanism and relative motion of ions and electrons. Their relative motions can be defined based on the variation of their neutral collision frequency and gyrofrequencies. They are namely as the D layer (60-90 km), E layer (90-160 km), and F layer (>160 km), and are shown in Figure 1.2.

The D layer is primarily composed of ions formed by the ionization of neutral atoms and molecules by Lyman-α (121.5 nm), extreme ultraviolet (EUV, in the range of 102.7 nm – 111.8 nm), and hard X-rays (0.2-0.8 nm) from the Sun. The cosmic rays can also contribute to some ionization. In the nighttime, ionospheric D-layer nearly vanishes in the absence of production, which can be seen in Figure 1.2. In this region, the collision frequency of ions and electrons with neutrals (ν_{in} & ν_{en}, respectively) is greater than their respective gyrofrequencies (ω_i & ω_e, respectively) that means their motions are controlled by neutral dynamics. The E region is formed due to ionization by the radiation in the EUV (80-102 nm) and soft X-rays (1-10 nm) domain. A part of the E-layer exists in the nighttime due to the presence of metallic ions which have longer lifetimes (**?**). On some occasions, a sporadic-E layer occurs in the E regions, which can cause radio wave reflections and signal enhancements (**?**). In the E layer, the electrons are driven by the electromagnetic forces, as $\nu_{en} << \omega_e$, whereas, the dynamics of ions depend on the neutral winds, as $\nu_{in} = 2\ \omega_i$. The F layer is the highest layer of the ionosphere where the primary source of ionization is EUV (10-80 nm). In the F region, ions and electrons are driven by the electrodynamic forces as their gyrofrequencies are greater than their collision frequencies ($\nu_{in} = \omega_i\ /300$ and $\nu_{en} << \omega_e$). On some occasions, around noontime, the F layer splits into F1 and F2 due to the competing effects of production and loss mechanisms.

The ionospheric plasma exists up to 4-5 R_E (R_E =Earth's radius) in very small densities and this region is called the *plasmasphere*, which is also the regions where the magnetic field co-rotates with the Earth's rotation. Beyond this region, the plasma density falls by three orders of magnitude, and this region is called the *magnetosphere*. Magnetosphere is the outermost region and can extend typically up to around 10 R_E on the dayside and much farther (30 - 200 R_E) on the nightside depending on the solar activity. In the region, the plasma dynamics is controlled by the convective electric fields of solar origin. The boundary where magnetosphere ends is called the *magnetopause*.

1.2 Atmospheric waves

Atmospheric waves refer to periodic disturbances in the parameters, such as, pressure, temperature, winds, and densities, which can be propagating, stationary, and evanescent in nature. These waves can carry energy away from their origin and play a vital role in the energy budget of the atmosphere. These waves are mostly generated in the lower atmosphere and can propagate deep into the upper atmosphere and alter the prevailing dynamics. The waves can be classified based on their period, wavelength, and on the basis of their direction of propagation and oscillation. Based on the propagation and oscillation directions, atmospheric waves are classified into three different categories, namely, longitudinal (waves propagate along the direction of displacements, e.g., sound waves), vertical

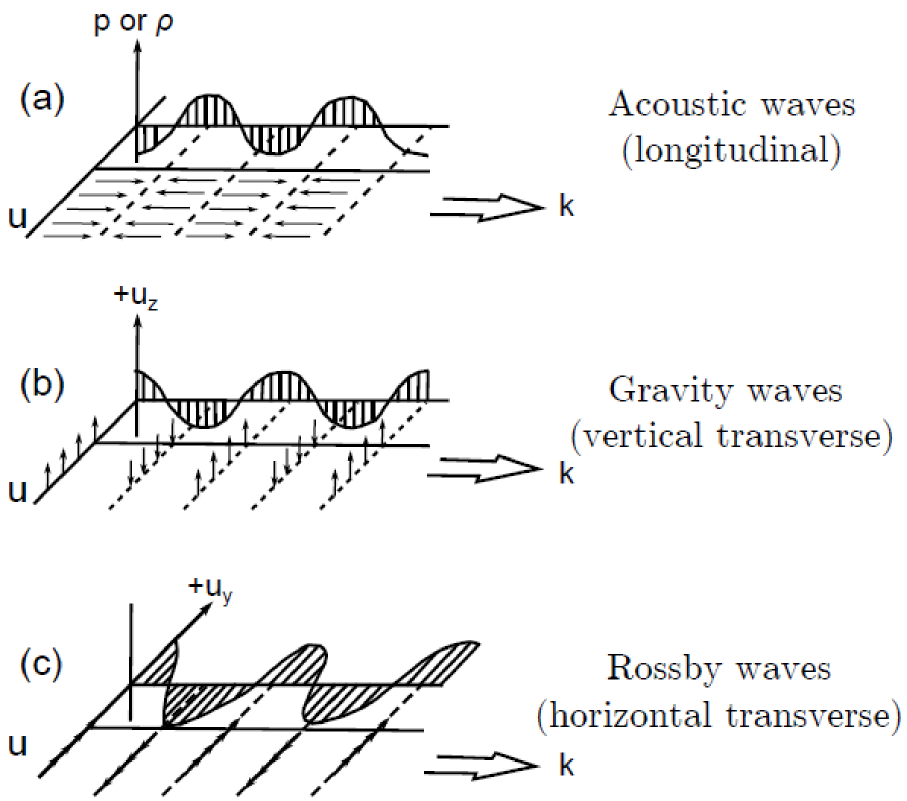

Figure 1.3: The classification of atmospheric waves based on the propagation and oscillation direction. (From *Beer* (1974))

Table 1.1: Classification of atmospheric waves into different categories based on their temporal scale, spatial scale, and their importance in the atmosphere. Here, BV stands for Brunt-Väisälä period, which is the natural oscillation period of an air parcel in the atmosphere; and UA stands for Upper Atmosphere.

Waves	Period	Horizontal Scale Sizes	Importance
Acoustic	<270 seconds	0.01s - 10s m	speech
Gravity Waves	BV to 3 hrs	10s - 1000s km	UA, Ionosphere
Tided	24/n; n=1,2,3,4	1000s km	UA, Ionosphere
Planetary Waves	2 - 30 days	1000s km	UA, meteorology

transverse (waves propagate horizontally with vertical displacements, e.g., gravity waves (GWs)), horizontal transverse (waves propagate in the horizontal direction with horizontal displacements, e.g., Rossby waves) as shown in Figure 1.3. The time periods, horizontal scale sizes, and importance of these waves are mentioned in Table 1.1. Depending on the temporal and spatial scale, atmospheric waves can be further characterized. Detailed descriptions on them can be found in classic books (e.g., *Beer*, 1974; *Hines*, 1964; *Andrews*, 2010). The broad categories are tabulated above:

In the following sections, gravity waves, planetary waves, and tides are discussed in detail.

1.2.1 Gravity waves (GWs)

Atmospheric GWs are caused by the buoyancy and gravitational force acting on air parcels. These waves strongly influence atmospheric processes as they transfer energy and momentum across the different parts of the atmosphere, and drive variability in temperature, pressure, density, and winds. GWs can occur on a wide range of scales, from small-scale waves with wavelengths of a few km to large-scale waves with wavelengths of hundreds of km or more, and they can have periods ranging from a few minutes to several hours.

Let us consider a GW propagating in the three-dimensional plane as shown in Figure

1.4 in which the wave solution is in the form of $exp[i(\omega t - k_x x - k_y y - k_z z)]$. The wave vector of wave can be written as,

$$k^2 = k_x^2 + k_y^2 + k_z^2 \tag{1.1}$$

where, $k_x(=2\pi/\lambda_x)$, $k_y(=2\pi/\lambda_y)$, and $k_z(=2\pi/\lambda_z)$ are the wave number in the x (zonal), y (meridional), and z (vertical) directions and λ_x, λ_y, and λ_z are the wavelengths in those directions. The horizontal and vertical phase propagation direction (θ_H and θ_v) can be obtained as,

$$\theta_H = tan^{-1}\left(\frac{k_y}{k_x}\right) \quad \& \quad \theta_v = tan^{-1}\left(\frac{k_z}{k_H}\right) \tag{1.2}$$

where, $k_H^2(=k_x^2+k_y^2)$ is the horizontal wave number. The phase velocity of GWs in the

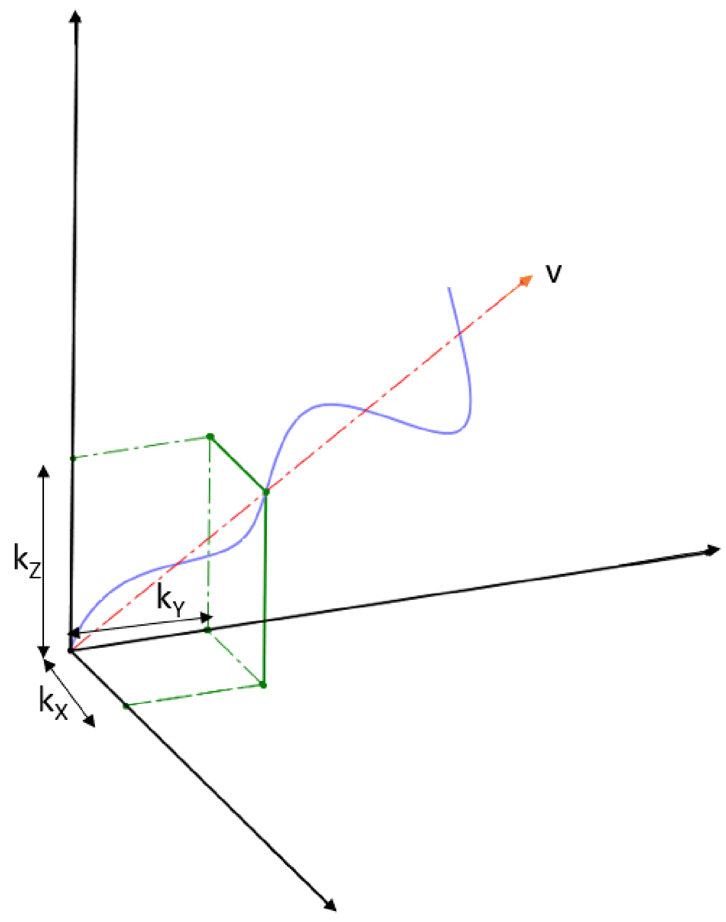

Figure 1.4: A schematic showing the wave in three dimensions.

direction of wave propagation can be derived as,

$$c = \frac{\omega}{k} = \frac{\lambda}{\tau} \tag{1.3}$$

where, τ is the time period of the wave.

Earth's atmosphere acts as an anisotropic and dispersive medium for these waves due to the presence of density gradients. The dispersion relation of acoustic-GWs for a basic state of the atmosphere that is isothermal, in uniform motion, and assuming sinusoidal variations for the perturbed quantities in the equation of motion, continuity equation, and equation of state can be expressed as follows:

$$k_z^2 = \left(1 - \frac{\omega_a^2}{\omega^2}\right)\frac{\omega_a^2}{\omega^2} - k_H^2\left(1 - \frac{\omega_b^2}{\omega^2}\right) \tag{1.4}$$

where, ω is the angular frequency of GWs, s is the speed of the sound. ω_a ($= \gamma g/2s$, where γ is the ratio of specific heat at constant pressure (c_p) and at constant volume (c_v), g is the acceleration due to gravity) is the resonance angular frequency of a column of air of whole atmosphere and also known as acoustic cut-off angular frequency. ω_b ($= (1-\gamma)^{1/2} g/s$) is the Brunt-Väisälä (BV) frequency. In the above dispersion relation of acoustic GW, the effect of the Coriolis force is not considered as it can be neglected for shorter scale GWs. Figure 1.5 represents the dispersion diagram according to Equation 1.4.

It can be seen from Figure 1.5 that the Acoustic waves are those whose frequencies greater than ω_a and when frequency is lower than ω_b, they are internal GW. For $k_z^2 < 0$, these waves are called evanescent waves (*Salby*, 1996)). The frequency of GWs is referred to $\omega_b > \omega > f$ ($f = 2\Omega sin\phi$, is the Coriolis parameter, where, Ω = Earth's rotation rate, ϕ = latitude).

According to the linear theory, for an inhomogeneous and non-isothermal atmosphere, the GW dispersion relation takes the following form,

$$\omega^2 = \frac{\omega_b^2 k_H^2}{k_H^2 + k_z^2 + \frac{1}{4H^2}} \tag{1.5}$$

where, H is the constant atmospheric scale height ($H = kT/mg$, where, k = Boltzmann

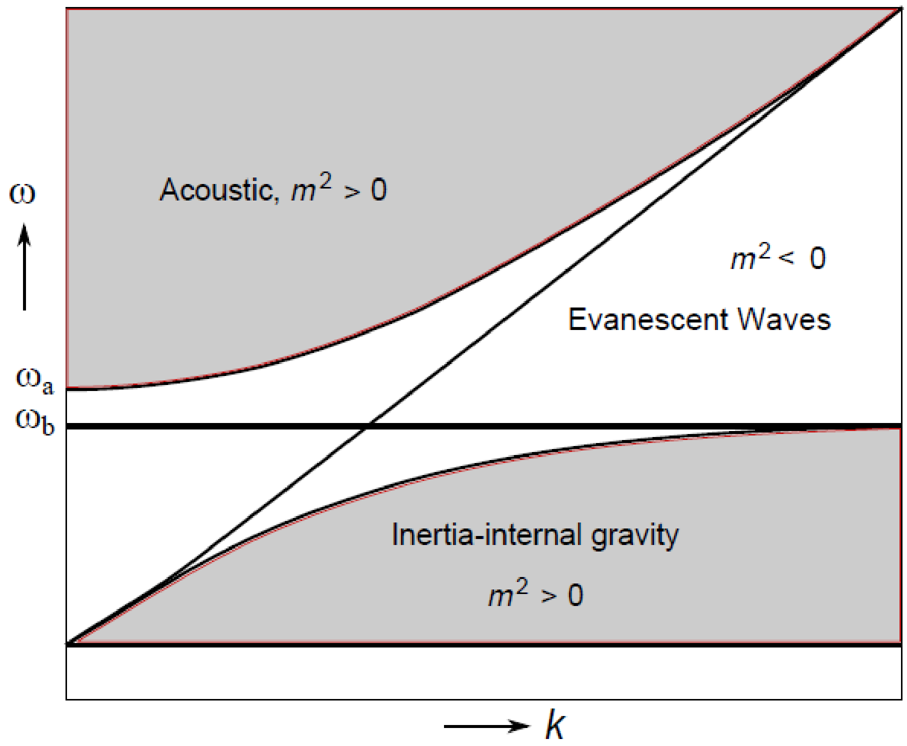

Figure 1.5: Gravity wave dispersion diagram. Here, m denotes the vertical wave number (k_z). (Adapted from *Kelley* (2009))

constant; T = neutral temperature; m = atomic mass). The vertical phase velocity (c_{pz}) and group velocity (c_{gz}) can be derived using the above equation which are given by:

$$c_{pz} = \frac{\omega}{k_z} = \pm \frac{\omega_b k_H}{k_z(k_H^2 + k_z^2 + \frac{1}{4H^2})^{1/2}} \tag{1.6}$$

$$c_{gz} = \frac{\partial \omega}{\partial k_z} = \mp \frac{\omega_b k_H k_z}{(k_H^2 + k_z^2 + \frac{1}{4H^2})^{3/2}} \tag{1.7}$$

It can be noted from equations 1.6 and 1.7 that the phase and group velocity are oppositely directed; thus, upward propagating GWs are associated with downward phase propagation (e.g., *Hines*, 1960; *Djuth et al.*, 1997; *Pallamraju et al.*, 2016; *Mandal et al.*, 2019). This can be seen in Figure 1.6, which depicts the GW propagation in the upward direction along to the downward directed phase propagation. The associated energy flows in the perpendicular to the phase and wave propagation, and in the displacement direction. The energy density of a wave is related to the air density of the atmosphere (ρ) and amplitude

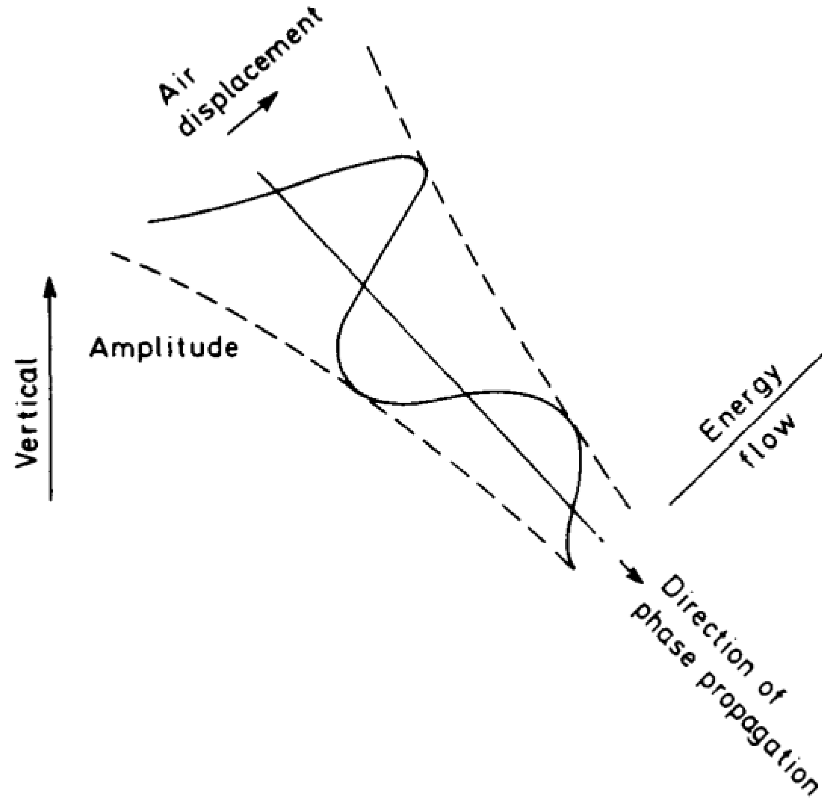

Figure 1.6: A schematic diagram showing phase propagation, energy flow, and air displacement associated with a upward propagating GWs. (From *Hargreaves* (1992))

of the wave (A) as below:

$$< E > \propto \rho A^2 \tag{1.8}$$

Therefore, in order to conserve the energy density, wave amplitude grows with altitude as the density of the atmosphere decreases.

These waves are mostly generated in lower atmosphere and propagate away from their source regions and hence play a crucial role in the coupling between the different regions of the atmosphere. GWs can be generated by a variety of mechanisms, such as, wind blowing over mountains as shown in Figure 1.7(a) (e.g., *Long*, 1955; *Smith and Lyjak*, 1985; *Alexander*, 1996; *Lott and Miller*, 1997; *Farmer and Armi*, 1999), convective processes in the troposphere due to negative gradient of temperature (Figure 1.7(b)) (e.g., *Sato*, 1993; *Alexander et al.*, 1995, 2000; *Sato et al.*, 1995; *Dewan et al.*, 1998; *Singh and Pallamraju*, 2016), or wind shear (e.g., *Davis and Peltier*, 1979; *Fritts*, 1982,

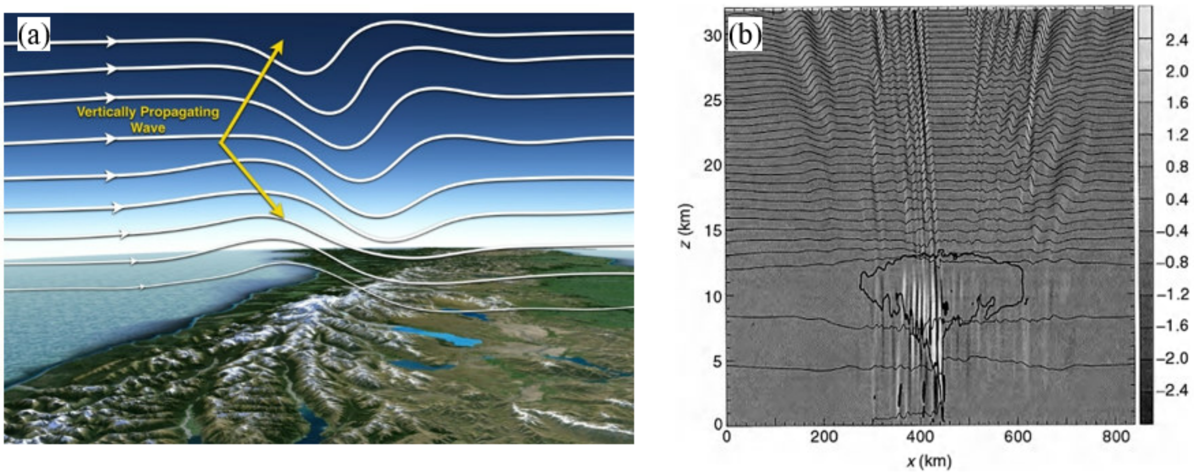

Figure 1.7: (a) An illustration of GWs generation due to the mountains (source: UCAR). (b) Isentropes in thin lines obtained by numerical simulation. Vertical velocity is presented in shaded contours and a thick black line shows the outline of cloud (From *Alexander et al.* (1995)).

1984; *Pallamraju et al.*, 2014; *Pramitha et al.*, 2015). Further, these waves can also be generated due to auroral processes over the high-latitudes (*Hocke*, 1996; *Pallamraju et al.*, 2001, 2004b), and equatorial electrojet over the low-latitudes (*Raghavarao et al.*, 1988b; *Pallamraju et al.*, 2010).

As GWs propagate in the vertical direction, their amplitude grows exponentially. When the amplitudes of these waves become very large, waves get unstable and break down into smaller-scale disturbances as shown in Figure 1.8. This can happen through several mechanisms, including: (i) wind shear: GWs can break down due to shear instability, which occurs when there is a strong vertical shear in the horizontal wind (i.e., change in wind speed and/or direction with height). Shear instability can cause the wave to tilt and deform, leading to the generation of smaller-scale vortices or eddies. (ii) Critical layer: when the wind speed matches the phase speed of the GWs, the GWs get absorbed. This can result in the trapping of wave energy within a specific layer of the atmosphere. Also, in the lower thermosphere, GWs dissipate due to the larger molecular viscosity and thermal diffusivity.

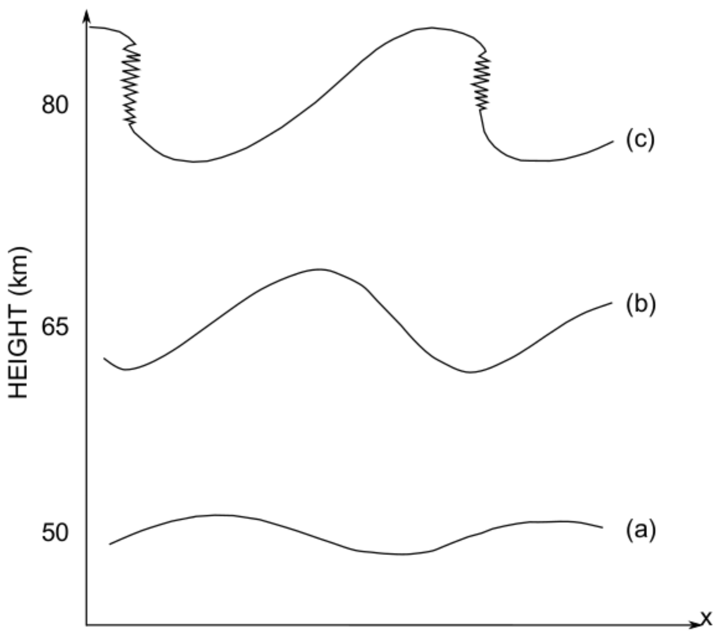

Figure 1.8: The schematic representation of non-linear wave breaking when their amplitude becomes very large. (From *Salby* (1996))

1.2.2 Planetary waves (PWs)

PWs are global scale waves and can have significant impacts on weather patterns and climate. These waves are characterized by their large horizontal wavelengths (order of thousands of kms) and are often associated with the dynamics of the mid-latitude and polar regions of the atmosphere. Their vertical wavelengths can be tens of km and time period lies between $2-20$ days. The effects of Earth's curvature, rotation or Coriolis force are neglected for GWs, however in case of PWs, these effects must be considered owing to their very large scales. PWs are mostly generated in the lower atmosphere but can also impact the UA through direct propagation up to the thermosphere or through interaction with GWs and tides (e.g., *Liu et al.*, 2010; *Chang et al.*, 2011). In their simplest form, these are generated due to the latitudinal variation of the Coriolis parameter and known as Rossby waves. The Rossby waves are absolute vorticity (η) conserving motion under the barotropic conditions. The absolute vorticity, which is a conserved quantity, is the sum of the relative vorticity (ζ) and planetary vorticity (f). The relative vorticity is the curl of the relative velocity of the flow, whereas, the planetary vorticity is the vertical component that arises due to the rotation of the Earth, which is also known as the Coriolis parameter ($f = 2\Omega \sin\phi$).

The generation and propagation of a PW can be understood from Figure 1.9. Let us consider a perturbation occurs in y-direction (meridional) due to some external force on the air parcel flowing in the x-direction (zonal) at location A. Assuming $\zeta = 0$ and $f = f_o$ at point A. As air parcel moves towards higher latitudes, f increases and becomes f_1 which gives rise to a declination in the ζ due to the conservation of the absolute vorticity. Then we have the values of ζ as,

$$\zeta = f_0 - f_1 = \beta\delta y \tag{1.9}$$

where, $\beta(= df/dy)$ is the planetary vorticity gradient. The negative values of ζ occurred in the movement of the air parcel from A to B position drives a clockwise movement of air parcel. This leads to the air parcel movement towards low-latitudes. Then the positive perturbation of ζ leads to the anti-clockwise movement of an air parcel and it again goes towards high-latitudes. The perturbation in vorticity causes the generation of the Rossby waves. The clockwise and anti-clockwise movements of an air parcel lead to the westward propagation of Rossby waves.

The speed of westward propagating Rossby wave can be calculated by considering a sinusoidal variation due to wave, $\delta y = a \cdot sin[k(x - ct)]$, where a is the maximum displacement and k is the horizontal wave number. Therefore,

$$v = D(\delta y)/Dt = -kca \cdot cos[k(x - ct)] \tag{1.10}$$

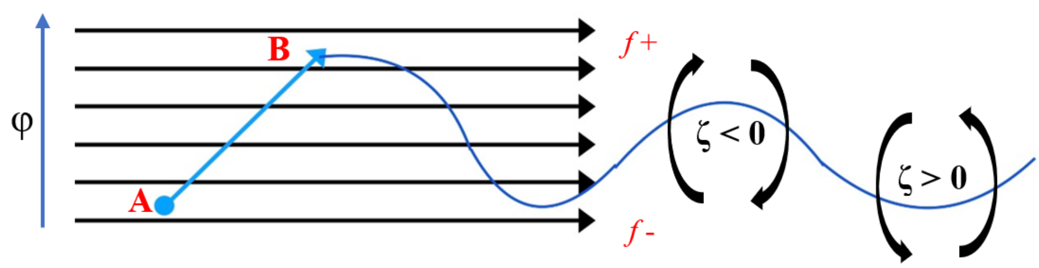

Figure 1.9: A PW generation and propagation is shown in the x-y plane.

$$\zeta = \partial y/\partial x = k^2 ca \cdot sin[k(x-ct)] \tag{1.11}$$

By putting values of δy and ζ in Equation 1.9, we obtain,

$$c = -\frac{\beta}{k^2} \tag{1.12}$$

From the above relation, it can be noted that the phase speed is westward with respect to the mean flow, and inversely proportional to the square of horizontal wave number. The β value is maximum over the equator that is why higher phase speed Rossby waves are found over the equatorial region, whereas low-speed or stationary waves are present over high-latitudes. The dispersion relation of Rossby waves can be obtained by solving the vorticity equation (*Holton*, 1980) and it is given by,

$$k_z^2 = \frac{\omega_b^2}{f^2}\left[\frac{\beta}{u-c} - k^2\right] \tag{1.13}$$

where, u is the zonal mean velocity. The Charney-Drazin (*Charney and Drazin*, 1961) gave the criteria for upward propagating PWs which is,

$$0 < u - c < \beta/k^2 = U_c$$

where, U_c is the Rossby critical velocity. Thus, only waves with phase speeds relative to the zonal mean flow is less than U_c will be able to propagate vertically. Therefore, this condition constraints the Rossby waves to exist in the winter hemispheres when the zonal mean flow is eastward.

1.2.3 Tides

Atmospheric tides are periodic global-scale oscillations of the atmosphere that are primarily caused by the radiative heating due to the Sun and gravitational force due to the Moon. In addition, secondary tides are generated due to the non-linear interactions of tides with PWs and large-scale release of latent heat resulting from deep convection in the tropical region (*Teitelbaum and Vial*, 1991; *Hagan et al.*, 2001; *Immel et al.*, 2006). The atmospheric tides are simply modified GWs which are affected due to the rotation of the Earth because of their large-scales (*Beer*, 1974). These tides can be observed as regular variations in pressure, temperature, wind, density, and geopotential height. At ground level, atmospheric tides appear as small regular oscillations in surface pressure. However, at higher altitudes, their amplitudes can become extremely large, and it can reach more than 50 ms^{-1} in the mesosphere. The increase in amplitude with height is due to the decrease in density as the waves propagate upwards. If a wave is not dissipating, then its kinetic energy density must remain constant, resulting in an increase of amplitude to compensate the decrease in density. Atmospheric tides are more prominent in the middle and upper atmosphere and play a crucial role in atmospheric dynamics. There are two main types of atmospheric tides based on their sources: solar tides and lunar tides.

1.2.3.1 Solar tides

Atmospheric solar tides are generated when the sun heats up different parts of the atmosphere. Solar energy is absorbed throughout the atmosphere, with some of the most significant absorbers being water vapor in the troposphere, ozone in the stratosphere, and molecular oxygen, atomic oxygen, and nitrogen in the thermosphere (*Forbes and Garrett*, 1979). This regular heating generates thermal tides that have periods related to the solar day, which is approximately 24 hours. However, observations show that the large amplitude tides are generated with periods of both 24 (diurnal) and 12 (semi diurnal) hours. Smaller tides with periods of 8 and 6 hours have also been observed, but they generally have smaller amplitudes. This set of periods occurs because the solar heating of the atmosphere takes place in an approximate square wave profile, which is rich in harmonics. When this pattern is analyzed through a Fourier transform, significant oscillations with periods of 12, 8 and 6 hours are produced. Tides generated by the gravitational effect of the sun are much smaller than those generated by solar heating. Changes in the global distribution and density of these absorbers can lead to variations in the amplitude of the solar tides. As the tides propagate vertically through the atmosphere, the zonal wind and horizontal temperature distribution affect their characteristics (e.g., *Chapman and Lindzen*, 1970; *Lindzen and Hong*, 1974; *Jin et al.*, 2012).

Solar tides in the atmosphere have two components: migrating and non-migrating.

Migrating tides are synchronous with the Sun's motion and move westward relative to a stationary observer on the ground. On the other hand, non-migrating tides are global-scale waves with the same periods as the migrating tides but do not follow the Sun's apparent motion. Non-migrating tides can either propagate eastwards or westwards at a different speed than that of the solar effects on the Earth. The generation of non-migrating tides is influenced by various factors, such as, spatial differences in topography, land-sea contrast, and non-linear interaction of planetary waves with migrating tides. Deep convection in the tropics also plays a significant role in the generation of non-migrating tides due to the release of latent heat.

1.2.3.2 Lunar tides

The atmospheric lunar tides are primarily generated by the gravitational pull of the Moon on the lower atmosphere. Also, induced movement of solid Earth and oceans can work as a source of lunar tides (e.g., *Hollingsworth*, 1971; *Vial and Forbes*, 1994). The influence of the Moon on the ocean has been known long back before modern scientific ages. *Sabine* (1847) first reported atmospheric lunar tides in the tropical pressure data. The amplitude

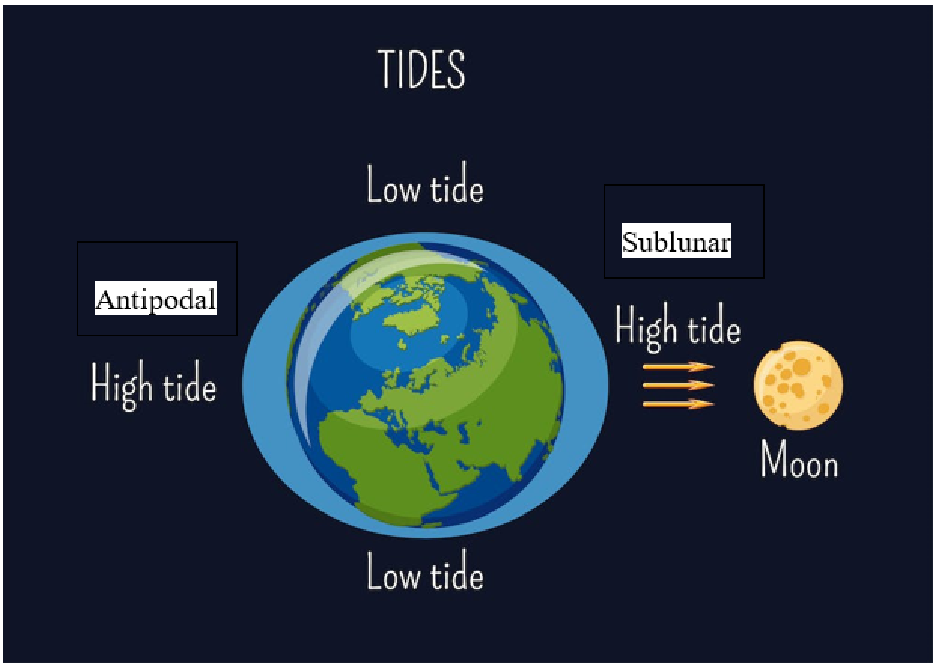

Figure 1.10: The effect of gravitational attraction on the Earth's atmosphere by the moon is shown. (Source: theconversion.com)

of these tides also grows exponentially like other waves while propagating upward up to around 120 km before dissipating where its amplitude maximizes (*Vial and Forbes*, 1994). The semidiurnal (12.42 h) component dominates in the atmospheric lunar tide. The semidiurnal lunar tide peaks at two times in a day when the Moon is overhead (sublunar) and when moon located in the opposite side (antipodal) as show in Figure 1.10. In the dynamo region (∼90-150 km), amplitude of the lunar semidiurnal tide in winds can reach up to 10-15 ms^{-1} (*Zhang and Forbes*, 2013). The lunar semidiurnal tidal amplitude generally remains at least 3 times smaller than the solar semidiurnal tide at those altitudes

The classical tidal theory describes the basic characteristics of atmospheric tides (*Chapman and Lindzen*, 1970). It assumes the motion of waves as a linear perturbation in the motionless initial zonal mean states neglecting dissipation in the horizontally stratified and isothermal atmosphere. The classical tidal theory concludes that the atmospheric tides are eigenmodes of the Hough function (eigenfunction).

The latitudinal and altitudinal structure can be described by Laplace's tidal equation which is

$$L\Theta_n + \varepsilon_n \Theta_n = 0 \tag{1.14}$$

where, L is the Laplace operator given by

$$L = \frac{\partial}{\partial \mu}\left[\frac{(1-\mu^2)}{(\eta^2-\mu^2)}\frac{\partial}{\partial \mu}\right] - \frac{1}{\eta^2-\mu^2}\left[\frac{s}{\eta}\frac{(\eta^2+\mu^2)}{(\eta^2-\mu^2)} + \frac{s^2}{1-\mu^2}\right] \tag{1.15}$$

where, $\mu = sin\phi$; $\eta = \sigma/(2\Omega)$; s = zonal wave number of a wave; ϕ = geographic latitude; σ = frequency; and Ω = angular velocity of the Earth. Its eigenvalue are given by,

$$\varepsilon_n = \frac{(2\Omega r)^2}{gh_n} \tag{1.16}$$

where, r denotes the Earth's radius, g denotes the gravity acceleration, and h_n denotes the *equivalent depth* which defined the tide's latitudinal structure with altitudinal structure. Therefore, each pair of frequency and wavenumber is superposed of the different Hough mode of index n. The vertical wavelength is linked to the h_n and can be defined as,

$$\lambda_{(z,n)} = \frac{2\pi H}{\sqrt{\frac{kH}{h_n} - \frac{1}{4}}} \tag{1.17}$$

The Hough function, θ_n are labeled by (m, n) where m corresponds to the longitudinal structure and n stands for latitudinal structure. The different Hough functions for the diurnal (m=1) and semidiurnal tides (m=2) are shown in Figure 1.11. Even and odd

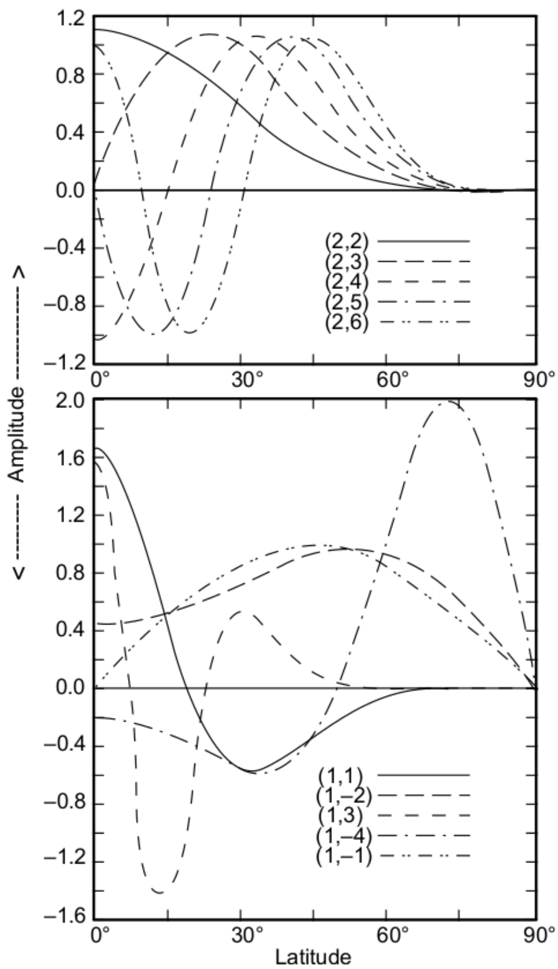

Figure 1.11: Different Hough mode correspond to the solar semidiurnal (above) and diurnal (below) tide are shown. Due to the small difference between the period of solar and lunar semidiurnal, these Hough mode structures can also represent good approximations for the lunar semidiurnal tide. (From *Forbes and Garrett* (1979))

values of n represent the symmetric and anti-symmetric modes, respectively, and negative values correspond to the non-propagating Hough modes.

Upward propagation of these tides is significantly influenced by the atmospheric winds and temperature variations (e.g., *Chapman and Lindzen*, 1970; *Lindzen and Hong*, 1974; *Jin et al.*, 2012). The atmospheric circulation and temperature distribution up to an extent depends on the strength of the stratospheric polar vortex that is discussed below.

1.3 Stratospheric polar vortex (SPV)

Over the northern hemisphere during winter, the Arctic stratospheric polar vortex (SPV) manifests itself in the form of planetary-scale eastward winds that encircle the mid-to-high latitudes polar region. During winter months, the northern polar region experiences prolonged darkness due to the latitudinal variation of solar insolation, which leads to cooling in the stratospheric polar region than the surrounding areas. Thus, the temperature gradient between mid-latitudes and pole causes a poleward flow which spins up due to the Coriolis force, and causes an eastward flow around mid-latitudes. The SPV span from about 100 hPa to above 1 hPa in altitude and it also extends up to mesosphere (*Waugh et al.*, 2017; *Harvey et al.*, 2018). The strong eastward winds associated with the SPV trap the cold(warm) air inside(outside) the polar circular pattern.

The strength of the SPV can get modulated by the coupling with the upward propagating tropospheric PWs. The lack of PW activity leads to an anomalous strong polar vortex (e.g., *Lawrence et al.*, 2020) that exhibits a cool polar stratosphere and strong zonal eastward flow. However, the breaking of the upward propagating amplified PWs which are coming from the troposphere leads to deposition of momentum in the westward direction. This westward drag causes a reduction in the eastward winds or in extreme cases, it can reverse the direction of the eastward zonal wind within a few days (*Matsuno*, 1971b) which leads to the weakening of the SPV. The SPV is displaced from the pole or split into two parts via the interaction between the zonal mean flow and PWs which are associated with the wave number 1 or 2 of the PWs, respectively (*Charlton and Polvani*, 2007). The descending of the polar atmosphere results in a sudden enhancement in the stratospheric temperature due to adiabatic heating. In this background, the polar stratospheric temperature enhancement and the weakening of the polar vortex are known as stratospheric sudden warming (SSW).

According to World Meteorological Organization (WMO), SSWs are classified into 2 categories: major SSW and minor SSW. If the zonal mean temperature (ZMT) at 10 hPa pressure level (∼30 km) or below increases poleward from 60° N latitude and zonal mean zonal winds (ZMZW) at 60° N latitude reverse its direction then it is associated with the major SSW. If only ZMT increases poleward from 60° N latitude and ZMZW reduced but remains westward, then it is called minor SSW (*Charlton and Polvani*, 2007). Figure 1.12 gives the overview of the ZMZW and ZMT variability with day of the year from 1st December to 1st April obtained from ERA 5 (European Environment Agency) during weak and strong SPV at 10 hPa at 60° N latitude. The variation of ZMZW during the 2015-2016 winter having a strong SPV and during the 2008-2009 winter having a weak SPV is shown in Figure 1.12a as solid blue and red lines, respectively. Similarly,

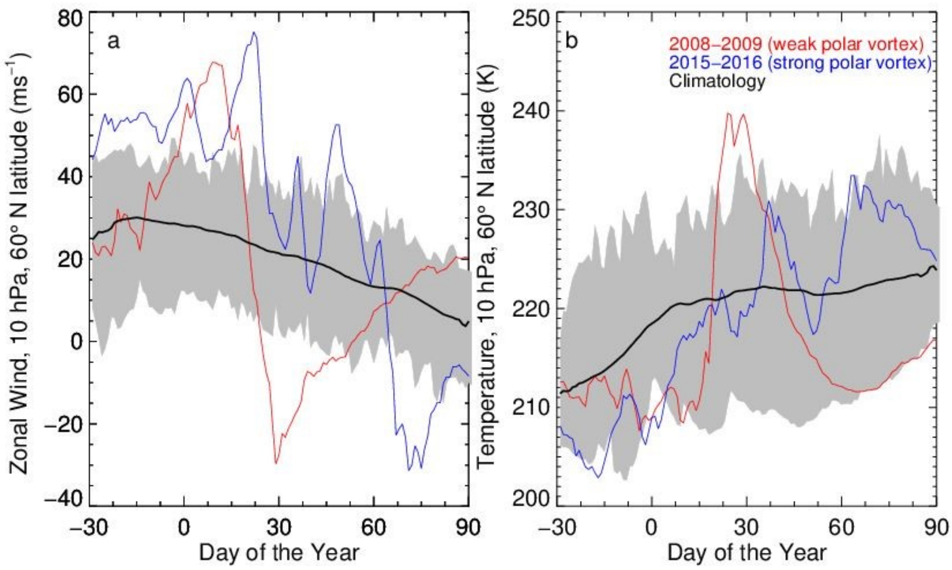

Figure 1.12: The ZMZW and ZMT variation from 1st December to 1st April are shown here at 10 hPa altitude at 60° N latitude in panels a and b, respectively. The grey-shaded regions represent the range of ZMZW and ZMT when the polar vortex is neither strong nor weak during 1980-2020. The black line shows the mean value of each day across these years which represents the seasonal variation (climatology). The red line denotes the ZMZW and ZMT variability in the winter of 2008-2009 having a weak polar vortex at the end of January 2009. The ZMZW and ZMT variation for the winter of 2015-2016 having a strong polar vortex are shown by the blue colored line.

ZMT is shown in Figure 1.12b. The climatology represented by the black line is obtained by averaging each day across the years 1980-2020 when the SPV is neither strong nor weak (for values of Northern Annular Mode (NAM) < 1 & > -2). The NAM index is discussed in Chapter-2. The gray shaded area corresponds to the range of ZMZW and ZMT values considered when calculating climate variation. As mentioned earlier, the Arctic SPV is cooled via radiative cooling and manifests itself as the strong westerly winds in the northern hemispheric winter. The zonal mean flow is reduced or reversed after interacting with the upward propagating tropospheric planetary waves, which causes the weak stratospheric polar vortex. During 2008-2009 winter, the ZMZW decreases rapidly and gets reversed at around day 30 whereas the ZMT shows sudden enhancement of more than 30 K. At around day 10, the SPV was strong before the occurrence of weak as ZMZW was more around 40 ms^{-1} and ZMT was low around 10 K than their seasonal variations and lasted for around 20 days. In the winter of 2015-2016, the strong SPV lasted more than one month as ZMZW (blue line) is very strong, exceeding 75 ms^{-1} in late January and remaining above its climatological levels from December 2015 to January 2016. ZMT for the same period is about 10 K lower than their climatological value. In early February 2016, the ZMZW drops sharply and ZMT increased, which belongs to a marginal weakening of the SPV.

The effects of the SSW have been found throughout the atmosphere even though it occurs in the middle atmosphere, and extensively investigated. The effects of SSW in the middle and upper atmosphere are extensively discussed in several review articles (*Holton*, 1980; *Chau et al.*, 2012; *Baldwin et al.*, 2021; *Goncharenko et al.*, 2021). As shown in Figure 1.13, the SSW is associated with the cooling in the stratosphere over low-latitudes and in the mesosphere at high latitudes, and heating in the lower thermosphere over high-latitudes and in the mesosphere over low-latitudes that occur due to the changes in the residual circulation and filtration of waves (e.g., *Körnich and Becker*, 2010). The upper atmospheric dynamics altered during the SSW period is primarily driven by the modulated atmospheric tides which occur due to the changes in the atmospheric wind field and temperature. Also, the lunar tides, which are generally very small relative to the solar tides, enhanced during the SSW period (e.g., *Forbes and Zhang*, 2012; *Pedatella et al.*, 2014). The effect of the strong SPV on the upper atmosphere is relatively less known. *Pedatella and Harvey* (2022) have shown that the behavior of the ZMT and ZMZW are

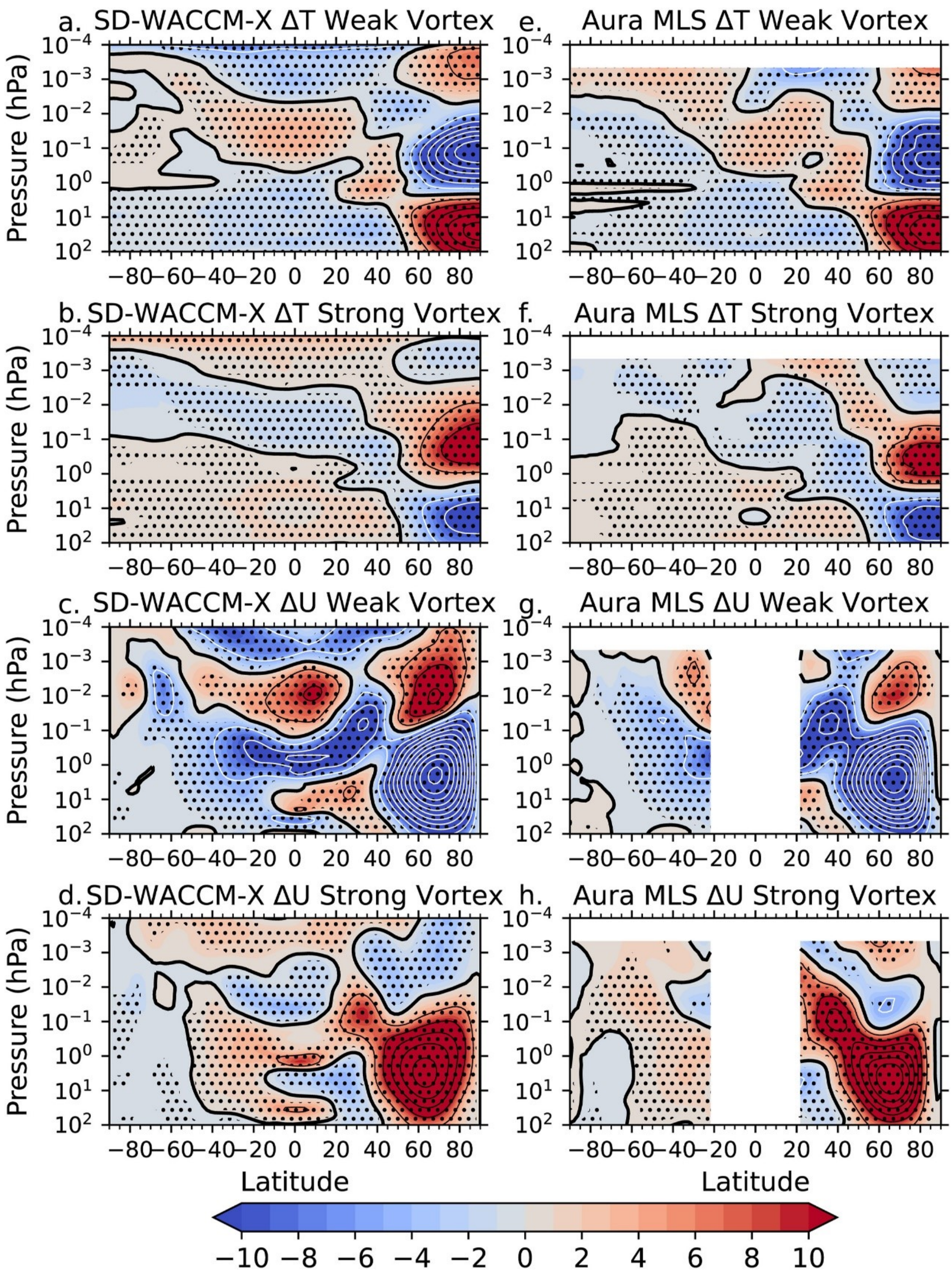

Figure 1.13: The SD-WACCM-X zonal means anomalies (a) in temperature during weak SPV, (b) in temperature during strong SPV, (c) in zonal winds during weak SPV, and (d) zonal winds during strong SPV. Panels (e-h) are the same as (a-d) except for Aura MLS observations. Stippling represents the 99% significance. The thick line corresponds to the zero values whereas thin black lines denote each 5 K or ms^{-1}. (From *Pedatella and Harvey* (2022))

opposite to those occurred during SSWs in the middle atmosphere, and Mesosphere and Lower Thermosphere (MLT) region as shown in Figure 1.13. This figure shows the anomalies in ZMT and ZMZW during weak and strong SPV using SD-WACCM-X (Specified

Dynamics version of Whole Atmosphere Community Climate Model with thermosphere-ionosphere extension) simulations and Aura MLS (Microwave Limb Sounder) observation. The effect of the SPV on the MLT and ionosphere is discussed in Chapter-3 in greater detail.

1.4 Daytime upper atmospheric Phenomena over low- and equatorial-latitudes

1.4.1 Solar quiet (Sq) and equatorial electrojet (EEJ) currents

In the recording of geomagnetic field variations, the main contribution comes from the geodynamo current that is flowing in the Earth's core, along with some other sources which are just a fraction of the total field strengths recorded. Among these, one is the ionospheric current called *Solar quiet* (Sq). Due to the dependence on local time, these variations are called solar variations. These variations are called quiet because the variation due to the geomagnetic disturbance can easily mask Sq variations. First time, *Graham* (1724) made Sq observations using a long magnetic needle. *Stewart* (1882) proposed a hypothesis that Sq current generates in the conductive region of the upper atmosphere. When an electrically conducting wind (U) moves across the magnetic field of the Earth (B), it gives rise to an electromotive force (U × B). These electromotive forces cause electric fields and currents. The strength of the Sq current density that exists in the dynamo region of the atmosphere, is of the order of μAm^{-2}.

The basic pattern of Sq current is consistent throughout the year despite the seasonal variations, which refers to counter clock-wise pattern in the Northern Hemisphere, and a clockwise pattern in the Southern Hemisphere as seen in Figure 1.14. The enhanced Sq variations over the dip equatorial region is associated with the strong zonal currents which is known as *Equatorial Electrojet* (EEJ) (*Chapman*, 1951). This enhancement occurs due to the strong Cowling Conductivity which gets enhanced locally over the dip equatorial E-region in the presence of the horizontal nature of geomagnetic field lines (*Hirono*, 1950; *Baker and Martyn*, 1953). The EEJ is confined in the ±3° magnetic latitudinal belt

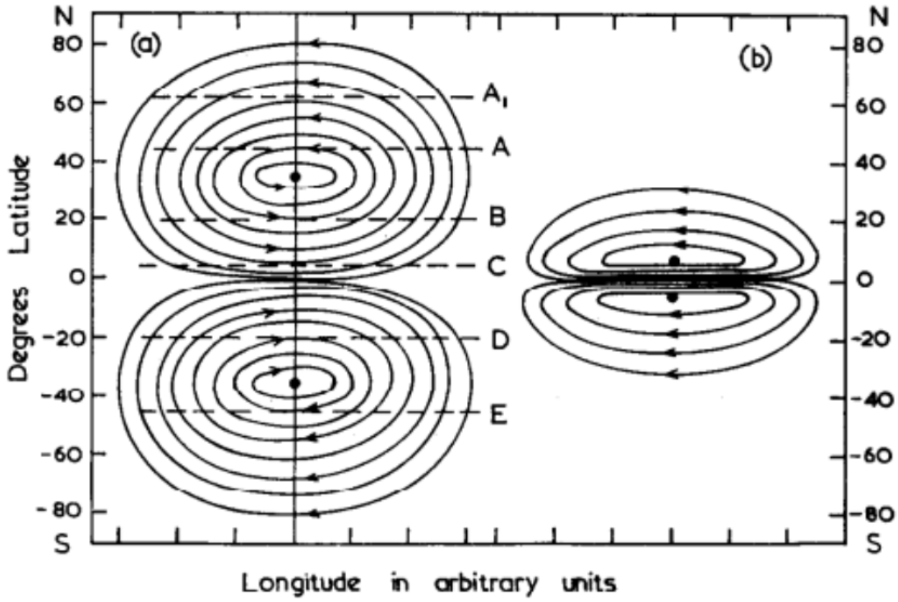

Figure 1.14: The schematic diagram of Sq and EEJ currents are shown in (a) and (b), respectively. (From *Ogbuehi et al.* (1967))

around the dip-equator. The effect of cowling conductivity is illustrated in Figure 1.15. In the daytime, an eastward electric field generated due to the westward neutral winds (E_y in Figure 1.15) exits over the dip equatorial region due to charged separation in the dynamo region. This E_y being completely orthogonal to the northward geomagnetic field lines above the dip equator, gives rise to a current in the direction of the electric field due to Pedersen current ($J_{P1} = \sigma_P E_y$) in the eastward direction along to the downward Hall current ($J_{H1} = \sigma_H E_y$). A charge accumulation occurs around the boundary of the dynamo region as this downward Hall current is inhibited by the D and F regions due to smaller conductivities below and above. This charge separation in the vertical direction causes an upward electric field (E_p) which again leads to the Pedersen current ($J_{P2} = \sigma_P E_P$) in the upward direction and Hall current in the Eastward direction ($J_{H2} = \sigma_H E_P$). The downward Hall and upward Pedersen currents balance each other i.e.,

$$\sigma_H E_y = \sigma_P E_P \tag{1.18}$$

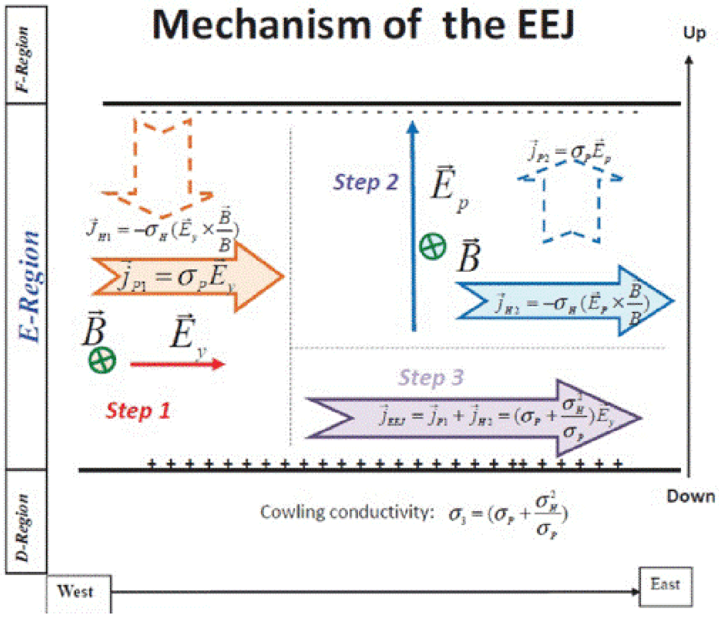

Figure 1.15: Figure illustrates the mechanism of the EEJ. (From *Grodji et al.* (2017))

Thus, the net current in the eastward direction, EEJ, can be defined as

$$J_{EEJ} = J_{P1} + J_{H2} = \sigma_P E_y + \sigma_H E_p \tag{1.19}$$

$$J_{EEJ} = \left(\sigma_P + \frac{\sigma_H^2}{\sigma_P}\right) E_y = \sigma_C E_y \tag{1.20}$$

where, σ_C is the cowling conductivity.

Occasionally, the strength of the EEJ becomes negative which is known as the counter Electrojet (CEJ), and occurs due to the westward electric field in the dynamo region.

Neutral winds in dynamo region are driven by the upwards propagating tides from lower atmosphere, therefore, their variations are also propagated into the EEJ. *Lühr and Manoj* (2013); *Soares et al.* (2022) investigated the contribution of different migrating and non-migrating solar tides on the EEJ. In addition, lunar tides influence the EEJ strength but, generally, their contribution is smaller than solar tides(e.g., *Bartels and Johnston*, 1940).

Some earlier studies showed the effect of the SSW on the ionospheric dynamo (e.g., *Brown and Williams*, 1969; *Matsushita and Xu*, 1984; *Stening et al.*, 1996; *Rastogi*, 1999).

Stening (1977) and *Stening et al.* (1996) found the occurrence of CEJ events during SSWs. *Vineeth et al.* (2009) also discussed that CEJ is prone to quasi 16 days wave modulation during SSW. *Sridharan et al.* (2009) have shown that semidiurnal tides get enhanced in the mesosphere during CEJ events associated with SSW. *Fejer et al.* (2010) identified several characteristics of CEJ events during SSW, including a tendency for onset near new or full moon, CEJ is associated with an enhanced eastward flow in the morning, and a shift in the timing of maximum currents to later local times on succeeding days. These features suggest the influence of lunar currents, leading to the proposal that strongly enhanced atmospheric lunar tides drive electrodynamic perturbations during SSW events. Later, numerical and observational studies have shown that both solar and lunar semidiurnal tides get enhanced during SSW (e.g., *Pedatella et al.*, 2012, 2014; *Siddiqui et al.*, 2018). More details of the tidal variations with the strength of the SPV are available in Chapter-3.

1.4.2 Equatorial ionization anomaly (EIA)

It is expected that during equinoxes, greater plasma density should exist over the equator due to more photoionization as compared to low-latitudes. However, in observation, a different scenario is observed in which higher density is found over low-latitudes on either side of the dip equator than in the equatorial region. This behavior is called Equatorial Ionization Anomaly (EIA) or Appleton anomaly (*Appleton*, 1946). The EIA is a result of two processes, namely, the equatorial vertical E×B drift and the plasma diffusion along the geomagnetic field lines as illustrated in Figure 1.16. As discussed above, an eastward electric field is generated by the charge separation in the E- region of ionosphere due to the tidal winds. This electric field is mapped along to the geomagnetic field lines from low-latitudes of E-region to the dip equatorial region into F- region due to large conductivity, and gives rise to the vertical E×B drift over equatorial region. Therefore, plasma gets uplifted over the equatorial region and diffuses along the geomagnetic field lines due to the pressure gradient forces and gravity after reaching certain altitudes. It results in an enhancement in the plasma density over low-latitudes (15°-20° magnetic latitude) in both hemispheres (crest of EIA) and a reduction in density over the magnetic equatorial region (trough of EIA). The strength of EIA can be quantified by the product of the latitude difference between crest & trough and the plasma density ratio over crest & trough (*Rush*

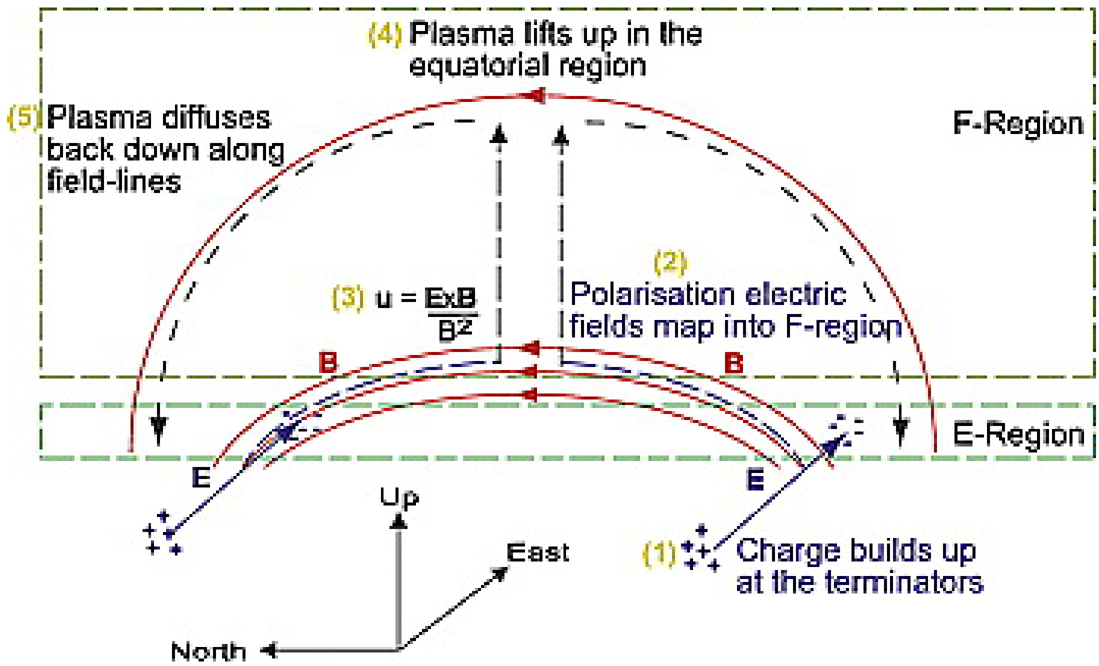

Figure 1.16: Schematic diagram of the EIA process. (1) Charge separation gives rise to an eastward electric field, (2) electric field maps from E-region to F-region along the geomagnetic field lines due to higher conductivity, (3) it gives rise to an E×B drift in the upward direction, (4) Plasma lifts up over the equatorial region, and (5) diffuses along the geomagnetic field lines due to the pressure gradient and gravitational forces. (From *Immel et al.* (2006))

and Richmond, 1973). The strength of the EIA has been shown to be directly proportional to the strength of the prenoon integrated EEJ strength (e.g., *Raghavarao et al.*, 1978a). The EIA plays an important role in bringing about latitudinal changes in plasma densities. The strength of the EIA can be altered by the neutral winds (*Anderson*, 1973; *Balan et al.*, 1995, 1997a; *Khadka et al.*, 2018), magnitudes of vertical drift (*Woodman*, 1970; *Fejer*, 1981; *Rastogi and Klobuchar*, 1990; *Stolle et al.*, 2008; *McDonald et al.*, 2011; *Venkatesh et al.*, 2015), solar activity (*Sastri*, 1990; *Huang et al.*, 2013; *Oluwadare et al.*, 2019), and compositional variation brought in during geomagnetic storms (*Fuller-Rowell et al.*, 2008; *Pedatella et al.*, 2010; *Karan and Pallamraju*, 2018). The EIA is also influenced by other factors, such as, tidal effects (e.g., *Goncharenko et al.*, 2010; *Chau et al.*, 2012; *Goncharenko et al.*, 2021; *Pedatella et al.*, 2014), planetary waves (e.g., *Laskar et al.*, 2013; *Yamazaki*, 2018; *Mo and Zhang*, 2020; *Miyoshi and Yamazaki*, 2020), and gravity waves (e.g., *Varney et al.*, 2009; *Pallamraju et al.*, 2010; *Yiğit and Medvedev*, 2016; *Karan and Pallamraju*, 2017; *Rakesh et al.*, 2022), which can modulate the strength and location of the EIA. The effect of the neutral winds on the modulation of the EIA has been discussed in detail in Chapter-4.

As a consequence of the EIA, the plasma density is greater over the low-latitudes. Due to that, neutrals experience more ion-drag force over low-latitudes than over equator. As a result, more neutral density accumulated over low latitudes in both hemisphere and seems anomalous, which is called neutral anomaly (*Hedin and Mayr*, 1973). They have

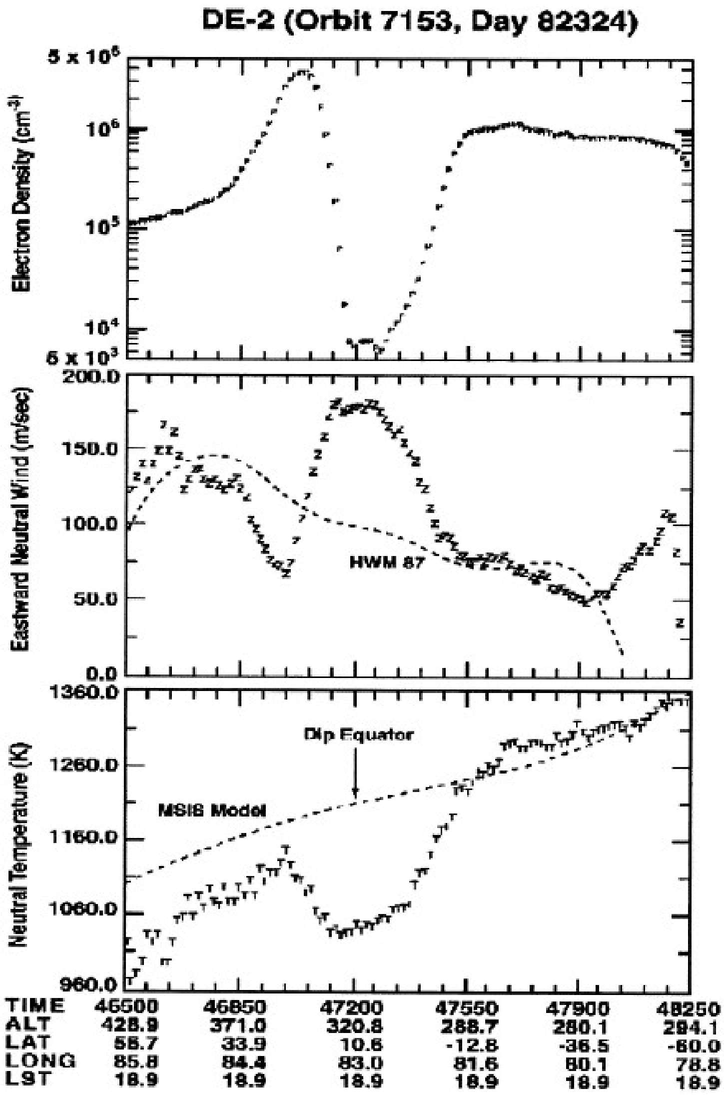

Figure 1.17: The figure shows three panels from top to bottom representing the measurement of electron density, zonal wind, and neutral temperature, respectively. The measurement was obtained from the DE-2 satellite on 20 November 1982 at 18.9 local time. The measured values are compared with the predictions from two empirical models: the Horizontal Wind Model 1987 (HWM87) and the Mass Spectrometer Incoherent Scatter 1986 (MSIS86). (From *Raghavarao et al.* (1991))

reported that molecular nitrogen density at the crest region was enhanced by around 20% than that of the trough. *Raghavarao et al.* (1991) observed that the plasma density, measured from Langmuir Probe, neutral winds, and temperature obtained from Wind And Temperature Spectrometer (WATS) on-board Dynamic Explorer-2 (DE-2) show different kind of behavior with latitudes than the model data as shown in Figure 1.17. It can be seen that the electron density and temperature are higher over low-latitudes than at the equator, whereas the zonal winds show opposite behavior than the electron density and temperature as it is higher over equator than low-latitudes. This kind of structure in temperature and zonal winds has been named as Equatorial and Temperature Anomaly (ETWA). This structure is due to the ion-drag caused by EIA as larger plasma density over low-latitudes cause a reduction in wind and enhancement in neutral density and temperature, whereas opposite happens over the equator. The difference in wind and temperature between their crest and trough are found to be around 100 ms^{-1} and 50 K, respectively.

1.4.3 Thermospheric neutral winds

Neutral winds in lower thermosphere are driven by the upwards-propagating tides from lower atmosphere. In general, tides generated in the lower atmosphere dominate the winds field below ∼150 km, whereas, in the region above, neutral winds are dominated by in-situ generated tides due to solar heating. Thermospheric neutral winds can have significant impacts on the dynamics of the UA as these winds can affect the distribution and density of neutral species and ions in the ionosphere.

Thermospheric neutral winds are affected by the Coriolis force. Also, the winds are influenced by the viscosity of air and collision of neutrals with ions which is called the ion-drag. In the daytime during equinoctial months, winds flow from equator to pole due to the pressure difference created by the differential heating by the solar insolation. Over the polar region, electric currents are generated due to particle precipitation which gives rise to the heating. Therefore, winds get set up towards the equator from the polar region. As ions move along the magnetic field line, exert ion-drag force on neutral which is $\nu_{ni}(v_n - v_i)$, where, ν_{ni} is the collision frequency of neutrals with ions, v_n is the velocity of the neutral winds, and v_i is the ion drift. Generally, daytime winds are weaker than nighttime winds due to the ion-drag force which is different in daytime and nighttime due to the difference in ion density. Also, meridional winds influence the altitude of ion density as they exert a drag along the geomagnetic field lines. The poleward/equatorward winds bring the ions at lower/higher altitudes which causes change in the plasma density due to the altitudinal dependence of the recombination rate of ions (e.g., *Rishbeth*, 1977; *Su et al.*, 1994; *Balan et al.*, 1997b; *Shim et al.*, 2010; *Saha et al.*, 2021; *Kumar et al.*, 2022). The zonal winds in thermosphere are generally in west(east) direction in daytime(nighttime) due to the differential solar radiation heating in day and night side. As discussed above, this zonal winds in the dynamo region gives rise to the electric field (*Gouin and Mayaud*, 1967; *Onwumechilli*, 1967; *Rishbeth*, 1997; *Yamazaki et al.*, 2021).

The measurements of the thermospheric neutral winds are carried out from satellites (e.g., *Spencer et al.*, 1981; *Hedin et al.*, 1988; *Shepherd et al.*, 1993b; *Killeen et al.*, 2006; *Englert et al.*, 2017) and ground-based (e.g., *Burnside et al.*, 1981; *Meriwether et al.*, 1984, 1986; *Shiokawa et al.*, 2003; *Makela et al.*, 2013; *Kumar et al.*, 2023a). The diurnal, day-to-day, and seasonal variation in the upper atmospheric dynamics due to neutral winds is well known (e.g., *Mayr et al.*, 1978). Empirical results of the neutral winds are presented for different geomagnetic conditions (*Kohl and King*, 1967; *Roble et al.*, 1987; *Hedin et al.*, 1996; *Emmert et al.*, 2008; *Drob et al.*, 2008, 2015). In this thesis, one empirical model, Horizontal Wind Model (HWM-14) (*Drob et al.*, 2015) has been used to derive the thermospheric winds.

1.5 Summary

In this chapter, the atmospheric structure is discussed which is classified into different regions based on the temperature. In the upper atmosphere, solar radiation causes the ionization of neutral species (atoms & molecules) to form the ionosphere, which affects the radio wave propagation. The ionosphere is divided into different layers based on the energetic spectrum of solar radiation and the relative behavior of the ions and electrons with regard to neutral motions vis-á-vis the constraint imposed by the magnetic field. The upper atmospheric dynamics is significantly governed by different kinds of waves, such as, GWs, PWs, and tides that are mainly generated in the lower atmosphere. Their roles on the upper atmospheric dynamics under different backgrounds, sources, and dynamics have been discussed in detail in this chapter. Also, a few equatorial- and low-latitudinal upper atmospheric electrodynamical phenomena are described that drive the upper atmospheric dynamics over low- and equatorial-latitudes. The electrodynamics is significantly driven by the lower atmospheric forcing through these waves and has been discussed in this chapter. These waves can be modulated during different state of the SPV. The weak and strong SPV and their effects on the atmosphere has been discussed.

1.6 The objective of the thesis

The main objective of the thesis work is to understand the daytime ionospheric and neutral dynamics of UA over low- and equatorial-latitudes, and its plasma-neutral coupling. OI 630.0 nm dayglow emission, which acts as a tracer of the thermospheric altitudes (around 230 km) from where they emanate, is used as primary data in this thesis work. In addition, we have also used other data sets, such as, geomagnetic observation, neutral winds, ionospheric data, etc. Several interesting observations have been obtained, listed as follows, and investigated in this thesis work to understand the daytime variability of the ionosphere-thermosphere system.

I. It is well known that during weak SPV, tidal waves get amplified and alter the equatorial electrodynamics of the UA significantly. Is there any effect of strong SPV as well on the upward propagating waves? If it does, how much can it contribute to the variation in the electrodynamics?

II. What is the contribution of the equatorial electrodynamics in the variability of the OI 630.0 nm dayglow emissions measured over $5° - 18°$ MLAT? Besides, is there any significant role of the meridional winds in the plasma distribution?

III. We have three-dimensional upper atmospheric information using collocated large FOV optical and radio measurements. Is it possible to derive the three-dimensional GWs characteristics using this information and subsequently the thermospheric neutral winds?

1.7 Layout of the thesis

The thesis is structured as given below,

Chapter 1 gives an overview of the atmospheric structure and different phenomena that drive the upper atmospheric dynamics over low-and-equatorial latitudes.

Chapter 2 describes the instrumentation and different data sets used in this thesis work. Further, data filtering and analysis techniques have been discussed in detail.

Chapter 3 presents the effect of the state of the stratospheric polar vortex on the equatorial electrodynamics through modulations in the semidiurnal tides.

Chapter 4 describes the effect of the equatorial electrodynamics and meridional winds on the distribution of the electron density in large spatial extent using OI 630.0 nm dayglow emissions.

Chapter 5 discusses the estimation of the thermospheric neutral winds using a three-dimensional gravity wave structure, wherein OI 630.0 nm dayglow and electron density data have been used innovatively.

Chapter 6 presents the summary and future scope of the thesis.

Chapter 2

Measurement techniques and data analysis

2.1 Introduction

In the previous chapter, the background and motivation of this thesis work on the effect of lower atmospheric forcing on the equatorial electrodynamics which drives the upper atmospheric dynamics over low-latitudes have been discussed. Also, shorter- to larger-scale waves presented in the atmosphere that influence the UA are discussed. Systematic measurements of various atmospheric parameters, such as, airglow emission rates, neutral winds, plasma dynamics (density & drifts), electric field, and magnetic fields are crucial to gain a comprehensive understanding of the upper atmospheric processes. In this thesis work, we have used different kinds of ionospheric and thermospheric ground-based and satellite-based observations. The OI 630.0 nm dayglow emission measured from the ground is used as primary data and it is obtained using Multi-wavelength Imaging Spectrograph using Echelle grating (MISE) from two different locations Ahmedabad (AHD, 23° N, 73° E, 15° MLAT) and Hyderabad (HYD, 17° N, 78° E, 9° MLAT) in the Indian longitudes (as shown in Figure 2.1). In addition, I have used other datasets, such as, radio measurements from AHD and geomagnetic observations from Indian and American longitudes, and they are shown in Figure 2.1. Further, I have used satellite-based measurements of thermospheric neutral winds by Ionospheric CONnection explorer (ICON) satellite. This chapter discusses these datasets and the details of different techniques that

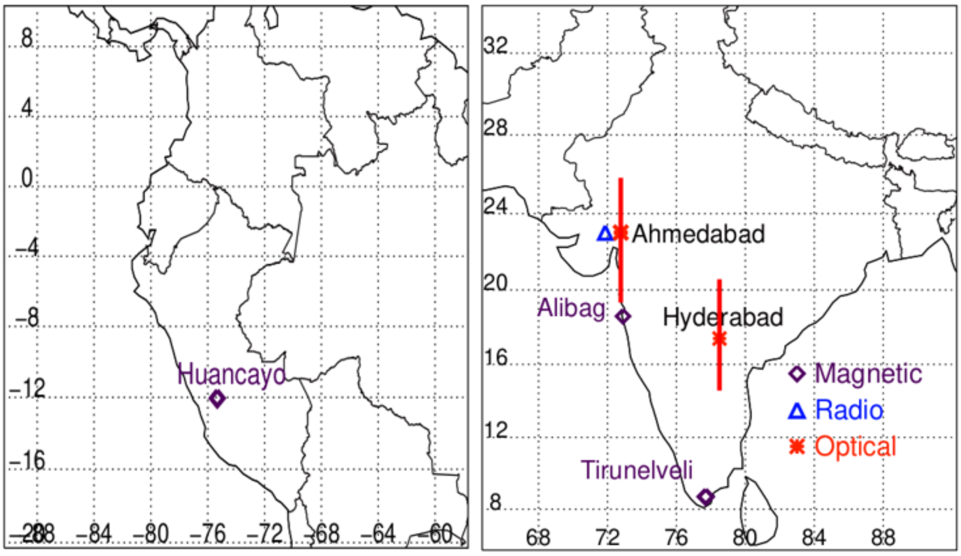

Figure 2.1: The locations over Indian and American longitudes from where optical (red asterisks), magnetic (purple squares), and radio (blues triangles) data have been obtained for this thesis work, are shown. The red bars over Ahmedabad and Hyderabad represent the field-of-view of optical spectrographs.

have been used for analyses of these datasets.

2.2 OI 630.0 nm dayglow emissions and measurement technique

Airglow refers to the naturally occurring atmospheric emissions in the UA as a result of photochemical reactions. The production mechanism of these emissions is different from one another and they originate at different altitude ranges. Emissions that occur in the daytime are referred to as the dayglow, nighttime as the nightglow, and twilight-time as twilight-glow. These emissions originate due to the transition from higher energy states to lower energy states in atoms, molecules, and ions. Airglow emissions are observed in wavelengths ranging from ultraviolet to infrared, and based on the densities of the reactants and background conditions these emissions at different wavelength peaks at different altitudes. Since the densities of the reactants get altered by the background processes, the airglow emissions serve as effective tracers of atmospheric dynamics of their origin altitudes. In the thesis work, we have used optical oxygen OI 630.0 nm dayglow emissions which peaks around 230 km. The details on the production of the OI 630 nm photons in our atmosphere and the instrumentation used to detect them have been described in the following sections.

2.2.1 Production mechanism of OI 630.0 nm dayglow emission

The airglow emission at 630.0 nm wavelength occurs due to the transition of atomic oxygen from $O(^1D)$ to $O(^3P)$ state. The excited state of atomic oxygen $O(^1D)$ in the daytime is mainly produced by the photoelectron impact excitation of atomic oxygen (O), photodissociation of molecular oxygen (O_2), and dissociative recombination (DR) of atomic oxygen ion (O_2^+) with ambient electrons (e_{th}) (*Solomon and Abreu*, 1989). The loss of $O(^1D)$ state occurs either through the emission of photons at 630.0 nm wavelength or quenching with the atmospheric constituents.

(a) Photoelectron impact excitation of atomic oxygen:

The energy associated with the $O(^1D)$ state is 1.96 eV. When a photoelectron with energy above 1.96 eV interacts with the atomic oxygen, it transfers its energy to produce the $O(^1D)$ state.

$$O + e_{ph}\,(energy > 1.96eV) = O(^1D) + e_{ph} \tag{2.1}$$

where, e_{ph} is photoelectron.

(b) Photodissociation of molecular oxygen:

The photons in the wavelength range of 135-175 nm (Schuman-Runge continuum) dissociate O_2 to produce $O(^1D)$.

$$O_2 + h\nu_{(135-175\,nm)} = O(^1D) + O \tag{2.2}$$

(c) Dissociative recombination (DR) of molecular oxygen ion with ambient electrons:

$$O_2^+ + e_{th} = O(^1D) + O \tag{2.3}$$

The molecular oxygen ions (O_2^+) in the atmosphere are produced due to the charge exchange process of atomic ion (O^+) with molecular oxygen (O_2).

$$O_2 + O^+ = O_2^+ + O \tag{2.4}$$

Thus, the $O(^1D)$ produced by all the above mechanisms can come to the ground state by emitting radiation,

$$O(^1D) \rightarrow O(^3P) + h\nu \tag{2.5}$$

or by quenching.

$$O(^1D) + O_2\ or\ N_2 \rightarrow O(^3P) + O_2\ or\ N_2 \tag{2.6}$$

The peak emission altitudes are different for different mechanisms, wherein, the

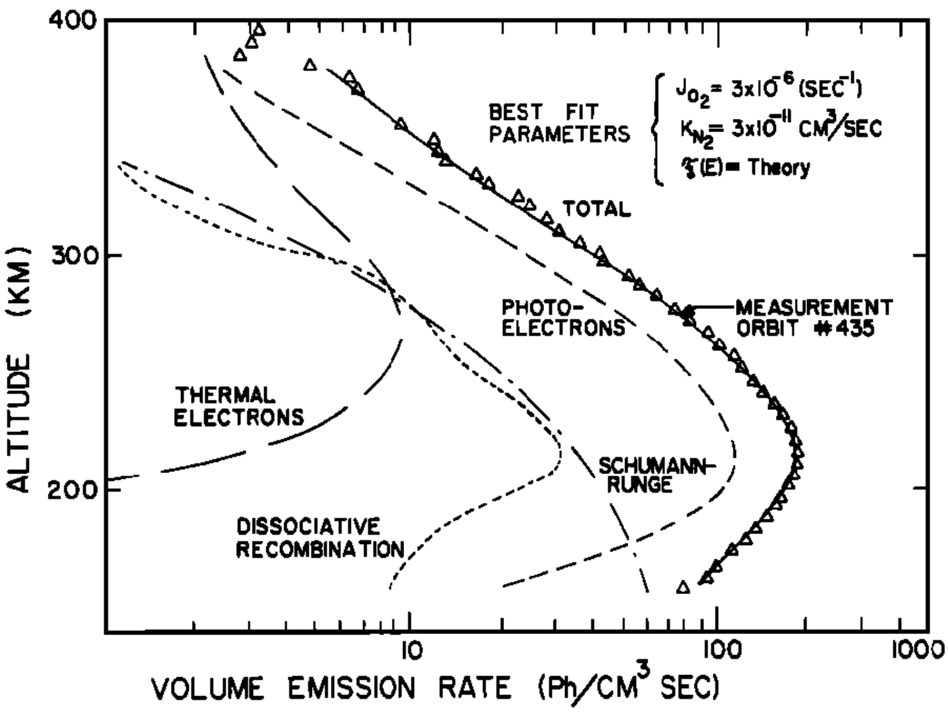

Figure 2.2: The volume emission rate of OI 630.0 nm dayglow emissions is shown with altitude obtained by visible airglow experiment onboard AE-C satellite along to the model-derived emission profile through different mechanisms. (From *Hays et al.* (1978))

emission due to DR peaks at the highest altitudes (around 230-250 km) in comparison to other production mechanisms as can be seen in Figure 2.2. Since photoelectron impact excitation of atomic oxygen and photodissociation of molecular oxygen depend on solar flux and solar zenith angle (SZA), therefore, information on the charge transport in the ionosphere gets imprinted in the OI 630 nm emission through the DR mechanism. In general, the DR mechanism contributes to around 30% of the total emissions but over low-latitudes this can be larger by a factor of 1.5-2 (*Solomon and Abreu*, 1989).

The volume emission rate (VER) of OI 630.0 nm airglow emission through DR mechanism can be estimated as:

$$VER\,(photons\,cm^{-3}s^{-1}) = \frac{\beta_1 K_1 [O^+][O_2] \cdot A_{630.0}}{A_{^1D} + K_2[N_2] + K_3[O_2] + K_4[e_{th}]} \tag{2.7}$$

where, β_1= yield of $O(^1D)$ production; $A_{630.0}$ = transition coefficient for $O(^1D)$ state to $O(^3P_2)$; $A_{^1D}$ = transition coefficient for $O(^1D)$ state to the triplet ground state $O(^3P)$; $K1$, $K2$, $K3$, and $K4$ = rate coefficients of their respective reactants. The values of these parameters have been obtained from (*Link and Cogger*, 1988) (and reference therein). From the equation 2.7, it can be noted that the production of state $O(^1D)$ depends on the density of O^+ ions and O_2 molecules. The excited state $O(^1D)$ can release a photon of 630.0 nm wavelength following a transition to ground state or lost via quenching through collision with N_2, O_2, and e_{th} (equation 2.5 and 2.6). For the ion density and electron temperature information, we have used the model International Reference Ionosphere-16 (IRI-16) (*Bilitza et al.*, 2017), and the neutral temperature and density of neutral species have been obtained using NRLMSISE-00 (*Picone et al.*, 2002). Thus, the VER of OI 630.0 nm emissions as a function of altitude are obtained.

Conventionally, ground-based techniques, such as, photometers, spectrometers, interferometers, and imagers (e.g., *Hernandez and Roble*, 1976; *Kulkarni*, 1976; *Shepherd et al.*, 1993b; *Mendillo and Baumgardner*, 1982; *Meriwether et al.*, 1986; *Sridharan et al.*, 1991; *Shiokawa et al.*, 1999)have been used to obtain airglow emission rates in the nighttime (nightglow) or twilighttime (twilightglow). However such measurements are extremely challenging in the daytime due to the presence of a strong scattered solar background continuum which is several orders more intense than the airglow intensity. Several methods have been applied to retrieve dayglow emissions buried in the background of strong solar radiation. These include the use of polarized and unpolarized nature of scattered sunlight and dayglow emissions, respectively, to measure $O(^1D)$ dayglow (*Noxon and Goody*, 1962); using the resonant scattering properties of Sodium atoms to measure Sodium emissions (*Blamont and Donahue*, 1964); use of Fabry-Perot (FP) etalons to achieve the required high spectral resolution for the measurement of dayglow (*Jarrett and Hoey*, 1963; *Bens et al.*, 1965; *Cocks and Jacka*, 1979). All these techniques could work within their own limitations (*Pallamraju*, 1996). *Narayanan et al.* (1989) and *Pallamraju et al.* (1996) presented a technique that can successfully measure dayglow emissions using a pressure-tuned low-resolution FP etalon along with a temperature-tuned narrow-band interference filter of bandwidth 0.3 nm, radial chopper, and up/down counting system. This technique involved photons collected from two spectral zones (separated by around 0.05 nm) with one region containing the information on dayglow contribution along with that of solar background and the other containing only that of the strong solar background. Then these photon counts from two regions are subtracted from one another and the contribution of OI 630.0 nm emission buried in the strong solar scattered background continuum is retrieved. *Sridharan et al.* (1993, 1998) further modified this instrument with a spiral mask to make the instrument capable of operating at multiple wavelengths, which was called the multiwavelength daytime photometer. This instrument has been used to study the behavior of daytime low- and equatorial-latitudes electrodynamics and daytime aurora from high latitudes (e.g., *Pallamraju*, 1996; *Pallamraju et al.*, 1995, 1996; *Sridharan et al.*, 1992b, 1995; *Pallamraju and Sridharan*, 1998; *Chakrabarty et al.*, 2005). This technique required a significant manual operation and later it has been upgraded to achieve automated operation. This new instrument is called, CCD-based daytime airglow photometer, CDAP (*Pallamraju et al.*, 2023).

Echelle gratings can yield high spectral resolution spectra but the issue of order overlapping have limited their comprehensive use. However, with the availability of interference filters and array detectors, echelle gratings have been explored to build spectrographs capable of measuring airglow emissions in the daytime. *Chakrabarti et al.* (2001) presented the High Throughput Imaging Echelle Spectrograph (HiTIES) to obtain the OI 630.0 nm nightglow emissions with a spectral resolution of 0.03 nm over a large field-of-view (FOV). This was followed by an echelle spectrograph, High Resolution Imaging Spectrograph using

Echelle grating (HIRISE) (*Pallamraju et al.*, 2002), capable of measuring daytime optical airglow emission intensity. Later, HIRISE was modified to carry out dayglow measurements simultaneously at multiple wavelengths, 557.7, 630.0, and 777.4 nm, and this new instrument is known as MISE (*Pallamraju et al.*, 2013). The principal dataset, OI 630.0 nm dayglow emissions, used in this thesis work are obtained from MISEs operational at AHD and HYD in India. The details of the MISE have been described below.

2.2.2 Multi wavelength imaging spectrograph using echelle grating (MISE)

MISE is a high-resolution echelle spectrograph that is capable of dayglow observations at three wavelengths, OI 557.7 nm, OI 630.0 nm, and OI 777.4 nm, simultaneously. In this thesis work, I have used only OI 630.0 nm dayglow emission. MISE has a large

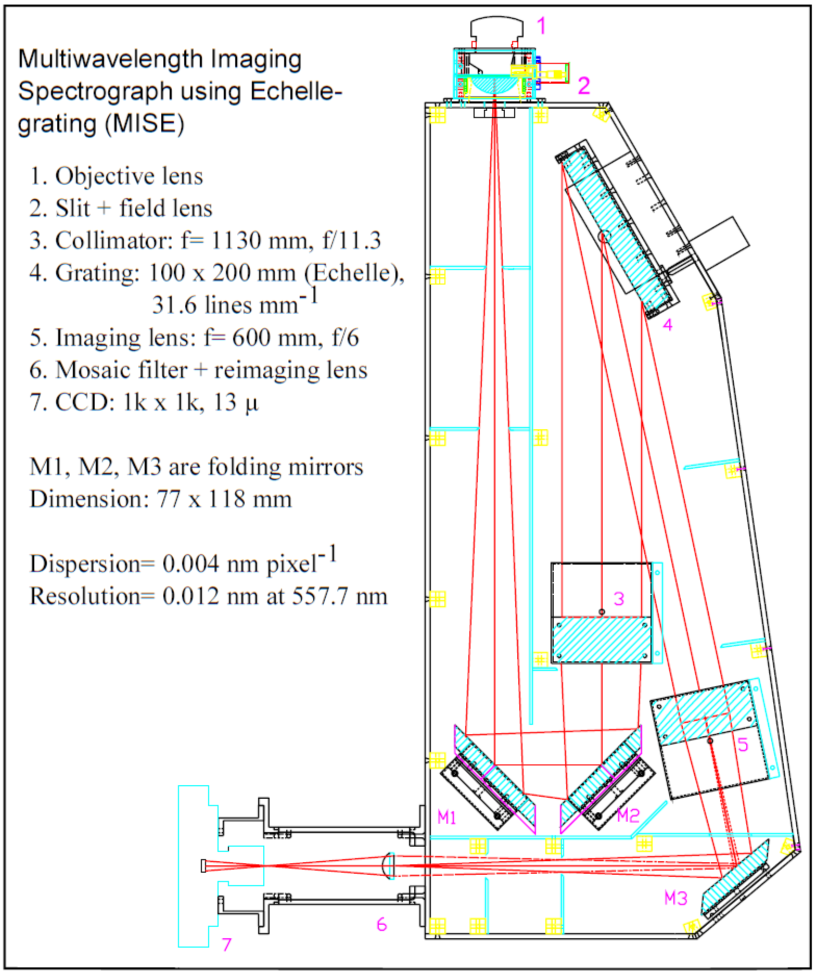

Figure 2.3: Schematic diagram of MISE. The specification of different optical components are mentioned. The red lines denote the ray diagram. (From *Pallamraju et al.* (2013))

FOV (~140°) which is around 650 km spatial region along the slit orientation for 230 km altitude where OI 630.0 nm emission peaks. Figure 2.3 represents the schematic diagram of MISE which shows different elements including: objective lens, slit, field lens, echelle grating, collimator, mirrors, imaging lens, detector. The specification of MISE and details of its components are given in Table 2.1.

2.2.3 Components of MISE

The main optical components of MISE are discussed as follows:

Table 2.1: Characteristics of MISE and details of its optical components are given. (From *Pallamraju et al.* (2013))

Slit length	39 mm
Slit width	0.12 mm
Throughput (AΩ)	2.8785 $\times 10^{-4} cm^2 sr$
Collimator	F = 113 cm (f/11 Apochromat)
Grating	31.6 lines mm^{-1}, blaze angle = 63.5° (Size = 110 mm × 220 mm × 30 mm)
Camera lens	F = 60 cm (f/5 Apochomat)
Total optical transmission	0.010197 (557.7 nm); 0.030775 (630.0 nm); 0.066338 (777.4 nm)
CCD	quantum eff., q(λ): q (557.7 nm) = 0.95, q (630.0 nm) = 0.93, q (777.4 nm) = 0.8, Gain, g = 1.5259 $e^{-} DN^{-1}$
Total efficiency, $Q(\lambda)$	Q (557.7 nm) = 0.62259, Q (630.0 nm) = 0.6095, Q (777.4 nm) = 0.5243 $DN ph^{-1}$, 13 μ m, 1k × 1k, E2V Chip
No. of rows (n_{rows})	110 for 8-pixels binning along the slit
Dispersion, $d(nm\ pixel^{-1})$	d (557.7 nm) = 0.004, d (630.0 nm) = 0.0049, d (777.4 nm) = 0.0059

(i) Objective lens: A fish-eye lens has been used as the objective lens which is installed in the front of MISE. Like fish who can see all the sky from one horizon to the other, a fish-eye lens is a type of camera lens that has a very wide FOV up to 180 degrees. The lens used in MISE has a focal length of ~12 mm.

(ii) Slit and field lens: After the light passes through the objective lens, it falls on the slit of MISE. The length and width of the slit are ~39 mm and ~0.12 mm, respectively. Here, the curved slit is designed to reduce the curvature of the image that arises due to diffraction of the off-axis beam and it is also discussed later. A field lens is then placed just after the slit of MISE as can be seen in Figure 2.3, to restrict the divergence of the light beams coming from the fish-eye lens through the slit. The focal length of the field lens is 75 mm.

(ii) Mirrors and collimating lens: The purpose of mirrors (M1, M2, and M3) is to fold the light beams. The light falls on the f/11 apochromatic collimating lens after transmitting from the field lens with the help of mirrors M1 and M2, which are orthogonal to each other as shown in Figure 2.3. This light is collimated by this apochromatic lens. The apochromatic lens uses three elements to reduce chromatic aberration over a large spectral range and converges the light from different wavelengths to a single point.

(iv) Echelle grating: Collimated light falls onto the Echelle grating after passing through the collimator. Echelle grating works at high incidence and diffraction angles which enables it to achieve a high-resolution at higher orders. The groove density of echelle grating is around 31.6 lines/mm. This is much smaller than that of any standard grating, wherein, the groove density is of the order of thousand lines/mm. The grating equation is given by,

$$n\lambda = d(sin\alpha + sin\beta) \cdot cos\gamma \tag{2.8}$$

where, n = diffraction order, λ = wavelength of the light, d = groove spacing, α = incidence angle of the light, β = diffraction angle, and γ = lateral angle. Due to this lateral angle, the beam diffracted from the off-axis points gets shifted, which results in a curvature in the diffraction pattern (*Pallamraju et al.*, 2002, 2013, 2014). To overcome this curvature effect in the image, the slit is designed in a curved shape but in the opposite

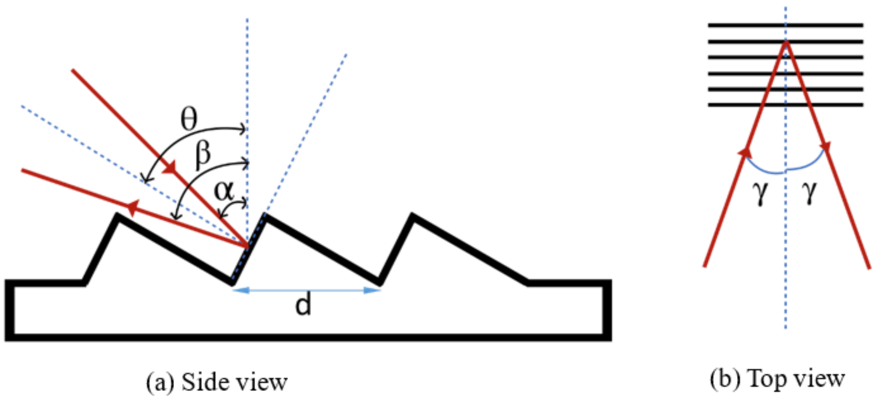

Figure 2.4: The echelle grating view is shown from side (a) and top (b) where incident angle (α), diffraction angle (β), blaze angle (θ), groove spacing (d), and, lateral angle (γ) are depicted.

direction, so that it can reduce the curvature in the diffraction pattern as mentioned above. The geometry of the grooves, incidence angle, diffracted angles, and lateral angle are shown in Figure 2.4.

By differentiating equation 2.8, the angular dispersion can be obtained for $\gamma = 0$ and is given by,

$$\frac{d\beta}{d\lambda} = \frac{sin\alpha + sin\beta}{\lambda \cdot cos\beta} \tag{2.9}$$

From equation 2.9, it can be seen that the angular dispersion of the grating depends upon the α and β for a given λ. The angular dispersion will be high for higher values of α and β, therefore, echelle gratings generally are used at higher angles. To get the higher grating efficiency (ratio of the diffracted intensity to the incident intensity), the α, and β should be close to the blaze angle ($\theta = [\alpha + \beta]/2$), and hence, the facet length, $d \cdot \cos\theta$, should be higher. However, for a large θ, d must be higher for higher grating efficiency that causes lower groove density of echelle grating than standard grating. Further, an echelle grating operates at higher diffraction orders (n)(equation 2.8) as large value of d, α, and β leads to higher values of n for a given λ. In MISE, the diffraction orders at which the images for 557.7, 630.0, and 777.4 nm are obtained on the CCD are 102, 90, and 73, respectively.

The higher resolution can be achieved at high diffraction angle using echelle grating if the issue of order overlap is taken care of. It can be seen from equation 2.8 that for a given d, α, and β, the product of nλ can be satisfied with different values of n and λ. This issue of order overlapping can be eliminated by using interference filters of narrow-bandwidth which allows light from a narrow spectral region to pass through. In the past, the issue of order overlap limited the use of echelle gratings but with the advent of interference filters these gratings are now being used widely (e.g., *Chakrabarti et al.*, 2001, 2012; *Pallamraju et al.*, 2002, 2013, 2014; *Pallamraju and Chakrabarti*, 2006; *Marshall et al.*, 2011).

(v) Imaging lens: The imaging lens is used to image the spectrum on the detector. The f/6 lens reduces the size of the image coming from the f/11 collimator by a factor of approximately 2. This helps to fit images from three different spectral regions around the emission lines at 555.7, 630.0, and 777.4 nm wavelengths onto the image plane of $1'' \times 1''$. There is another macro lens behind the mosaic filter which reimages the diffraction pattern by further reducing the size of the image by a factor of 1.8 so that it fits on the CCD-detector chip size of $0.5'' \times 0.5''$.

(vi) Mosaic filter: The light from the imaging lens is allowed to fall on the mosaic filter, which is basically the combination of three different interference filters glued together. The full width at half maxima (FWHM) of these interference filters vary from 10-20 nm and the central wavelengths are at 557.7, 630.0, and 777.4 nm.

(vii) CCD detector: A CCD (Charge Coupled Device) is a 2-D array detector with high sensitivity. It consists of a large number of light-sensitive small areas (called pixels), which can be used to construct an image of interest. Photons that fall within the defined area of a pixel generate photoelectrons. The number of electrons collected is directly proportional to the intensity of the incident light on each pixel. The number of electrons generated in each pixel is converted into counts with the help of CCD electronics. In MISE, a back-illuminated 1024 $\times$ 1024 (where the size of each pixel is 13 µm) CCD is used. Each CCD has its own source of noise, which needs to be accounted to get a more accurate estimate of the intensity of the incident light. The dark noise of CCD depends on the temperature of the detector, therefore, CCD temperature is maintained at a low temperature (around -75°C) to reduce the dark noise. The readout noise of the CCD is around 3.3 electrons RMS at the readout frequency of 50 kHz. In MISE, CCD is binned by

8-pixels in the spatial direction, which further reduces the readout noise and increases the signal-to-noise ratio of the measurement. This 8-pixel binning in the y-direction means that the light (airglow emissions) over a spatial region (8-pixels) is integrated. This integrated region is smaller than the spatial features being investigated in this thesis work using airglow emission measurements. Finally, data is collected in automated mode using a program written in visual basic language and interfaced with MaximDL software.

2.2.4 Spectral image as obtained by MISE

A typical spectral image obtained by MISE is shown in Figure 2.5 where the pixel numbers in the x-axis represent wavelength (as mentioned in the upper x-axis) and those in the y-axis are associated with the different view directions (spatial coverage). Three horizontal sections separated by the black dark regions correspond to the three different spectral bands containing emissions lines at 557.7, 630.0, and 777.4 nm wavelengths as shown by white-colored dashed-vertical lines. The dark regions between these spectral bands are the opaque regions (places where interference filters are glued with each other) in the mosaic filter. There is 8-pixel binning in the y-direction of the CCD detector; therefore, the spectral image that is formed has a size of 1024 × 128.

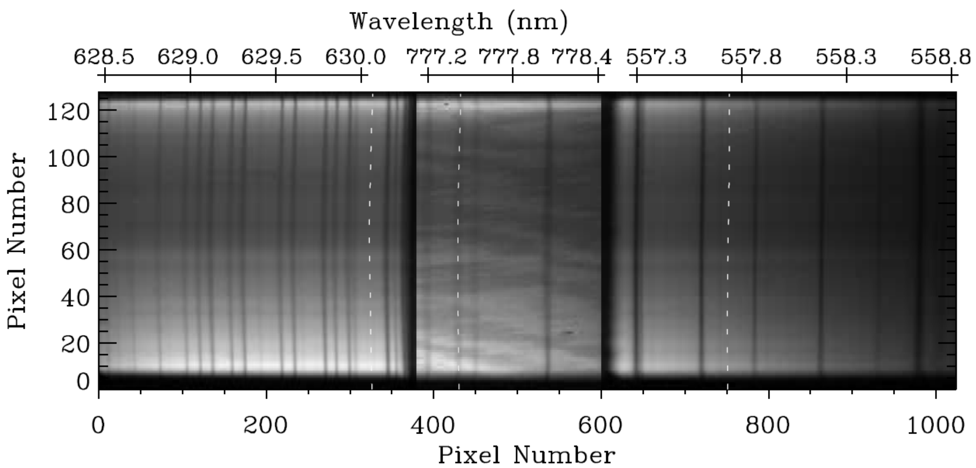

Figure 2.5: The spectral image is obtained by the MISE. (From *Pallamraju et al.* (2013))

2.2.5 Dayglow extraction

The OI 557.7, 630.0, and 777.4 nm dayglow emissions can be extracted using the spectral image obtained by MISE (*Pallamraju et al.*, 2002, 2013). In the thesis work, OI 630.0 nm dayglow emissions have been used, therefore, the dayglow extraction method for 630.0 nm wavelength is described in this section. As discussed earlier, dayglow emissions are embedded in the solar background brightness. We have used normalized solar spectrum

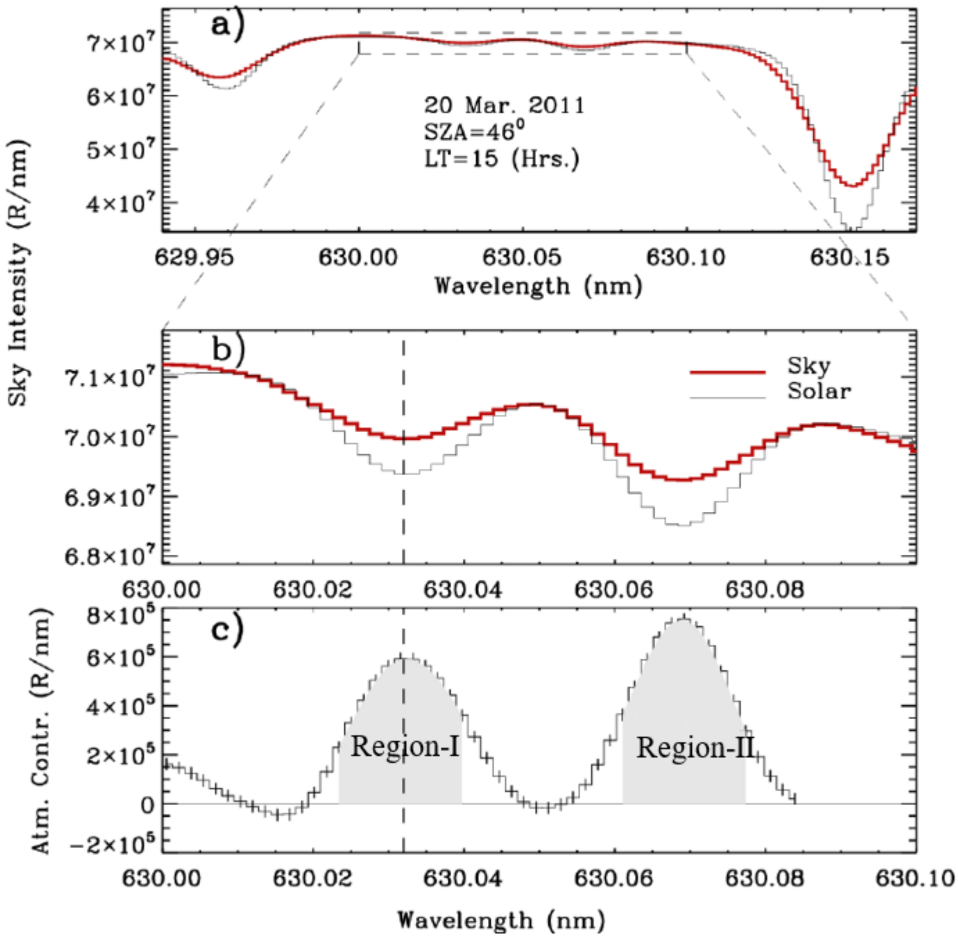

Figure 2.6: (a) The sky spectrum obtained by MISE and the solar spectrum obtained by BASS2000 for a given time are shown in red and black colored lines, respectively. (b) The zoom image of these two spectra is shown where a vertical dashed line is drawn on the position of the oxygen (630.03 nm) line and another dip corresponds to the scandium (630.06) Fraunhofer line. (c) After subtraction of the solar spectrum from the sky spectrum, the atmospheric contribution is obtained where Region-I contributed by the emissions and Ring effect, whereas, Region-II involves Ring effect contribution. (From *Pallamraju et al.* (2013))

obtained from Solar Atlas BASS2000 (http://bass2000.obspm.fr/solar_spect.php) to remove the solar background from the image. This normalized solar spectrum is then scaled to the continuum region of the sky spectra (obtained from the spectral image taken by MISE) which contains oxygen (630.03 nm) and scandium (630.06 nm) Fraunhofer lines. Figure 2.6a shows the sky and solar spectra in red and black lines, respectively. The spectral region of interest is zoomed and shown in Figure 2.6b where the vertical dashed line is drawn at the wavelength of 630.0 nm. The sources for differences between the sky and solar spectra can be emissions, telluric absorption, and scattering. The filling-in of Fraunhofer lines due to atmospheric scattering (Rotational Raman Scattering) is called the Ring effect (*Grainger and Ring*, 1962). The spectral region of interest does not get affected by any telluric absorption and therefore, the filling-in of Fraunhofer lines is due to the emissions and Ring effect. The solar background contribution is removed by the subtraction of the scaled solar spectrum from the sky spectrum to obtain the atmospheric contribution, and the resultant is shown in Figure 2.6c. This atmospheric contribution in intensity at the oxygen line is due to the OI 630.0 nm dayglow emissions and the Ring effect, whereas that at the scandium line is only due to the Ring effect. Without removing the Ring effect contribution, the OI 630.0 nm emissions intensities can be overestimated. Therefore, the Ring effect contribution is taken into account as discussed in *Pallamraju et al.* (2002, 2013). In an earlier work, *Pallamraju et al.* (2000) have shown that scattered contribution will be same for two nearby Fraunhofer lines if their equivalent widths (normalized depth $\times$ width) are identical. Since equivalent widths of oxygen and scandium lines are not identical; for a more accurate estimation of dayglow intensity, we, therefore, used a factor (f), which scales the contribution of the Ring effect from the scandium line to the oxygen line as discussed in *Pallamraju et al.* (2002, 2013).

$$f = \frac{(I_{c1} - I_{d1}) \times \lambda_{\omega 1}}{(I_{c2} - I_{d2}) \times \lambda_{\omega 2}} \tag{2.10}$$

where, I_{c1} is the intensity at the continuum level, I_{d1} is the intensity at the depth of the oxygen line, and $\lambda_{\omega 1}$ is the half-width of the oxygen line, whereas, I_{c2}, I_{d2}, and $\lambda_{\omega 2}$ are similar parameters but for the scandium line. Thus, f represents the ratio of the equivalent width of the oxygen and scandium lines.

The OI 630.0 nm dayglow emission is obtained by the following relation.

$$Dayglowemissions = [Area1] - [Area2] \times f \tag{2.11}$$

where, *Area1* and *Area2* denote the area under the curve of the oxygen (Region-I in Figure 2.6c) and scandium Fraunhofer line (Region-II in Figure 2.6c), respectively. This method of dayglow extraction is well-established and a detailed description is available in the literature (*Pallamraju et al.*, 2002, 2013)

The CCD detector provides the data in unit of counts. The following relation can be used to change counts into the unit of Rayleigh ($10^6 photons\ cm^{-2} s^{-1}$).

$$N(\lambda) = B(\lambda) \cdot S(\lambda) \cdot t \tag{2.12}$$

where, $N(\lambda)$ denotes the sky counts obtained by the CCD detector, $B(\lambda)$ is the sky brightness in Rayleigh unit, $S(\lambda)$ is the sensitivity per nm of the MISE, and t is the integrated time.

The sensitivity of the MISE is given by (*Pallamraju et al.*, 2013),

$$S(\lambda) = \frac{10^6}{4\pi} \times Q(\lambda) \times A \times \Omega \times \tau(\lambda) \times d(\lambda)/n_{rows} \tag{2.13}$$

where, $Q(\lambda)$ denotes the overall efficiency of CCD (quantum efficiency/gain), A denotes the area of the slit, Ω denotes the sky solid angle that slit sees, $\tau(\lambda)$ represents the optical efficiency of the MISE, d(λ) denotes the dispersion in nm pixel^{-1}, n_{rows} denotes the number of rows obtained in spatial direction after on-chip binning. The values of all these above-mentioned parameters are given in Table 2.1, and used to estimate the value of the sensitivity of MISE for OI 630.0 nm emissions which turns out to be $1.8837 \times 10^{-5} (DN\ nm\ R^{-1} S^{-1})$. This value is used to convert the dayglow intensity at 630.0 nm from counts to Rayleigh.

The sources of uncertainty in the values of dayglow emissions intensity are dark noise, readout noise, and background noise. As CCD provides counts which are generated due to photons inducing electrons, therefore, the emissions follow Poisson distribution. Thus, the SNR for OI 630.0 nm will be,

$$SNR = \sqrt{\frac{S}{S+B+D+R}} \tag{2.14}$$

where, S is the signal; B is the background; D is the dark noise; and R is the readout noise. The uncertainty of dayglow emissions will be $1/SNR$. The dark and readout noises are discussed above and their values are very small in comparison to the background noise in daytime. Therefore, in the calculation of SNR, only signal and background are considered. The SNR is estimated as described in CEDAR tutorial (*Pallamraju*, 2003) wherein the different parameters, such as, time integration, co-added pixels, binning, etc. are taken into account. The SNR for the OI 630.0 nm dayglow emissions is found to be in the range of 5-28 depending on the time of the day.

The above-described method to extract the OI 630.0 nm dayglow emissions is processed by programmable codes developed in the Interactive Data Language (IDL).

2.3 Other data sets

In this thesis work, along with the OI 630.0 nm dayglow emissions, several other data sets have also been used to supplement the results obtained. These datasets are described below.

2.3.1 Equatorial electrojet (EEJ)

EEJ is an intense electric current that flows in the eastward direction over the magnetic equatorial region in the daytime as discussed in Chapter-1. As this intense band of current induces magnetic fields, therefore, the strength of EEJ can be estimated by measuring the horizontal component of the magnetic field on the ground. In the thesis work, we have used the geomagnetic data from three stations: Tirunelveli (TIR, 8.7° N, $77.8°E, 0.4°$ N MLAT), Alibag (ABG, 18.6° N, 72.9 ° E, 10.65° N MLAT), and Huancayo (HUA, 12.05° S, 284.67 ° E, 0.6° S MLAT). Variations in the horizontal component of the geomagnetic field (H) are contributed by the Earth's main magnetic field (H_{MF}), the magnetospheric current (H_{MP}), and magnetic field induced by solar quiet (Sq) current (H_{sq}) and EEJ (H_{EEJ}).

$$H = H_{MF} + H_{MP} + H_{Sq} + H_{EEJ} \tag{2.15}$$

To remove the contribution due to the Earth's magnetic field, nighttime values of H on 5 International Quiet Days (IQD) of a given month are subtracted from H for each station. The horizontal geomagnetic values from low-latitude station (ABG) are subtracted from those of TIR values to remove the contribution of H_{MP} and H_{Sq} as EEJ is confined to the dip equatorial ($\pm 3°$) region and H_{MP} is a global-scale current system (*Chandra and Rastogi*, 1974). Thus, in this way only the contribution due to the H_{EEJ} remains in the H which represents the strength of the EEJ. The geomagnetic data of the station of TIR and ABG are obtained from the Indian Institute of Geomagnetism, Mumbai, India. The HUA data is obtained from the World Data Centre (WDC) for Geomagnetism, Edinburgh. (https://wdc.bgs.ac.uk/catalog/master.html)

In the case of the data from HUA observatory, the geomagnetic data from the off-equatorial location at that longitude is not available. Therefore, the Disturbance Storm Time (Dst) index has been used to remove the contribution of H_{MP}.

2.3.2 Neutral winds

The neutral winds data used in this thesis work have been obtained by Michelson Interferometer Global High-resolution Thermospheric Imaging (MIGHTI) (*Englert et al.*, 2017) onboard the ICON satellite. ICON is a low inclination (27°) satellite orbiting around 575 km altitude (*Immel et al.*, 2018). The MIGHTI instrument yields information on neutral winds from the Doppler shift measurements of naturally occurring airglow emissions at OI 555.7 and 630.0 nm wavelengths in the range of 90-300 km altitudes (*Harding et al.*, 2017). Two identical MIGHTI instruments onboard ICON looking in orthogonal directions measure the line-of-sight winds which are then used to derive the cardinal winds with an accuracy of 3 - 10 ms^{-1} (*Harding et al.*, 2017). In this thesis, the level 2.2 data of version 4 with quality factor 1 have been used and obtained from https://icon.ssl.berkeley.edu/Data. We have used the meridional winds for around

250 km altitude which are derived from the OI 630.0 nm airglow emissions.

ICON, being a low-inclination satellite, passes through a particular longitude 15 times in a day where it covers different latitudes between $12°S - 42°N$. Figure 2.7 shows the latitudes (geographic and magnetic) with time in black dots for the longitude of $75° \pm 5°$ E on a given day 29 January 2020. The diurnal variation of meridional winds corresponding to these latitudinal locations is presented in Figure 2.7a by black solid line. The latitudinal variations in meridional winds can present due to the different tidal modes as discussed in Chapter-1. Therefore, it is important to remove the latitudinal variations in order to use the wind variation for a particular latitude. For this purpose, we have used the Horizontal Wind Model-14 (HWM-14) which provides the climatological variation of neutral winds with latitudes (*Drob et al.*, 2015). Here, the difference between the wind values from MIGHTI and HWM-14 along with MIGHTI observation locations (shown in dotted magenta line in Figure 2.7b) is applied to the HWM-14 winds for a

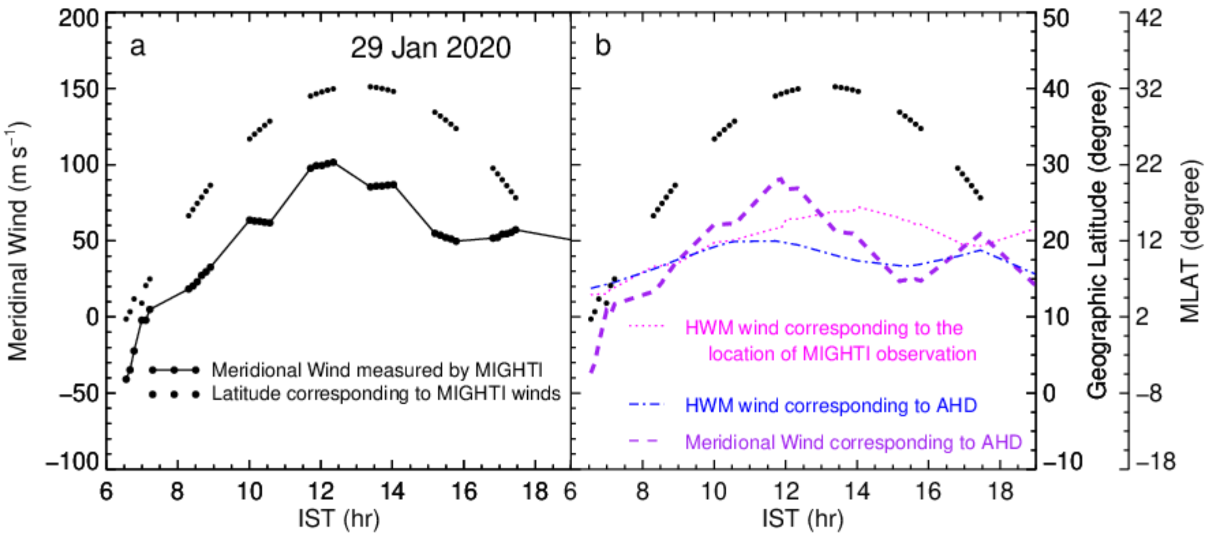

Figure 2.7: In Panel (a), the diurnal variation of meridional winds is represented by black solid lines for the Indian longitude (75°±5° E) from different latitudes on 29 January 2020, where, latitudes are denoted by black dots corresponding to the right-side y-axis. In Panel (b), HWM-14 model-derived meridional winds along with the MIGHTI observation and for a particular latitude (AHD) are shown in dotted magenta and dotted-dashed blue lines, respectively. The dashed purple line denotes the meridional wind corresponding to AHD after applying the correction using HWM-14 model-derived meridional winds as described in the text.

particular latitude of our interest (here it is for AHD as shown by blue dash-dotted line in Figure 2.7b). The diurnal variation of meridional winds obtained for AHD is shown in purple-colored dashed line in Figure 2.7b for a given day. In such a way, one can obtain the cardinal winds for a latitude of interest at the time when MIGHTI observations are available using a climatological model. In the thesis work, we have obtained the neutral winds for the latitude range of $13° - 26°N$ ($5° - 18°$ N MLAT) over Indian longitude.

This method is developed to obtain neutral wind variations at a given latitude (*Kumar et al.*, 2022). To validate the effectiveness of the method in removing latitudinal variations from the MIGHTI observations, a comprehensive analysis is carried out using a large data set for a given longitude (75°). The analysis aimed to assess the agreement between the observed meridional winds and the HWM-14 model-derived meridional winds for the year 2020. In Figure 2.8a, the MIGHTI winds and HWM-14 winds at the latitudes of MIGHTI observations are compared, and the correlation coefficient (R) and standard deviation (σ) between them are presented. It can be noted that HWM-14 modeled winds show a good agreement with MIGHTI observed winds for 61% of the time with an σ value of 28.7 ms^{-1}. This strong relationship between the winds from the HWM-14 model and the MIGHTI observations motivates us to use the HWM-14 as a climatological model, while MIGHTI provides the necessary corrections to obtain accurate estimates of winds for a latitude of interest. On the other hand, Figure 2.8b illustrates the relationship between the MIGHTI winds from different latitudes without considering the latitudinal corrections and HWM-14 winds correspond to the AHD latitude (a latitude of our interest). This analysis has been carried out to observe that if we use these winds for a given latitude of our interest without latitudinal correction. In this case, the match between the MIGHTI winds from different latitudes and HWM-14 winds from AHD latitude is observed only 38% of the time, with a higher σ value of 35.9 ms^{-1}. This emphasizes the significance of accounting the latitudinal variations when using the MIGHTI winds for a given latitude. After applying corrections for latitudinal variations in the MIGHTI winds, a significant improvement is observed in the comparison between the corrected MIGHTI winds and the HWM-14 winds for the AHD latitude. In Figure 2.8c, it is evident that the match between the corrected MIGHTI winds and HWM-14 winds is significantly improved as a good agreement observed approximately 61% of the time with a σ values of 27.6 ms^{-1} (Figure 2.8c). The R and σ values obtained after the latitudinal correction

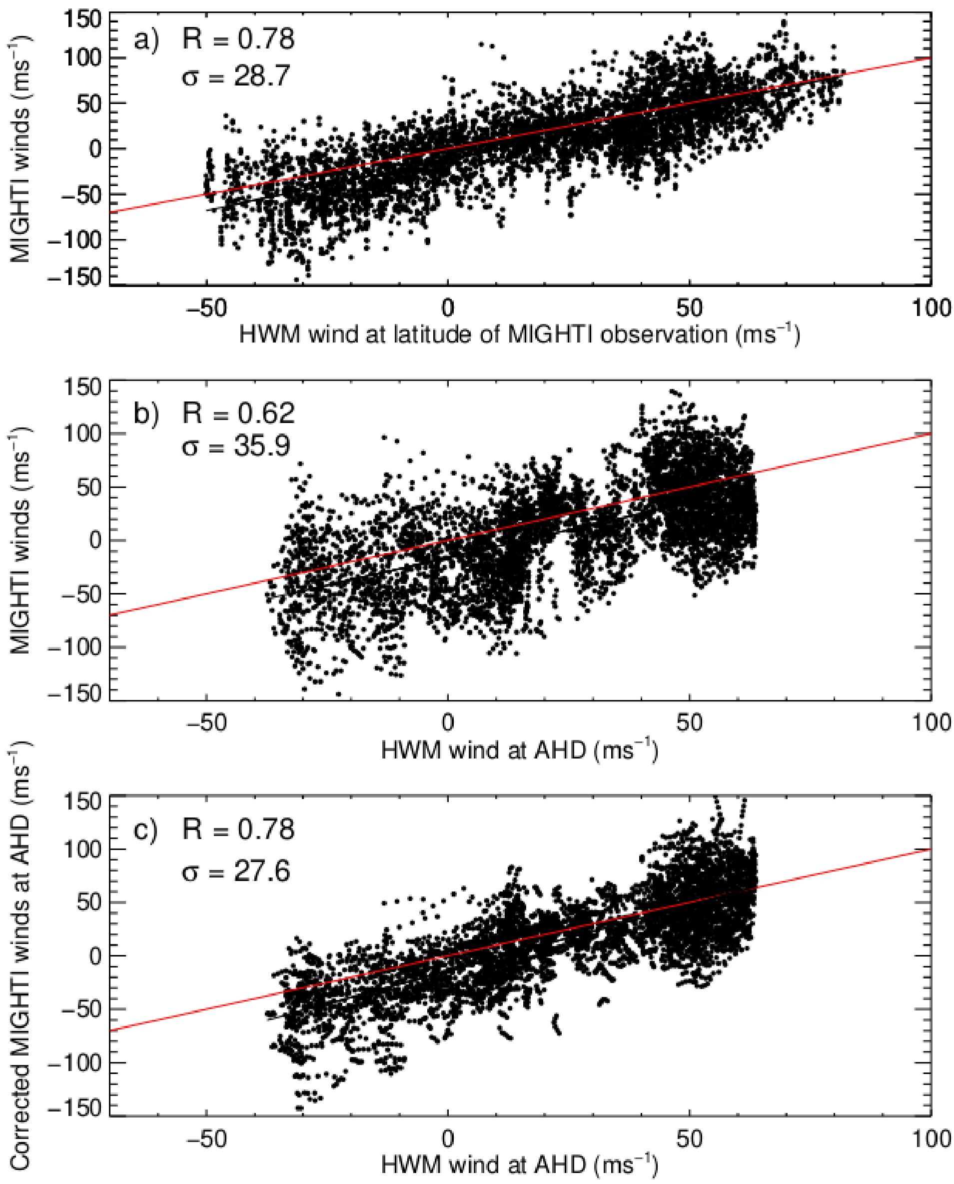

Figure 2.8: Panel (a) shows the scatter plot between the MIGHTI winds and HWM-14 winds for a given longitude (75° ± 5° E) during 1 January to 31 December 2020. Panel (b) corresponds to the scatter plot between MIGHTI winds from the different latitudes and HWM-14 winds from AHD latitude. In Panel (c), the corrected MIGHTI winds and HWM-14 winds for AHD latitude are presented. The correction of MIGHTI winds is described in the text. The correlation coefficients (R) and standard deviation (σ) are depicted in corresponding figures.

of the MIGHTI observations for the AHD latitude (Figure 2.8c) are comparable to the values obtained when considering the MIGHTI and HWM winds from the latitudes of the MIGHTI observations (Figure 2.8a). This confirms the effectiveness of the latitudinal correction process in eliminating the latitudinal variations in the MIGHTI winds, enabling a reliable assessment of the diurnal wind variations for a latitude of our interest. This exercise further strengthens the argument for the need of latitudinal corrections to study diurnal variation in the wind magnitudes at a particular latitude. Using this process, we have used the derived cardinal winds in Chapters-3 & 4.

2.3.3 Electron density

Electron density data have been used to study the ionospheric part of the UA along with the thermospheric behavior from OI 630.0 nm dayglow emission. Ionospheric data is obtained from the digisonde operational at Ahmedabad.

Plasma frequency depends on the electron density through the following relation

$$\omega_N = \sqrt{\frac{N_e e^2}{\varepsilon_0 m_e}} \tag{2.16}$$

where, N_e = electron density; e = electronic charge; m_e = mass of electron; and ε_0 = permittivity of the free space.

Digisonde transmits radio waves in the frequency range of 1 – 20 MHz. The interaction of radio waves with the ionosphere can be understood in the light of magneto-ionic theory. The refractive index for the radio wave propagation in the ionosphere is given by the Appleton-Hartree equation which, in the simplified form, is as follows (*Hargreaves*, 1992):

$$n^2 = 1 - \frac{\omega_N^2}{\omega^2} \tag{2.17}$$

where, ω is the angular frequency of the radio waves. In this equation, the absorption of radio waves and effect of the magnetic field are not considered. From equation 2.17, it is clear that the radio wave echoes are reflected from the altitude where same frequency for the radio waves and plasma exists. While, n becomes imaginary and radio waves get absorbed when the plasma frequency is greater than the transmitted radio wave frequency.

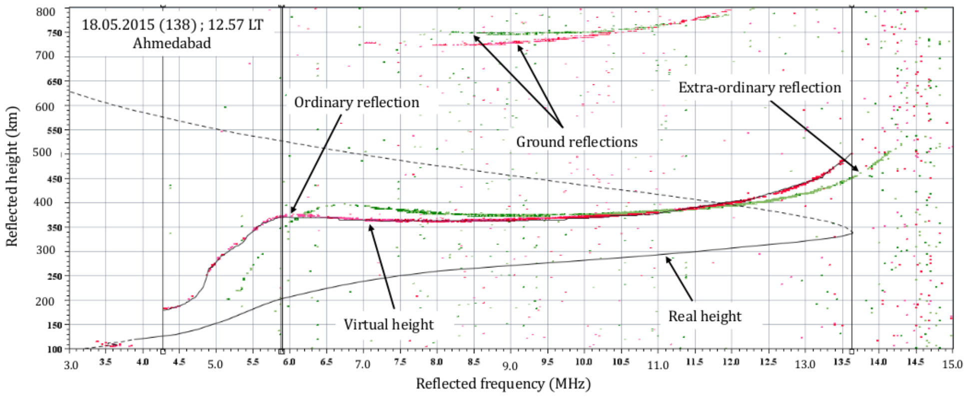

Figure 2.9: A typical ionogram obtained from digisonde at AHD is shown. The red and green lines present the ordinary and extraordinary reflection of radio waves.

Based on the time delay between the transmitted and received echoes, the heights of reflection for different frequencies are calculated. In this way, digisonde provides the information of height as a function of frequency, which is known as an ionogram (as shown in Figure 2.9). Further processing of an ionogram provides the electron density profile with altitude at a given instant. The electron density data obtained from digisonde that is used in this thesis, have been obtained from careful manual scaling of all the ionograms.

2.3.4 Solar F10.7 flux

The solar flux F10.7 is a measurement of the radio emissions from the Sun at a wavelength of 10.7 cm (2800 MHz) in the band of 100 MHz. The F10.7 cm solar flux is measured in solar flux units (sfu), where one sfu is equal to $10^{-22}\, Wm^{-2}Hz^{-1}$. It is often used as an indicator of solar activity, as the level of radio emissions from the Sun depend on the activity level on the Sun's surface (*Floyd et al.*, 2005). Therefore, it can be used to estimate the direct effect of solar EUV radiation in the thermosphere. The F10.7 data is obtained from `http://omniweb.gsfc.nasa.gov`.

2.3.5 E × B drifts

The vertical E × B drift data obtained from Ion Velocity Meter (IVM) on-board ICON satellite (*Heelis et al.*, 2017) have also been used in this thesis work. In-situ measurements of E × B drift are available from around 575 km in the latitudinal range of $27°S - 27°N$.

The IVM consists of two planer sensors, namely, ion drift meter (IDM) and retarding potential analyzer (RPA). The RPA and IDM are mounted to view along the velocity vector of the spacecraft, and they configure the energy distribution of existing ions and their arrival angles, respectively. The version 6 of the vertical drift data is used with a data quality flag of 0 (good data).

2.3.6 Disturbance storm time (Dst) index

Dst index is widely used as an indicator of the strength of geomagnetic storms. During geomagnetic storms, the ring current in the magnetosphere gets enhanced due to the circular movement of solar wind origin particles. This enhanced current induces the magnetic field in the southward direction and the strength of this magnetic field as measured from ground-based magnetometers is used as the Dst index. This measurement is carried out from low-latitude stations in order to avoid the effect of strong equatorial (EEJ) and high-latitude currents (auroral current). The Dst data used in the thesis work have been obtained from `https://wdc.kugi.kyoto-u.ac.jp/`.

2.3.7 Northern annular mode (NAM) index

In the thesis work, we have used the Northern Annular Mode (NAM) as a proxy for the strength of the stratospheric polar vortex (SPV) (*Thompson and Wallace*, 1998; *Baldwin and Dunkerton*, 2001). The calculation of NAM can be understood in the following steps:

i. The daily averaged anomalies of geopotential height at 10 hPa altitude are obtained (illustrated in Figure 2.10a) after removing the annual cycled values which is 60-day smooth values of the mean of each day over the record.

ii. Then the global mean of geopotential height, northern polar cap height, and southern polar cap (>65°) height are computed as shown in Figure 2.10b.

iii. The raw NAM and SAM (Southern Annular Mode) are obtained by subtraction of the global mean values from the northern and southern polar cap height anomalies. Further, it is multiplied by the negative sign to keep standard convention as introduced in *Thompson and Wallace* (1998).

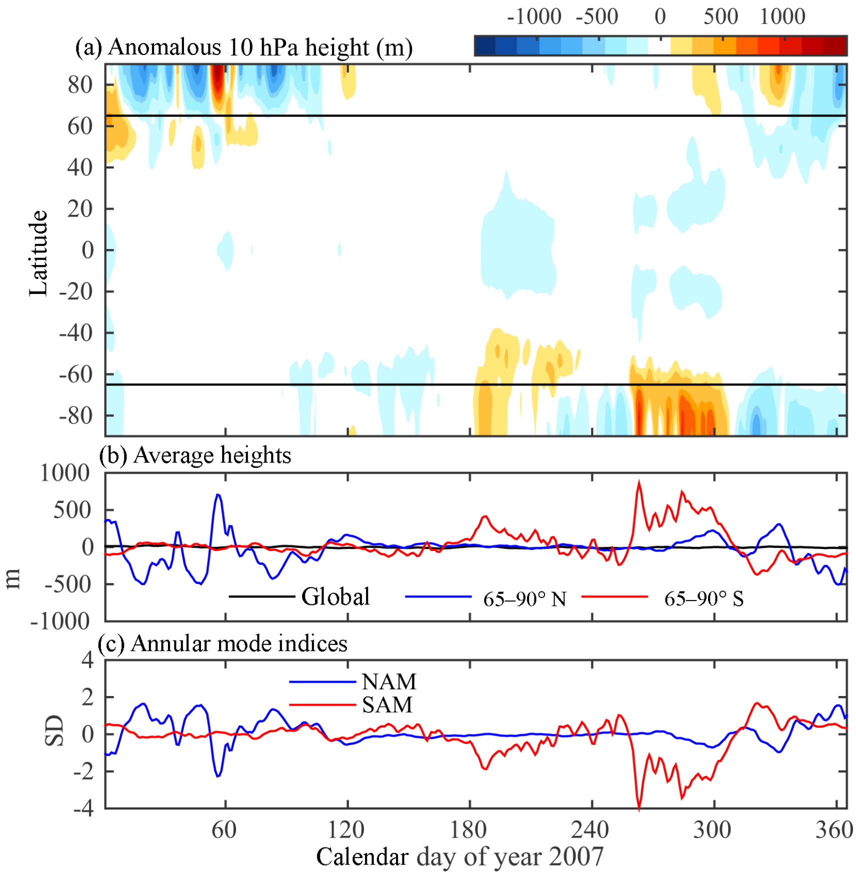

Figure 2.10: Panel (a) shows zonal mean anomaly of geopotential heights at 10 hPa altitude with day of year 2007. The average geopotential heights at polar cap (> 65°) for both hemisphere and global mean are shown in Panel (b). The northern and southern annular mode (NAM and SAM) values are shown in Panel (C). (From *Gerber and Martineau* (2018))

iv. The standard NAM and SAM are obtained by the ratio of their raw values and standard deviation and presented in Figure 2.10c.

More details on the calculation can be found in *Gerber and Martineau* (2018). The values of NAM less than -3 and greater than 2 are referred to as the weak and strong polar vortex conditions, respectively, following the work of *Baldwin and Thompson* (2009). The NAM values are used in Chapter-3 to describe the state of the stratospheric polar vortex. The geopotential height data is obtained from the National Aeronautics and Space Administration (NASA) Modern-Era Retrospective analysis for Research and Application version 2 (MEERA-2) reanalysis data (e.g., *Gelaro et al.*, 2017).

2.4 Spectral analysis

Spectral analysis is a very effective tool to obtain the wave characteristics present in the upper atmosphere. There are different methods one can use to obtain spectral features in the data, such as, Fourier transforms, Lomb-Scargle analysis, least-square fitting of sine and cosines functions, wavelet transform, Wigner distribution function, etc. Each of these methods has some advantages and disadvantages. The methods used in the thesis work are briefly described below.

2.4.1 Fourier transform

The Fourier Transform (FT) is a mathematical technique used to transform a time-domain signal into its frequency-domain representation.

The FT takes a function of time, $f(t)$, and represents it as a function of frequency, $f(\omega)$, where, ω is the angular frequency. The transform is defined by the following equation:

$$f(\omega) = \int_{-\infty}^{\infty} f(t) exp^{-i\omega t}\, dt \tag{2.18}$$

where, $i(\sqrt{-1})$ represents the imaginary unit, and the integral is taken over all time. The $f(\omega)$ gives us information about the frequency content in the original signal $f(t)$.

The inverse FT is another equation that allows us to transform a frequency-domain representation of a signal back into the time-domain representation. It is defined as follows:

$$f(t) = \frac{1}{2\pi} \int_{-\infty}^{\infty} f(\omega) exp^{i\omega t}\, d\omega \tag{2.19}$$

The presence of the experimental data is discrete in nature, therefore, the Discrete Fourier Transform (DFT) of the temporal function, $f(ti), i = 0, 1. \ldots\ldots, N-1$ is given below for $j = 0, 1 \ldots, N-1$.

$$f(\omega_j) = \frac{1}{N} \sum_{i=0}^{N-1} f(t_i)\, exp^{-i\omega_j t_i} \tag{2.20}$$

And the inverse DFT is given as,

$$f(t_i) = \frac{1}{N} \sum_{j=0}^{N-1} f(\omega_j)\, exp^{i\omega_j t_i} \tag{2.21}$$

DFT computes N^2 times however the computational time can be reduced by $Nlog_2N$ using the Fast Fourier Transform (FFT). The shortcoming of FT is that it works only for evenly-spaced data. If it is not so due to various physical considerations then the Lomb-Scargle spectral analysis and least-square fitting of sine and cosine functions can be used.

2.4.2 Least-square fitting (LSF)

Least-square fitting (LSF) is a statistical method used to find the best-fitting curve or line that describes the relationship between two variables. This method can be used for non-uniform data which could be due to instrument limitations, weather conditions, or other factors. The basic concept in this method is to minimize the sum of the squared differences between the observed values of the dependent variable and the values predicted by the model. The advantages of LSF are (i) it can be applied to the non-uniform data and (ii) it provides error estimates (e.g., *Bevington*, 1969). A simplified form of this method is developed by *Lomb* (1976) and *Scargle* (1982). A wave form presented in the data $yi, i = 0, 1 \ldots\ldots, N-1$ having uncertainty ε_i can be written as,

$$y_i = R \sin(\omega t_i + \phi) \tag{2.22}$$

where, R and ϕ are the amplitude and phase of a wave of frequency ω. On expansion, we get,

$$y_i = A \cos \omega t_i + B \sin \omega t_i \tag{2.23}$$

where, A and B parameters are defined as follows (Lomb, 1976; Wu et al., 1995),

$$A(\omega) = \frac{\sum_i \frac{1}{\varepsilon_i^2} y_i \cos(\omega t_i - \tau)}{\sum_i \frac{1}{\varepsilon_i^2} \cos^2(\omega t_i - \tau)} \tag{2.24}$$

$$B(\omega) = \frac{\sum_i \frac{1}{\varepsilon_i^2} y_i \sin(\omega t_i - \tau)}{\sum_i \frac{1}{\varepsilon_i^2} \sin^2(\omega t_i - \tau)} \tag{2.25}$$

where, time offset parameter (τ),

$$\tan 2\tau = \frac{\sum_i \sin 2\omega t_i}{\sum_i \cos 2\omega t_i} \tag{2.26}$$

Finally, the amplitude (R) of the frequency (ω) is given by,

$$R(\omega)^2 = A(\omega)^2 + B(\omega)^2 \tag{2.27}$$

This method is very useful to obtain the amplitude and phase of a wave if its frequency is known. For multiple frequencies, we have to process the least-square method to equation 2.22 for multiple frequencies, simultaneously. The variance in the amplitude R can be given by the following relation (*Bevington*, 1969),

$$Var(R) = \left(\frac{\partial R}{\partial A}\right)^2 Var(A) + \left(\frac{\partial R}{\partial B}\right)^2 Var(B). \tag{2.28}$$

The LSF is applied in the estimation of the tidal amplitude in Chapter-3.

2.4.3 Lomb-Scargle analysis

Lomb-Scargle spectral analysis (*Lomb*, 1976; *Scargle*, 1982) is capable of extracting the information of frequencies present in a non-uniform time-series data. The classical periodogram (*Deeming*, 1975) is given by,

$$P(\omega) = \frac{1}{N} \left| \sum_{i=0}^{N-1} f(t_i)\, exp^{-i\omega_j t_i} \right|^2 \tag{2.29}$$

$$P(\omega) = \frac{1}{N} \left[\left(\sum_i f(i) \cos \omega t_i \right)^2 + \left(\sum_i f(i) \sin \omega t_i \right)^2 \right] \tag{2.30}$$

where, $P(\omega)$ is the power spectral density function of the frequency ω. It is pertinent to note that $P(\omega)$ will be an exponentially varying function of ω if sample data $f(t)$ follows the Gaussian distribution. From equation 2.30, it can be noted that the $P(\omega_0)$ value will be larger in the case of $f(t)$ containing a signal of a frequency of ω_0, whereas, it becomes very low for other values of ω. *Scargle* (1982) derived a new form of equation 2.30 by including a time translation invariance, wherein, the statistical properties remain same. The modified equation is given by,

$$P(\omega) = \frac{1}{2} \left\{ \frac{[\sum_i f(i) \cos \omega(t_i - \tau)]^2}{\sum_i \cos^2 \omega(t_i - \tau)} + \frac{[\sum_i f(i) \sin \omega(t_i - \tau)]^2}{\sum_i \sin^2 \omega(t_i - \tau)} \right\} \tag{2.31}$$

where, time offset parameter (τ) is given by the equation 2.26.

Equation 2.31 is equivalent to the least-square fitting of sine and cosine function to the data (equation 2.22) which is described in the above section (*Lomb*, 1976; *Scargle*, 1982; *VanderPlas*, 2018). It is shown that $P(\omega)$ needs to be normalized by the total variance of the data for the proper normalization (*Horne and Baliunas*, 1986).

The uncertainty in the estimated frequency can be defined as follows (*Horne and Baliunas*, 1986),

$$P(\omega) = \frac{3\pi\sigma_N}{2\sqrt{N}TA} \tag{2.32}$$

where, σ_N = standard deviation of the noise after subtraction of the signal; A = amplitude of the signal; and T = total length of the data set.

The significant power level of the frequencies is defined by the False Alarm Probability (FAP). As discussed above, the $P(\omega)$ follows the exponential distribution in the case of the Gaussian distribution of the sample data (as applicable for the random error) (*Scargle*, 1982). For that case, the probability of $P(\omega_1)$ for a particular frequency ω_1 having equal or greater than power level z is e^{-z}. Let's assume that z is the maximum power of N_i number of independent frequencies. Then, the probability of each frequency with power lower than z is $1-e^{-z}$ and the probability of all frequencies having small power than z is $(1-e^{-z})^N$. Thus, the probability (FAP, P_0) of frequency which have power equal to z or greater than z is given as follows,

$$P_0 = 1 - [1 - e^{-z}]^{N_i} \tag{2.33}$$

And, the significant power level can be defined as,

$$z = -ln[1 - [1 - P_0]^{1/N_i}] \tag{2.34}$$

Hence, the spectral power above the power level z is statistically significant. For FAP, P_0 = 0.01, the significant power z is considered to be with 99% confidence level.

As can be seen in equation 2.34, the significance power level depends upon the number of independent frequencies, N. Actually, the N varies from $2\pi/T$ (T is the total time interval) to Nyquist frequency, but not all the frequencies in this range are independent. To find the true value of N, *Horne and Baliunas* (1986) performed a simulation on the large unevenly spaced data. They found that the number of independent frequencies depends on the number of data points as follows,

$$N_i = -6.362 + 1.193N + 0.00098N^2 \tag{2.35}$$

Using the Lomb-Scargle analysis, we have obtained the frequencies and wave numbers of gravity waves present in the different data sets which have been discussed in detail in Chapter-5.

An example to illustrate the FFT and Lomb-Scargle technique, we have used a periodic signal with known periodicities 12 and 24 hrs as shown in Figure 2.11. It can

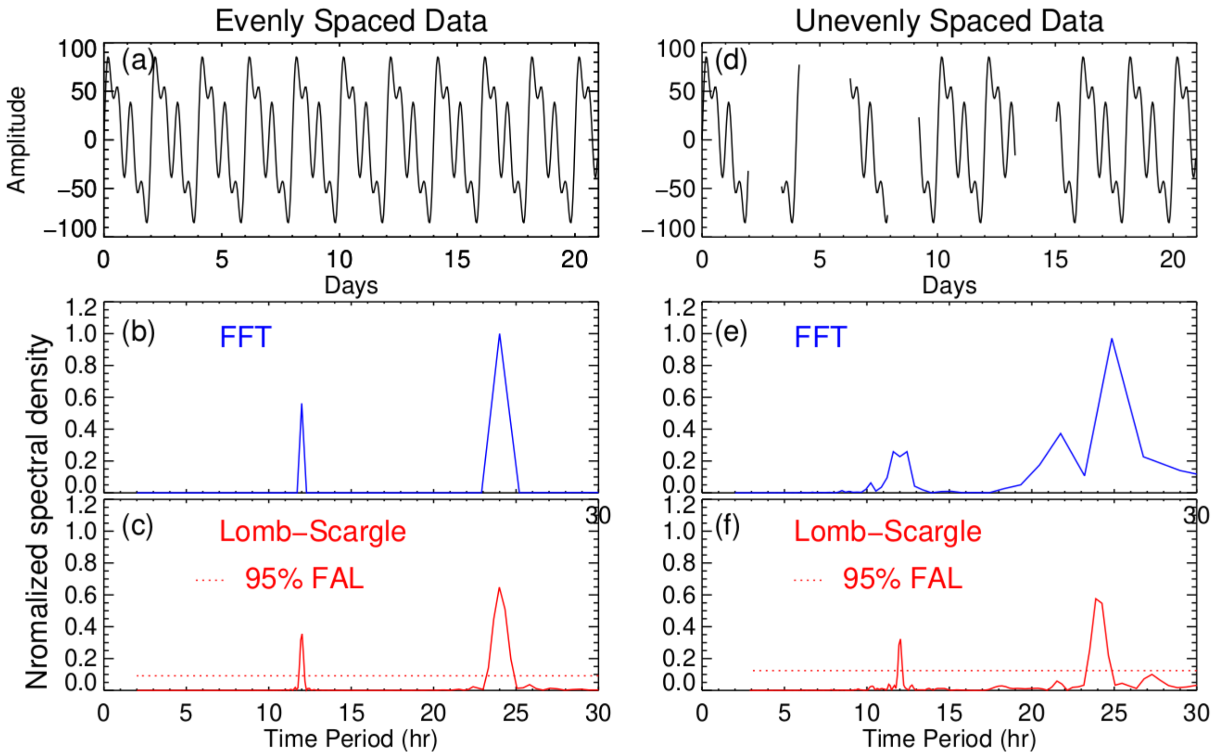

Figure 2.11: (a) A periodic signal with 12 and 24 hrs periods is shown. The FFT and Lomb-Scargle analysis results are presented in Panels (b) and (c). (d), (e), and (f) are similar to those (a), (b), and (c) but for the uneven data wherein some of the data are removed from (a).

be seen that both periods are present in the FFT and Lomb-Scargle analysis in Figures 2.11b and c. This same periodic signal when made non-uniform by removing various data points (shown in Figure 2.11d), it can be noted that the Lomb-Scargle analyses result in the same periods as before, whereas, a clear difference can be noted in case of FFT analysis.

2.5 Summary

In this chapter, the different data sets, techniques, and analysis methods are discussed. The OI 630.0 nm dayglow emissions obtained using two MISE located at HYD and AHD has been used as primary data in the thesis work. The production mechanism and theoretical estimation of OI 630.0 nm dayglow emissions through dissociative recombination are discussed in this chapter. A detailed description is given on the optical design and the components of MISE which is used to measure OI 630.0 nm dayglow emissions. The image processing to extract the dayglow brightness has been discussed. The estimation of the strength of the EEJ using the magnetometer data and the ionosonde data used in this thesis are described. We have also discussed the neutral winds obtained from the ICON satellite and provided a method to derive the diurnal variation of neutral winds for a particular latitude at a given longitude. For that, the HWM14 winds are used to provide latitudinal corrections which is applied to the ICON/MIGHTI winds. Further, other ground-based datasets including NAM index, solar flux, and Dst, satellite-based vertical $E \times B$ drift data obtained by IVM onboard ICON are explained briefly. In addition to that the different spectral analysis methods methods, such as, Fourier transform, least-square fitting, and Lomb-Scargle analysis, which have been used to obtain the information of wave dynamics, are discussed with their advantages and shortcoming. The detailed analyses of these datasets resulted in several exciting and new results which are discussed in the following chapters.

Chapter 3

Response of equatorial electrodynamics to the stratospheric polar vortex

3.1 Introduction

As discussed in Chapter-1, during winter, the latitudinal variation in insolation causes a large-scale temperature gradient between the mid-latitude and the polar regions, which results in the formation of the polar vortex in the stratosphere (*Baldwin et al.*, 2021). The Stratospheric Polar Vortex (SPV) manifests itself in the form of planetary-scale eastward winds and experiences large variability due to interaction with upward propagating tropospheric PWs (e.g., *Charney and Drazin*, 1961; *Matsuno*, 1971a). These interactions lead to the weakening of the SPV which is also known as Stratosphere Sudden Warming (SSW). Conversely, in the absence of strong tropospheric PW activity, strong SPV is formed (e.g., *Lawrence et al.*, 2020) as discussed in detail in Chapter-1.

The states of the SPV play a crucial role in the atmospheric coupling processes and thus they have significant impacts across different layers of the atmosphere (e.g., *Baldwin et al.*, 2021; *Pedatella and Harvey*, 2022). The SSW-associated effects can significantly alter the mesospheric, thermospheric, and ionospheric dynamics and chemistry (e.g., *Chau et al.*, 2012; *Laskar and Pallamraju*, 2014; *Singh and Pallamraju*, 2015). The SSW drives the variabilities in MLT region primarily due to the altered GW forcing caused by the deceleration and reversal of eastward winds of SPV (e.g., *Holton*, 1983; *Liu and Roble*, 2002). Additionally, variations in the ionosphere and thermosphere during SSWs are predominantly driven by changes in upward propagating migrating and nonmigrating solar and lunar tides, which arise due to a combination of changes in background winds and tidal forcing conditions (e.g., *Jin et al.*, 2012; *Forbes and Zhang*, 2012). While the effects of SSW events have been extensively studied, the impact of strong SPV events has only been investigated in the troposphere (e.g., *Baldwin and Dunkerton*, 2001), and the understanding of their influence on the middle and UA is still relatively limited.

Recently, *Pedatella and Harvey* (2022), hereafter PH22, showed the impact of strong and weak northern hemispheric (NH) SPV on the MLT which is examined using specified dynamics – whole atmosphere community climate model with ionosphere/thermosphere extension (SD-WACCMX) simulations. This was the first such study in which the anomalies in zonal-mean temperature, zonal-mean winds, and tides in the MLT during strong and weak SPV periods are compared. In this study, it was found that the zonal mean and tidal anomalies during strong SPV generally show opposite behavior to that during weak SPV periods. The zonal mean behavior during weak and strong SPV is discussed in Chapter-1. They further examined the anomalies in specific atmospheric tides during the periods of strong and weak SPV and observed, in particular, that the migrating solar semidiurnal tide (SW2) shows a notable change in the MLT with a reduction in amplitudes of about 25-35% at NH mid-latitudes during strong SPV periods. Conversely, during weak SPV periods, an even stronger enhancement in SW2 tides was also observed. On the other hand, the migrating solar diurnal tide (DW1) and non-migrating semidiurnal solar tides with wavenumbers 1 and 3 (SW1 and SW3) showed smaller variations during strong and weak SPV conditions. The study by PH22 did not consider the changes in migrating semidiurnal lunar tide (M2) during either strong or weak SPV periods as the SD-WACCM-X did not explicitly include the lunar tidal forcing.

Also, the observed changes in migrating and non-migrating solar tides in the MLT region during strong and weak SPV can potentially contribute to the ionospheric variations as it is well-known that the upward propagating tides upon reaching the E-region dynamo heights lead to the EEJ generation (e.g., *Baker and Martyn*, 1953) and the vertical E $\times$ B drift (e.g., *Fejer et al.*, 2010; *Chau et al.*, 2012) through the zonal electric field. It is shown that the upward-propagating tides drive around one-half variation of the electric field in the dynamo region (*Yamazaki et al.*, 2014). The findings of PH22 in the MLT motivate us to examine the semidiurnal solar and lunar tides in the ionosphere during strong and weak SPV periods. For this purpose, we have investigated the geomagnetic semidiurnal solar and lunar tides derived using the magnetic field observation from the HUA observatory and also migrating semidiurnal lunar tides that are estimated using the vertical E $\times$ B drifts obtained by the IVM onboard the ICON satellite. We found that in addition to the well-known enhancement in geomagnetic semidiurnal solar and lunar tides during SSWs periods, the response of semidiurnal tides to strong SPV is generally weaker but shows an opposite nature. The geomagnetic solar and lunar tides show a notable decline during the strong SPV periods. These results demonstrate that in addition to SSWs, strong SPV conditions also have a considerable impact on the ionosphere.

3.2 Data sets and analysis methodology

In this work, we have used the Northern Annular Mode (NAM) at the altitude of 10 hPa which works as a proxy for the strength of the SPV as discussed in Chapter-2. The values of NAM less than -3 and greater than 2 represent the weak and strong polar vortex, respectively, (*Baldwin and Thompson*, 2009).

Hourly mean values of the horizontal component, $\boldsymbol{H}$, of the geomagnetic field observed by the ground-based magnetometer at HUA have been used in this study to estimate the amplitude of the geomagnetic solar and lunar tides for the periods 1980-1991 and 1997-2020. The data for the years 1991-1996 from HUA remains unavailable. For that, we have used a similar technique that is applied in earlier studies by *Yamazaki et al.* (2012) and *Siddiqui et al.* (2015) to investigate the geomagnetic lunar tidal variations in relation to SSWs. Our analysis is focused on the time period from 15 December to 1 March. The method to obtain the magnetic field variations due to the EEJ (ΔH) from geomagnetic field observations is discussed in detail in Chapter-2.

3.2.1 Determination of geomagnetic tides using EEJ data

The ΔH variations show a dependence on the solar activity as shown in Figure 3.1 (*Alken and Maus*, 2007; *Yamazaki et al.*, 2012), therefore, we use the solar flux values, $F10.7$ (in sfu) to consider this dependence. We calculate the index $\boldsymbol{P}$ using the observed value of

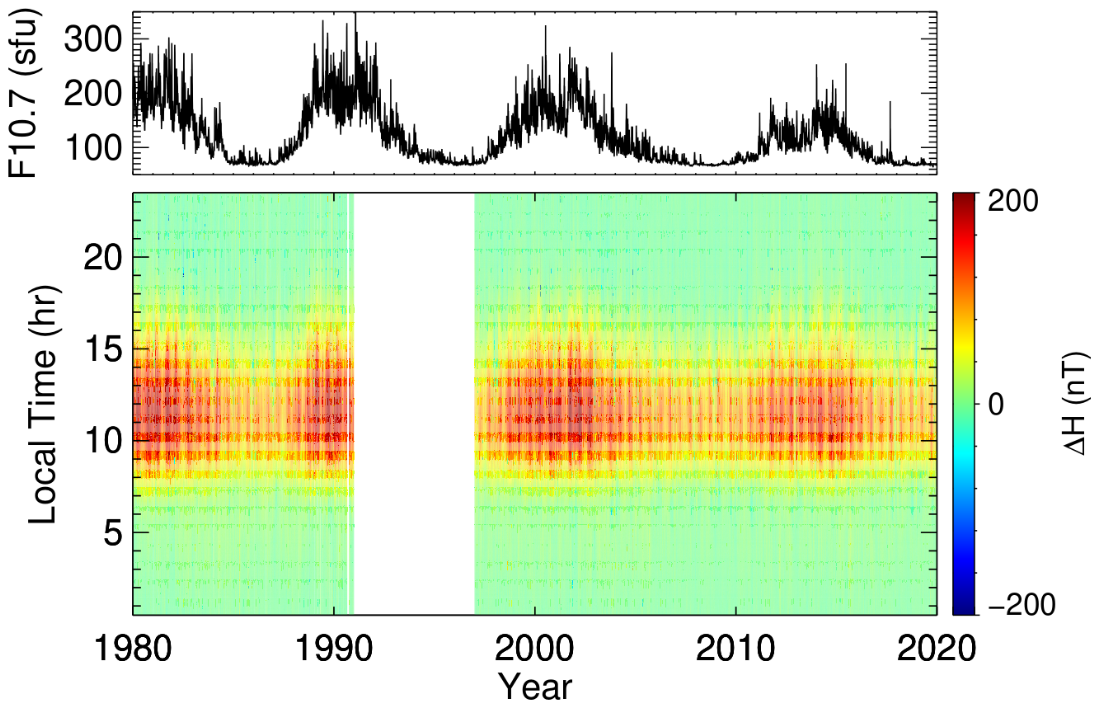

Figure 3.1: The local time variations of ΔH obtained from the HUA observatory are shown with the solar flux, where, solar flux values are shown in top panel.

$F10.7$ for each day and its 81-day-centered average, $F10.7$A, with the following relation:

$$P = \frac{F10.7 + F10.7A}{2} \tag{3.1}$$

and it is used to normalize ΔH variations to a solar flux level of 150 sfu using the method described in *Park et al.* (2012). The index P is used for normalizing the variations due to its ability to better represent the solar cycle variations of solar extreme ultraviolet (EUV) radiation, compared to $F10.7$ alone (e.g., *Richards et al.*, 1994). The daily variation in ΔH is largely controlled by the geomagnetic solar (S) tides, wherein, diurnal ($S1$) and semidiurnal (S2) components dominate the spectral components of the ΔH variations. The geomagnetic solar tides in ΔH arise from a combination of upward propagating solar tides and in situ generated solar tides in the thermosphere (e.g., *Forbes*, 1982a,b). In addition to the geomagnetic solar tides, ΔH shows the tidal components which are dependent on the phase of the Moon and are called the geomagnetic lunar (L) tides. The corresponding lunar semidiurnal (L2) component dominates in L as the atmospheric lunar tides are dominated by the semidiurnal component (12.42 h). The amplitude of L in ΔH is typically an order of magnitude smaller than that of the amplitude of S due to weaker driving winds. However, on certain big-L days, which usually take place during NH winters, the amplitude of L can become comparable to or even larger than that of the S (*Bartels and Johnston*, 1940). Recent studies have found that these big-L days of enhanced lunar tidal amplitudes are associated with the occurrence of SSWs (e.g., *Fejer et al.*, 2010).

Here, the variations of the S and L in ΔH are determined using the Chapman-Miller method, which has been summarized in *Malin and Chapman* (1970). Mathematically, the components of S and L can be expressed as follows:

$$S_n = s_n \sin\left(\frac{2\pi}{24}nt + \sigma_n\right) \tag{3.2}$$

$$L_n = l_n \sin\left(\frac{2\pi}{24.84}nt - \frac{2\pi}{24}(2\nu) + \lambda_n\right) \tag{3.3}$$

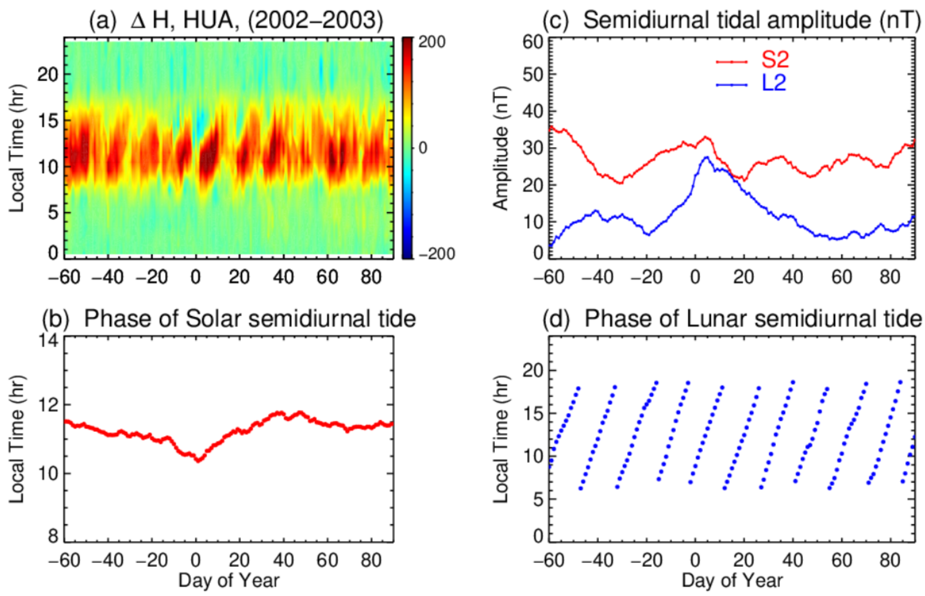

Figure 3.2: (a) The local time ΔH variation from 1 November to 31 March is shown with day of the year for a given winter of the years of 2002-2003. Panel (b) depicts the variations of the amplitudes of semidiurnal solar and lunar tides for this winter in red and blue lines, respectively. Panel (c) show the phase of solar semidiurnal tide. (d) Phase of lunar semidiurnal tide.

Here, S_n and L_n represent the nth component of S and L, respectively, with corresponding to amplitudes s_n and l_n. The σ_n and λ_n represent the phase angle of the nth component of S and L, respectively. The ν denotes the lunar age in hours and the solar local time in hours is denoted by t. The S and L variations are simultaneously obtained by fitting their four respective Fourier coefficients to ΔH over a 21-day moving window through a least-squares approach by using equations 3.2 and 3.3. The least-square fitting method is described in detail in Chapter-2. It is important to note that the determined amplitudes of S and L using this method include contributions from both migrating and non-migrating semidiurnal solar and lunar tides, respectively. Figure 3.2 gives an overview of the tidal amplitude variability with day of the year. The daily diurnal ΔH variations normalized to 150 sfu between 1 November 2002 to 31 March 2003 are shown in Figure 3.2a, where 01 January is marked as day 01 and negative values in the x-axis indicate the days of the previous year. In this figure, the daily diurnal variation of ΔH with maxima during the local noontime can be easily identified. The obtained amplitudes of S2 and L2 tides using this approach are shown in Figure 3.2b with day of the year and Figures 3.2c & d show the obtained phases of S2 and L2, respectively.

3.2.2 Determination of lunar tide using vertical drift

In addition to the geomagnetic observation, we have used the vertical drift data obtained from IVM onboard ICON satellite to estimate the migrating semidiurnal lunar tidal amplitude. As the satellite covers the whole globe, therefore, the M2 components can be estimated using this vertical E $\times$ B drift. But the temporal coverage for a particular location is very sparse, therefore, the above-discussed method applied on the ΔH, cannot be used as the periods of SW2 and M2 are very close. In order to accurately separate and analyze these tides, it is important to have data which is sufficiently abundant and sampled frequently. It is well-known that the time periods of M2 and SW2 can be totally different from the perspective of satellite platforms (e.g., *Ray and Luthcke*, 2006) which has been discussed below. The angular frequency of self-rotation of the Earth on the point of P with respect to the Moon and Sun are

$$\sigma_r^L = \sigma_0 - \sigma_R^L \tag{3.4}$$

$$\sigma_r^S = \sigma_0 - \sigma_R^S \tag{3.5}$$

where σ_0 (Earth's rotation frequency) = 2π /sidereal day (24 hr), σ_R^L (Lunar rotation frequency with respect to the Earth) = 2π /sidereal lunar month (27.32 days), and σ_R^S (Sun's rotation frequency with respect to the Earth) = 2π /sidereal year (365 days). Figure 3.3 describes the relation between lunar local time, τ, solar local time, t, and lunar phase, ν for a location P on the Earth which is given by $\tau = t - \nu$. The lunar phase is almost proportional to the universal time, therefore, for each sinusoidal mode, the lunar phase speed is constant. By subtracting equation 3.5 from equation 3.4, we obtain,

$$\sigma_r^L = \sigma_r^S - C \tag{3.6}$$

where C is the lunar phase. The difference between the angular frequency for the perspective of the Earth (σ_r^L) and satellite with respect to the Moon using equation 3.6 will be as follows,

$$\sigma_s^L = \sigma_s^S - \sigma_e^S + \sigma_e^L \tag{3.7}$$

where subscripts e and s denote the Earth and satellite perspective, respectively. The values of $1/\sigma_e^L$ and $1/\sigma_e^S$ are 1.035 days and 1 day, respectively. ICON satellite covers 24 hr solar time in 41 days for a particular location (*Cullens et al.*, 2020), therefore, $1/\sigma_s^S$ will be 41 days. In this background, the M2 period in the perspective of the ICON satellite is 17.16 days. The two periods of SW2 and M2 from the ground-based point of view are very close as 1/2 day and 1.035/2 days, however in the satellite frame, the difference is magnified as these periods become 21 days and 17 days, respectively. More details about the analysis can be found in *Forbes et al.* (2013), and *Lieberman et al.* (2022).

As discussed above, the major components of tides in the electric field of the dynamo region are migrating solar tides, and M2 components are embedded in these. To obtain

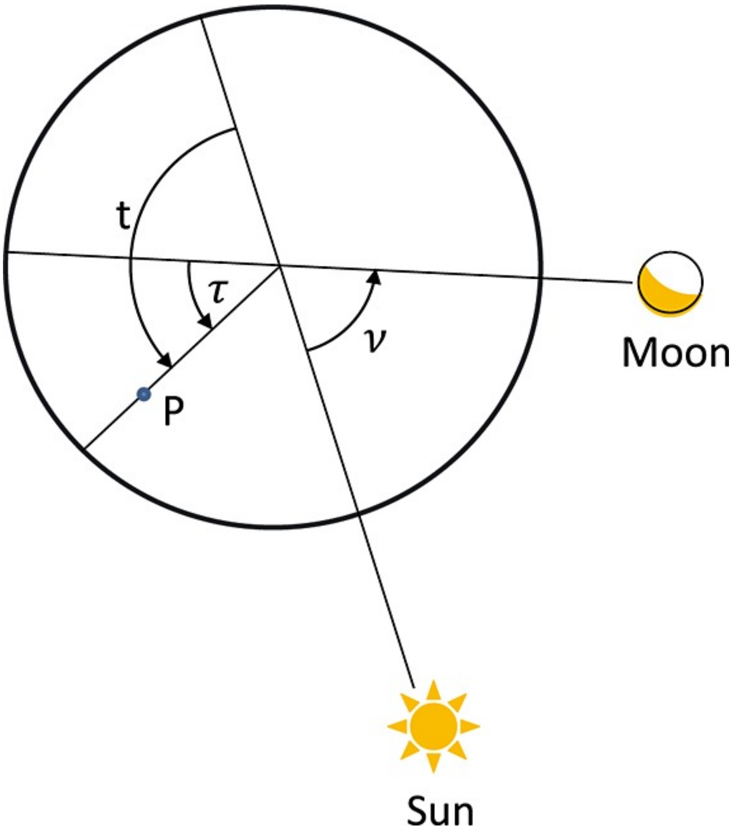

Figure 3.3: Figure describes the relationship between the lunar local time (τ), the solar local time (t), and the lunar phase angle (ν) for a given location (P) on the Earth. The circle denotes the equatorial plane of Earth. (From *Forbes et al.* (2013))

the contribution of M2, firstly, we have to remove the variations which arise due to the solar migrating tides. For that, we remove 9-days averaged value as ICON satellite covers 12 lunar local time (LLT) and 4 hr solar local time (SLT) in 8.58 days for a given latitude (*Lieberman et al.*, 2022). A single 9 days mean could not be able to remove the solar tidal components; therefore, we repeat this filtering process for 9 adjacent days until 24 hr are spanned for each latitude. Then, once this filtering process is attained, all the filtered data are binned in LLT and a 12-hr harmonic component is fitted using the least-square approach in the latitude range of -10 to 10 MLAT. This filtered data for a time window of 41 days (9 February to 20 March 2020) is shown in Figure 3.4a. Figure 3.4b illustrates the fitted vertical drift with a 12-hr harmonic component which denotes the M2 variations. In accomplishing this analysis, the days when the solar flux values ($F10.7$ cm) exceed 2.5 times of standard deviation (*Tapping*, 2013; *Lieberman et al.*, 2022) and Kp values are greater than 3 (*Matzka et al.*, 2021) in this time period, are omitted. The uncertainty in the estimation of M2 for vertical drift turns out to be in the range of 0.5 - 1 ms^{-1}

Lieberman et al. (2022). In such way, the M2 amplitude is obtained in the period of 9 February to 20 March 2020 which turns out to be in the range of 6-14 ms^{-1} in this latitude window and this value is assigned to the mean day (1 March 2020).

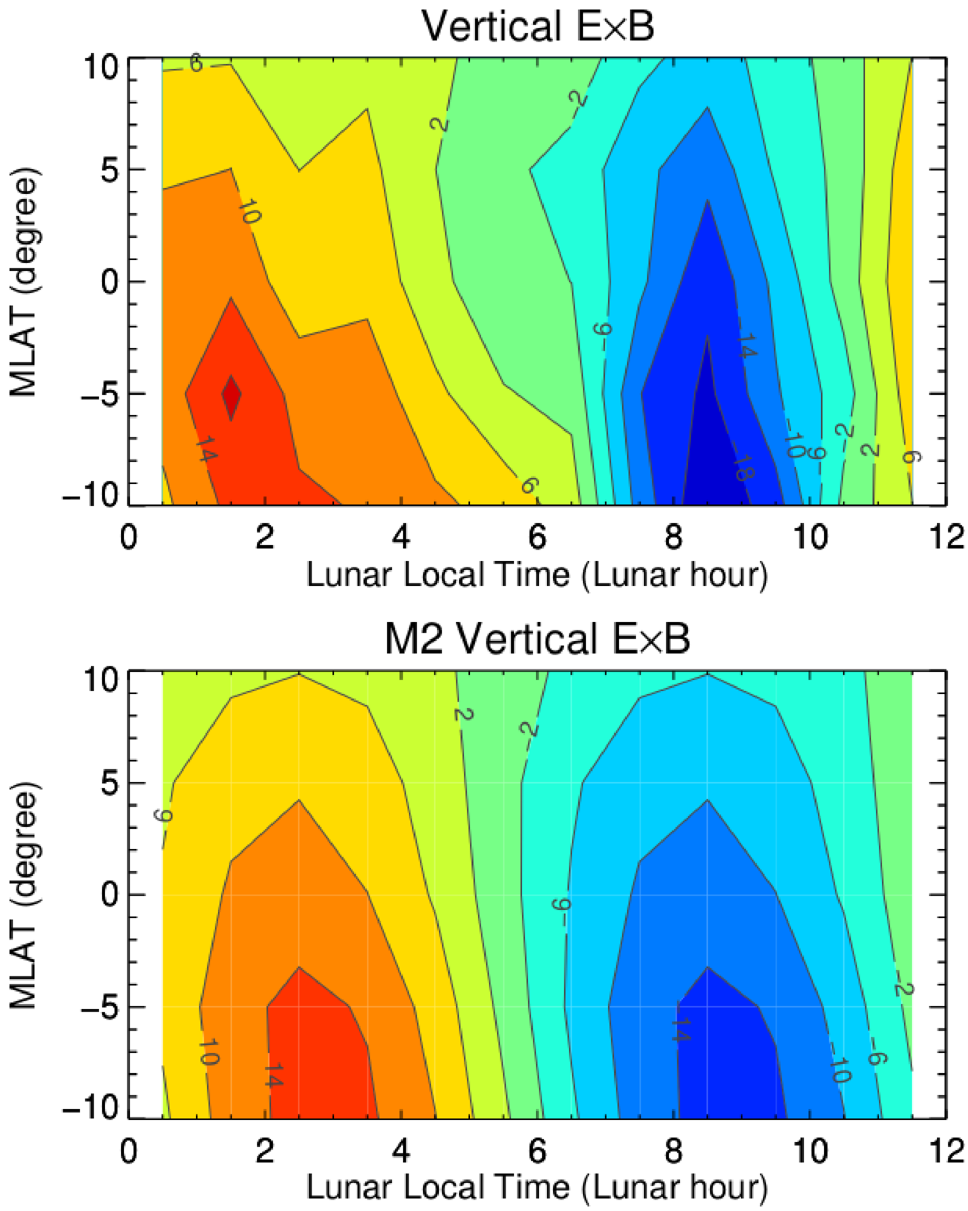

Figure 3.4: (a) The lunar local time variation of the vertical E $\times$ B drift obtained by IVM onboard ICON satellite during 9 February to 20 March 2020 is shown with magnetic latitudes. (b) The migrating lunar semidiurnal tidal fitting to the vertical E $\times$ B drift as shown in (a).

3.3 Results

As discussed above, PH22 for the first time found the impact of the strong SPV on the SW2 tide in the MLT region. In Figure 3.5, the latitudinal variations of SW2 tide in the zonal winds are shown with day of the year from 1 November 1980 and 31 March 1981 at the altitude of around 110 km for three winters of the years of 1980-1981, 1982-1983,

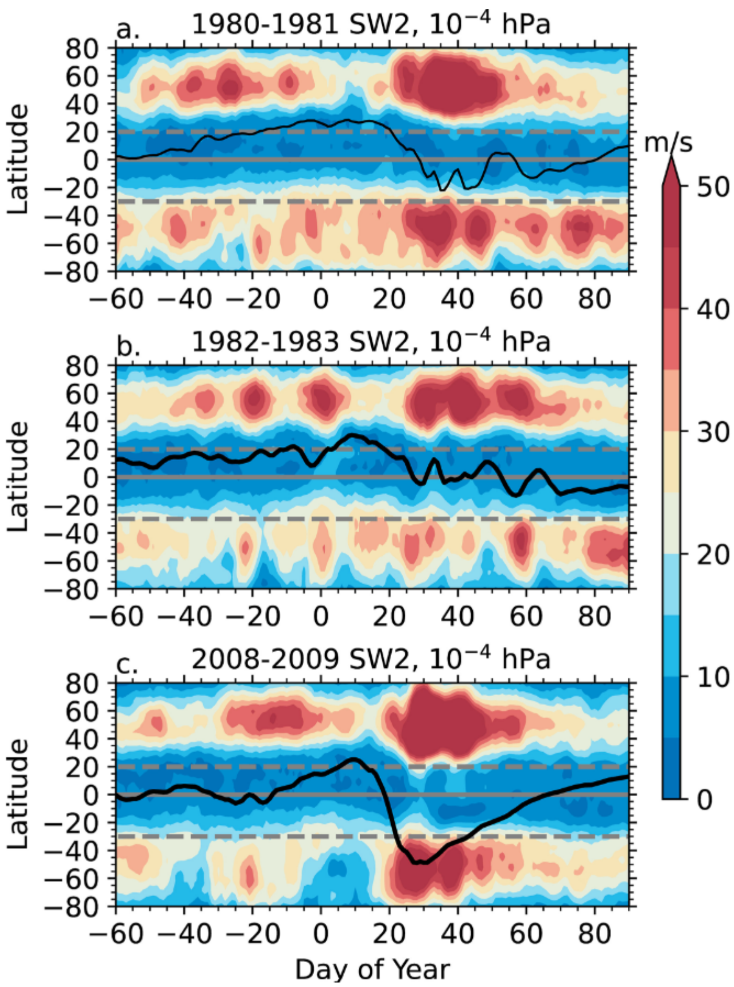

Figure 3.5: The amplitude of SW2 tide in zonal wind at altitude of around 110 km is shown with the day of the year from 1 November to 31 March at different latitudes for three winters of the years of 1980-1981, 1982-1983, and 2008-2009, respectively in Panel (a), (b), and (C). The black solid lines represent the NAM variation at 10 hPa altitude whereas dashed gray lines correspond to the reference level of strong (NAM = 2) and weak (NAM = -3) SPV. Here, to overplot with the Figures, NAM is multiplied by 10. (From *Pedatella and Harvey* (2022))

and 2008-2009. The zonal winds are obtained from the SD-WACCM-X model. Here, the black solid lines denote the NAM index variations at 10 hPa altitude which represent the variability in the strength of NH SPV, whereas, gray dashed lines represent the reference level for the strong and weak SPV by 2 and -3 of NAM values, respectively. The state of SPV can be identified as strong when NAM index $>$ 2 and weak when NAM index $<$ - 3. Here, it is multiplied by a factor of 10 to overplot with the SW2 amplitude. The solid gray lines denote the zero level of NAM. It can be seen that for the winter of 1980-1981 (3.5a), SPV is strong from day -15 to 23 as NAM values are greater than 2, and it could be seen that SW2 amplitude decreases in this period. Thereafter, SW2 amplitude rises as NAM values go below -2.0 around day 40. Similarly, for the winter of 1982-1983 (3.5b), most of the time, SPV remains strong from day -40 to 20 excluding a slight fluctuation around day 0. After that NAM remains around 0. It can be noted that the SW2 amplitude is anti-correlated with the NAM variatiuons. For the winter of 2008-2009, there is a notable reduction in the SW2 amplitude around day 10 during the period of strong SPV and thereafter, it shows a strong enhancement around day 30 when SPV is anomalously weak. This discussion makes it clear that along with the impact of weak SPV on the MLT region, strong SPV also can potentially affect the dynamics of dynamo region.

To analyze the impact of SPV conditions on the EEJ, the winters of the years of 1980-1981, 1982-1983, and 2008-2009 as shown in Figure 3.6 are selected for this purpose since these time periods are also analyzed above. In Figure 3.6a, the daily variations of ΔH, which is normalized to 150 sfu, are shown between the period of 1 November 1980 and 31 March 1981. The gray solid line in this figure represents the day-to-day variability of the NAM values corresponding to the right y-axis. The dashed gray lines correspond to the NAM value of 2 and -3 associates with the reference values for strong and weak SPV, respectively. The amplitudes of S2 (black line) and L2 (red line) tides are presented in Figure 3.6b. The dashed black and red lines denote the climatological level of S2 and L2 tides, respectively, that have been calculated using the median values of S2 and L2 tides for each day across the years 1980-2020. In Figure 3.6c, the bar plot presents the daily averaged Kp levels (black bars) and the blue lines that correspond to the right y-axis depict the daily $F10.7A$ values.

From Figure 3.6c, it can be observed that this analyzed time period was marked by high $F10.7A$ levels and was also geomagnetically active on days -12 and 64 as indicated

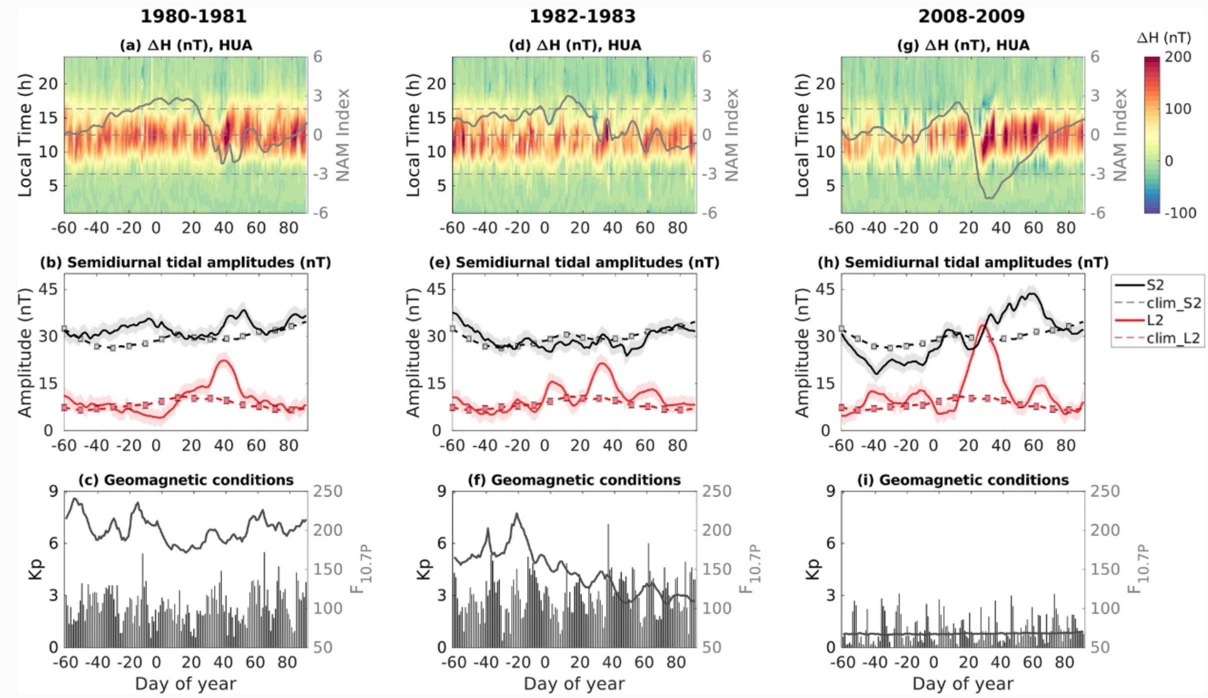

Figure 3.6: Panels (a), (d), and (g) show the local time variation of ΔH from 1st November to 31st March for the winters of years 1980-1981, 1982-1983, and 2008-2009, respectively. The solid blue line in the top panels represents the NAM values, while dashed blue lines correspond to the NAM value of 2 and -3 associate with the reference values for strong and weak SPV, respectively. In panels (b), (e), and (h), the amplitudes of solar semidiurnal (solid black line) tide and its climatology (dashed black line) are shown for the same years as mentioned above. In a similar way, the amplitudes of lunar semidiurnal (solid red line) tide and its climatology (dashed red line) are shown in these figures. Panels (c), (f), and (i) show the daily averaged Kp values (black bars) and $F10.7$A levels (solid blue line) for the above-mentioned time periods.

by the high daily averaged Kp values on these days. As we account for variability due to geomagnetic activity and solar flux levels in the estimation of tidal amplitudes, it is opened that our tidal estimates are robust as no abrupt changes in tidal variability due to geomagnetic effects are seen. From Figure 3.6a, it can be noted that the period between mid-December (day -15) and late January (day 23) was characterized by strong SPV conditions as the NAM index remained above 2 during this period. In response to strong SPV conditions, the amplitudes of S2 (in Figure 3.6b) decline from ∼36 nT on day -8 to below its climatological levels to ∼30 nT by day 8 and remain at these levels until day 35. A more significant decline is observed in L2 with its amplitude reducing from

~7 nT (close to its climatological levels) on day -30 to ~4 nT by day 0. Compared to the slightly lagged response of S2 to strong SPV conditions, the decline in L2 amplitudes begins soon after the initial NAM increase from day 35 onward. After day 21, the SPV conditions start to weaken, and NAM index sharply declines and eventually reaches -2 by day 37. It remains around this value until mid-February before recovering and rising to 0 at the beginning of March. During this weakening of SPV, the shifting semidiurnal structure in ΔH associated with L2 enhancement during SSWs (e.g., *Chau et al.*, 2009; *Fejer et al.*, 2010) appear around day 40 in Figure 3.6a. During this weakened state of SPV, an enhancement in S2 amplitudes can be observed in Figure 3.6b as it rises above its climatological levels to ~36 nT by day 42 and reaches a peak of ~39 nT on day 52. In contrast, the response of L2 to weakening SPV is slightly earlier than that of S2. The L2 amplitudes show a peak enhancement on day 40 with an amplitude of ~22 nT, which is nearly double of its climatological levels. During the recovery of SPV as NAM values increase from their minima, there is a sharp decline in both S2 and L2 amplitudes. The amplitudes of L2 return back to its climatological level by day 60, however, the S2 amplitudes decline below its climatological level in early March and gradually begin to return toward this level by the end of March. It can be noted that the observation of S2 in ΔH is generally consistent with SW2 amplitude in zonal winds for this event as can be seen in Figure 3.6b and 3.5a.

Figure 3.6d is similar to Figure 3.6a, but for the winter of the year of 1982 -1983. From the NAM index, which is presented in bold gray line in this figure, it can be seen that strong SPV is presented between late December and mid-January for this winter. The SPV slightly weakens first in late January and early February, and then again towards the end of February and from mid-March onward. However, it can be seen that the extent of weakening of the SPV during the 1982-1983 winter is slightly weaker in comparison to the 1980-1981 winter as indicated by the NAM index. From Figure 3.6e, it can be observed that S2 amplitudes (solid black line) respond to strong SPV conditions with a decline from ~30 nT on day -15 to below their climatological levels (dashed black line) by day -8 and reach their minima of ~25 nT by day 2. As the NAM values begin to decline, S2 amplitudes show a small enhancement around day 0, reaching a maximum of 28 nT by day 8. However, as the NAM values rise again and reach a peak value of ~3 on day 11, S2 amplitudes respond with a decline and reach their minimum of ~26 nT by day 21.

With a decline in NAM values in late January to levels below 0, S2 amplitude increases and rise slightly their climatological levels to ∼31 nT on day 32 before falling back when NAM values increase after this day. Another rise in S2 amplitudes occurs towards the end of February when NAM values decline and SPV weakens which results in S2 amplitudes rising above their climatological levels to ∼33 nT after day 60. Compared to S2 tides, the response of L2 tides to the variability of NAM index is more easily recognizable during this winter in Figure 3.6e as the minima and maxima in the amplitudes of L2 are seen to occur concurrently with increasing and decreasing NAM values, respectively. With a local minimum in NAM values around day -20, an enhancement can be seen in L2 amplitude, which rises slightly above their climatological levels to ∼10 nT. Thereafter, as NAM values increase and relatively stronger SPV conditions exist until day -5, L2 amplitudes decline below their climatological levels to ∼6 nT. Another local minimum in NAM ensues around day 0 and L2 amplitudes enhance to a local maximum of 15 nT on day 1. As NAM rises above 2 between days 0 and 20, L2 amplitudes decline below their climatological level under these strong SPV conditions. Once NAM starts its sharp decline in late January, L2 amplitudes rise to a maximum of ∼22 nT on day 31. Associated with this L2 tidal enhancement, the shifting semidiurnal structure in ΔH again appears between days 30 and 40 in Figure 3.6d. In Figure 3.6e, a decline is seen in L2 amplitudes again as they fall back close to their climatological levels by day 50 when NAM values increase above 0 after day 46 and peak around day 50. Another enhancement in L2 is also seen when NAM values decline below 0 around day 60. In Figure 3.6f, it can be noted that this time period was marked by moderate-to-high $F10.7A$ levels and was also geomagnetically active especially on day 61 as the daily averaged Kp values reached above 6 on this day.

Figures 3.6g, h, and i are similar to Figures 3.6a, b, and c, but for the winter of the year 2008-2009. In Figure 3.6i, It can be noted that this time period was marked by low $F10.7A$ levels and was also geomagnetically quiet as the daily averaged Kp values remained low. In Figure 3.6g, the NAM values remain around 0 in November and mid-December before gradually rising to levels above 2 between late December and mid-January. These higher NAM values correspond to strong SPV conditions during these times. In late January, the NAM values decline sharply to levels below -3 and remain there till mid-February before gradually rising and returning to 0 by mid-March. The period between late January and mid-February correspond to weak SPV conditions, which resulted in the strong 2009 SSW event in these times. Corresponding to strong SPV conditions, the L2 amplitudes decline from ∼13 nT in late December to reach below their climatological levels to ∼5 nT in mid-January (in Figure 3.6h). When the SPV conditions become weak in late January, L2 amplitudes increase by up to more than 3 times their climatological levels and reach ∼33 nT by day 28. With the subsequent recovery of the SPV in February, L2 amplitudes decline to their climatological levels. As seen earlier for the 1980-1981 and 1982-1983 winters, S2 amplitudes in Figure 3.6h also show a slightly delayed response to both strong and weak SPV conditions during the 2008-2009 winter. With strengthening SPV, S2 amplitudes decline from ∼31 nT in early January to reach below their climatological levels to ∼26 nT around day 20. With the weakening of the SPV between late January and mid-February and thereafter its subsequent recovery, S2 amplitude gradually increases past its climatological levels by day 24 and eventually reaches up to ∼42 nT on day 50. As the SPV recovers by early March, S2 amplitudes begin to decline back to their climatological levels.

So far, we have seen that the strength of the NH SPV has a large impact on the variability of S2 and L2 tides during the winters of the years of 1980-1981, 1982-1983, and 2008-2009. Recently, *Lawrence et al.* (2020) marked a record-breaking Arctic oscillation and ozone depletion during remarkably strong SPV in the 2020 winter. *Ma et al.* (2022) found a role of the SPV strength in the modulation of the wave activity in MLT region during the winter of 2019-2020. *Matthias et al.* (2016) reported unusual zonal wind and planetary wave activity in MLT region during 2015-2016 winter having strong SPV. With this in mind, the variations in S2 and L2 tides during 2015-2016 and 2019-2020 winters, in which a mighty strong SPV is present, have been explored.

Figure 3.7 is similar to Figure 3.6 but belongs to the winter of years 2015-2016 and 2019-2020. For the winter of 2015-2016, the diurnal variation of ΔH is shown between 1 November 2015 and 31 March 2016 in Figure 3.7a. The blue line presents the variation in NAM values. It can be seen that the S2 decreases and reaches ∼16 nT around day 0 when the SPV is strong and differ by ∼8 nT from the climatological level. This deviation continues until the weakening of the SPV then it becomes approximately equal to the climatological level. We have not found any enhancement in S2 during the marginal weakening of SPV around day 40. The L2 tides reach a minimum value ∼1 nT of the 2015-2016 winter around day 0 during strong SPV. Then, L2 begins to recover and becomes

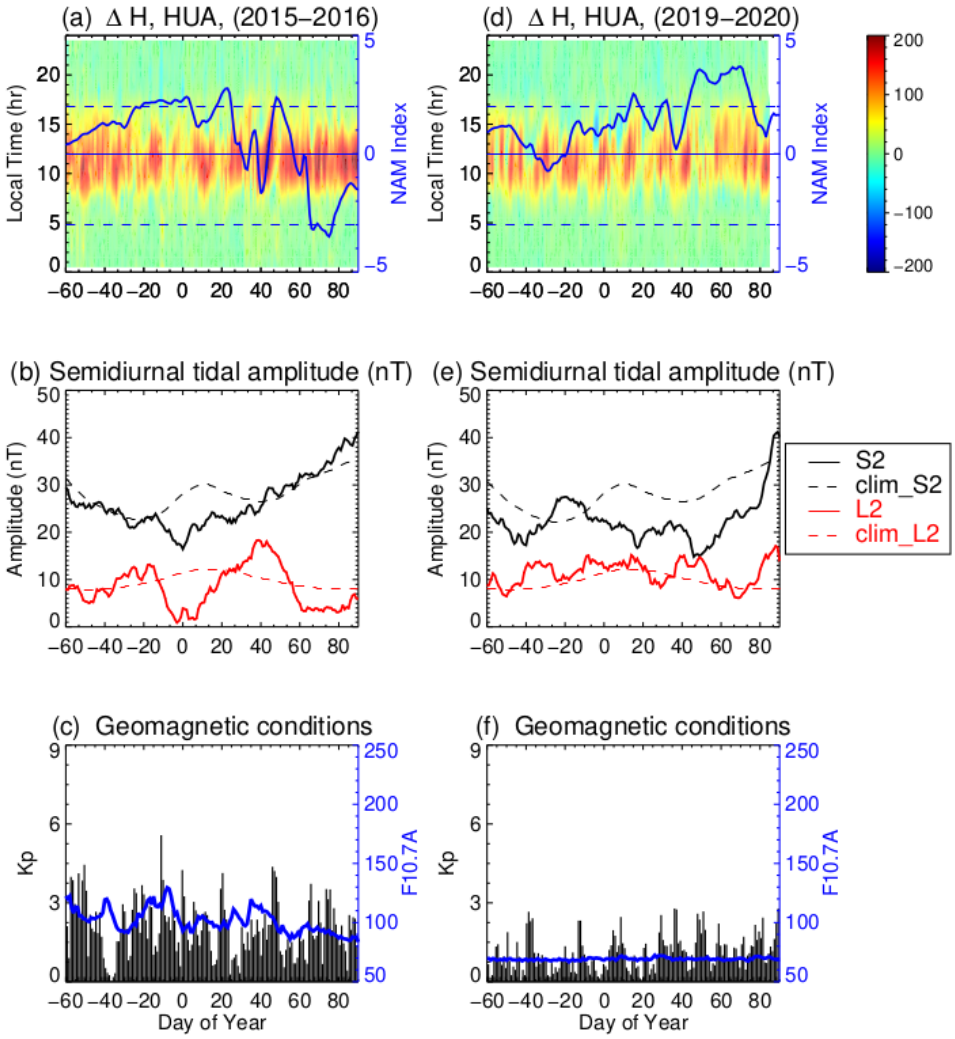

Figure 3.7: This figure is similar to Figure 3.6, but for winters of years 2015-2016 and 2019-2020.

larger than that of the climatological one around day 40 during slightly weak SPV, and after that, it decreases again. Around day 70, both S2 and L2 tides did not show any increment with the weakening of the polar vortex, therefore, this weakening may belong to the final warming by radiative heating. During 2019-2020 winter in Figure 3.7e, the S2 amplitudes begin to decrease as the polar vortex develops stronger around day 40. The difference between the amplitude of S2 and its climatological level increases with increasing strength of the SPV. At the time of the strongest SPV in this winter, the difference between S2 and its climatology approach to the maximum ∼10 nT around day 45. The L2 tide clearly shows an anti-correlation with the NAM values. It reduces around day 30 by ∼8 nT when SPV starts to become stronger and again enhanced with the decline of NAM. At around day 60, a decrease of about ∼8 nT is found in the background of anomalous strong SPV. In this case, the values of L2 are more than climatology even the variations can be seen with the SPV strength.

As discussed above, the vertical E $\times$ B drift is used to explore the M2 variability for the winter of the year 2019-2020 using the above-discussed method in Section 3.2. The analysis is conducted using the vertical drift data between 16 November 2019 and 30 April 2020, and the results are shown in Figure 3.8. This figure represents the variation in L2 amplitude obtained from ΔH (in red color), M2 amplitude (purple color) obtained from E $\times$ B drift, and NAM index (black line) between 1 December 2019 and 31 March 2020. The black-dotted lines denote the reference level for strong and weak SPV as discussed above. Here, it can be noted that M2 and L2 amplitudes show a clear proportionality with each other. M2 and L2 both are enhanced during the period from day -20 to 20, and a reduction can be seen in the period of day 20 to 35. Subsequently, both amplitude rise again during the period of around 40 to 50, followed by a strong decline between around day 50 to around 65. It is clear that the decrease in M2 is more prominent than L2 during anomalous strong SPV conditions between days 40 and 60. The relationship between M2 and L2 is not perfectly linear, which could be due to that the L2 amplitude varies at

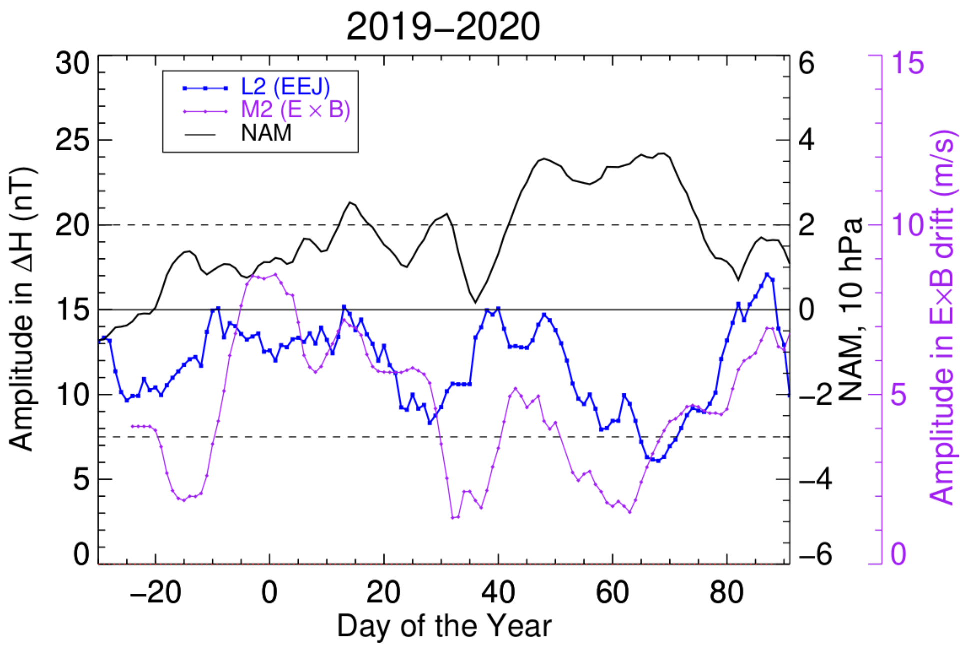

Figure 3.8: Amplitude of migrating lunar semidiurnal tide in the vertical E $\times$ B drift, semidiurnal lunar tide in ΔH variations, NAM values are shown between 1 December 2019 and 31 March 2020 in blue, purple, and black line, respectively. The dashed lines are associated with the reference values for weak (NAM =-3) and strong (NAM = 2) SPV.

different longitudes (*Siddiqui et al.*, 2017) and due to unable to separate the migrating and non-migrating components in L2.

3.4 Discussion

Based on the obtained results, it can be clearly inferred that the response of geomagnetic semidiurnal tidal to strong SPV conditions is generally opposite and slightly weaker than weak SPV conditions. It can also be inferred from our results that S2 and L2 tidal amplitudes are anti-correlated with the NAM index, especially during strong and weak SPV conditions as larger semidiurnal tidal amplitudes are observed during the weak state of SPV and vice-versa. To further quantify the relationship between geomagnetic semidiurnal tides (S2 and L2) and the state of SPV, the S2 and L2 tidal anomalies are plotted against the NAM at 10 hPa in Figure 3.9. In our results, we found that contrary to L2 tides, S2 tides generally respond to the state of the SPV with a time lag. While the enhancement and reduction of L2 amplitudes generally coincide with the fall and rise of NAM index, the S2 amplitudes do not show enhancement or reduction immediately but with a time lag of several days. To account for this lag, we have forwarded the considered time window for S2 tide (from 15 December to 1 March) from day 1 to 20 for each of the winters during the years 1980-2020, whereas, the time window for NAM index is same. The analysis reveals that the mean response of S2 tide to the state of SPV is around 10 days. Following PH22, the S2 and L2 tidal anomalies are plotted between 15 December and 1 March against NAM with a lag of 10 and 0 days, respectively. The results show a clear linear relationship between the S2 and L2 tides across the different ranges of states of the SPV. The linear correlation coefficient is -0.36 for S2 and is -0.38 for L2, indicating that $\sim 15\%$ of the variability in S2 and L2 tides during NH winter can be explained by the state of the SPV.

Also, we have calculated the linear correlation coefficients for each month from October to April between tidal amplitudes and NAM which are shown in Figure 3.10. The x-axis is the month, whereas, the y-axis shows the value of correlation coefficients. It should be noted that the time lag of 10 days between S2 and NAM is considered in the correlation analysis. As seen in Figure 3.10 that the correlation coefficient between S2

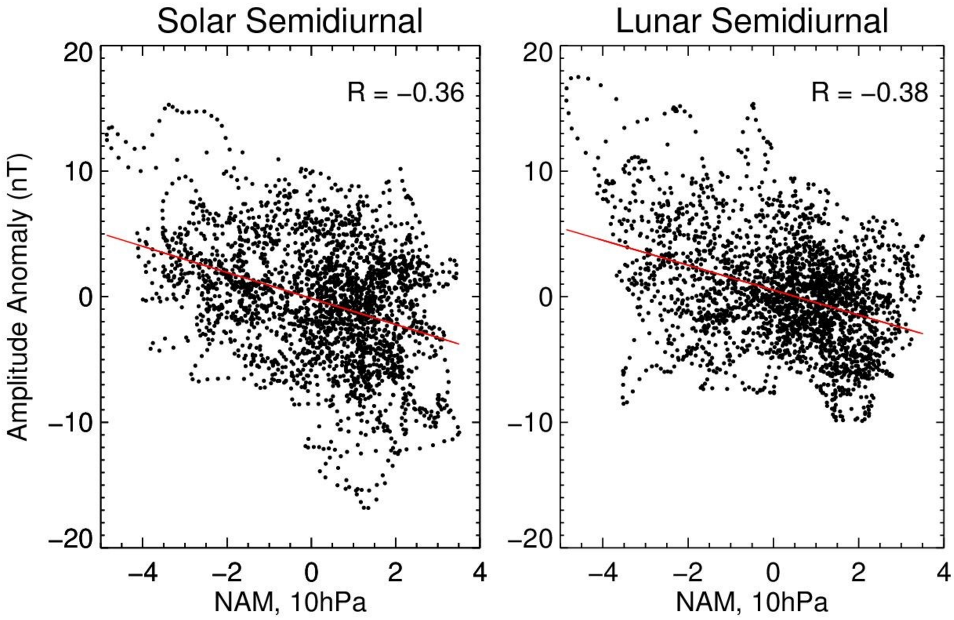

Figure 3.9: Scatter plot between the anomalies in S2 and L2 tides versus the Northern Annular Mode (NAM) at 10 hPa. Results are restricted to the period of 15 December to 1 March.

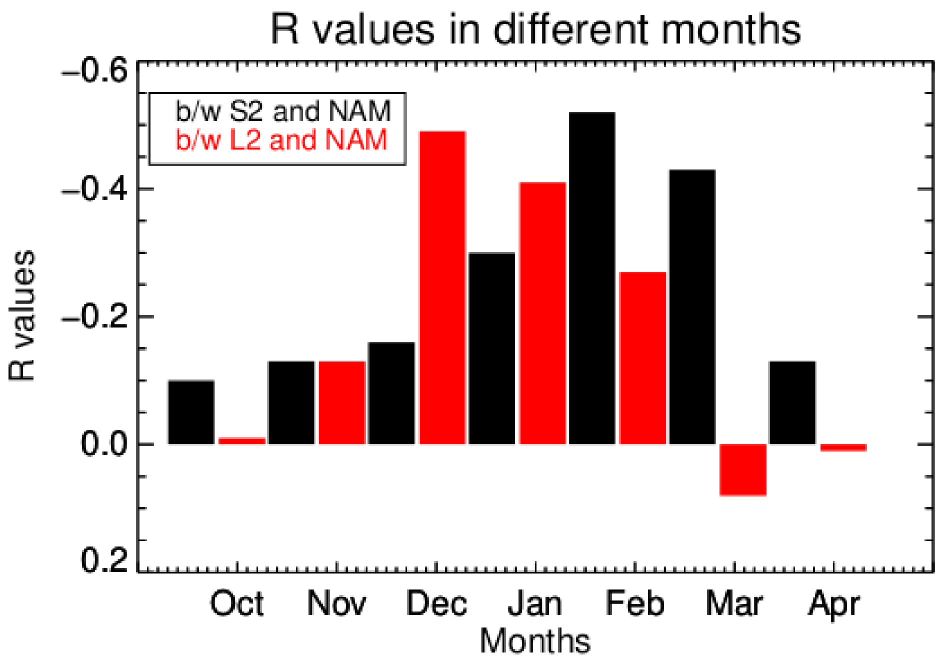

Figure 3.10: The red & black bars show the correlation coefficients between S2 & L2 tides and NAM index in different months from October to April during 1980 to 2020.

and NAM is highest in February month (as R value is around -0.53) followed by 0.45 in March month. While L2 shows a good response to SPV states in December and January as R values are around 0.5 and 0.4, respectively.

In comparison to the results of PH22, we find that the absolute value of the linear correlation coefficient between S2 and NAM is lower and almost half of their reported value for SW2 and NAM. There could be various reasons for this inconsistency between the responses of S2 and SW2 tides to NAM. It is hypothesized that the differences relate to the fact that S2 tides in ΔH comprise of different migrating and non-migrating semidiurnal components that have the following main sources: (1) in situ thermal forcing in the thermosphere, and (2) upward-propagating tides that are generated in the lower atmosphere. The contributions from nonmigrating semidiurnal tides are also present in our calculation of S2 amplitudes since it is not possible to separate the migrating and non-migrating semidiurnal components from single-station observations. The contributions from non-migrating semidiurnal tides can certainly be non-negligible during SSWs as it has been reported that longitudinal changes in ozone distributions could possibly lead to their excitation (*Goncharenko et al.*, 2021). Additionally, the contributions of in-situ generated thermospheric semidiurnal tides, although small (e.g., *Forbes and Garrett*, 1979), are also present in our calculated S2 amplitudes. Also, it was found by PH22 that the relationship between non-migrating semidiurnal tides (SW1 & SW3) and NAM (see their supporting information) is considerably weaker in comparison to SW2. Based on these factors, we can presume that the contributions of nonmigrating semidiurnal tides and in situ generated semidiurnal tides in S2 amplitudes may be a reason for the lower correlation coefficient seen between S2 and NAM in our results in comparison to the results of PH22.

From our results, it was also found that L2 tidal variations respond without any lag to the state of SPV while S2 tidal variations responded with a median lag of around 10 days. It is plausible that the difference in the timing of L2 and S2 tidal response could be due to the mechanisms that drive these tidal variations. Although a detailed analysis of the sources of S2 and L2 tidal variability during strong polar vortex times is beyond the scope of the present study, we may hypothesize the sources of these tidal variations based on our knowledge of mechanisms that are behind S2 and L2 tidal variability during weak polar vortex times. The L2 tidal enhancement during SSWs has been explained through the shifting of the Pekeris resonance peak of the atmosphere towards the lunar semidiurnal (M2) period (*Forbes and Zhang*, 2012). The resonance peak shifts due to the changes in the zonal mean temperature and winds in the middle atmosphere during SSWs.

Large changes in zonal mean zonal wind and temperature have also been seen from the results of PH22 during strong SPV. It is plausible that changes in zonal mean zonal winds and temperature during strong SPV influence the tidal propagating conditions of M2 tide leading to its decline and eventually reducing L2. The correlation coefficient between L2 and NAM is moderate which could be possible due to the fact that the separation of migrating and nonmigrating semidiurnal tides is not possible for single station data. This could be understood from Figure 3.8 that the M2 amplitude significantly reduced rather than L2 during strong SPV as discussed above.

During weak SPV, the role of stratospheric ozone in influencing SW2 tide has been demonstrated using controlled simulations (*Siddiqui et al.*, 2019). As the accumulation in stratospheric ozone at low-latitudes during weak SPV can remain for extended periods, its influence on the SW2 tide is also seen to be protracted. Since strong ozone depletion at low-latitudes have already been observed during the strong SPV in 2020 (*Rao and Garfinkel*, 2020; *Lawrence et al.*, 2020), it is likely that S2 tidal variations may be influenced by changes in SW2 due to stratospheric ozone during times of strong SPV. The influence of stratospheric ozone on SW2 could potentially explain the lagged response of S2 to strong SPV conditions. The response of S2 and L2 with the state of SPV different in different months could be understood that the driving mechanisms of both tides are different. To understand the complete variations of semidiurnal during weak and strong SPV, we need to understand the variability of driving parameters, such as, winds, ozone variation with SPV state, PWs activity in the MLT region.

3.5 Summary

In this study, we have used the horizontal magnetic field recordings from the Huancayo observatory to study the geomagnetic S2 and L2 tidal variabilities during periods of strong and weak SPV. Also, vertical E $\times$ B drift obtained from IVM onboard ICON satellite has been used to derive the amplitude of M2 tide. The strength of SPV is defined by the NAM index which has been calculated using the anomalies in geopotential height over the north polar region (65°). Then, the variation in the ΔH, and the variation in the S2 and L2 tidal amplitudes with the NAM values have been seen for some individual winters of the years of 1980-1981, 1982-1983, 2008-2009, 2015-2016, and 2019-2020. We have found the enhancement and diminution in the S2 and L2 tidal amplitudes during weak and strong SPV, respectively. The response of the S2 tide with the strength of the SPV appeared after around 10 days, whereas the L2 responds immediately with the variation of NAM. For the winter of the year of 2019-2020, a noteworthy reduction was present in the M2 amplitude during February-March months, whereas, L2 also shows a decrease in amplitude. Month-wise responses of S2 and L2 with the state of SPV are quite different as L2 responded during December-January months whereas S2 shows a better dependence in the month of February-March. These results clearly show the strong SPV, in addition to the weak SPV, also has a notable impact on the ionosphere. Most of the content of this chapter has been published in the journal Earth, Planets and Space, 2023 (*Kumar et al.*, 2023b). These electric field variations also propagate to the upper atmosphere through vertical drift that we will see in the next chapter.

Chapter 4

Latitudinal dependence of equatorial electrodynamics and meridional winds in the redline dayglow

4.1 Introduction

As it has been seen in Chapter-3 that the ionospheric eastward electric field over the equatorial region is generated and modulated by the tidal winds in the dynamo region (e.g., *Lühr and Manoj*, 2013; *Soares et al.*, 2022). This electric field primarily drives the upper atmospheric dynamics over low- and equatorial-latitudes. It has been shown by the radar and geomagnetic observations from ground and space that the EEJ strength is proportional to the vertical drift (*Anderson et al.*, 2004; *Stolle et al.*, 2008; *Kumar et al.*, 2016) as their source is the same equatorial electric field. The EIA plays a vital role in bringing about latitudinal variations in electron densities as shown in earlier studies (e.g., *Anderson*, 1973; *Raghavarao et al.*, 1988a,b; *Sridharan et al.*, 1994; *Pallamraju et al.*, 1996, 2002; *Pallam Raju and Sridharan*, 1998). *Dunford* (1967) showed the positive correlation between electron density observed by the Alouette 1 topside sounder and the horizontal component of geomagnetic field data over Indian longitude. In terms of TEC, *Deshpande et al.* (1977) reported a relationship between EIA and EEJ as EIA was found to be strong on a strong EEJ day and absent of EIA on a CEJ day. They have proposed the response time of the EIA crest around 2-3 hr with EEJ. The strength of the EIA (*Rush and Richmond*, 1973) is shown to be directly proportional to the pre-noon integrated (7–12 IST) strength of the EEJ (*Raghavarao et al.*, 1978b) and so, the pre-noon integrated EEJ strength has been used as a proxy to the equatorial electrodynamics. *Rastogi and Klobuchar* (1990) found a good linear relationship between the EIA strength and EEJ in Indian longitude. The varying EIA anomaly strength using the OI 630.0 nm airglow emissions in daytime from ground-based observation is shown with EEJ strength by *Pallamraju et al.* (1996). *Karan et al.* (2016) showed the asymmetricity of the peak in the OI 557.7 nm, 630.0 nm, and 777.7 nm dayglow emissions which vary with the strength of the EEJ, later the asymmetricity in the diurnal variations in dayglow emissions is used to estimate the equatorial vertical drift (*Karan et al.*, 2020).

The strength of EIA shows hemispheric asymmetric variation with respect to the dip equator as it is usually stronger in one hemisphere than another. The cause of this asymmetric variation is believed to be the thermospheric meridional winds. The meridional winds move the plasma to different altitudes as the plasma gets pushed along the geomagnetic field lines. Thus, the neutral meridional winds modulate the EIA strength (e.g., *Anderson*, 1973; *Rishbeth*, 1977; *Balan et al.*, 1995; *Khadka et al.*, 2018; *Saha et al.*, 2021). The plasma and neutrals are coupled to each other through ion-neutral collision via meridional winds, which give rise to the asymmetric variation of the EIA with respect to the dip equator (e.g., *Rishbeth*, 1972; *Valladares and Chau*, 2012). Sometimes, it can create another ionospheric layer (*Rishbeth*, 1972; *Herrero et al.*, 1993; *Makela et al.*, 2013). Recently, the occurrences of post-sunset enhancements in the OI 630.0 nm nightglow over low-latitudes have been shown to be due to the poleward meridional wind as it brings more plasma at the emission altitudes (*Saha et al.*, 2021).

Investigations on the equatorial upper atmospheric dynamic processes in the daytime carried out using thermospheric dayglow emissions as tracers showed both latitudinal and longitudinal variabilities (e.g., *Pallamraju et al.*, 1996, 2010; *Sridharan et al.*, 1999; *Shepherd et al.*, 1993a; *Chakrabarty et al.*, 2004; *Karan and Pallamraju*, 2017, 2018). As discussed above, the effect of both equatorial electrodynamics and meridional winds has been seen on the upper atmospheric dynamics over low-latitudes. Here, an investigation of the equatorial electrodynamics along with the thermospheric meridional winds has been carried out in the upper atmosphere using OI 630.0 nm dayglow emissions over a large spatial extent using the data of January-February 2020 to investigate the influence of their relative roles. As the solar flux did not show any significant variation in this time window (range of variation is only 68–72 sfu) and there were no geomagnetic storms (maximum daily average value of Ap is 15) as well in this chosen window. Therefore, it presents a unique opportunity to carry out this study. Investigations have been carried out using the OI 630.0 nm dayglow data from two large FOV imaging spectrographs one located at HYD and the other at AHD in Indian longitudes, which collectively cover a large latitudinal extent from 5°-18° MLAT.

4.2 Data used

For this work, we used the OI 630.0 nm dayglow emission intensity, EEJ, thermospheric meridional winds from the MIGHTI on-board ICON satellite and HWM-14 model, electron density information from the IRI model, and neutral thermospheric density from NRLMSISE-00 model during January-February 2020. These data sets and measurement techniques are described in Chapter-2.

Figure 4.1shows the schematic of the observational locations, wherein the x-axis

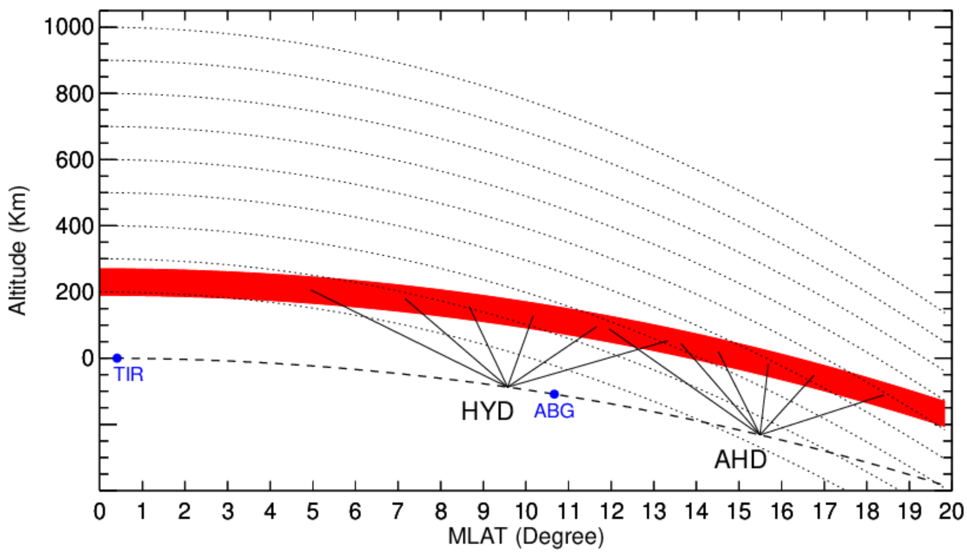

Figure 4.1: Schematic showing the regions of OI 630.0 nm dayglow emissions over different MLAT in red color. The field-of-view of MISE is shown by black solid lines from HYD and AHD. The geomagnetic field lines are represented by dotted black line. TIR and ABG indicate the locations of geomagnetic field measurements.

and y-axis depict MLAT and altitude, respectively. Red colored region centered at 230 km corresponds to the OI 630.0 nm dayglow emission region with a width of 100 km. For this study, the FOV of each of the spectrographs is partitioned into 5 independent segments as shown by black straight lines, and so a total of 10 viewing directions exist over spatial regions from 5° to 18° MLAT. The EEJ strength is obtained using geomagnetic observations from the TIR and ABG.

4.3 Observation and results

Dayglow emission rates vary with the solar flux, solar zenith angle (SZA), and also include the contribution from transportation. The production mechanisms for the OI 630.0 nm dayglow emissions mainly are photoelectron impact excitation of ambient atomic oxygen (O), photodissociation of molecular oxygen (O_2), and dissociative recombination (DR) of molecular oxygen ions (O_2^+) with electrons (*Solomon and Abreu*, 1989) as mentioned in Chapter-2. Out of three, first two mechanisms depend on the solar flux and SZA values, but the third, namely the DR mechanism also responds to the transportation of plasma and neutral caused due to electrodynamics, neutral winds, and waves. Contributions from all these three mechanisms are altitude dependent with DR mechanism being at the highest altitude among them (*Solomon and Abreu*, 1989). It has been shown that OI 630.0 nm dayglow emissions over low-latitudes show dependency on the solar flux (*Zhang and Shepherd*, 2004; *Pallamraju et al.*, 2010) and equatorial electrodynamics as it causes the plasma transportation from the equatorial region (e.g., *Sridharan et al.*, 1992a, 1994; *Pallamraju et al.*, 1996, 2010; *Chakrabarty et al.*, 2002; *Karan et al.*, 2016). Also, the meridional winds can change the altitude distribution of the plasma (*Balan et al.*, 1995; *Valladares and Chau*, 2012) which can affect the OI 630.0 nm emission intensity. For the nighttime OI 630.0 nm nightglow emissions, it has been shown clearly that the poleward meridional winds in the northern hemisphere bring down the plasma density to lower altitudes, which thereby contributes to the enhancement of the nightglow emissions (*Saha et al.*, 2021). Figure 4.2 gives an overview of the variations of daily averaged OI 630.0 nm dayglow emissions obtained from Carmen Alto, Chile, (a low latitude location in American longitude, 10.5° MLAT) with the variation of daily sunspot numbers varying from around 60-180 and daily integrated EEJ strength (obtained by $\Delta H_{Jicamarca} - \Delta H_{Piura}$). It can be noticed that in this observational window, the dayglow emission variability is controlled by the number of sunspots and not by the EEJ strength as the primary factor for the production of OI 630.0nm emissions is still the solar flux on a given day.. From the above discussion, it is clear that dayglow emission variability is mainly driven by the solar flux, whereas, electric field and neutral winds also can play a role in the OI 630.0 nm dayglow emission variability. As mentioned above, the solar flux varied only from 68 to 72 sfu during January-February 2020. Therefore, it is expected that the variation in dayglow emissions due to solar flux will be very small in this period. So, the transport effect in terms of equatorial electrodynamics, neutral winds, and waves are the main causes for the day-to-day variations in the OI 630.0 nm dayglow emission.

Firstly, the daily variation in the dayglow emissions due to the equatorial electrodynamics and meridional winds is investigated wherein a comparison is made for neighboring days but with differing electrodynamics and neutral dynamics conditions: Case (I) when the magnitude of meridional winds is similar and EEJ strengths are different, Case (II)

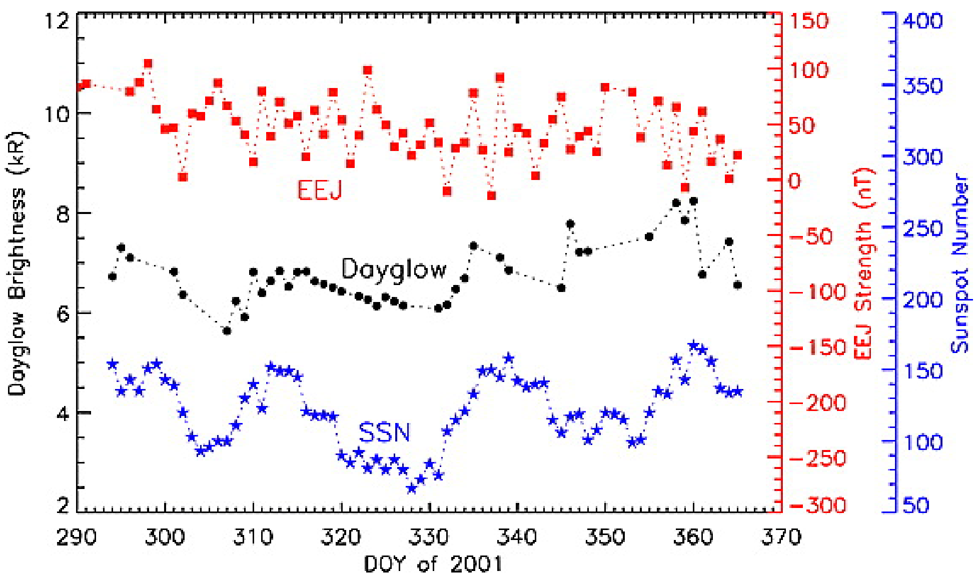

Figure 4.2: The daily averaged OI 630.0 nm dayglow emissions obtained from Carmen Alto (10.5° MLAT in American longitude), Chile, is shown in black line. The blue line denotes the daily values of sunspot numbers. Daily averaged EEJ values obtained by $\Delta H_{Jicamarca} - \Delta H_{Piura}$ are shown in red line. The dayglow emissions varied in phase with the sunspot number, not with EEJ which represents that the sunspot numbers govern the long-term variability in the emissions. (After *Pallamraju et al.* (2010))

EEJ strength is similar but meridional winds are different, and Case (III) EEJ strength and meridional wind are larger than another day are compared. These different cases are shown in Figures 4.3, through 4.5, respectively.

Case (I): Panels a & d in Figure 4.3 show the diurnal variation of the EEJ where prenoon (7-12 IST) integrated EEJ values are depicted in nT-hr for 22 & 24 January 2020. Diurnal meridional wind variations are shown in panels b & e wherein daily averaged meridional wind (9-16 IST) values (in unit of ms^{-1}) are presented. Diurnal dayglow emissions are shown in panels c and f corresponding to the zenith view direction of the HYD and AHD in red and black lines. The daily averaged values (9-16 IST) of dayglow emissions are also shown in respective colors. Missing values in the noon-time of dayglow emissions are linearly interpolated. On these two days, Ap values (1 & 3) are very small and the magnitudes of the daily averaged meridional wind (47 & 46 ms^{-1}) are almost similar. Whereas the EEJ strength is quite different (61 & 15 nT-hr) as it is around 4 times

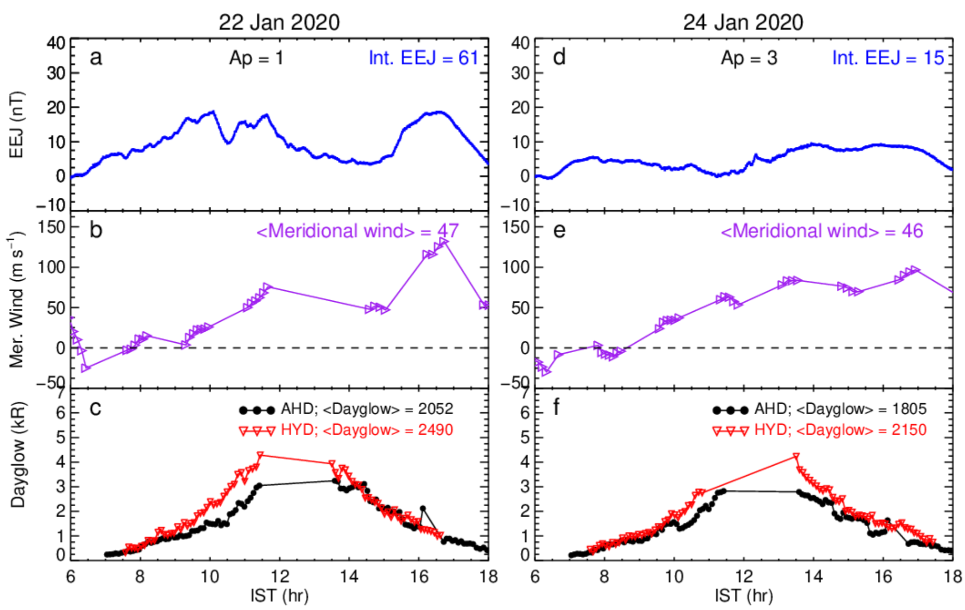

Figure 4.3: The diurnal EEJ, meridional wind, and OI 630.0 nm dayglow emission (over zenith at HYD and AHD) for 22 January (panel a, b, and c) and 24 January 2020 (panels d, e, and f) corresponding to Case (I), when magnitudes of meridional winds are similar, but pre-noon integrated EEJ strengths are different, are shown. Pre-noon integrated EEJ strengths, daily averaged meridional wind (<meridional wind>), and daily averaged OI 630.0 dayglow emission intensities (<Dayglow>) (in the unit of nT-hr, ms^{-1}, and Rayleigh, respectively) are also shown in the relevant panels.

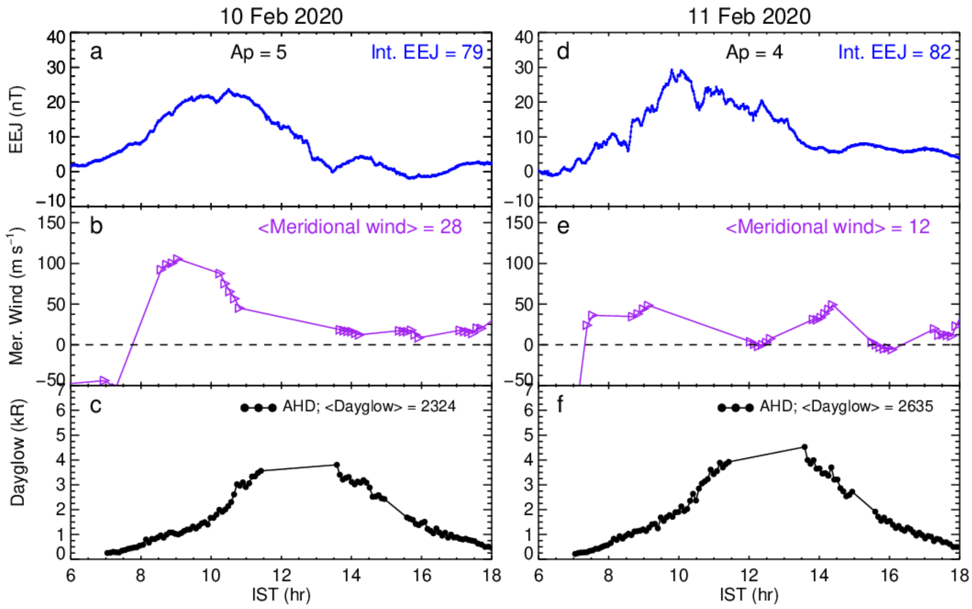

Figure 4.4: Similar to Figure 4.3 but for 10 and 11 February 2020 corresponding to Case (II), when EEJ strengths are similar, but magnitudes of meridional winds are different.

higher on 22 January than 24 January. Therefore, it can be expected that the contribution in dayglow emissions from compositional changes will be almost similar on these two days and, mainly, the difference will be originated due to the equatorial electrodynamics. It can be seen that the values of averaged dayglow emissions over zenith at HYD and AHD are larger on 22 January (as compared to 24 January), essentially due to the effect of strong equatorial electrodynamics.

Case (II): Figure 4.4 corresponds to the 10 and 11 February 2020 where all panels are arranged in a manner similar to that described in Figure 4.3. The Ap values (5 & 4) are almost similar. On these two days, the equatorial electrodynamics strength is almost similar (as EEJ is 79 & 82 nT-hr) but the poleward meridional winds were larger on the 10 (28 February ms^{-1}) as compared to 11 February (12 ms^{-1}). Interestingly, the daily averaged dayglow emission over AHD is smaller on 10 February when meridional wind is larger. The dayglow data is not available from HYD on these two days.

Case (III): Two other sample days are discussed when one day (13 February) the EEJ strength is 56 nT-hr and meridional wind is 23 ms^{-1}, and on another day (14 February) EEJ strength was 90 nT-hr and meridional wind magnitude was 41 ms^{-1} as shown in Figure 4.5. Both days are geomagnetically quiet as Ap values were 1 & 2. Interestingly, although the dayglow over HYD responds to the increase in the equatorial electrodynamic

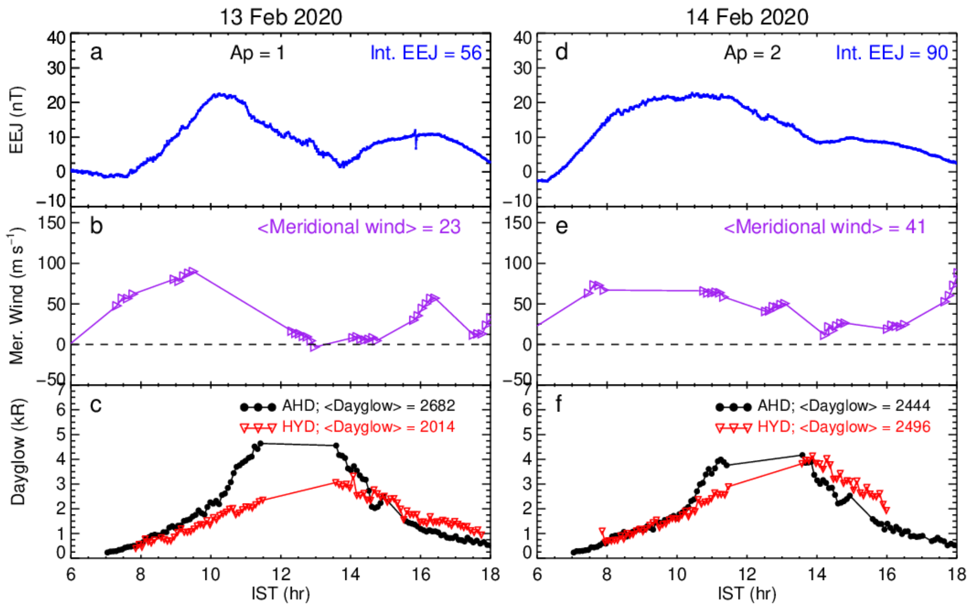

Figure 4.5: Similar to Figure 4.3 but for 13 and 14 February 2020 corresponding to Case (III), when magnitudes of both meridional winds and EEJ strengths are different than the other day.

strength on 14 February, the dayglow emission over AHD is larger on the 13 even though the electrodynamic strength was smaller by around 34 nT-hr. On 13 February, this enhancement in emission over AHD can most likely to be associated with a small value of poleward meridional wind which indicates that the dayglow emissions over AHD are more critically dependent on the meridional winds. Thus, it clears that the influence of the equatorial electrodynamics on the OI 630.0 dayglow emissions is stronger over HYD but at AHD, the effect of meridional winds dominates.

Case (IV): Four days of data over AHD wherein two days with extremely strong counter electrojet and two days with large EEJ strengths (marked as 1,2,3,4 in panel b of Figure 4.7) are discussed here. Out of the four, on two days (31 January & 6 February) wind data from MIGHTI are available and are shown in Figure 4.6. On these days, the Ap values were 7 and 15. It can be seen from Figure 4.6 that on 31 January, EEJ strength (-53 nT-hr) is much weaker than on 6 February (145 nT-hr). In spite of the comparatively large equatorial electrodynamic effect on 6 February, dayglow emission over AHD shows only marginal enhancement compared to that on 31 January, presumably due to larger meridional wind magnitude on the 6 February. Based on the discussion so far and data are shown in Figures 4.3-4.5, it is expected that if the dayglow data over HYD were present,

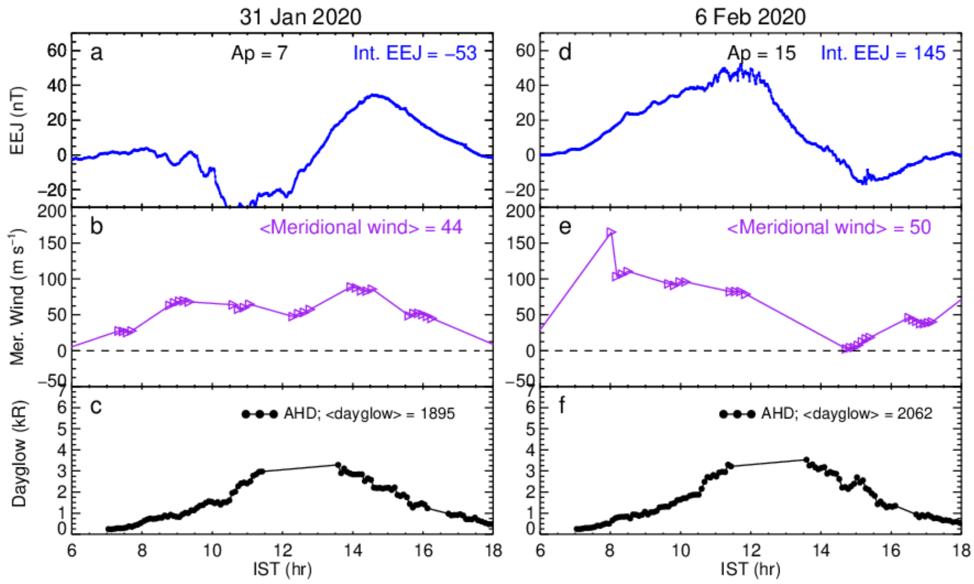

Figure 4.6: Similar to Figure 4.3 but for 31 January 2020 and 6 February 2020 corresponding to Case (IV), in which days with strong counter electrojet and strong EEJ strengths are compared.

it would have shown larger magnitudes.

To investigate the day-to-day effect of the equatorial electrodynamics and meridional winds on the variability of OI 630.0 nm dayglow emission in the months of January and February 2020 over the zenith of HYD and AHD, daily averaged OI 630.0 nm dayglow emission, prenoon integrated EEJ, and daily averaged meridional wind are considered and are shown in Figure 4.7 for HYD and Figure 4.7b for AHD with day of the year (DOY) in red, blue, and purple lines, respectively. The numbers of clear sky data available over HYD and AHD are 16 and 32, respectively. All the days are geomagnetically quiet (maximum daily average value of Ap is 15) and, therefore, modulations in the dynamics from high-latitudes in terms of compositional changes are not expected on the OI 630.0 nm dayglow variations over low-latitudes (e.g., *Pallamraju et al.*, 2004b; *Karan and Pallamraju*, 2018). It can be noted in Figure 4.7 that the OI 630.0 nm dayglow emissions vary with the strength of the equatorial electrodynamics (EEJ taken as proxy) over zenith location of HYD with a moderate value of correlation (R = 0.57) (In the estimation of this correlation, the counter electrojet days are not considered). The dayglow emissions over AHD (panel b) are also found to be influenced by the equatorial electrodynamics to a similar extent as over HYD (R value = 0.53). Hence, the moderate R values clear that other forces rather than equatorial electrodynamics are also affecting the dayglow emissions variability. Then,

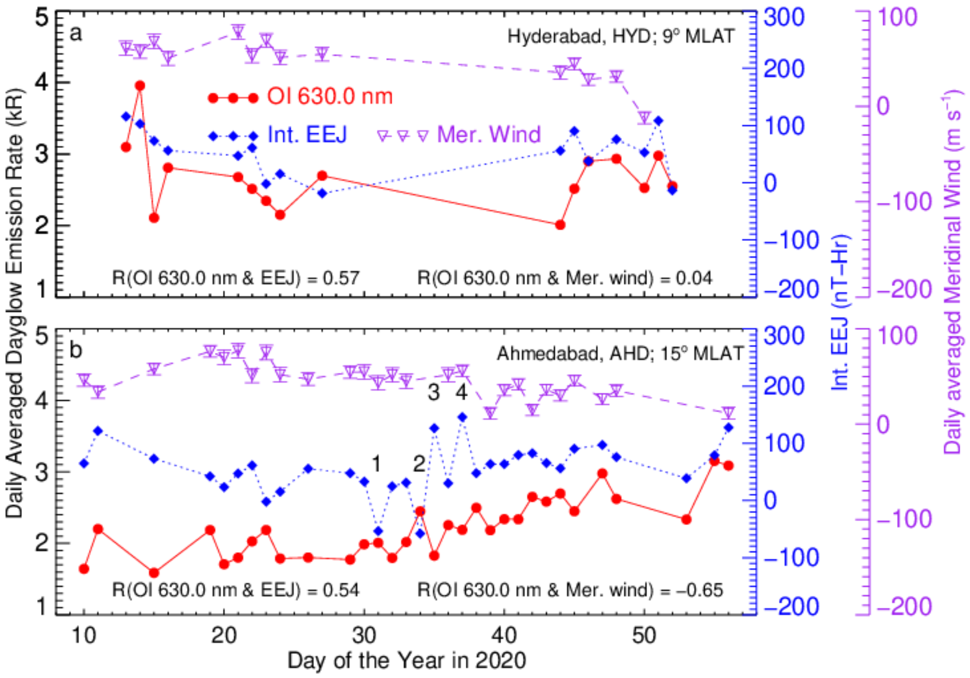

Figure 4.7: The daily averaged OI 630.0 nm dayglow emissions (solid red line), pre-noon integrated EEJ (dotted blue line) and daily averaged meridional wind (dashed purple line) as obtained for the corresponding latitude of HYD & AHD are shown in Panel a & b, respectively. The R values between these parameters are also depicted.

the values of correlation coefficient between dayglow emission and meridional wind is found to be 0 for HYD but for AHD it is -0.65. As discussed above, the four days between DOY 30-40 (marked by numbers 1 to 4 in Figure 4.7b) are not considered in the linear regression analysis. From these R values, it can be said that over HYD, the effect of the equatorial electrodynamics is more significant than the meridional wind. But, for AHD, meridional wind plays a more important role in the variability of the dayglow emissions than the equatorial electrodynamics.

So far, the dayglow emissions variability over zenith of HYD and AHD have been analyzed which showed varying impacts of the equatorial electrodynamics and meridional wind on the variation of the upper atmospheric behavior over two low-latitude locations. It seems that the effects of equatorial electrodynamics and meridional winds are different at different latitudes. Hence, as described above, the total spatial coverage is organized into 10 different spatial regions spanning 5°-18° MLAT. Column-integrated dayglow emissions measured in each of the 10 directions are considered separately. The contribution to the dayglow emission due to the ionization brought in from the magnetic equatorial

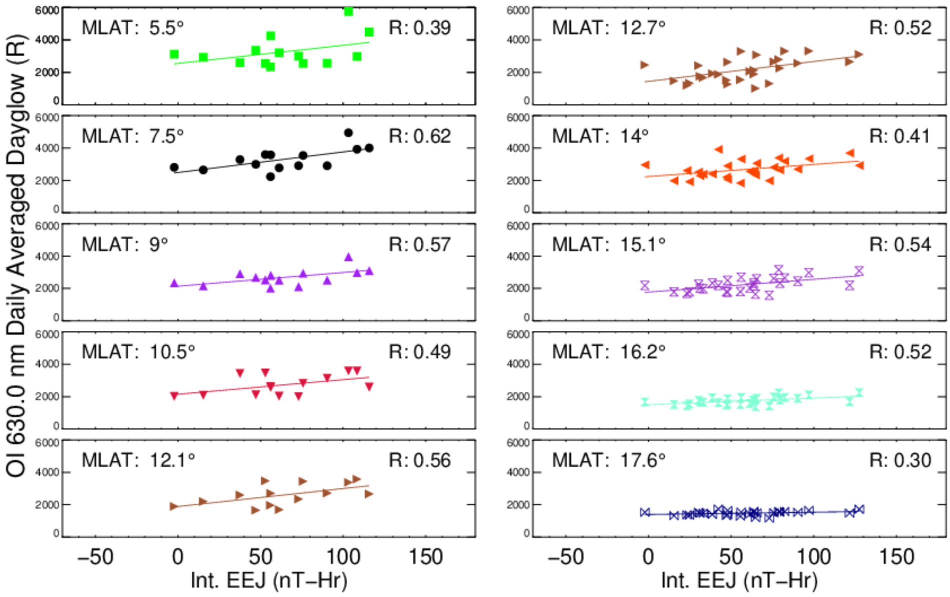

Figure 4.8: OI 630.0 nm daily averaged dayglow emission intensities with pre-noon integrated EEJ strengths along with linear fits corresponding to different view directions (MLAT).

regions will be different at different view directions at any given time. To gain a comprehensive understanding of the systemic nature of these variations as a function of equatorial electrodynamics strength at any given location, the daily averaged OI 630.0 nm dayglow emissions are considered. As shown in Figure 4.8, daily averaged OI 630.0 nm dayglow obtained along each of the view direction is plotted corresponding to the prenoon integrated EEJ strength values on that day, and linear regression analyses have been carried out. Each of the plots corresponds to a different MLAT which progressively increases as we move from top to bottom. Similarly, the linear regression analyses have been carried out between OI 630.0 nm dayglow emissions and meridional winds for each of the view directions to see the impact of the magnitude of meridional winds on the dayglow emission variability and are shown in Figure 4.9.

It can be seen that the effect of equatorial electrodynamics on OI 630.0 nm dayglow emission is nearly similar over all latitudes as shown in Figure 4.8, however, the effects of meridional winds on the OI dayglow emission rates gradually changes from the favorable to adverse as one moves away from the dip equator (Figure 4.9). These correlation values are summarized in Figure 4.10. Here, the x-axis represents the MLAT and the y-axis represents the R values, where, blue and purple lines show the R values between dayglow

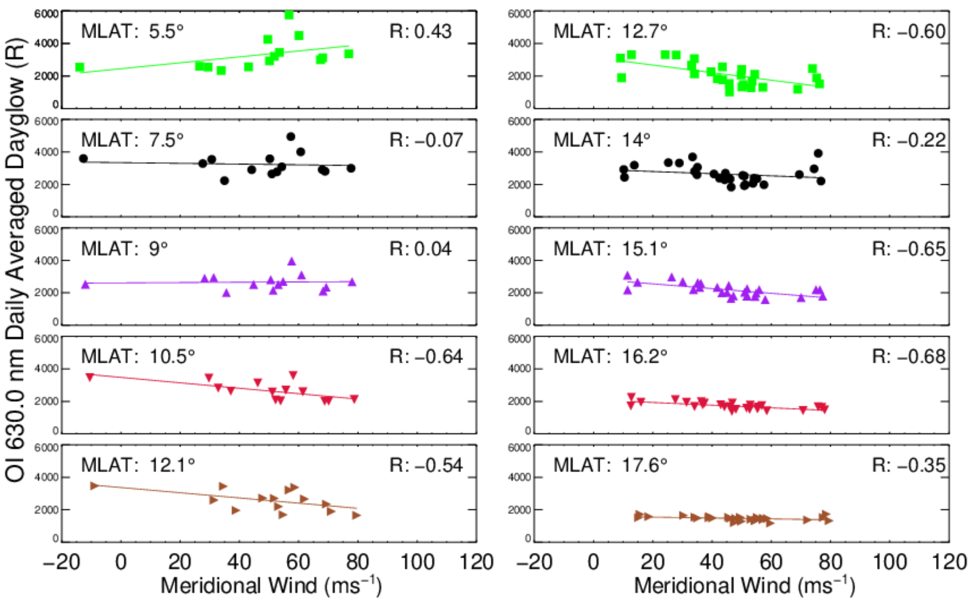

Figure 4.9: OI 630.0 nm daily averaged dayglow emission intensities as a function of daily averaged meridional winds along with linear fits corresponding to different view directions (MLAT).

emission and EEJ strength, and dayglow emission and meridional wind at different MLAT. It can be noted that the equatorial electric field effect on the OI 630.0 nm dayglow emission over large MLAT is nearly the same with correlation coefficients varying from 0.62 to 0.4 (except 17.5° MLAT where it is 0.3).

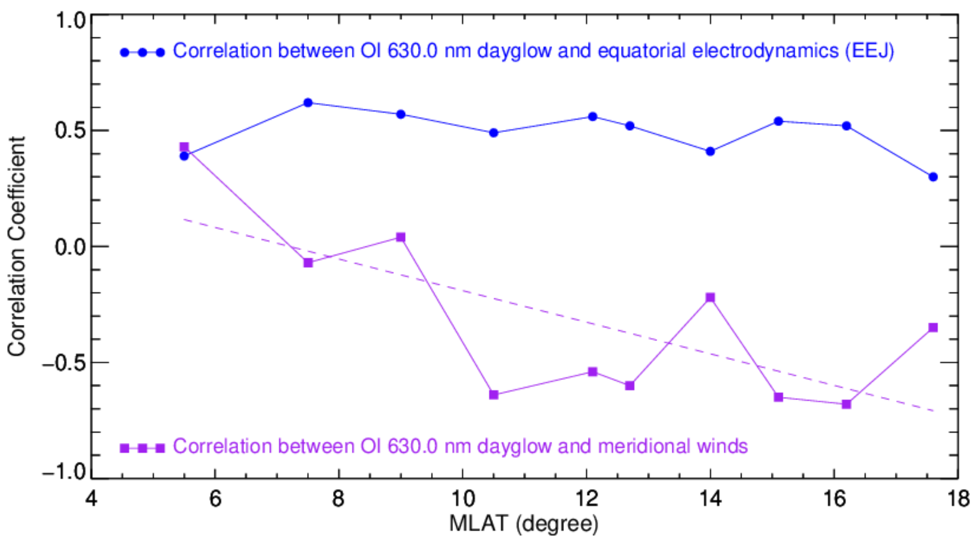

Figure 4.10: Correlation coefficient values as in Figure 4.8 and 4.9 are shown along with MLAT. The dashed purple line denotes the linear fit between the correlation coefficients of the OI 630.0 nm averaged dayglow emission intensities with meridional wind and MLAT.

The R values between dayglow emissions and meridional winds vary from 0.42 to -0.67 (Figure 4.10) in the range of $5° - 18°$ MLAT. This means that closer to the dip equator the poleward meridional wind assists the OI 630.0 nm dayglow emission rates, while at latitudes further away, it reduces the OI 630.0 nm emission rates. There are a few excursions in the correlation coefficients at 14° and 17.5° MLAT. As the main objective here is to study the systemic nature of variation in the OI 630.0 nm dayglow emissions due to different forcing factors, a linear fit is drawn to these variations in the R values for the correlation of meridional winds with OI 630.0 nm dayglow emissions which is shown by purple dashed line. From this fitted line it can be noted that near the equator, the meridional wind assists in the enhancement of the dayglow emission, but, as one moves further away from the dip equator, it reduces the dayglow emission rates.

4.4 Discussion

Here, the varying effects of the equatorial electrodynamics and meridional wind (in the range of 5°-18°) on the OI 630.0 nm dayglow emissions at different MLAT are investigated. For that, the OI 630.0 nm dayglow emissions data from two MISEs located at HYD & AHD are considered. These two locations are separated by around 6° in longitude. It has been shown earlier that longitudinal differences can exist at such distances (*Karan and Pallamraju*, 2017). However, such longitudinal differences in equatorial electrodynamic processes are not expected to significantly alter the results arrived in this study, as, (i) a systemic nature of variation is being investigated here for which the daily averaged values are being considered and hence, any longitudinal variations within a day will be averaged out, (ii) the correlation coefficient between the equatorial electrodynamics variation and dayglow emission for segments 1-5 and 6-10 shown in Figure 4.8 are all similar and the view directions of all these segments are within the crest of the EIA. The R values of dayglow emissions with EEJ and meridional winds for the almost overlapping view direction 5 & 6 are nearly similar as shown in Figure 4.10.

To understand the cause of such varying effects of the meridional wind on the dayglow emissions, the production mechanism and ionospheric state as a function of latitude are analyzed. The variability in OI 630.0 nm emissions is expected due to the DR mechanism.

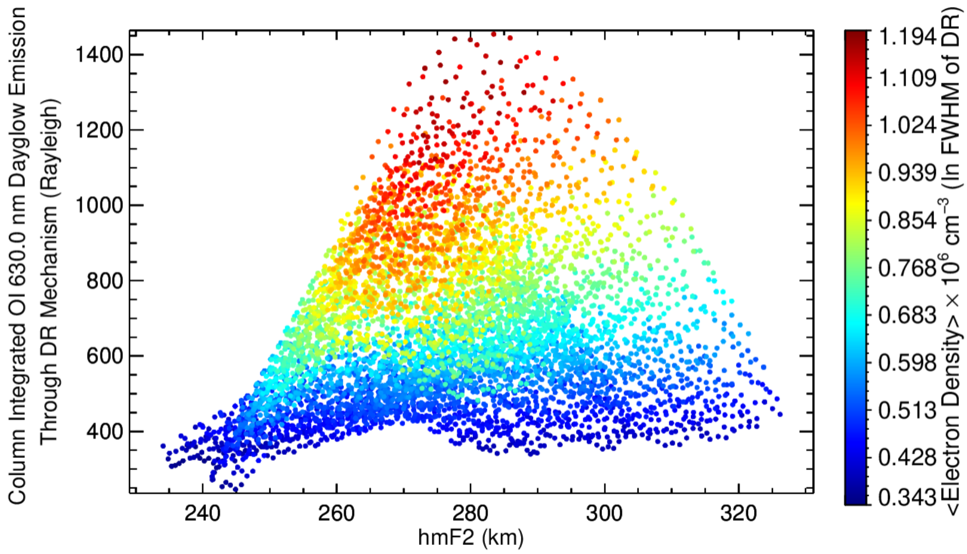

Figure 4.11: The column integrated OI 630.0 nm dayglow emission intensity through DR mechanism is shown with the hmF2 of the ionosphere. Different color data points denote the averaged electron density in the FWHM of DR (230 ± 30 km). The dayglow emissions belong to the January-February 2020 duration in the range of 5°-18° MLAT, and obtained by using IRI-16 electron density and NRLMSISE-00 neutral density data.

Therefore, the OI 630.0 nm dayglow emissions through DR mechanism are estimated using the electron density data from the IRI-16 model (*Bilitza et al.*, 2017), and neutral density and temperature data from the NRLMSISE-00 model (*Picone et al.*, 2002) for the similar period and spatial region to the measurements. The method of estimation is described in Chapter-2. Figure 4.11 shows the column integrated OI 630.0 nm dayglow emissions with hmF2 values (ionospheric altitude where electron density peaks), whereas, the color bar represents averaged electron density in the full-width at half maximum (FWHM) of DR emissions. Here, it can be noted that the dayglow emissions maximize when hmF2 is around 280 km in the considered period and latitude range. Therefore, for this duration (January & February 2020) and spatial region (5°-18° MLAT), the optimum hmF2 altitude (when dayglow emission is maximum) of the ionosphere is 280 km which has been selected as a reference height for further analysis. It could be slightly different for the different temporal and spatial windows. Further, the ionospheric state is analyzed, wherein, the hmF2 values are obtained from IRI-16 model for the same period and spatial region as observations for each latitude which is shown by black solid line in Figure 4.12. The correlation coefficient (purple line) values between dayglow emissions and meridional

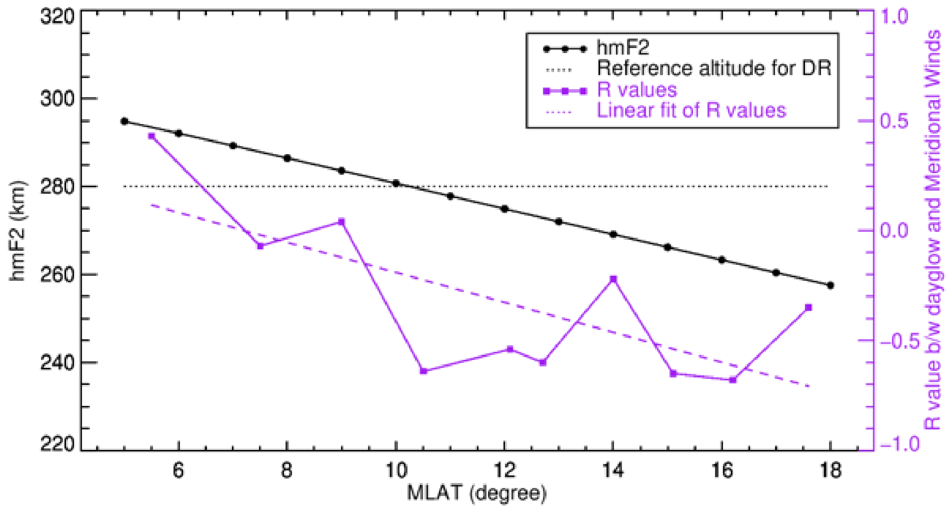

Figure 4.12: The averaged hmF2 during January-February 2020 obtained from IRI-16 model is shown with MLAT in black solid line. The dashed black line denotes the reference altitude (280 km) as described in text. The correlation coefficient values between dayglow emissions and meridional winds (also shown in Figure 4.10), and its linear fitting with MLAT is shown in purple solid and dashed lines, respectively.

winds are shown in purple solid line in Figure 4.12.

Here, it can be noted that the hmF2 altitude is higher near the equator than the reference level, whereas, it is lower after 10 MLAT. It is known that the equatorial electrodynamics drift contributes to the upliftment of the ionosphere to high altitudes over the dip equator, while, at latitudes away from the dip equator, other effects along with the equatorial electrodynamics get convolved resulting in the hmF2 values. The effect of poleward meridional wind in the northern hemisphere contributes to a downward motion of the ionospheric F-layer with heights proportional to U.cosI.sinI, where U is the meridional wind and I is the dip angle at a given latitude, consequently, the hmF2 decreases. Similarly, the equatorward wind lifts the ionospheric layer upward. Therefore, the positive or negative contribution by the DR mechanism in OI 630.0 nm dayglow emissions depends on whether the plasma density increases or is taken away by the meridional winds around the peak emission altitude region of DR. From hmF2 altitudes, as shown in Figure 4.12, it can be understood that whenever the height of hmF2 is greater than the reference altitude of DR, a poleward wind assists in the enhancement of the dayglow emission rates as plasma is brought into the region of greater production of excited atomic state ($O(^1D)$) via the DR mechanism. When hmF2 is lower than the reference altitude of DR, meridional wind takes away the plasma from the altitude region where the production by the DR is most effective to lower altitudes. This feature is clearly reflected in the correlation analysis between the variation in the meridional wind magnitudes and the dayglow emission rates as seen in Figure 4.12. The correlation between dayglow and meridional wind is positive closer to the dip equator when the hmF2 is higher than the reference altitude and it systematically changes to negative as one moves away from the dip equator where the hmF2 is lower than the reference altitude.

Further, from Figure 4.3, it is seen that around 75% decrease in the EEJ strength due to equatorial electrodynamics results in around 14% and 12% decrease in the daily integrated OI dayglow emission rates over HYD and AHD. From Figure 4.4, it is seen that about 57% decrease in the meridional winds contributes to a 13% enhancement in the diurnal integrated dayglow emission over AHD. While competing effects due to enhancements in EEJ strength (by 61%) and meridional wind (by 78%) resulted in a decreased of the dayglow over AHD by 9% (Figure 4.5). Over HYD, however, it resulted in an enhancement of dayglow by 24%. Therefore, it can be surmised that the relative contributions of equatorial electrodynamics and meridional winds to the OI 630.0 nm dayglow emission rates are non-linear and vary with latitude. The linear fit shown in Figure 4.10, therefore, can, at best, be described as a zeroth order estimate wherein only one parameter is considered. This result also opens up further possibilities in characterizing the OI 630.0 nm dayglow emissions as a function of equatorial electrodynamics and meridional winds in addition to the known variables.

To the best of our knowledge, the effect of the equatorial electrodynamics and meridional winds on the latitudinal variations in the dayglow emissions is reported for the first time. Such characterization will not only help in improving our understanding of the ionosphere-thermosphere system but also helps in modeling the influence of the equatorial electrodynamics and meridional winds on the low-latitude upper atmosphere.

4.5 Summary

The variations in the OI 630.0 nm dayglow emissions which originate from thermospheric altitudes can represent the dynamics of the upper atmosphere at those altitude regions.

The dynamics of the upper atmosphere can vary on short scales in latitudes and longitudes. In the observational duration considered in this study (January-February 2020), the variation in the solar flux was very small (68-72 sfu), and so it provided an opportunity to investigate the variation in the OI 630.0 nm dayglow emission rates in response to the equatorial electrodynamics and meridional winds. To investigate the latitudinal variation of these effects, linear regression analyses have been carried out for the optical data corresponding to each of the viewing directions with respect to the EEJ and meridional wind, and the correlation coefficients between them have been obtained. It is shown that for this duration, the effect of the equatorial electrodynamics on the variability of OI 630.0 nm dayglow emissions shows only a small variation with MLAT, whereas, the effect of the meridional winds has a greater role to play in the variations of the OI 630.0 nm dayglow emission with MLAT. Due to meridional winds, the variation over 5°-18° MLAT varied from a positively correlated behavior closer to the dip equator to that of negative as one moves away from the dip equator. To understand the cause of this behavior, the ionospheric state and production of OI 630.0 nm dayglow emissions are analyzed. The content of this chapter has been published in the journal Advances in Space Research, 2022 (*Kumar et al.*, 2022).

Chapter 5

Estimation of thermospheric neutral winds using measured 3D gravity waves characteristics

5.1 Introduction

As seen in the previous chapter, neutral winds play an important role in the upper atmospheric dynamics as it affects the plasma density distribution. It is well known that the measurement of the thermospheric wind in daytime from ground-based instruments is a very challenging task as huge solar brightness in the background is present. Earlier reports have discussed the use of ground-based Fabry-Perot etalons to measure neutral winds (*Burnside et al.*, 1981; *Meriwether et al.*, 1986; *Makela et al.*, 2013), but these measurements are limited to nighttime, with the exception of a triple etalon system capable of daytime measurements (*Gerrard and Meriwether*, 2011). While satellite-based instruments have been used to measure daytime neutral winds (*Herrero et al.*, 1988; *Shepherd et al.*, 1993b; *Englert et al.*, 2017). Therefore, we have developed a method to estimate the thermospheric horizontal neutral winds using three-dimensional characteristics of gravity waves (GWs) which has been discussed in this chapter.

As discussed in Chapter-1, different spatial and temporal scale waves have significant effects on the upper atmospheric dynamics. The roles of large-scale waves, such as, planetary waves (PWs) and tides in the upper atmospheric dynamics are relatively well known, but the understanding of GWs dynamics is less understood, particularly during daytime when the observations are limited. There have been numerous modeling studies and theoretical simulations conducted to examine the impact of GWs on the dynamics of the upper atmosphere (e.g., *Vadas*, 2007; *Vadas and Liu*, 2009). GWs can cause the heating or cooling of the thermosphere by up to 170 $K - day^{-1}$ till the peak F-layer altitudes which is comparable to the ion-drag (e.g., *Yiğit and Medvedev*, 2009; *Miyoshi et al.*, 2014). Also, the GW characteristics can be modulated due to the changes in background conditions, such as, temperature, winds, and neutral density as they strongly influence the propagation features of GWs. It is well known that neutral winds control the horizontal and vertical characteristics of GWs as neutral winds flowing in the same direction of GW propagation increase/decrease the horizontal/vertical scale sizes of the GWs (e.g., *Vadas et al.*, 2009; *Pallamraju et al.*, 2016; *Mandal et al.*, 2019; *Mandal and Pallamraju*, 2020; *Li and Lu*, 2021). Also, the GWs characteristics can be modulated by the dissipation conditions and scale height of the medium which depend upon the neutral temperature and density. As these atmospheric parameters are changed by the variation in the incoming EUV and X-ray solar radiation, the number of GWs in the thermosphere, their vertical propagation speeds, and vertical wavelengths have been shown to increase with an increase in the solar activity in the daytime (e.g., *Laskar et al.*, 2015; *Mandal et al.*, 2020).

The GWs in the UA can be observed using the temporal and spatial information of atmospheric parameters, such as, temperature, pressure, density, and winds, but their measurements are a critical task. Therefore, one of the most extensively used methods is the monitoring of naturally occurring airglow emissions that can be used to characterize the GW dynamics in the UA. As any wave propagates in the medium, it perturbs the density and temperature of the reactants that produce airglow emissions. In this background, waves leave their imprint on the airglow emissions variability (e.g., *Teitelbaum et al.*, 1981; *Pallamraju et al.*, 2010). Photometric measurements of airglow emissions can provide only the time periods information of waves, whereas, the scale sizes and propagation directions of waves can be obtained using large FOV measurements (e.g., *Taylor et al.*, 1995; *Shiokawa et al.*, 2009; *Lakshmi Narayanan et al.*, 2010). As discussed in Chapter-2, owing to the large FOV of MISE, it is possible to obtain scale sizes of GWs by carrying out wave number analysis (e.g., *Pallamraju et al.*, 2016; *Karan and Pallamraju*, 2017, 2018). By rotating the orientation of MISE in the zonal and meridional directions over the day, the temporal variation of horizontal characteristics of GWs can be obtained. Such observation is reported earlier (*Pallamraju et al.*, 2016) in which the GW horizontal structure is obtained from three different altitudes using three dayglow emissions, namely, OI 557.7 nm, OI 630.0 nm, and OI 777.4 nm.

Here, in this work, we have obtained the three-dimensional characteristics of GWs in the daytime using optical and radio measurements. The horizontal propagation characteristics of GWs, such as, time periods, scale sizes, and propagation directions are derived using large FOV observation of OI 630.0 nm dayglow emissions from AHD. To obtain the GWs vertical propagation characteristics (time periods and scale sizes), the phase delays in the height variation of multiple isoelectron densities obtained from digisonde have been used (*Mandal et al.*, 2019). And, as discussed above, the neutral winds and GWs are interrelated. Therefore, using the three-dimensional information of GWs obtained from optical and radio measurements as inputs into the GW dispersion relation, the thermospheric horizontal neutral winds in the direction of wave propagations are estimated. These estimated winds by this method are found to be compared with those measured by the MIGHTI onboard ICON satellite.

5.2 Data sets

For the present study, a combination of different data sources are used including: (i) OI 630.0 nm dayglow emissions as measured by the MISE, (ii) isoelectron density data from the digisonde, (iii) thermospheric neutral winds measured by MIGHTI on board the ICON satellite, (iv) HWM14 model derived neutral winds, and (v) neutral atmospheric parameters, such as, temperature and mass density, which are obtained from the NRLMSISE model. These datasets are used for the duration of 05-19 February 2021, and discussed in more details in Chapter-2.

5.3 Data analysis

For the present study, a combination of different data sources is used including: (i) OI 630.0 nm dayglow emissions as measured by the MISE, (ii) isoelectron density data from the digisonde, (iii) thermospheric neutral winds measured by MIGHTI on board the ICON satellite, (iv) HWM14 model derived neutral winds, and (v) neutral atmospheric parameters, such as, temperature and mass density, which are obtained from the NRLMSISE model. These datasets are used for the duration of 05-19 February 2021, and discussed in more detail in Chapter-2.

5.3.1 Estimations of horizontal propagation characteristics of GWs

In a special campaign mode observation, we have rotated the MISE from AHD in the meridional (north-south) and zonal (east-west) directions in such a way that the slit is

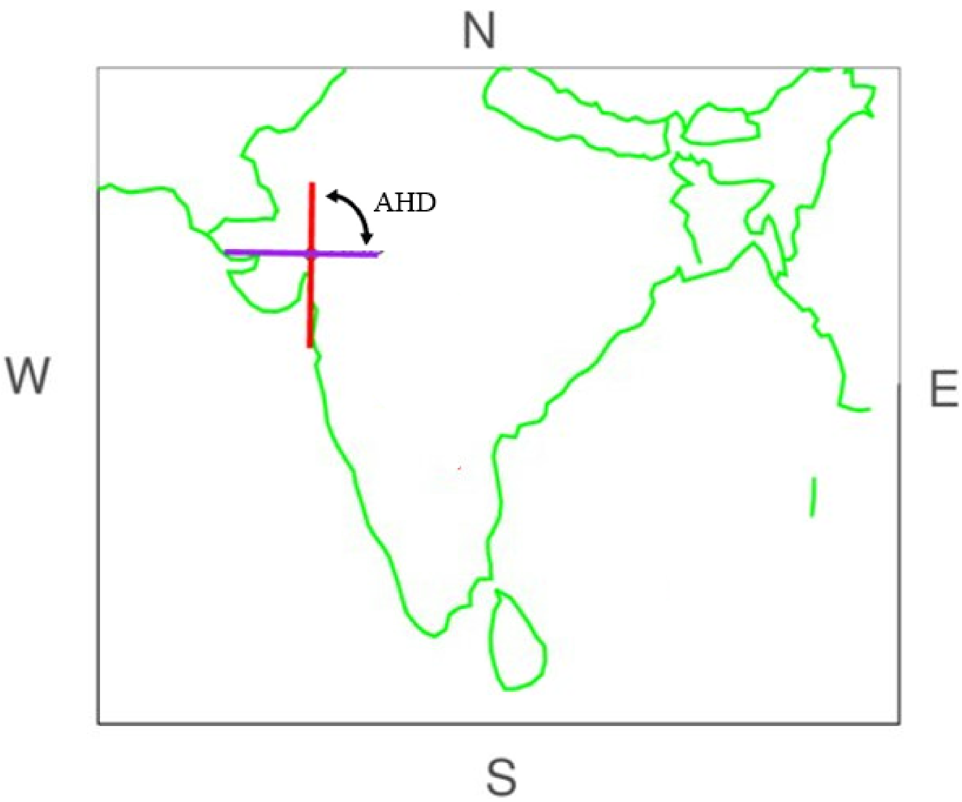

Figure 5.1: This figure shows the FOV of MISE operated from AHD in meridional and zonal directions by red and purple color shaded bars, respectively.

oriented in each of the directions for 30 minutes. Although the FOV of MISE is $\sim$140°, we have used dayglow observations within the FOV of 106° (zenith − 57° to zenith + 49°), which corresponds to a spatial distance of 622 km (355 km away from the zenith in one direction and 267 km in the other). We have restricted ourselves to this FOV to avoid the effects of filling-in due to atmospheric scattering from low-elevation angles. The whole spatial coverage of the MISE in meridional and zonal directions is shown in Figure 5.1 by red- and purple-colored bars, respectively. These repeated observations in two orthogonal directions enable us to obtain the GW scale sizes in both meridional and zonal directions over a spatial distance of 622 km as a function of time at the altitude 230 km, where OI 630.0 nm emission peaks. The dayglow emission rates at zenith, which is common in both these orientations, are used to obtain the diurnal variation of dayglow emissions. Further, the images are co-added for 5 minutes and over 21 pixels centered around the zenith to improve the SNR. The diurnal variation of OI 630.0 nm dayglow emission rate on a given day (05 February 2021) is shown in Figure 5.2a. It can be noted that in addition to the broad diurnal variations, there are smaller scale fluctuations, which are understood to be caused by the wave activity that exists in those regions. In order to derive more accurate information on the periodic behavior of these fluctuations in the GW regime, residuals (shown as red-dotted line) have been obtained by subtracting 2-hour running-averaged values (black-dashed line) from the actual dayglow values. Thus, the residuals obtained will contain information on the periodicities smaller than the sub-harmonic of the tidal periods (3 hr). The dayglow data used in this work are non-uniformly sampled in the course of observation on a given day. This unequal spacing of data arises due to different exposure times, the presence of clouds in the FOV, on occasions, and the lack of data around local noon, when the CCD gets saturated by the solar glare. Thus, to carry out spectral analysis of the data, the Lomb-Scargle periodogram (*Lomb*, 1976; *Scargle*, 1982) technique has been used that is capable of yielding frequencies present in the non-uniformly sampled data. More details of the Lomb-Scargle periodogram technique have been discussed in Chapter-2.

The results from such analyses of diurnal variation of dayglow emission rates on 5 February 2021 are shown in Figure 5.2c, wherein, significant time periods (time periods with power spectral density, PSD, higher than 90% FAL) can be seen. It can be noted that GWs of time periods around 37, 66, and 101 minutes are presented on that day.

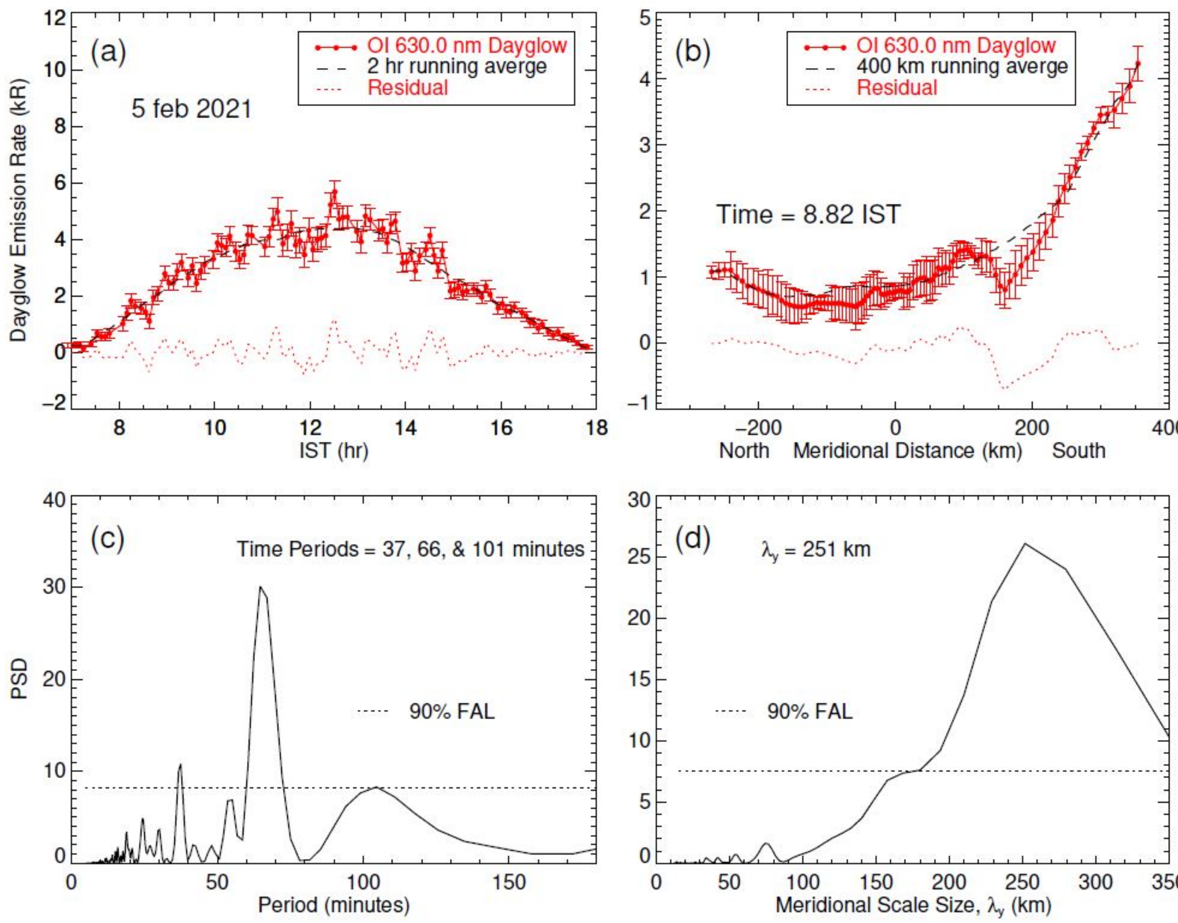

Figure 5.2: The diurnal variation of the OI 630.0 nm dayglow emissions on a sample day of 05 February 2021 is shown in red-color, while the black-dashed curve represents the 2-hour running average values. The red-dotted curve represents the residual, obtained by subtracting the 2-hour running average from the original data. (b) Meridional variation of the OI 630.0 nm dayglow emission at 8.82 IST is shown in red line, where the black-dashed line represents the 400 km running average. The red-dotted line shows the residual, obtained by subtracting the 400 km running average values from the original data. (c) The Lomb-Scargle periodogram of the diurnal residual of the dayglow emissions is shown in panel (a). Significant time periods of 37, 66, and 101 minutes are identified, indicated by peaks in the periodogram. The black dash-dotted line represents the statistical significance level of 90%. (d) The results from spectral analysis of the residual from meridional dayglow data as presented in (b) are shown here. Clearly, the presence of a dominant meridional scale size of around 250 km can be seen.

Similarly, GW scale sizes are obtained from the spatial variations in dayglow emission rates over 622 km. For the spatial variations, the data obtained for 10-15 minutes have been co-added and 11-pixels running average values have been considered to improve the SNR. As an example, the dayglow emission variability along the meridional direction at a given time 8.82 IST is shown in Figure 5.2b. The covered spatial regions corresponding to each pixel are different at different view angles, as they vary non-linearly. It is 4 km pixel^{-1} over the zenith and 12 km pixel^{-1} at the farthest view direction. By considering a 2-pixel separation to estimate spatial resolution, the maximum uncertainty for scale sizes is determined to be 24 km. To find the significant scale sizes, wave number analyses are conducted on the residual of the dayglow emission, which is obtained by subtracting the 400 km running averaged values from the original data. The residual values are represented by a red-dotted line in Figure 5.2b. Thus, the meridional scale sizes (λ_y) of GWs are obtained by performing wave number analysis on the data presented in Figure 5.2b. Figure 5.2d reveals the presence of a meridional scale size of approximately 251 km at around 8.82 IST on that particular day. Similarly, the zonal scale sizes (λ_x) of GWs are determined by analyzing the spatial variation of dayglow emissions in the zonal direction. This approach enables the retrieval of GW scale sizes in both the zonal and meridional directions throughout the day.

Earlier observational studies have provided evidence that GWs in the thermosphere exhibit characteristics of monochromatic wave packets. i.e., they are coherent waves or have similar characteristics throughout the day (e.g., *Oliver et al.*, 1994; *Djuth et al.*, 2004). Further, each wave packet typically persists for about 1-2 hours and is separated from another wave packet by approximately 20-60 minutes. Based on this knowledge, we can safely assume that the GWs observed within 30 minutes are part of the same wave packet (as the time periods of these GWs are 37, 66, and 101 minutes as shown in Figure 5.2c). As mentioned above, the duration of observations in zonal and meridional directions is 30 minutes each. Hence, to estimate the horizontal scale sizes (λ_H) of these GWs, we have combined the λ_x and λ_y information obtained over 30 minutes as per equation 1.1.

The temporal information associated with derived λ_H is based on the mean values of the time corresponding to λ_x and λ_y. The values of λ_H of GWs are calculated for all those 10 days on which bi-directional observation of OI 630.0 nm dayglow emission is available. Table-5.1 presents the time periods of GWs obtained from the analysis of the diurnal dayglow emission, and it can be noted that all of these periods exceed 30 minutes. Thus, our assumption of considering the scale sizes obtained in orthogonal directions within 30 minutes as being part of the same GW, for the purpose of calculating λ_H, is valid for all these days. Figure 5.3 illustrates the diurnal variations of λ_H for the 10 days. In this figure, λ_H values are displayed only when both λ_x and λ_y are significant (above the 90% FAL) in the wave number spectral analysis. Around local noon, to prevent the saturation of the detector due to the direct falling of sunlight on the slit, the instrument has been kept in the zonal direction from 12 to 13.5 IST. Consequently, only the values of λ_x are available for this period. The λ_y values for these times are interpolated by considering the λ_y values around 12 and 13.5 hr IST (the nearest pre- and post-noon time). These interpolated λ_y values were combined with λ_x values to obtain the corresponding λ_H values, which are represented by the joined black dots in Figure 5.3 to distinguish them from the other values.

Further, to determine the phase propagation angles (θ_H) of the waves, the measured λ_x and λ_y are utilized, as they are related according to equation 1.2. However, there

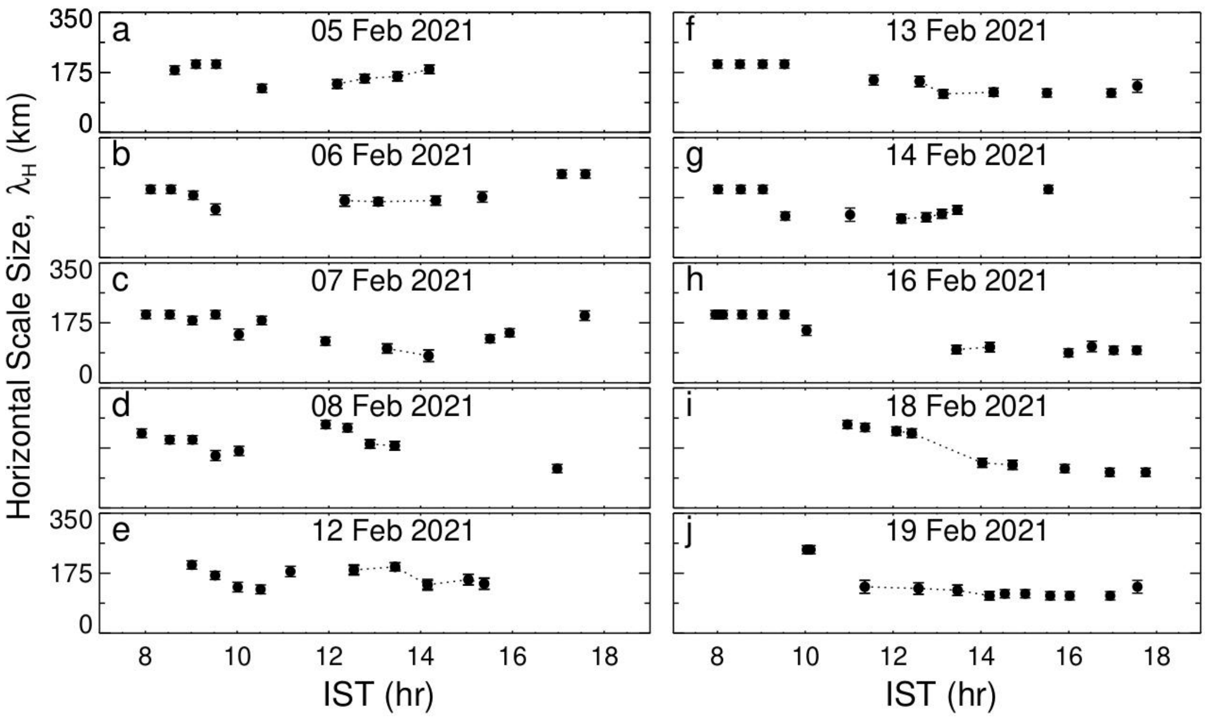

Figure 5.3: The diurnal variation of horizontal scale sizes of GWs for all 10 days of bi-directional observation of OI 630.0 nm dayglow emissions during 05-19 Feb 2021 are shown. The joined points by black-dotted line during noon-time correspond to those obtained by interpolating the values of meridional scale size before and after noon as discussed in the text.

is 180° ambiguity in θ_H values. In order to derive the propagation direction unambiguously, a method described in a previous study (*Pallamraju et al.*, 2016) is employed. In this method, the spatial state of a significant scale size at a specific time is obtained by performing an inverse Fourier transform while retaining only the power spectral signal associated with the dominant scale size in the frequency domain. In that, the spectral power signal corresponding to the dominant scale size with a bandwidth of 24 km (representing the uncertainty in scale sizes as discussed earlier) is retained, while the power of the rest of the scale sizes has been set to zero. This procedure is repeated over the day for both directions. The results from this analysis for a given day, 05 February 2021, are presented in Figure 5.4, wherein, the spatial locations of the wave crests and troughs become clearly visible throughout the day. The left panel of the figure represents the wave characteristics in the meridional direction, with the y-axis indicating the wave characteristics and the x-axis representing the time in IST. In the right panel, the waves in the zonal direction are shown along the x-axis, and time along the y-axis. One can note that the crests and troughs of the GW scale sizes are oriented in orthogonal directions in both these panels.

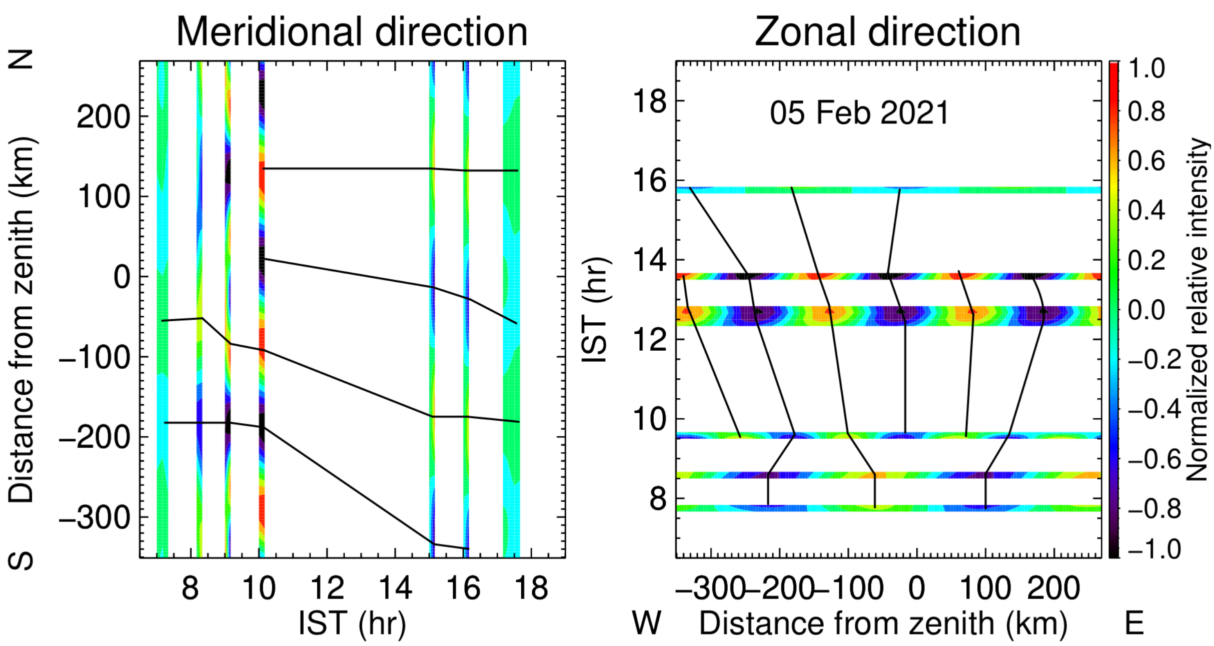

Figure 5.4: The normalized relative dayglow intensity variations obtained by inverse Fourier transform of a band centered on the dominant scale size as discussed in text are shown for 5 February 2021. The left and right panels correspond to meridional and zonal directions, respectively. Black solid lines connect the crest and trough at different time, facilitating the visual observation of the movement of crests and troughs over time.

The black lines in both panels trace the crests and troughs of the GWs over time, illustrating the movement of the phase fronts of the waves. In the left panel, the phase fronts of the GWs propagate southward, while in the right panel, they propagate westward. This combined information suggests that the GWs are broadly propagating in the south-west

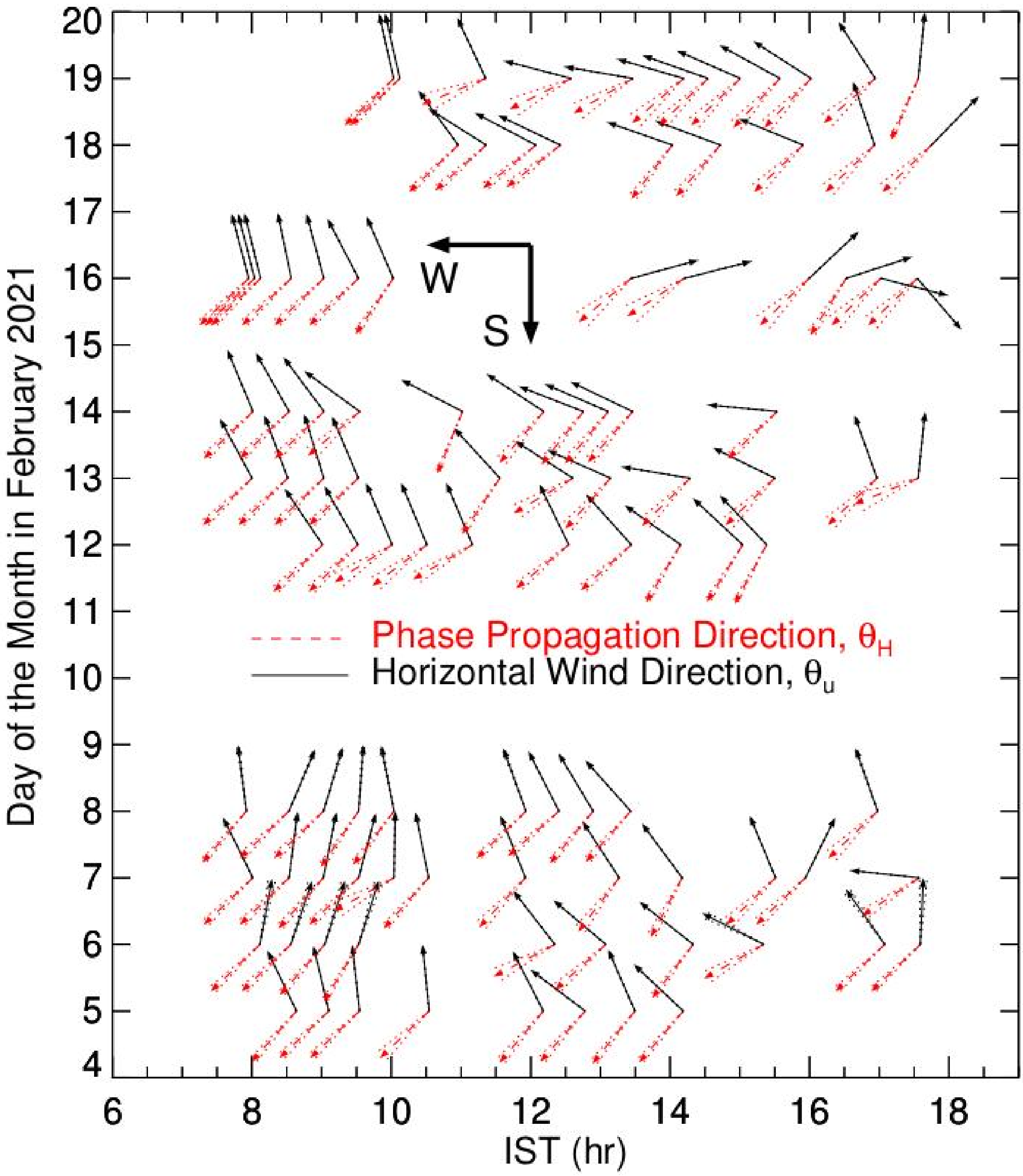

Figure 5.5: The time variation in GW propagation directions for all the ten days considered in this study is indicated by red-dashed arrows, while the directions of the observed thermospheric winds by MIGHTI are represented by black-colored arrows.

direction on the given day. This analysis has been conducted for all ten days, and it has been observed that the GWs consistently propagate in the south-west direction during that period. Figure 5.5 presents the propagation directions of these waves as red-colored dashed arrows for all 10 days of available bi-directional optical data shown in Figure 5.3 (Here, the solid black arrows denote the direction of thermospheric winds as described below in section 5.4.4). The y-axis values correspond to the day of the month in February 2021. Such methods have been shown earlier (e.g., *Hocke and Kämpfer*, 2009; *Pallamraju et al.*, 2016) to bring out the exact information on the spatio-temporal variations of a given periodic fluctuations. In an earlier study (*Mandal and Pallamraju*, 2020), it is shown that GWs mostly propagate in the south-westward direction in the daytime UA over AHD based on comparisons between vertical speeds of GWs obtained from digisonde measurements and HWM14 model-derived winds. Hence, values of λ_H and propagation directions of GWs obtained here in the daytime UA over AHD are consistent with the previous findings as well. The GW horizontal characteristics (time period, λ_x, λ_y, λ_H, and θ_H) on all these 10 days are found to be in the range of 31-138 minutes, 88-344 km, 123-344 km, 78-243 km, and 203-248 degrees from the east direction, respectively, and are listed in Table 5.1.

5.3.2 Estimation of vertical propagation characteristics of GWs

The height variations of isoelectron densities obtained from digisonde have been used to derive the vertical scale sizes (λ_z) of the atmospheric GWs present in the UA. In this, we have monitored the height variations of constant electron densities corresponding to 5.0, 5.5, and 6.0 MHz transmission frequencies of digisonde, which is shown in Figure 5.6a for a given day of 05 February 2021. The phases are seen to appear first at higher altitudes i.e., in the 6.0 MHz isoelectron density contour (red line, and appear later in time in the 5.0 MHz contour (orange line). To aid visualization, black-dashed lines are drawn to identify the downward phase propagation, which is a characteristic feature of upward propagating GWs (*Hines*, 1960). To ascertain that these phase offsets are indeed caused by upward propagating GWs, Lomb-Scargle periodogram analyses are performed on each isoelectron density contour and are shown in Figure 5.6b. The Lomb-Scargle periodogram reveals the presence of multiple significant periods (66 and 94 minutes) in all three isoelectron density contours as can be seen in Figure 5.6b. As fluctuations of different temporal scales are superposed in the height variations of these isoelectron density contours, each of these

Table 5.1: GW parameters, such as, time periods in OI 630.0 nm dayglow data, time periods in isoelectron density data, λ_X, λ_Y, λ_H, θ_H, estimated λ_Z from GW dispersion relation using horizontal characteristics of GWs as obtained by optical measurement, and measured λ_Z from digisonde are shown for all the days. No vertical propagations (NVP) of GWs are found on 6, 16, and 19 February 2021.

A	B	C	D	E	F	G	H	I	J
S.N.	Date	Optical Period (minutes)	Radio Period (minutes)	Zonal Scale Size, λ_x ±24 (km)	Meridional Scale Size, λ_y ±24 (km)	Horizontal Scale Size, λ_H (km)	Phase Propagation angle, θ_H	Estimated Vertical Scale Size, λ_z (km)	Measured Vertical Scale Size,λ_z (km)
1	5 Feb	37, 66, **101**	**94**	182-281	182-344	128-199	207-232	40-61, 19-36, 9-25	65-90
2	6 Feb	33, 53, 65, 126	NVP	206-344	123-344	140-243	208-239	36-109, 15-74, 9-64, 1-44	-
3	7 Feb	**41**, 55, 66, 99	**41**	88-281	162-344	78-199	207-243	18-72, 13-57, 11-51, 4-40	71-81
4	8 Feb	**49**, 63, 79, 135	37, **52**, 109	162-344	162-344	115-243	222-237	30-51, 21-39, 15-31, 6-23	51-75, 69-82, 149-247

5	12 Feb	**40**, 54, 67, 116	**37**	162-344	182-344	128-199	211-242	34-53, 22-39, 16-32, 3-19	28-36
6	13 Feb	**31**, 63, **94**, 126	**37**, **104**	147-281	162-344	112-199	203-237	28-72, 8-40, 2-32, 1-28	56-83, 85-167
7	14 Feb	**37**, 56, 65, 138	**37**	147-344	134-281	113-199	221-248	30-56, 3-38, 1-30, 1-26	26-41
8	16 Feb	37, 90	NVP	123-281	123-281	87-199	214-239	5-59, 6-31	-
9	18 Feb	**45**, **90**	**44**, **95**, 143	147-344	147-344	104-243	219-233	17-59, 2-38	63-76, 108-160, 84-96
10	19 Feb	33, 49, 65, 90	NVP	147-344	147-344	109-243	203-246	14-79, 2-53, 0-43, 2-36	-

contours for a given time period (around 94 minutes) is filtered. In this, we retain the spectral power within a ±10 minutes window (corresponding to the BV period) centered around this period. The power for the remaining time periods is equated to zero as also discussed above. Subsequently, we perform an inverse Fourier transform to obtain height variations in the isoelectron density contours only for the chosen common time period of the GWs. Figure 5.6c illustrates the filtered height variations of the isoelectron density contours for the 94 minutes GW time period on 05 February 2021. In these filtered contours, the downward phase propagation becomes more evident (as observed in Figure 5.6c). However, for the time period of 66 minutes, no downward phase propagation was

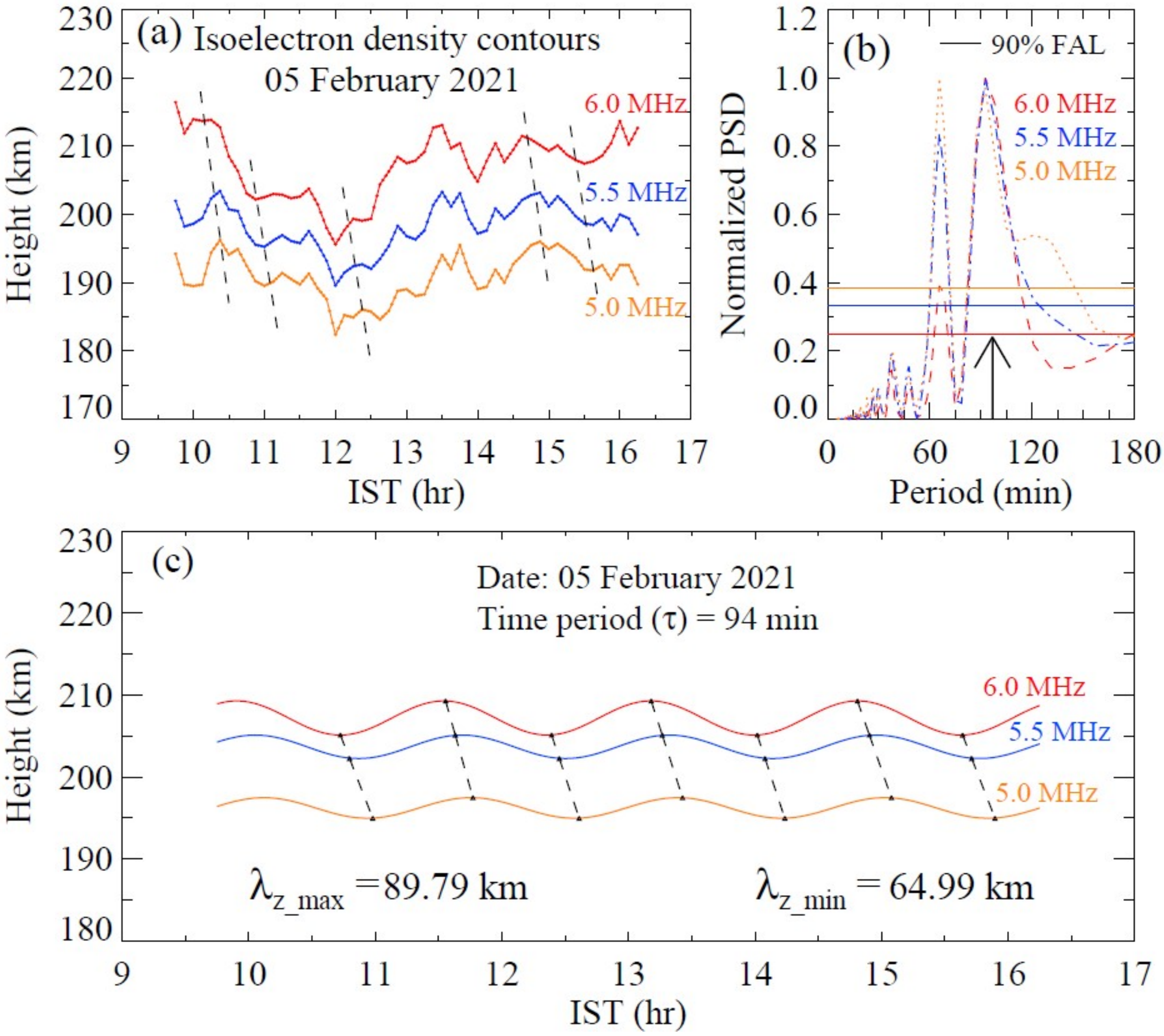

Figure 5.6: Height variations of isoelectron densities corresponding to frequencies of 5.0 (orange), 5.5 (blue), and 6.0 MHz (red) are shown. (b) The Lomb-Scargle periodogram of the isoelectron density height variations shown in (a) is presented, wherein significant time periods of 66 and 94 minutes are found to be present in all of them. (c) Filtered height variations of isoelectron density contours for the time period of 94 minutes.

observed in the filtered height variation across all frequencies. To determine the vertical propagation speeds of GWs, we use the height and time differences between the crests and troughs of successive isoelectron density contours. The λ_z are obtained by taking a product of the time periods and vertical propagation speeds. Using this technique to derive the vertical characteristics of GWs, several insightful results obtained with regard to GW dynamics in relation to seasonal variations, solar flux changes, geomagnetic conditions, and day-to-day behavior have been reported in the literature (*Mandal et al.*, 2020, 2022;

Mandal and Pallamraju, 2020). On 05 February 2021, the λ_z values of the GW with a time period of 94 minutes were found to vary between 65 and 90 km. It is important and pertinent to note that this 94 minutes period observed in the digisonde data analysis (Figure 5.6) is very close within the limit of the BV period of the 101 minutes periodicity obtained from the optical data (Figure 5.2). This clearly strengthens the conjecture that the λ_x & λ_y obtained from optical data and the λ_z obtained from the digisonde data combinedly describe the three-dimensional characteristics of the same GW in the daytime. In this study, digisonde data have been analyzed for all 10 days of bi-directional mode of operation of optical data. Among these 10 days, vertical propagation is seen to be existing on 7 days. In an earlier study (*Mandal and Pallamraju*, 2020), based on the analyses of two years of data, it has been shown that the vertical propagation of GWs is presented on only approximately 40% of the days. This study revealed that although GWs are omnipresent, not on all days they propagate upwards as also seen from the results of the present study. In these seven days, the time periods and λ_z are found to be in the range of 37 - 143 minutes and 26 - 247 km, respectively (as listed in Table 5.1). For a given day, only the time periods of GWs showing vertical propagation are listed in Table 5.1. The time periods in bold fonts correspond to those with a match between the optical and the radio measurements within the window of BV period. Thus, they combinedly are considered to represent the three-dimensional behavior of GWs on that day. Therefore, collocated and simultaneous optical and radio measurements, enable obtaining unique information on the horizontal and vertical propagation characteristics of the daytime thermospheric GWs.

5.4 Results

The horizontal characteristics of GWs, obtained using optical measurement are used as inputs into the GW dispersion relation to estimate the λ_z of GWs. Further, all the three-dimensional GWs characteristics are used to estimate the thermospheric horizontal winds. These estimated values are then compared with the measured values and described in the subsequent sections.

5.4.1 Estimation of vertical scale sizes using GW dispersion relation

The GW dispersion relation is used to estimate the values of λ_z of GWs using the measured horizontal characteristics of GWs obtained by the optical measurement. In the thermosphere, various factors, such as, molecular viscosity, thermal diffusivity, and ion-drag contribute to the dissipation of upward propagating GWs. These forces become more prominent in the upper thermosphere above 300 km as shown in earlier studies (*Fukao et al.*, 1993; *Oliver et al.*, 1997; *Vadas and Nicolls*, 2012; *Nicolls et al.*, 2012). *Oliver et al.* (1997) observed that the thermospheric GW characteristics obtained by the MU radar are in line with those of non-dissipative GWs, and they found no downward phase propagations of GWs at altitudes around 500 km and above. Additionally, *Nicolls et al.* (2012) reported amplitude growth of GWs with increasing altitude in the range of 200 - 300 km, which indicates that these GWs are not dissipating yet at these altitudes. In this study, the OI 630.0 nm dayglow emission is used to study the horizontal propagation characteristics of thermospheric GWs and the peak emission altitude of this dayglow is around 230 km, which exists within the non-dissipative region of GWs. Hence, the Hines' GW dispersion relation (*Hines*, 1960) given by equation 1.4 for non-dissipating GWs is used here to estimate the λ_z values of these observed GWs.

The HWM14 model-derived (*Drob et al.*, 2015) horizontal winds corresponding to an altitude of 230 km over AHD, have been used as inputs into the GW dispersion relation. This approach allowed us to estimate the λ_z values of GWs throughout the day, whenever λ_H values are present. For comparison, such estimations have been carried out for all seven days, when measured values of λ_z are also available from collocated radio measurement. These calculations have been carried out only for the common time periods observed in both optical and radio measurements (as listed in Table 5.1 in bold fonts). These are presented in different panels in Figure 5.7 by black circles for all 7 days.

5.4.2 Comparison of estimated vertical scale Sizes with those obtained from digisonde measurements

In section 5.3.2, we have discussed the digisonde data analyses to derive λ_z of upward propagating GWs. Thus, we made a comparison of the estimated λ_z obtained from the GW dispersion relation (as described in section 5.4.2) with the measured values of λ_z derived from digisonde data for all 7 days (Figure 5.7). The measured values are represented by violet-colored squares, which were obtained through the analysis of digisonde-derived isoelectron density contours (as described in section 5.4.2). From this figure, it can be seen that the estimated λ_z values match reasonably well on some days with the independently measured λ_z values from digisonde data. However, there are days (5, 7, and 8

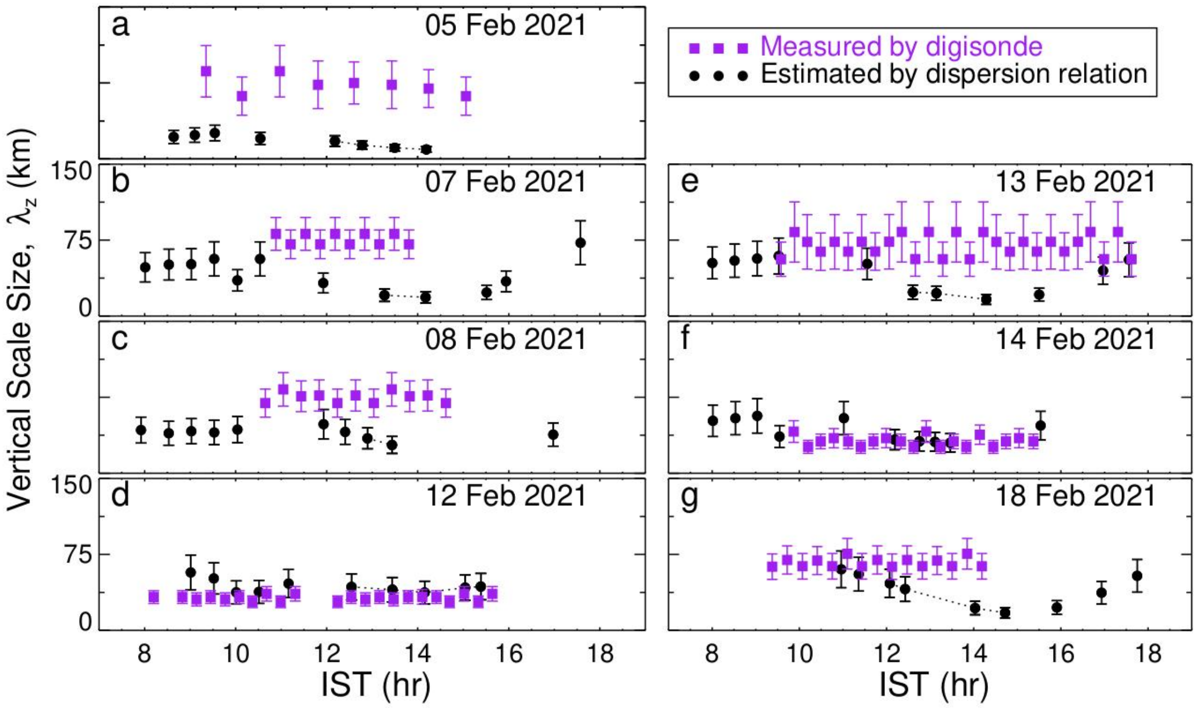

Figure 5.7: (a) Estimated values of vertical scale sizes, obtained using the GW dispersion relation, are denoted by black-circles. The violet squares represent the measured values of vertical scale sizes derived from the digisonde data for 5th February 2021. Panels (b), (c), (d), (e), (f), and (g) show the corresponding results as shown in Panel (a), but for 7, 8, 12, 13, 14, and 15 Feb 2021, respectively. In each panel, the values connected by black-dotted lines indicate cases where interpolated meridional scale sizes have been used as described in the text.

February) when the matching is not encouraging. One possible reason could be that the model-derived winds and neutral atmospheric parameters may not accurately represent the behavior of the UA on those particular days. Among these two factors, the model-derived winds have a higher level of uncertainty in their values compared to the neutral atmospheric parameters. This aspect is discussed in more detail below. The reasonable match motivates us to explore the estimation of the thermospheric neutral winds using three-dimensional GW information as input into the dispersion relation.

5.4.3 Estimation of thermospheric neutral winds

So far, we have observed a reasonably well match between estimated λ_z values obtained from the GW dispersion relation and independently λ_z values derived from radio measurement. However, it is important to note that the estimation of λ_z using the dispersion relation relies on the use of HWM14 model-derived neutral winds, which are climatological in nature and may not accurately represent the true atmospheric conditions on a given day, particularly if there are some developments away from the normal. Despite this, as GW parameters in all three dimensions are obtained, it presents a unique possibility of obtaining information on the thermospheric neutral winds. In this regard, we have made an attempt to estimate the ambient thermospheric neutral winds by using the measured values of GW parameters as inputs into the GW dispersion relation. The results obtained from this approach are discussed below.

The measured horizontal and vertical propagation characteristics of the GWs, obtained from the collocated optical and radio observations, are utilized as inputs in the GW dispersion relation. Then the equation is solved for the wind values which are directed to the wave propagation directions. Since the measured values of λ_z from digisonde data correspond to different times than those obtained for λ_H from optical data (as shown in Figure 5.7), the nearest measured λ_z values are considered for a given time during this calculation. The estimated magnitudes of the neutral winds, in the direction of GW propagation, are depicted as black dots in Figure 5.8 for each of the 7 days. In this way using this method, we are able to estimate the neutral winds in the GW propagation directions correspond to a broad altitudinal region centered around 230 km where OI 630.0 nm emissions peak.

5.4.4 Comparison of neutral wind derived by the 3-D GWs with measured MIGHTI winds onboard ICON

The measured winds obtained from MIGHTI provide an opportunity to compare the estimated winds by this presented method with them. As discussed in Chapter-2, these measured winds cannot be readily used for comparison due to the sparse temporal resolution of the MIGHTI winds for a specific location. Therefore, a methodology described in Chapter-2 is used to derive the diurnal variation of these measured neutral winds over the observational location AHD. In this methodology, the HWM14 (*Drob et al.*, 2015) model-derived winds are used to describe the climatological variations between the latitude of interest and the latitude of MIGHTI observations in a longitude region at a given time. This MIGHTI added HWM14 winds method was successfully also applied

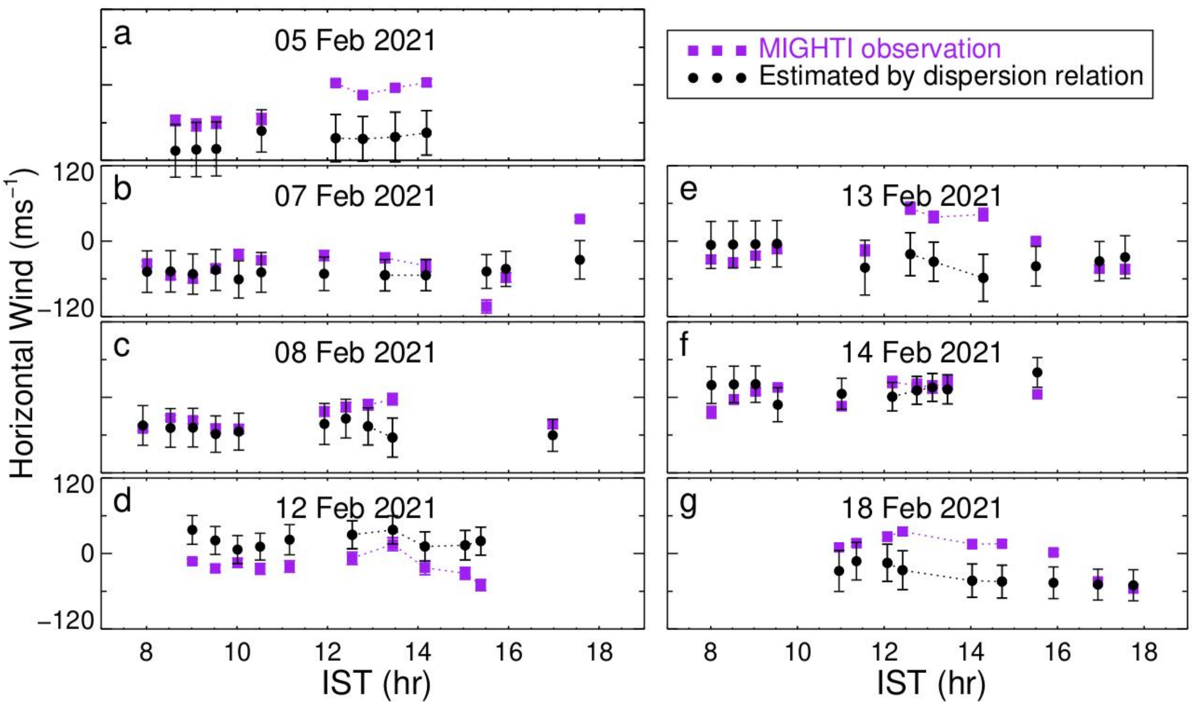

Figure 5.8: (a) Estimated horizontal wind magnitudes in the direction of GW wave propagation are denoted by black-dotted line for 05 Feb 2021. The violet-colored squares denote the magnitudes of the measured wind along the wave propagation direction obtained from the MIGHTI. Panels (b), (c), (d), (e), (f), and (g) show the results as shown in Panel (a) but for 7, 8, 12, 13, 14, and 18 Feb 2021, respectively. The joined values by dotted lines correspond to those where meridional scale sizes are interpolated as described in text.

to obtain neutral winds in Indian longitudes at different low-latitudinal locations and interesting dynamics of meridional winds in the OI 630.0 nm dayglow emissions variability were obtained (*Kumar et al.*, 2022) as presented in Chapter-4. To compare these measured winds with the estimated winds in the current study, it is necessary to consider the measured winds along the direction of wave propagation. For this purpose, the cosine components of these winds are calculated along the wave propagation direction using the measured angle between the wind and wave propagation directions as depicted in Figure 5.4. The wind propagation directions are determined based on the magnitudes of the zonal and meridional winds and are presented by black-colored arrows in Figure 5.4. Consequently, the magnitudes of the measured thermospheric wind obtained by MIGHTI along the wave propagation directions are calculated. These measured winds are presented by violet-colored squares in Figure 5.8. It is worth to note that these winds, derived through independent measurements: one estimated using the measured three-dimensional GW characteristics from collocated ground-based optical and radio measurements; and the other measured by MIGHTI onboard ICON satellite, show a very good match. Therefore, the three-dimensional information of GWs derived from ground-based measurements can be used to obtain a very good estimate of daytime thermospheric winds at a very high temporal resolution.

5.5 Discussion

We have presented a new approach and a new possibility of obtaining (i) λ_z of GWs in the daytime using optical measurements alone (section 5.4.1), and (ii) thermospheric neutral winds through the combined use of collocated optical and radio measurements (section 5.4.3). All these measurements and model outputs are independent of each other. The match in these parameters derived in the current study, namely, (i) estimated λ_z values using the optical measurement with the derived λ_z values from radio measurement (section 5.4.2), and (ii) estimated horizontal winds from the combined optical and radio measurements with the MIGHTI observed horizontal winds (section 5.4.4), are remarkable. However, there are deviations observed in the comparison between the estimated and measured λ_z values as noted on 5, 7, and 8 February 2021 (as shown in Figure 5.7a, b,

& c) with a few times on other days as well. It is well-known that the UA is a highly dynamic and coupled system, with winds controlling the horizontal and vertical propagation characteristics of GWs. The neutral winds in the same/opposite direction of GW propagation increase/decrease the λ_H as discussed above. Thus, GW horizontal propagation characteristics, which are used as inputs into the GW dispersion relation, are sensitive to surrounding wind fields. In this background, the differences between the estimated and measured values of λ_z on 5, 7, and 8 February 2021 could be understood as the estimated winds on 7 and 8 February, showing a good match with measured MIGHTI winds over the day. On 5 February, winds obtained by the two different techniques match reasonably well except around noon-time. On some of the days (5, 13, and 18 February 2021), the values of estimated and measured winds around noon time as shown in Figure 5.8 do not match with each other. The possible reason for this difference could be that the λ_H and θ_H values in this duration were interpolated and not measured as discussed in section 3.1. Nevertheless, by reducing the duration of optical observation in the zonal direction and carefully allowing a few meridional observations, this time gap can be reduced, which will be attempted in the future.

We further carried out an exercise to estimate λ_z using these measured MIGHTI winds instead of HWM14 model-derived winds which is shown in Figure 5.9. This figure is similar to Figure 5.7, except that the measured horizontal winds are used here. In that case, the estimated λ_z values have been found to show a better agreement with the measured ones. This further strengthens the discussion carried out in section 4.2 that the locally varying neutral dynamics, do not get accurately described by the outputs of climatological models (HWM14 and NRLMSISE-00) at all times. This could be the probable source of deviations between the measured and estimated values of λ_z and winds on some occasions (Figures 7 & 8).

Here, one should note that the estimation of neutral winds solely based on optical measurements is not possible due to the presence of two unknown parameters in the dispersion relation: λ_z and time period, which need to be ascertained first. While various GW parameters can be derived from the optical data and digisonde data independently, the key is to track the time period of GWs that are common in both optical and radio measurements. Attention is drawn to Table-5.1, wherein, the nearly similar time period values obtained from the optical and radio measurements are listed in bold fonts, which

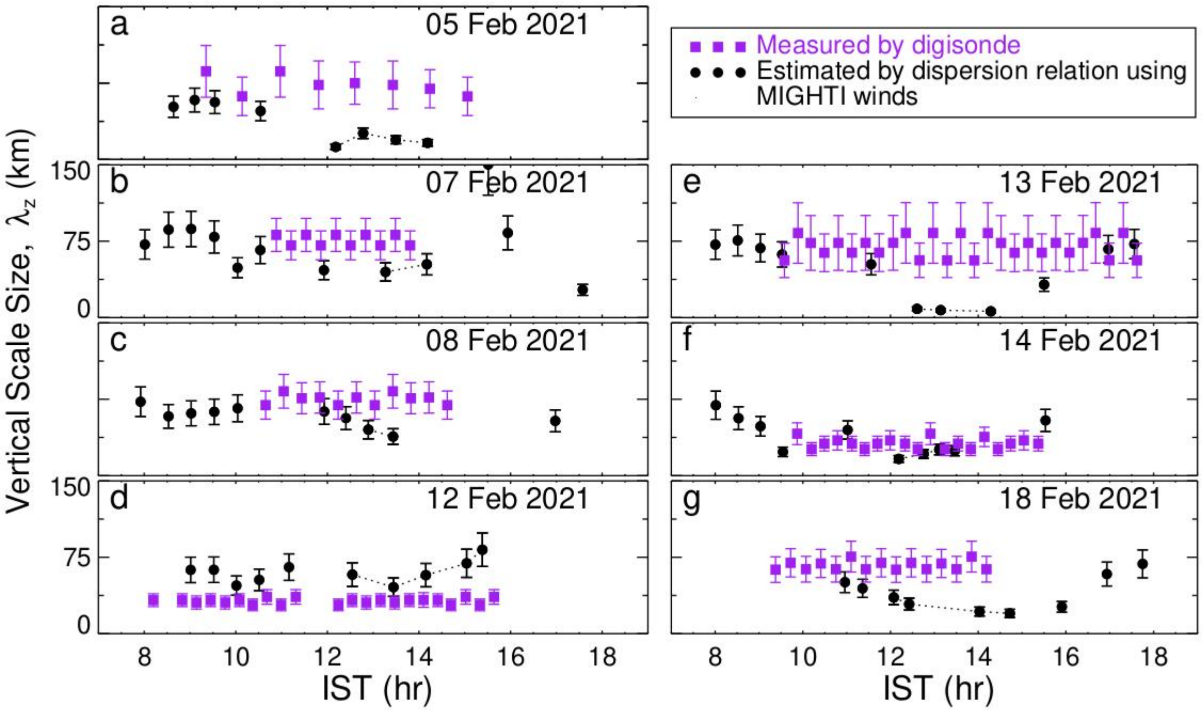

Figure 5.9: (a) Estimated values of vertical scale sizes from the gravity dispersion relation, where the measured MIGHTI winds have been used, are shown in black-dots and violet-squares are the measured values of vertical scale sizes from digisonde data for 05 Feb 2021. (b) Same as in (a) but for 07th. (c) Same as in (a) but for 08th. (d) Same as in (a) but for 12th. (e) Same as in (a) but for 13th. (f) Same as in (a) but for 14th. (g) Same as in (a) but for 18th. The joined values by black dotted lines represent those for that meridional scale sizes are interpolated in noon time as described in the text.

are attributed to the same GW. Thus, the GW information obtained by the combined optical and radio measurements complements each other in describing the three-dimensional characteristics of GWs in the daytime from the ground-based measurements at a high temporal resolution. These describe the GW structure in three dimensions accurately, which is also confirmed by the encouraging comparison between the horizontal winds derived by our measurements and those measured independently by MIGHTI onboard the ICON satellite. These kinds of results provide a new direction for the investigation of the upper atmospheric dynamics from ground-based measurements. These results and the approach described assume a greater significance, as it is now possible to derive thermospheric neutral winds from ground-based techniques as this is a very challenging task, especially in daytime conditions. To the best of our knowledge, this study is the first of its kind, and represents the first experimental demonstration of the intricate interplay between thermospheric neutral winds and GWs in the daytime using high-cadence ground-based experiments.

5.6 Summary

The detailed analyses of dayglow emissions over a large FOV and digisonde-derived height variations of isoelectron density contours have been carried out to obtain the daytime behavior of thermospheric GWs in three dimensions over AHD. Various parameters related to the atmospheric GWs, such as, time periods observed in the optical data and radio data, λ_x, λ_y, λ_H, phase propagation angle, estimated and measured λ_z are obtained using collocated optical and radio measurements, and are listed in Table-5.1. Among the 10 days of bi-directional mode operation of MISE, vertical propagations of GWs are observed on 7 days. During this period, GW parameters, such as, time period, θ_H, λ_x, λ_y, λ_H, and λ_z obtained from optical and radio measurements showed variations in the range of 31-138 minutes, 203-248 degrees from east, 88-344 km, 123-344 km, 78-243 km, and 26-247 km, respectively. Further, using the horizontal propagation characteristics of GWs obtained from large FOV optical measurements of OI 630.0 nm dayglow, along with the model-derived winds and neutral atmospheric parameters, the λ_z of GWs are estimated. These estimated λ_z values showed a reasonable match with those derived from the digisonde-derived isoelectron density contours. As the combination of optical and radio measurements described the GW behavior in three dimensions, by using all the measured wave parameters as input into the GW dispersion relation, the thermospheric neutral winds in the wave propagation direction are estimated. These estimated wind magnitudes showed a good match with the measured winds obtained from MIGHTI. These results make the present work unique, and it is expected that such findings on the daytime thermospheric neutral GWs and wind dynamics provide new directions and insights into the investigation of the upper atmospheric research. The content of this chapter has been published in the Journal of Geophysical Research: Space Physics, 2023 (*Kumar et al.*, 2023a).

Chapter 6

Summary and Future scope

6.1 Summary

In the thesis work, the upper atmospheric dynamics in daytime over low- and equatorial-latitudes is investigated. The effect of the lower atmospheric forcing (tidal waves) in the varying background conditions in terms of the stratospheric polar vortex (SPV) on the equatorial electrodynamics is investigated. The upper atmospheric variations over low-latitudes due to the equatorial electrodynamics and meridional winds are studied. In addition to the large–scale waves, smaller scale gravity wave (GW) dynamics in three dimensions has been obtained. Such information on the GW in three dimensions is used to estimate the thermospheric neutral winds in the daytime.

The background information of the ionosphere-thermosphere system is detailed in Chapter-1. In this chapter, the composition and chemistry of neutrals and plasma is discussed. The upper atmospheric dynamics is significantly governed by various kind of waves of different scale sizes, such as, GWs, PWs, and tides which are mainly generated in the lower atmosphere. Their roles on the upper atmospheric dynamics in different background conditions, sources, and dynamics have been discussed in detail in this chapter. Also, a few equatorial- and low-latitudinal upper atmospheric electrodynamical phenomena, such as, Equatorial Electrojet (EEJ), Equatorial Ionization Anomaly (EIA), Equatorial Temperature and Wind Anomaly (ETWA), and Neutral Anomaly NA are described that drive the upper atmospheric dynamics in this region. The electrodynamics is significantly affected by the lower atmospheric forcing through these waves which is also discussed in chapter-1.

To carry out the investigation of the thesis work, different data sets, techniques, and analyses methods are used and discussed in Chapter-2. The primary data utilized is the OI 630.0 nm dayglow emissions obtained using two MISE located at HYD and AHD wherein they jointly cover a spatial region of 5°-18° MLAT. Additionally, other ground-based data sets including electron density, EEJ, Northern Annular Mode (NAM) index, and solar flux $F10.7$ are briefly explained. Furthermore, satellite-based data, such as, neutral winds and vertical E × B drift obtained from the ICON satellite are also discussed in detail. The methodology used for estimating neutral winds for a particular latitude using the MIGHTI observations and HWM-14 model-derived winds is discussed in detail. This chapter also outlines the different spectral analyses techniques utilized in the thesis work, including Fourier transform, least-square fitting, and Lomb-Scargle analysis, along with their advantages and limitations.

We briefly summarize the results of this thesis work which answers the questions put forth in section 1.6 of Chapter-1 in view of the understanding of upper atmospheric dynamics over low- and equatorial-latitudes.

i. It is well known that during weak SPV, tidal waves get amplified and alter the equatorial electrodynamics of the UA significantly. Is there any effect of strong SPV as well on the upward propagating waves? If it does, how much can it contribute to the variation in the electrodynamics?

The variation of the semidiurnal solar and lunar (S2 and L2) tides in the EEJ during strong and weak SPV is investigated in Chapter-3. The EEJ data obtained from the Huancayo observatory is used to estimate the amplitude of tidal components. For the state of the SPV, NAM values are used. In this study, the variation in S2 and L2 tidal amplitudes with the NAM values have been seen for some individual winters of the years of 1980-1981, 1982-1983, 2008-2009, 2015-2016, and 2019-2020. An enhancement in the S2 and L2 tidal amplitudes during weak SPV conditions has been found which is in line with earlier findings. In addition to this, a reduction in amplitudes of S2 and L2 tides have been observed during the strong state of the SPV, which is opposite to those that occur during weak SPV conditions but with a relatively small amplitude. The response of the S2 tide with the strength of the SPV is observed with a time lag of around 10 days, whereas, the L2 responds immediately with the variation of NAM values. For the winter of the year of 2019-2020, a noteworthy reduction was present in the M2 amplitude, derived using vertical E $\times$ B drift obtained from IVM onboard ICON satellite, during the anomalously strong state of the SPV in February-March 2020. Month-wise response of S2 and L2 with state of SPV is quite different as L2 responded strongly to the strength of SPV during December-January months, whereas, S2 showed a better dependence in the month of February-March. These results clearly demonstrate that in addition to the influence of weak SPV conditions on the ionosphere, which is well known, strong SPV conditions also have a pronounced impact on the ionosphere (*Kumar et al.*, 2023b).

ii. What is the contribution of the equatorial electrodynamics in the variability of the OI 630.0 nm dayglow emissions measured over 5°-18° MLAT? Besides, is there any significant role of the meridional winds in the plasma distribution?

As seen in Chapter-3, the equatorial electrodynamics is significantly driven by the forcing from below. In Chapter-4, we have investigated the effect of the equatorial electrodynamics and thermospheric meridional winds on the plasma distribution in a large spatial region over low-latitudes. For this study, the variations in the OI 630.0 nm dayglow emissions are used. Dayglow emissions are obtained in a spatial region of 5°–18° MLAT from two spectrographs (MISE) operating from HYD and AHD, where, the whole FOV is divided into 10 different independent viewing directions. The observational duration for this study was January - February 2020, wherein, the variations in the solar flux was very small (68-72 sfu), and so it provided an opportunity to investigate the variation in the OI 630.0 nm dayglow emission rates in response to both the equatorial electrodynamics and meridional winds. To investigate the latitudinal variation of these effects, linear regression analyses have been carried out for the optical data corresponding to 10 different spatial locations with the EEJ and meridional wind, and the correlation coefficients between them have been obtained. It is shown that for this duration the effect of the equatorial electrodynamics on the variability of OI 630.0 nm dayglow emissions shows only a very small variation (almost constant) with MLAT until 18° MLAT. Whereas, the effect of the meridional winds has a greater role to play in the OI 630.0 nm dayglow emission variability with MLAT. Due to meridional winds, the variation in dayglow emissions over 5°-18° changed from positive correlated behavior closer to the dip equator to that of negative as one moved away from the dip equator. It is interpreted that as the meridional winds brings down the height of the ionosphere, it enhances the emissions closer to the equator through the dissociative recombination (DR) mechanism. At latitudes further from the equator as this poleward meridional wind in the daytime takes away the plasma density from the altitude of peak contribution due to DR, it causes a reduction in the OI 630.0 nm emission intensities (*Kumar et al.*, 2022).

iii. We have three-dimensional upper atmospheric information using collocated large FOV optical and radio measurements. Is it possible to derive the three-dimensional GWs characteristics using this information and subsequently the thermospheric neutral winds?

As discussed in Chapter-4, the thermospheric neutral winds play a vital role in the upper atmospheric dynamics. Therefore, a methodology is developed to estimate the thermospheric horizontal neutral winds using the knowledge of three-dimensional information of GWs characteristics measured from the ground (Chapter-5). Horizontal characteristics of GWs, such as, time periods, zonal scale sizes, meridional scale sizes, horizontal scale sizes, and phase propagations angle are derived using large FOV data of OI 630.0 nm dayglow observation from AHD. Spectral analyses have been carried out on the emission variability that is present in a given spatial direction to obtain various GW parameters in the horizontal directions. Collocated digisonde measurements are used to derive the GW vertical information, such as, time periods and vertical scale sizes, λ_z. Further, horizontal propagation characteristics of GWs along with the model-derived winds and neutral atmospheric parameters are used as input into the GW dispersion relation to estimate the values of the λ_z of GWs. These estimated λ_z values show a good match with those obtained from the analyses of digisonde-derived isoelectron density height variations. As the combined measurements describe the GW behavior in three-dimensions very well, all the measured wave parameters are used into the GW dispersion relation to estimate the thermospheric neutral winds along the direction of wave propagation. These estimated wind magnitudes show a good match with those measured by MIGHTI onboard the ICON satellite (*Kumar et al.*, 2023a). These results make the present work very unique, and it is expected that such findings on the daytime thermospheric neutral GWs and wind dynamics provide new directions and insights into the investigation of the upper atmospheric research.

6.2 Future scope

In this thesis work, the daytime upper atmospheric dynamics is investigated over low- and equatorial-latitudes. In the course of these investigations, several insightful results, as described above, are obtained that improve the knowledge and understanding of the equatorial electrodynamics and neutral dynamics in the upper atmosphere over low latitudes. Looking into the future directions of the thesis work, several ideas have emerged which are listed as follows:

i. We have developed a method to estimate the diurnal variations in neutral winds for a given latitude using the satellite-based neutral winds observed from different latitudes and climatological winds (model). The approach is such that while the model wind describes the climatology variations of winds at a given location, the difference between them and the ICON measured winds are suggested to provide the corrections that have been applied to the climatological winds correspond to a given latitude of our interest for a particular longitude. It has been shown that such corrected winds explain the observed latitudinal variations in the OI 630.0 nm dayglow emissions and showed a good match with the estimated winds using three-dimensional GW characteristics. This method provides a great potential to generate the wind field over a large spatial extent. Using satellite-based and ground-based measurements, this method can be verified.

ii. We have investigated the variation in the OI 630.0 nm dayglow emissions due to the equatorial electrodynamics and meridional winds. Using the long-term OI 630.0 nm emissions data, the relative contributions of the equatorial electrodynamics and meridional winds in terms of emission intensity and electron density, and relative contribution of DR can be investigated under different seasonal, geomagnetic, and solar conditions can be investigated.

iii. We have studied the GW dynamics in three dimensions using large FOV dayglow observations from AHD. As, observations of dayglow emissions from HYD exist as well, therefore, after merging the dayglow emissions, under reasonable assumptions, large-scale wave dynamics can be studied. Also, the vertical characteristics of GW can be derived from ionospheric observation using digisonde located at AHD.

iv. From a single station data, it is not possible to obtain the migrating and non-migrating tidal components. Therefore, the variation in the solar and lunar migrating tides using satellite-based vertical drift data can be explored along with the ground-based EEJ data during different states of the SPV.

v. The cause behind the different kinds of the response of solar and lunar semidiurnal tides to the stratospheric polar vortex in different months during winters needs further investigations.

vi. The horizontal neutral winds are estimated using three-dimensional characteristics of GWs on geomagnetic quiet days. In a similar fashion, the variations of neutral winds during geomagnetically disturbed days can be explored.

References

Alexander, M., J. R. Holton, and D. R. Durran, The gravity wave response above deep convection in a squall line simulation, *Journal of the Atmospheric Sciences*, *52*, 1995. [Cited on pages xi, 11, and 12.]

Alexander, M. J., A simulated spectrum of convectively generated gravity waves: Propagation from the tropopause to the mesopause and effects on the middle atmosphere, *Journal of Geophysical Research: Atmospheres*, *101*, 1571–1588, 1996. [Cited on page 11.]

Alexander, M. J., J. H. Beres, and L. Pfister, Tropical stratospheric gravity wave activity and relationships to clouds, *Journal of Geophysical Research: Atmospheres*, *105*, 22,299–22,309, 2000. [Cited on page 11.]

Alken, P., and S. Maus, Spatio-temporal characterization of the equatorial electrojet from champ, ørsted, and sac-c satellite magnetic measurements, *Journal of Geophysical Research: Space Physics*, *112*, 2007. [Cited on page 69.]

Anderson, D., A theoretical study of the ionospheric f region equatorial anomaly—i. theory, *Planetary and Space Science*, *21*, 409–419, 1973. [Cited on pages 28, 89, and 90.]

Anderson, D., A. Anghel, J. Chau, and O. Veliz, Daytime vertical e×b drift velocities inferred from ground-based magnetometer observations at low latitudes, *Space Weather*, *2*, 2004. [Cited on page 89.]

Andrews, D. G., *An Introduction to Atmospheric Physics*, Cambridge University Press, 2010. [Cited on page 7.]

Appleton, E. V., Two anomalies in the ionosphere, *Nature*, *157*, 691–691, 1946. [Cited on page 27.]

Baker, W., and D. F. Martyn, Electric currents in the ionosphere-the conductivity, *Philosophical Transactions of the Royal Society of London. Series A, Mathematical and Physical Sciences*, *246*, 281–294, 1953. [Cited on pages 24 and 68.]

Balan, N., G. J. Bailey, R. J. Moffett, Y. Z. Su, and J. E. Titheridge, Modelling studies of the conjugate-hemisphere differences in ionospheric ionization at equatorial anomaly latitudes, *J. Atmos. Terr. Phys.*, *57*, 279 – 292, 1995. [Cited on pages 28, 90, and 92.]

Balan, N., G. Bailey, M. Abdu, K. Oyama, P. Richards, J. MacDougall, and I. Batista, Equatorial plasma fountain and its effects over three locations: Evidence for an additional layer, the f 3 layer, *Journal of Geophysical Research: Space Physics*, *102*, 2047–2056, 1997a. [Cited on page 28.]

Balan, N., G. J. Bailey, M. A. Abdu, K. I. Oyama, P. G. Richards, J. MacDougall, and I. S. Batista, Equatorial plasma fountain and its effects over three locations: Evidence for an additional layer, the F3 layer, *J. Geophys. Res.*, *102*, 2047–2056, 1997b. [Cited on page 31.]

Baldwin, M. P., and T. J. Dunkerton, Stratospheric harbingers of anomalous weather regimes, *Science*, *294*, 581–584, 2001. [Cited on pages 57 and 68.]

Baldwin, M. P., and D. W. Thompson, A critical comparison of stratosphere–troposphere coupling indices, *Quarterly Journal of the Royal Meteorological Society: A journal of the atmospheric sciences, applied meteorology and physical oceanography*, *135*, 1661–1672, 2009. [Cited on pages 58 and 69.]

Baldwin, M. P., et al., Sudden stratospheric warmings, *Reviews of Geophysics*, *59*, e2020RG000,708, 2021. [Cited on pages 22 and 67.]

Bartels, J., and H. Johnston, Geomagnetic tides in horizontal intensity at huancayo, *Terrestrial Magnetism and Atmospheric Electricity*, *45*, 269–308, 1940. [Cited on pages 26 and 71.]

Beer, T., *Atmospheric Waves*, Wiley, 1974. [Cited on pages xi, 6, 7, and 16.]

Bens, A. R., L. L. Cogger, and G. G. Shepherd, Upper atmospheric temperatures from Doppler line widths-III: Observation of the OI dayglow emission at 6300 , *Planet. Space Sci.*, *13*, 551–563, 1965. [Cited on page 40.]

Bevington, P. R., *Data reduction and error analysis for the physical sciences*, 1969. [Cited on pages 60 and 61.]

Bilitza, D., D. Altadill, V. Truhlik, V. Shubin, I. Galkin, B. Reinisch, and X. Huang, International reference ionosphere 2016: From ionospheric climate to real-time weather predictions, *Space weather*, *15*, 418–429, 2017. [Cited on pages 39 and 102.]

Blamont, J. E., and T. Donahue, Sodium dayglow: Observation and interpretation of a large diurnal variation, *Journal of Geophysical Research*, *69*, 4093–4127, 1964. [Cited on page 40.]

Brown, G., and W. Williams, Some properties of the day-to-day variability of sq (h), *Planetary and Space Science*, *17*, 455–470, 1969. [Cited on page 26.]

Burnside, R., F. Herrero, J. Meriwether Jr, and J. Walker, Optical observations of thermospheric dynamics at arecibo, *Journal of Geophysical Research: Space Physics*, *86*, 5532–5540, 1981. [Cited on pages 31 and 107.]

Chakrabarti, S., D. Pallamraju, and J. Baumgardner, HiTIES: A High Throughput Imaging Echelle Spectrogragh for ground-based visible airglow and auroral studies, *J. Geophys. Res.*, *106*, 30,337–30,348, 2001. [Cited on pages 40 and 45.]

Chakrabarti, S., O.-P. Jokiaho, J. L. Baumgardner, T. A. Cook, J. Martel, and M. Galand, High-throughput and multislit imaging spectrograph for extended sources, *Optical Engineering*, *51*, 013,003, 2012. [Cited on page 45.]

Chakrabarty, D., R. Sekar, H. Chandra, R. Narayanan, B. M. Pathan, and K. S. V. Subbarao, Characterizations of the diurnal shapes of OI 630.0 nm dayglow intensity variations: inferences, *Ann. Geophys.*, *20*, 1851–1855, 2002. [Cited on page 92.]

Chakrabarty, D., R. Sekar, R. Narayanan, T. K. Pant, and K. Niranjan, Thermospheric gravity wave modes over low and equatorial latitudes during daytime, *J. Geophys. Res.*, *109*, 2004. [Cited on page 90.]

Chakrabarty, D., R. Sekar, R. Narayanan, C. V. Devasia, and B. M. Pathan, Evidence for the interplanetary electric field effect on the OI 630.0 nm airglow over low latitude, *J. Geophys. Res.*, *110*, 2005. [Cited on page 40.]

Chandra, H., and R. Rastogi, Geomagnetic storm effects on ionospheric drifts & the equatorial e s, over the magnetic equator, 1974. [Cited on page 51.]

Chang, L. C., J.-Y. Liu, and S. E. Palo, Propagating planetary wave coupling in saber mlt temperatures and gps tec during the 2005/2006 austral summer, *Journal of Geophysical Research: Space Physics*, *116*, 2011. [Cited on page 13.]

Chapman, S., The equatorial electrojet as detected from the abnormal electric current distribution above Huancayo, Peru, and elsewhere, *Archiv für Meteorologie, Geophysik und Bioklimatologie, Serie A*, *4*, 368–390, 1951, https://doi.org/10.1007/BF02246814. [Cited on page 24.]

Chapman, S., and R. S. Lindzen, Atmospheric tides: Thermal and gravitational, 201 pp., d, *D. Reidel, Norwell, Mass*, 1970. [Cited on pages 16, 18, and 20.]

Charlton, A. J., and L. M. Polvani, A new look at stratospheric sudden warmings. part i: Climatology and modeling benchmarks, *Journal of climate*, *20*, 449–469, 2007. [Cited on pages 20 and 21.]

Charney, J. G., and P. G. Drazin, Propagation of planetary-scale disturbances from the lower into the upper atmosphere, *Journal of Geophysical Research*, *66*, 83–109, 1961. [Cited on pages 15 and 67.]

Chau, J., B. Fejer, and L. Goncharenko, Quiet variability of equatorial e$\times$ b drifts during a sudden stratospheric warming event, *Geophysical Research Letters*, *36*, 2009. [Cited on page 79.]

Chau, J. L., L. P. Goncharenko, B. G. Fejer, and H.-L. Liu, Equatorial and low latitude ionospheric effects during sudden stratospheric warming events: Ionospheric effects during ssw events, *Space Science Reviews*, *168*, 385–417, 2012. [Cited on pages 22, 28, 67, and 68.]

Cocks, T., and F. Jacka, Daytime thermospheric temperatures, wind velocities and emission intensities derived from ground based observations of the oiλ630 nm airglow line profile, *Journal of Atmospheric and Terrestrial Physics*, *41*, 409–415, 1979. [Cited on page 40.]

Cullens, C. Y., et al., Atmospheric tidal study using icon/mighti observations, in *AGU Fall Meeting Abstracts*, vol. 2020, pp. SA036–0001, 2020. [Cited on page 73.]

Davis, P., and W. Peltier, Some characteristics of the kelvin-helmholtz and resonant overreflection modes of shear flow instability and of their interaction through vortex pairing, *Journal of the Atmospheric Sciences*, *36*, 2394–2412, 1979. [Cited on page 11.]

Deeming, T. J., Fourier analysis with unequally-spaced data, *Astrophys. Space Sci.*, *36*, 137–158, 1975. [Cited on page 62.]

Deshpande, M., et al., Effect of electrojet on the total electron content of the ionosphere over the indian subcontinent, *Nature*, *267*, 599–600, 1977. [Cited on page 89.]

Dewan, E. á., R. Picard, R. O'Neil, H. Gardiner, J. Gibson, J. Mill, E. Richards, M. Kendra, and W. Gallery, Msx satellite observations of thunderstorm-generated gravity waves in mid-wave infrared images of the upper stratosphere, *Geophysical Research Letters*, *25*, 939–942, 1998. [Cited on page 11.]

Djuth, F., M. Sulzer, J. Elder, and V. Wickwar, High-resolution studies of atmosphere-ionosphere coupling at arecibo observatory, puerto rico, *Radio Science*, *32*, 2321–2344, 1997. [Cited on page 10.]

Djuth, F., M. Sulzer, S. Gonzales, J. D. Mathews, J. Elder, and R. Walterscheid, A continuum of gravity waves in the arecibo thermosphere?, *Geophysical Research Letters*, *31*, 2004. [Cited on page 113.]

Drob, D. P., et al., An empirical model of the Earth's horizontal wind fields: HWM07, *J. Geophys. Res.*, *113*, 2008. [Cited on page 31.]

Drob, D. P., et al., An update to the horizontal wind model (hwm): The quiet time thermosphere, *Earth and Space Science*, *2*, 301–319, 2015. [Cited on pages 31, 52, 122, and 125.]

Dunford, E., The relationship between the ionospheric equatorial anomaly and the e-region current system, *Journal of Atmospheric and Terrestrial Physics*, *29*, 1489–1498, 1967. [Cited on page 89.]

Emmert, J. T., D. P. Drob, G. G. Shepherd, G. Hernandez, M. J. Jarvis, J. W. Meriwether, R. J. Niciejewski, D. P. Sipler, and C. A. Tepley, DWM07 global empirical model of upper thermospheric storm-induced disturbance winds, *J. Geophys. Res.*, *113*, 2008. [Cited on page 31.]

Englert, C. R., et al., Michelson interferometer for global high-resolution thermospheric imaging (MIGHTI): instrument design and calibration, *Space science reviews*, *212*, 553–584, 2017. [Cited on pages 31, 51, and 107.]

Farmer, D., and L. Armi, Stratified flow over topography: The role of small-scale entrainment and mixing in flow establishment, *Proceedings of the Royal Society of London. Series A: Mathematical, Physical and Engineering Sciences*, *455*, 3221–3258, 1999. [Cited on page 11.]

Fejer, B., M. Olson, J. Chau, C. Stolle, H. Lühr, L. Goncharenko, K. Yumoto, and T. Nagatsuma, Lunar-dependent equatorial ionospheric electrodynamic effects during sudden stratospheric warmings, *Journal of Geophysical Research: Space Physics*, *115*, 2010. [Cited on pages 27, 68, 71, and 79.]

Fejer, B. G., The equatorial ionospheric electric fields. a review, *Journal of Atmospheric and terrestrial physics*, *43*, 377–386, 1981. [Cited on page 28.]

Floyd, L., J. Newmark, J. Cook, L. Herring, and D. McMullin, Solar EUV and UV spectral irradiances and solar indices, *J. Atmos. Sol. Terr. Phys.*, *67*, 3–15, 2005. [Cited on page 56.]

Forbes, J. M., Atmospheric tides: 1. model description and results for the solar diurnal component, *Journal of Geophysical Research: Space Physics*, *87*, 5222–5240, 1982a. [Cited on page 70.]

Forbes, J. M., Atmospheric tide: 2. the solar and lunar semidiurnal components, *Journal of Geophysical Research: Space Physics*, *87*, 5241–5252, 1982b. [Cited on page 70.]

Forbes, J. M., and H. B. Garrett, Theoretical studies of atmospheric tides, *Reviews of Geophysics*, *17*, 1951–1981, 1979. [Cited on pages xii, 16, 19, and 86.]

Forbes, J. M., and X. Zhang, Lunar tide amplification during the january 2009 stratosphere warming event: Observations and theory, *Journal of Geophysical Research: Space Physics*, *117*, 2012. [Cited on pages 22, 68, and 86.]

Forbes, J. M., X. Zhang, S. Bruinsma, and J. Oberheide, Lunar semidiurnal tide in the thermosphere under solar minimum conditions, *Journal of Geophysical Research: Space Physics*, *118*, 1788–1801, 2013. [Cited on pages xv, 73, and 74.]

Fritts, D. C., Shear excitation of atmospheric gravity waves, *Journal of the Atmospheric Sciences*, *39*, 1936–1952, 1982. [Cited on page 11.]

Fritts, D. C., Shear excitation of atmospheric gravity waves. part ii: Nonlinear radiation from a free shear layer, *Journal of the Atmospheric Sciences*, *41*, 524–537, 1984. [Cited on page 12.]

Fukao, S., Y. Yamamoto, W. Oliver, T. Takami, M. Yamanaka, M. Yamamoto, T. Nakamura, and T. Tsuda, Middle and upper atmosphere radar observations of ionospheric horizontal gradients produced by gravity waves, *Journal of Geophysical Research: Space Physics*, *98*, 9443–9451, 1993. [Cited on page 122.]

Fuller-Rowell, T. J., A. D. Richmond, and N. Maruyama, Global modeling of storm-time thermospheric dynamics and electrodynamics, *Washington DC American Geophysical Union Geophysical Monograph Series*, *181*, 187–200, 2008. [Cited on page 28.]

Gelaro, R., et al., The modern-era retrospective analysis for research and applications, version 2 (merra-2), *Journal of climate*, *30*, 5419–5454, 2017. [Cited on page 58.]

Gerber, E. P., and P. Martineau, Quantifying the variability of the annular modes: reanalysis uncertainty vs. sampling uncertainty, *Atmospheric Chemistry and Physics*, *18*, 17,099–17,117, 2018. [Cited on pages xiv and 58.]

Gerrard, A. J., and J. W. Meriwether, Initial daytime and nighttime SOFDI observations of thermospheric winds from Fabry-Perot Doppler shift measurements of the 630-nm OI line-shape profile, *Ann. Geophys.*, *29*, 1529–1536, 2011. [Cited on page 107.]

Goncharenko, L. P., J. L. Chau, and A. J. Coster, Unexpected connections between the stratosphere and ionosphere, *Geophys. Res. Lett.*, *37*, 2010. [Cited on page 28.]

Goncharenko, L. P., V. L. Harvey, H. Liu, and N. M. Pedatella, Sudden stratospheric warming impacts on the ionosphere–thermosphere system: A review of recent progress, *Ionosphere dynamics and applications*, pp. 369–400, 2021. [Cited on pages 22, 28, and 86.]

Gouin, P., and P. N. Mayaud, A propos de Iéxistence possible dún contre electrojet aux latitudes magnetiques equatorials, *Ann. Geophys.*, *23*, 41–47, 1967. [Cited on page 31.]

Graham, G., Iv. an account of observations made of the variation of the horizontal needle at london, in the latter part of the year 1772, and beginning of 1723, *Philosophical Transactions of the Royal Society of London*, *33*, 96–107, 1724. [Cited on page 24.]

Grainger, J. F., and J. Ring, Anomalous Fraunhofer line profiles, *Nature*, *193*, 762, 1962. [Cited on page 48.]

Grodji, F., V. Doumbia, K. Boka, C. Amory-Mazaudier, Y. Cohen, and R. Fleury, Estimating some parameters of the equatorial ionosphere electrodynamics from ionosonde data in west africa, *Advances in Space Research*, *59*, 311–325, 2017. [Cited on pages xii and 26.]

Hagan, M. E., R. G. Roble, and J. Hackney, Migrating thermospheric tides, *J. Geophys. Res.*, *106*, 12,739–12,752, 2001. [Cited on page 15.]

Harding, B. J., J. J. Makela, C. R. Englert, K. D. Marr, J. M. Harlander, S. L. England, and T. J. Immel, The mighti wind retrieval algorithm: description and verification, *Space science reviews*, *212*, 585–600, 2017. [Cited on page 51.]

Hargreaves, J. K., *The Solar-Terrestrial Environment*, Cambridge University Press, 1992. [Cited on pages xi, 2, 4, 11, and 55.]

Harvey, V. L., C. E. Randall, L. Goncharenko, E. Becker, and J. France, On the upward extension of the polar vortices into the mesosphere, *Journal of Geophysical Research: Atmospheres*, *123*, 9171–9191, 2018. [Cited on page 20.]

Hays, P. B., D. W. Rusch, R. G. Roble, and J. C. G. Walker, The O-I (6300 $\AA$) airglow, *Rev. Geophys.*, *16*, 225–232, 1978. [Cited on pages xiii and 38.]

Hedin, A. E., and H. G. Mayr, Magnetic control of the near equatorial neutral thermosphere, *J. Geophys. Res.*, *78*, 1688–1691, 1973. [Cited on page 29.]

Hedin, A. E., N. W. Spencer, and T. L. Killeen, Empirical global model of upper thermosphere winds based on Atmosphere and Dynamics Explorer satellite data, *J. Geophys. Res.*, *93*, 9959–9978, 1988. [Cited on page 31.]

Hedin, A. E., et al., Empirical wind model for the upper, middle and lower atmosphere, *J. Atmos. Terr. Phys.*, *58*, 1421 – 1447, 1996. [Cited on page 31.]

Heelis, R., R. Stoneback, M. Perdue, M. Depew, W. Morgan, M. Mankey, C. Lippincott, L. Harmon, and B. Holt, Ion velocity measurements for the ionospheric connections explorer, *Space science reviews*, *212*, 615–629, 2017. [Cited on page 56.]

Hernandez, G., and R. G. Roble, Direct measurements of nighttime thermospheric winds and temperatures, 2. Geomagnetic storms, *J. Geophys. Res.*, *81*, 5173–5181, 1976. [Cited on page 39.]

Herrero, F., H. Mayr, and N. Spencer, Low latitude thermospheric meridional winds between 250 and 450 km altitude: AE-E satellite data, *J. Atmos. Terr. Phys.*, *50*, 1001 – 1006, 1988. [Cited on page 107.]

Herrero, F., N. Spencer, and H. Mayr, Thermosphere and f-region plasma dynamics in the equatorial region, *Advances in Space Research*, *13*, 201–220, 1993. [Cited on page 90.]

Hines, C., Atmospheric gravity waves-a new toy for the wave theorist, *Tech. rep.*, 1964. [Cited on page 7.]

Hines, C. O., Internal atmospheric gravity waves at ionospheric heights, *Canadian Journal of Physics*, *38*, 1441–1481, 1960. [Cited on pages 10, 117, and 122.]

Hirono, M., On the influence of the hall current to the electrical conductivity of the ionosphere. i, *Journal of geomagnetism and geoelectricity*, *2*, 1–8, 1950. [Cited on page 24.]

Hocke, K., and N. Kämpfer, Gap filling and noise reduction of unevenly sampled data by means of the Lomb-Scargle periodogram, *Atmos. Chem. Phys.*, *9*, 4197–4206, 2009. [Cited on page 117.]

Hocke, K. K. S., A review of atmospheric gravity waves and travelling ionospheric disturbances: 1982-1995, *Ann. Geophys.*, *14*, 917–940, 1996. [Cited on page 12.]

Hollingsworth, A., Modification of the atmospheric semi-diurnal lunar tide by oceanic and solid earth tides., Ph.D. thesis, Massachusetts Institute of Technology, 1971. [Cited on page 17.]

Holton, J. R., The Dynamics of Sudden Stratospheric Warmings, *Annu. Rev. Earth Planet. Sci.*, *8*, 169–190, 1980. [Cited on pages 15 and 22.]

Holton, J. R., The influence of gravity wave breaking on the general circulation of the middle atmosphere, *Journal of Atmospheric Sciences*, *40*, 2497–2507, 1983. [Cited on page 67.]

Horne, J. H., and S. L. Baliunas, A prescription for period analysis of unevenly sampled time series, *Astrophys. J.*, *302*, 757–763, 1986. [Cited on pages 62 and 63.]

Huang, L., J. Huang, J. Wang, Y. Jiang, B. Deng, K. Zhao, and G. Lin, Analysis of the north-south asymmetry of the equatorial ionization anomaly around 110°E longitude, *Journal of Atmospheric and Solar-Terrestrial Physics*, *102*, 354–361, 2013. [Cited on page 28.]

Immel, T. J., E. Sagawa, S. L. England, S. B. Henderson, M. E. Hagan, S. B. Mende, H. U. Frey, C. M. Swenson, and L. J. Paxton, Control of equatorial ionospheric morphology by atmospheric tides, *Geophys. Res. Lett.*, *33*, 2006. [Cited on pages xii, 15, and 28.]

Immel, T. J., et al., The ionospheric connection explorer mission: Mission goals and design, *Space Science Reviews*, *214*, 1–36, 2018. [Cited on page 51.]

Jarrett, A. H., and M. J. Hoey, A ground-level photographic observation of the day airglow emission of atomic oxygen at 6300 Å, *Planet. Space Sci.*, *11*, 1251–1252, 1963. [Cited on page 40.]

Jin, H., Y. Miyoshi, D. Pancheva, P. Mukhtarov, H. Fujiwara, and H. Shinagawa, Response of migrating tides to the stratospheric sudden warming in 2009 and their effects on the ionosphere studied by a whole atmosphere-ionosphere model gaia with cosmic and timed/saber observations, *Journal of Geophysical Research: Space Physics*, *117*, 2012. [Cited on pages 16, 20, and 68.]

Karan, D. K., and D. Pallamraju, Small-scale longitudinal variations in the daytime equatorial thermospheric wave dynamics as inferred from oxygen dayglow emissions, *Journal of Geophysical Research: Space Physics*, *122*, 6528–6542, 2017. [Cited on pages 28, 90, 101, and 108.]

Karan, D. K., and D. Pallamraju, Effect of geomagnetic storms on the daytime low-latitude thermospheric wave dynamics, *Journal of Atmospheric and Solar-Terrestrial Physics*, *170*, 35–47, 2018. [Cited on pages 28, 90, 97, and 109.]

Karan, D. K., D. Pallamraju, K. A. Phadke, T. Vijayalakshmi, T. K. Pant, and S. Mukherjee, Electrodynamic influence on the diurnal behaviour of neutral daytime airglow emissions, *Ann. Geophys.*, *34*, 1019–1030, 2016. [Cited on pages 90 and 92.]

Karan, D. K., R. E. Daniell, S. L. England, C. R. Martinis, R. W. Eastes, A. G. Burns, and W. E. McClintock, First zonal drift velocity measurement of equatorial plasma bubbles (EPBs) from a geostationary orbit using gold data, *Journal of Geophysical Research: Space Physics*, *125*, e2020JA028,173, 2020. [Cited on page 90.]

Kelley, M. C., *The Earth's Ionosphere: Plasma Physics and Electrodynamics*, vol. 96, Academic press, 2009. [Cited on pages xi and 10.]

Khadka, S. M., C. E. Valladares, R. Sheehan, and A. J. Gerrard, Effects of electric field and neutral wind on the asymmetry of equatorial ionization anomaly, *Radio Science*, *53*, 683–697, 2018. [Cited on pages 28 and 90.]

Killeen, T. L., Q. Wu, S. C. Solomon, D. A. Ortland, W. R. Skinner, R. J. Niciejewski, and D. A. Gell, TIMED Doppler Interferometer: Overview and recent results, *J. Geophys. Res.*, *111*, 2006. [Cited on page 31.]

Kohl, H., and J. W. King, Atmospheric winds between 100 and 700 km and their effects on the ionosphere, *J. Atmos. Terr. Phys.*, *29*, 1045–1062, 1967. [Cited on page 31.]

Körnich, H., and E. Becker, A simple model for the interhemispheric coupling of the middle atmosphere circulation, *Advances in Space Research*, *45*, 661–668, 2010. [Cited on page 22.]

Kulkarni, P. V., Rocket study of 5577Å OI emission at night over the magnetic equator, *J. Geophys. Res.*, *81*, 3740–3744, 1976. [Cited on page 39.]

Kumar, S., B. Veenadhari, S. T. Ram, S.-Y. Su, and T. Kikuchi, Possible relationship between the equatorial electrojet (EEJ) and daytime vertical E× B drift velocities in F region from ROCSAT observations, *Advances in Space Research*, *58*, 1168–1176, 2016. [Cited on page 89.]

Kumar, S., D. Pallamraju, P. Suryawanshi, T. Vijayalakshmi, and G. K. Seemala, On the latitudinal variation in oi 630.0 nm dayglow emissions in response to the equatorial electrodynamic processes and neutral winds, *Advances in Space Research*, *69*, 926–938, 2022. [Cited on pages 31, 53, 105, 126, and 134.]

Kumar, S., S. Mandal, and D. Pallamraju, Characterization of gravity waves in three dimensions in the daytime thermosphere using combined optical and radio measurements and estimation of horizontal neutral winds, *Journal of Geophysical Research: Space Physics*, *128*, e2022JA030,954, 2023a. [Cited on pages 31, 129, and 134.]

Kumar, S., T. A. Siddiqui, C. Stolle, N. M. Pedatella, and D. Pallamraju, Impact of strong and weak stratospheric polar vortices on geomagnetic semidiurnal solar and lunar tides, *Earth, Planets and Space*, *75*, 1–10, 2023b. [Cited on pages 88 and 133.]

Lakshmi Narayanan, V., S. Gurubaran, and K. Emperumal, Airglow imaging observations of small-scale structures driven by convective instability in the upper mesosphere over tirunelveli (8.7°n), *Journal of Geophysical Research: Atmospheres*, *115*, 2010. [Cited on page 108.]

Laskar, F. I., and D. Pallamraju, Does sudden stratospheric warming induce meridional circulation in the mesosphere thermosphere system?, *Journal of Geophysical Research: Space Physics*, *119*, 10–133, 2014. [Cited on page 67.]

Laskar, F. I., D. Pallamraju, T. V. Lakshmi, M. A. Reddy, B. M. Pathan, and S. Chakrabarti, Investigations on vertical coupling of atmospheric regions using combined multiwavelength optical dayglow, magnetic, and radio measurements, *J. Geophys. Res.*, *118*, 4618–4627, 2013. [Cited on page 28.]

Laskar, F. I., D. Pallamraju, B. Veenadhari, T. V. Lakshmi, M. A. Reddy, and S. Chakrabarti, Gravity waves in the thermosphere: Solar activity dependence, *Adv. Space Res.*, *55*, 1651 – 1659, 2015. [Cited on page 108.]

Lawrence, Z. D., J. Perlwitz, A. H. Butler, G. L. Manney, P. A. Newman, S. H. Lee, and E. R. Nash, The remarkably strong arctic stratospheric polar vortex of winter 2020: Links to record-breaking arctic oscillation and ozone loss, *Journal of Geophysical Research: Atmospheres*, *125*, e2020JD033,271, 2020. [Cited on pages 20, 67, 81, and 87.]

Li, J., and X. Lu, Global responses of gravity waves and zonal mean winds to the madden-julian oscillation and the latitudinal dependence of their relations using merra-2, *Geophysical Research Letters*, *48*, e2021GL094,717, 2021. [Cited on page 108.]

Lieberman, R. S., B. J. Harding, R. A. Heelis, N. M. Pedatella, J. M. Forbes, and J. Oberheide, Atmospheric lunar tide in the low latitude thermosphere-ionosphere, *Geophysical Research Letters*, *49*, e2022GL098,078, 2022. [Cited on pages 73, 74, and 75.]

Lindzen, R. S., and S.-s. Hong, Effects of mean winds and horizontal temperature gradients on solar and lunar semidiurnal tides in the atmosphere, *Journal of the atmospheric sciences*, *31*, 1421–1446, 1974. [Cited on pages 16 and 20.]

Link, R., and L. Cogger, A reexamination of the oi 6300-å nightglow, *Journal of Geophysical Research: Space Physics*, *93*, 9883–9892, 1988. [Cited on page 39.]

Liu, H.-L., and R. Roble, A study of a self-generated stratospheric sudden warming and its mesospheric–lower thermospheric impacts using the coupled time-gcm/ccm3, *Journal of Geophysical Research: Atmospheres*, *107*, ACL–15, 2002. [Cited on page 67.]

Liu, H.-L., W. Wang, A. Richmond, and R. Roble, Ionospheric variability due to planetary waves and tides for solar minimum conditions, *Journal of Geophysical Research: Space Physics*, *115*, 2010. [Cited on page 13.]

Lomb, N. R., Least-squares frequency analysis of unequally spaced data, *Astrophysics and space science*, *39*, 447–462, 1976. [Cited on pages 60, 61, 62, and 111.]

Long, R. R., Some aspects of the flow of stratified fluids: Iii. continuous density gradients, *Tellus*, *7*, 341–357, 1955. [Cited on page 11.]

Lott, F., and M. J. Miller, A new subgrid-scale orographic drag parametrization: Its formulation and testing, *Quarterly Journal of the Royal Meteorological Society*, *123*, 101–127, 1997. [Cited on page 11.]

Lühr, H., and C. Manoj, The complete spectrum of the equatorial electrojet related to solar tides: Champ observations, in *Annales Geophysicae*, vol. 31, pp. 1315–1331, Copernicus GmbH, 2013. [Cited on pages 26 and 89.]

Ma, Z., Y. Gong, S. Zhang, Q. Zhou, C. Huang, K. Huang, and G. Li, First observational evidence for the role of polar vortex strength in modulating the activity of planetary waves in the mlt region, *Geophysical Research Letters*, *49*, e2021GL096,548, 2022. [Cited on page 81.]

Makela, J. J., D. J. Fisher, J. W. Meriwether, R. A. Buriti, and A. F. Medeiros, Near-continual ground-based nighttime observations of thermospheric neutral winds and temperatures over equatorial Brazil from 2009 to 2012, *J. Atmos. Sol. Terr. Phys.*, *103*, 94 – 102, 2013. [Cited on pages 31, 90, and 107.]

Malin, S., and S. Chapman, The determination of lunar daily geophysical variations by the chapman-miller method, *Geophysical Journal International*, *19*, 15–35, 1970. [Cited on page 71.]

Mandal, S., and D. Pallamraju, Thermospheric gravity wave characteristics in the daytime over low-latitudes during geomagnetic quiet and disturbed conditions, *Journal of Atmospheric and Solar-Terrestrial Physics*, *211*, 105,470, 2020. [Cited on pages 108, 117, and 121.]

Mandal, S., D. Pallamraju, D. K. Karan, K. A. Phadke, R. P. Singh, and P. Suryawanshi, On deriving gravity wave characteristics in the daytime upper atmosphere using radio technique, *Journal of Geophysical Research: Space Physics*, *124*, 6985–6997, 2019. [Cited on pages 10, 108, and 109.]

Mandal, S., D. Pallamraju, and P. Suryawanshi, Changes in the daytime thermospheric gravity wave propagation characteristics over low-latitudes in response to the variation in solar flux, *Journal of Atmospheric and Solar-Terrestrial Physics*, *209*, 105,414, 2020. [Cited on pages 108 and 120.]

Mandal, S., D. Pallamraju, and T. Pant, Vertical propagation speeds of gravity waves in the daytime as a precursor to the onset of the equatorial spread-f, *Journal of Geophysical Research: Space Physics*, 2022. [Cited on page 120.]

Marshall, R. A., S. Smith, J. Baumgardner, and S. Chakrabarti, Continuous ground-based multiwavelength airglow measurements, *J. Geophys. Res.*, *116*, 2011. [Cited on page 45.]

Matsuno, T., A dynamical model of the stratospheric sudden warming, *Journal of Atmospheric Sciences*, *28*, 1479–1494, 1971a. [Cited on page 67.]

Matsuno, T., A dynamical model of the stratospheric sudden warming, *J. Atmos. Sci.*, *28*, 1479–1494, 1971b. [Cited on page 20.]

Matsushita, S., and W.-Y. Xu, Seasonal variations of l equivalent current systems, *Journal of Geophysical Research: Space Physics*, *89*, 285–294, 1984. [Cited on page 26.]

Matthias, V., A. Dörnbrack, and G. Stober, The extraordinarily strong and cold polar vortex in the early northern winter 2015/2016, *Geophysical Research Letters*, *43*, 12–287, 2016. [Cited on page 81.]

Matzka, J., C. Stolle, Y. Yamazaki, O. Bronkalla, and A. Morschhauser, The geomagnetic kp index and derived indices of geomagnetic activity, *Space Weather*, *19*, e2020SW002,641, 2021. [Cited on page 74.]

Mayr, H., I. Harris, and N. Spencer, Some properties of upper atmosphere dynamics, *Reviews of Geophysics*, *16*, 539–565, 1978. [Cited on page 31.]

McDonald, S. E., C. Coker, K. F. Dymond, D. N. Anderson, and E. A. Araujo-Pradere, A study of the strong linear relationship between the equatorial ionization anomaly and the prereversal E $\times$ B drift velocity at solar minimum, *Radio Science*, *46*, RS6004, 2011. [Cited on page 28.]

Mendillo, M., and J. Baumgardner, Airglow characteristics of equatorial plasma depletions, *J. Geophys. Res.*, *87*, 7641, 1982. [Cited on page 39.]

Meriwether, J. W., P. Shih, T. L. Killeen, V. B. Wickwar, and R. G. Roble, Nighttime thermospheric winds over Sondre Stromfjord, Greenland, *Geophys. Res. Lett.*, *11*, 931–934, 1984. [Cited on page 31.]

Meriwether, J. W., J. W. Moody, M. A. Biondi, and R. G. Roble, Optical interferometric measurements of nighttime equatorial thermospheric winds at Arequipa, Peru, *J. Geophys. Res.*, *91*, 5557–5566, 1986. [Cited on pages 31, 39, and 107.]

Miyoshi, Y., and Y. Yamazaki, Excitation Mechanism of Ionospheric 6-Day Oscillation During the 2019 September Sudden Stratospheric Warming Event, *Journal of Geophysical Research (Space Physics)*, *125*, e28,283, 2020. [Cited on page 28.]

Miyoshi, Y., H. Fujiwara, H. Jin, and H. Shinagawa, A global view of gravity waves in the thermosphere simulated by a general circulation model, *Journal of Geophysical Research: Space Physics*, *119*, 5807–5820, 2014. [Cited on page 108.]

Mo, X., and D. Zhang, Six-day periodic variation in equatorial ionization anomaly region, *Journal of Geophysical Research: Space Physics*, *125*, e2020JA028,225, 2020. [Cited on page 28.]

Narayanan, R., J. N. Desai, N. K. Modi, R. Raghavarao, and R. Sridharan, Dayglow photometry: a new approach, *Appl. Opt.*, *28*, 2138–2142, 1989. [Cited on page 40.]

Nicolls, M., S. Vadas, J. Meriwether, M. Conde, and D. Hampton, The phases and amplitudes of gravity waves propagating and dissipating in the thermosphere: Application to measurements over alaska, *Journal of Geophysical Research: Space Physics*, *117*, 2012. [Cited on page 122.]

Noxon, J. F., and R. M. Goody, Observation of day airglow emission, *J. Atmos. Sci.*, *19*, 342–343, 1962. [Cited on page 40.]

Ogbuehi, P., A. Onwumechilli, and S. Ifedili, The equatorial electrojet and the world-wide sq currents, *Journal of Atmospheric and Terrestrial Physics*, *29*, 149–160, 1967. [Cited on pages xii and 25.]

Oliver, W. L., S. Fukao, Y. Yamamoto, T. Takami, M. D. Yamanaka, M. Yamamoto, T. Nakamura, and T. Tsuda, Middle and upper atmosphere radar observations of ionospheric density gradients produced by gravity wave packets, *Journal of Geophysical Research: Space Physics*, *99*, 6321–6329, 1994. [Cited on page 113.]

Oliver, W. L., Y. Otsuka, M. Sato, T. Takami, and S. Fukao, A climatology of f region gravity wave propagation over the middle and upper atmosphere radar, *Journal of Geophysical Research: Space Physics*, *102*, 14,499–14,512, 1997. [Cited on page 122.]

Oluwadare, T. S., C. Nguyen Thai, A. O.-O. Akala, S. Heise, M. Alizadeh, and H. Schuh, Characterization of GPS-TEC over African equatorial ionization anomaly (EIA) region during 2009-2016, *Advances in Space Research*, *63*, 282–301, 2019. [Cited on page 28.]

Onwumechilli, A., Geomagnetic variations in the equatorial zone, in *Phys. of Geomagnetic Phenomena*, p. 426, 1967. [Cited on page 31.]

Pallam Raju, D., and R. Sridharan, High resolution 2-d maps of oi 630.0 nm thermospheric dayglow from equatorial latitudes, in *Annales Geophysicae*, vol. 16, pp. 997–1006, Copernicus GmbH, 1998. [Cited on page 89.]

Pallamraju, D., Studies of daytime upper atmospheric phenomena using ground-based optical techniques, Ph.D. thesis, Devi Ahilya Vishwa Vidyalaya of Indore, 1996. [Cited on page 40.]

Pallamraju, D., Errors in airglow & auroral emission measurements, 2003. [Cited on page 50.]

Pallamraju, D., and S. Chakrabarti, Contributions of imaging Echelle spectrographs to daytime optical aeronomy, *J. Atmos. Sol. Terr. Phys.*, *68*, 1459 – 1471, 2006. [Cited on page 45.]

Pallamraju, D., and R. Sridharan, Ground-based optical measurements of daytime auroral emissions: A new means of investigating space-weather related processes, *Proceedings of the Indian Academy of Sciences - Earth and Planetary Sciences*, *107*, 203–211, 1998. [Cited on page 40.]

Pallamraju, D., R. Sridharan, R. Narayanan, N. K. Modi, R. Raghavarao, and B. H. Subbaraya, Ground-based optical observations of daytime auroral emissions from Antarctica, *J. Atmos. Terr. Phys.*, *57*, 1591–1597, 1995. [Cited on page 40.]

Pallamraju, D., R. Sridharan, S. Gurubaran, and R. Raghavarao, First results from ground-based daytime optical investigation of the development of the equatorial ionization anomaly, *Ann. Geophys.*, *14*, 238–245, 1996. [Cited on pages 40, 89, 90, and 92.]

Pallamraju, D., J. Baumgardner, and S. Chakrabarti, A multiwavelength investigation of the ring effect in the day sky spectrum, *Geophys. Res. Lett.*, *27*, 1875–1878, 2000. [Cited on page 48.]

Pallamraju, D., J. Baumgardner, S. Chakrabarti, and T. R. Pedersen, Simultaneous ground based observations of an auroral arc in daytime/twilighttime OI 630.0 nm emission and by incoherent scatter radar, *J. Geophys. Res.*, *106*, 5543–5549, 2001. [Cited on page 12.]

Pallamraju, D., J. Baumgardner, and S. Chakrabarti, HIRISE: A ground-based high-resolution imaging spectrograph using echelle grating for measuring daytime airglow/auroral emissions, *J. Atmos. Sol. Terr. Phys.*, *64*, 1581–1587, 2002. [Cited on pages 41, 43, 45, 47, 48, 49, and 89.]

Pallamraju, D., S. Chakrabarti, and C. E. Valladares, Magnetic storm-induced enhancement in neutral composition at low latitudes as inferred by O(^{1}D) dayglow measurements from Chile, *Ann. Geophys.*, *22*, 3241–3250, 2004b. [Cited on pages 12 and 97.]

Pallamraju, D., U. Das, and S. Chakrabarti, Short-and long-timescale thermospheric variability as observed from oi 630.0 nm dayglow emissions from low latitudes, *Journal of Geophysical Research: Space Physics*, *115*, 2010. [Cited on pages xvii, 12, 28, 90, 92, 93, and 108.]

Pallamraju, D., F. I. Laskar, R. P. Singh, J. Baumgardner, and S. Chakrabarti, MISE: A multiwavelength imaging spectrograph using echelle grating for daytime optical aeronomy investigations , *J. Atmos. Sol. Terr. Phys.*, *103*, 176 – 183, 2013. [Cited on pages ix, xiii, 41, 42, 43, 45, 46, 47, 48, and 49.]

Pallamraju, D., D. K. Karan, and K. A. Phadke, First three dimensional wave characteristics in the daytime upper atmosphere derived from ground-based multiwavelength oxygen dayglow emission measurements, *Geophys. Res. Lett.*, *43*, 5545–5553, 2016. [Cited on pages 10, 108, 109, 115, and 117.]

Pallamraju, D., P. Suryawanshi, S. Urmalia, S. Kumar, S. Saha, R. P. Singh, P. K. Kushwaha, and M. Soni, Cdap: A portable ccd-based daytime airglow photometer for investigations of ionosphere-thermosphere phenomena, *Journal of Atmospheric and Solar-Terrestrial Physics*, *244*, 106,025, 2023. [Cited on page 40.]

Pallamraju, D., et al., Daytime wave characteristics in the mesosphere lower thermosphere region: Results from the balloon-borne investigations of regional-atmospheric dynamics experiment, *Journal of Geophysical Research: Space Physics*, *119*, 2229–2242, 2014. [Cited on pages 12, 43, and 45.]

Park, J., H. Lühr, M. Kunze, B. G. Fejer, and K. W. Min, Effect of sudden stratospheric warming on lunar tidal modulation of the equatorial electrojet, *Journal of Geophysical Research: Space Physics*, *117*, 2012. [Cited on page 70.]

Pedatella, N., and V. Harvey, Impact of strong and weak stratospheric polar vortices on the mesosphere and lower thermosphere, *Geophysical Research Letters*, *49*, e2022GL098,877, 2022. [Cited on pages xii, xv, 22, 23, 67, 68, and 76.]

Pedatella, N., H.-L. Liu, A. Richmond, A. Maute, and T.-W. Fang, Simulations of solar and lunar tidal variability in the mesosphere and lower thermosphere during sudden stratosphere warmings and their influence on the low-latitude ionosphere, *Journal of Geophysical Research: Space Physics*, *117*, 2012. [Cited on page 27.]

Pedatella, N., et al., The neutral dynamics during the 2009 sudden stratosphere warming simulated by different whole atmosphere models, *Journal of Geophysical Research: Space Physics*, *119*, 1306–1324, 2014. [Cited on pages 22, 27, and 28.]

Pedatella, N. M., J. Lei, J. P. Thayer, and J. M. Forbes, Ionosphere response to recurrent geomagnetic activity: Local time dependency, *Journal of Geophysical Research (Space Physics)*, *115*, A02,301, 2010. [Cited on page 28.]

Picone, J., A. Hedin, D. P. Drob, and A. Aikin, Nrlmsise-00 empirical model of the atmosphere: Statistical comparisons and scientific issues, *Journal of Geophysical Research: Space Physics*, *107*, SIA–15, 2002. [Cited on pages 39 and 102.]

Pramitha, M., M. V. Ratnam, A. Taori, B. Murthy, D. Pallamraju, and S. V. Bhaskar Rao, Evidence for tropospheric wind shear excitation of high-phase-speed gravity waves reaching the mesosphere using the ray-tracing technique., *Atmospheric Chemistry & Physics*, *15*, 2015. [Cited on page 12.]

Raghavarao, R., P. Sharma, and M. Sivaraman, Correlation of the ionisation anomaly with the intensity of the electrojet, 1978a. [Cited on page 28.]

Raghavarao, R., P. Sharma, and M. R. Sivaraman, Correlation of ionization anomaly with the intensity of the electrojet, *Space Res.*, *18*, 277–280, 1978b. [Cited on page 90.]

Raghavarao, R., M. Nageswararao, J. H. Sastri, G. D. Vyas, and M. Sriramarao, Role of equatorial ionization anomaly in the initiation of equatorial spread f, *Journal of Geophysical Research: Space Physics*, *93*, 5959–5964, 1988a. [Cited on page 89.]

Raghavarao, R., R. Sridharan, J. H. Sastri, V. V. Agashe, B. C. N. Rao, P. B. Rao, and V. V. Somayajulu, *The equatorial ionosphere; WITS handbook. World Ionosphere/Thermosphere Study, vol 1.*, SCOSTEP Secretariat, University of Illinois, Urbana, 1988b. [Cited on pages 12 and 89.]

Raghavarao, R., L. E. Wharton, N. W. Spencer, H. G. Mayr, and L. H. Brace, An equatorial temperature and wind anomaly (ETWA), *Geophys. Res. Lett.*, *18*, 1193–1196, 1991. [Cited on pages xiii, 29, and 30.]

Rakesh, V., S. Haridas, C. Sivan, M. G. Manoj, S. Abhilash, B. Paul, K. Unnikrishnan, K. Mohanakumar, and R. Sumesh Chandran, Impact of the Hunga Tonga-Hunga Ha'apai volcanic eruption on the changes observed over the Indian near-equatorial ionosphere, *Advances in Space Research*, *70*, 2480–2493, 2022. [Cited on page 28.]

Rao, J., and C. I. Garfinkel, Arctic ozone loss in march 2020 and its seasonal prediction in cfsv2: A comparative study with the 1997 and 2011 cases, *Journal of Geophysical Research: Atmospheres*, *125*, e2020JD033,524, 2020. [Cited on page 87.]

Rastogi, R., Morphological aspects of a new type of counter electrojet event, in *Annales Geophysicae*, vol. 17, pp. 210–219, Springer Verlag Göttingen, Germany, 1999. [Cited on page 26.]

Rastogi, R., and J. Klobuchar, Ionospheric electron content within the equatorial f 2 layer anomaly belt, *Journal of Geophysical Research: Space Physics*, *95*, 19,045–19,052, 1990. [Cited on pages 28 and 90.]

Ray, R., and S. Luthcke, Tide model errors and grace gravimetry: towards a more realistic assessment, *Geophysical Journal International*, *167*, 1055–1059, 2006. [Cited on page 72.]

Richards, P., J. Fennelly, and D. Torr, Euvac: A solar euv flux model for aeronomic calculations, *Journal of Geophysical Research: Space Physics*, *99*, 8981–8992, 1994. [Cited on page 70.]

Rishbeth, H., Thermospheric winds and the F-region: A review, *J. Atmos. Terr. Phys.*, *34*, 1 – 47, 1972. [Cited on page 90.]

Rishbeth, H., Dynamics of the equatorial f-region, *Journal of atmospheric and terrestrial physics*, *39*, 1159–1168, 1977. [Cited on pages 31 and 90.]

Rishbeth, H., The ionospheric E-layer and F-layer dynamos: A tutorial review, *J. Atmos. Sol. Terr. Phys.*, *59*, 1873 – 1880, 1997. [Cited on page 31.]

Roble, R. G., J. M. Forbes, and F. A. Marcos, Thermospheric dynamics during the march 22, 1979, magnetic storm: 1. model simulations, *J. Geophys. Res.*, *92*, 6045–6068, 1987. [Cited on page 31.]

Rush, C., and A. Richmond, The relationship between the structure of the equatorial anomaly and the strength of the equatorial electrojet, *Journal of Atmospheric and Terrestrial Physics*, *35*, 1171–1180, 1973. [Cited on pages 27 and 90.]

Sabine, E., V. on the lunar atmospheric tide at st. helena, *Philosophical Transactions of the Royal Society of London*, pp. 45–50, 1847. [Cited on page 17.]

Saha, S., D. Pallamraju, T. K. Pant, and S. Chakrabarti, On the cause of the post-sunset nocturnal oi 630 nm airglow enhancement over low-latitude thermosphere, *Journal of Geophysical Research: Space Physics*, *126*, e2021JA029,146, 2021. [Cited on pages 31, 90, and 92.]

Salby, M. L., *Fundamentals of Atmospheric Physics*, vol. 61, Academic press, 1996. [Cited on pages xi, 9, and 13.]

Sastri, J., Equatorial anomaly in f-region - a review, *Indian Journal of Radio and Space Physics*, *19*, 225–240, 1990. [Cited on page 28.]

Sato, K., Small-scale wind disturbances observed by the mu radar during the passage of typhoon kelly, *Journal of the Atmospheric Sciences*, *50*, 518–537, 1993. [Cited on page 11.]

Sato, K., H. Hashiguchi, and S. Fukao, Gravity waves and turbulence associated with cumulus convection observed with the uhf/vhf clear-air doppler radars, *Journal of Geophysical Research: Atmospheres*, *100*, 7111–7119, 1995. [Cited on page 11.]

Scargle, J. D., Studies in astronomical time series analysis. ii-statistical aspects of spectral analysis of unevenly spaced data, *The Astrophysical Journal*, *263*, 835–853, 1982. [Cited on pages 60, 61, 62, 63, and 111.]

Shepherd, G. G., et al., Longitudinal structure in atomic oxygen concentrations observed with windii on uars, *Geophysical research letters*, *20*, 1303–1306, 1993a. [Cited on page 90.]

Shepherd, G. G., et al., WINDII, the wind imaging interferometer on the Upper Atmosphere Research Satellite, *J. Geophys. Res.*, *98*, 10,725–10,750, 1993b. [Cited on pages 31, 39, and 107.]

Shim, J., L. Scherliess, R. Schunk, and D. Thompson, Neutral wind and plasma drift effects on low and middle latitude total electron content, *Journal of Geophysical Research: Space Physics*, *115*, 2010. [Cited on page 31.]

Shiokawa, K., Y. Katoh, M. Satoh, M. K. Ejiri, T. Ogawa, T. Nakamura, T. Tsuda, and R. H. Wiens, Development of Optical Mesosphere Thermosphere Imagers (OMTI), *Earth, Planets and Space*, *51*, 887–896, 1999. [Cited on page 39.]

Shiokawa, K., Y. Otsuka, and T. Ogawa, Propagation characteristics of nighttime mesospheric and thermospheric waves observed by optical mesosphere thermosphere imagers at middle and low latitudes, *Earth, planets and space*, *61*, 479–491, 2009. [Cited on page 108.]

Shiokawa, K., et al., Thermospheric wind during a storm-time large-scale traveling ionospheric disturbance, *J. Geophys. Res.*, *108*, 2003. [Cited on page 31.]

Siddiqui, T., A. Maute, and N. Pedatella, On the importance of interactive ozone chemistry in earth-system models for studying mesosphere-lower thermosphere tidal changes during sudden stratospheric warmings, *Journal of Geophysical Research: Space Physics*, *124*, 10,690–10,707, 2019. [Cited on page 87.]

Siddiqui, T. A., C. Stolle, H. Lühr, and J. Matzka, On the relationship between weakening of the northern polar vortex and the lunar tidal amplification in the equatorial electrojet, *Journal of Geophysical Research: Space Physics*, *120*, 10,006–10,019, 2015. [Cited on page 69.]

Siddiqui, T. A., C. Stolle, and H. Lühr, Longitude-dependent lunar tidal modulation of the equatorial electrojet during stratospheric sudden warmings, *Journal of Geophysical Research: Space Physics*, *122*, 3760–3776, 2017. [Cited on page 84.]

Siddiqui, T. A., A. Maute, N. Pedatella, Y. Yamazaki, H. Lühr, and C. Stolle, On the variability of the semidiurnal solar and lunar tides of the equatorial electrojet during sudden stratospheric warmings, in *Annales Geophysicae*, vol. 36, pp. 1545–1562, Copernicus GmbH, 2018. [Cited on page 27.]

Singh, R. P., and D. Pallamraju, On the latitudinal distribution of mesospheric temperatures during sudden stratospheric warming events, *J. Geophys. Res.*, *120*, 2926–2939, 2015. [Cited on page 67.]

Singh, R. P., and D. Pallamraju, Effect of cyclone Nilofar on mesospheric wave dynamics as inferred from optical nightglow observations from Mount Abu, India, *J. Geophys. Res.*, *121*, 5856–5867, 2016. [Cited on page 11.]

Smith, A. K., and L. V. Lyjak, An observational estimate of gravity wave drag from the momentum balance in the middle atmosphere, *Journal of Geophysical Research: Atmospheres*, *90*, 2233–2241, 1985. [Cited on page 11.]

Soares, G., et al., Using principal component analysis of satellite and ground magnetic data to model the equatorial electrojet and derive its tidal composition, *Journal of Geophysical Research: Space Physics*, *127*, e2022JA030,691, 2022. [Cited on pages 26 and 89.]

Solomon, S. C., and V. J. Abreu, The 630 nm dayglow, *Journal of Geophysical Research: Space Physics*, *94*, 6817–6824, 1989. [Cited on pages 37, 39, and 92.]

Spencer, N., L. Wharton, H. Niemann, A. Hedin, G. Carrignan, and J. Maurer, The dynamics explorer wind and temperature spectrometer., *Space Science Instrumentation*, *5*, 417–428, 1981. [Cited on page 31.]

Sridharan, R., R. Raghavarao, S. Gurubaran, and R. Narayanan, First results of OI 630.0 nm dayglow measurements from equatorial latitudes, *J. Atmos. Sol.-Terr. Phy.*, *53*, 521–528, 1991. [Cited on page 39.]

Sridharan, R., S. A. Haider, S. Gurubaran, R. Sekar, and R. Narayanan, OI 630.0-nm dayglow in the region of equatorial ionization anomaly: Temporal variability and its causative mechanism, *J. Geophys. Res.*, *97*, 13,715–13,721, 1992a. [Cited on page 92.]

Sridharan, R., R. Narayanan, and N. K. Modi, Improved chopper mask for the dayglow photometer, *Appl. Opt.*, *31*, 425–426, 1992b. [Cited on page 40.]

Sridharan, R., R. Narayanan, N. K. Modi, and D. P. Raju, A Novel mask design for multiwavelength dayglow photometry, *Appl. Opt.*, *32*, 4178–80, 1993. [Cited on page 40.]

Sridharan, R., D. P. Raju, R. Raghavarao, and P. V. S. Ramarao, Precursor to equatorial spread-F in OI 630.0 nm dayglow, *Geophys. Res. Lett.*, *21*, 2797–2800, 1994. [Cited on pages 89 and 92.]

Sridharan, R., D. Pallam Raju, R. Narayanan, N. K. Modi, B. H. Subbaraya, and R. Raghavarao, Daytime measurements of optical auroral emissions from Antarctica, *Current science*, *68*, 830–834, 1995. [Cited on page 40.]

Sridharan, R., N. Modi, D. P. Raju, R. Narayanan, T. K. Pant, A. Taori, and D. Chakrabarty, A multiwavelength daytime photometer-a new tool for the investigation of atmospheric processes, *Measurement Science and Technology*, *9*, 585, 1998. [Cited on page 40.]

Sridharan, R., D. P. Raju, V. Somayajulu, A. Taori, D. Chakrabarty, and R. Raghavarao, Imprint of equatorial electrodynamical processes in the OI 630.0 nm dayglow, *J. Atmos. Sol. Terr. Phys.*, *61*, 1143 – 1155, 1999. [Cited on page 90.]

Sridharan, S., S. Sathishkumar, and S. Gurubaran, Variabilities of mesospheric tides and equatorial electrojet strength during major stratospheric warming events, *Annales Geophysicae*, *27*, 4125–4130, 2009, https://doi.org/10.5194/angeo-27-4125-2009. [Cited on page 27.]

Stening, R., Magnetic variations at other latitudes during reverse equatorial electrojet, *Journal of Atmospheric and Terrestrial Physics*, *39*, 1071–1077, 1977. [Cited on page 27.]

Stening, R. J., C. E. Meek, and A. H. Manson, Upper atmosphere wind systems during reverse equatorial electrojet events, *Geophys. Res. Lett.*, *23*, 3243–3246, 1996. [Cited on pages 26 and 27.]

Stewart, B., Hypothetical views regarding the connection between the state of the sun and terrestrial magnetism, *Encyclopedia Brittanica*, *16*, 181–184, 1882. [Cited on page 24.]

Stolle, C., C. Manoj, H. Lühr, S. Maus, and P. Alken, Estimating the daytime equatorial ionization anomaly strength from electric field proxies, *Journal of Geophysical Research: Space Physics*, *113*, 2008. [Cited on pages 28 and 89.]

Su, Y., G. Bailey, and N. Balan, Night-time enhancements in tec at equatorial anomaly latitudes, *Journal of Atmospheric and Terrestrial physics*, *56*, 1619–1628, 1994. [Cited on page 31.]

Tapping, K., The 10.7 cm solar radio flux (f10. 7), *Space Weather*, *11*, 394–406, 2013. [Cited on page 74.]

Taylor, M. J., M. B. Bishop, and V. Taylor, All-sky measurements of short period waves imaged in the oi(557.7 nm), na(589.2 nm) and near infrared oh and o2(0,1) nightglow emissions during the aloha-93 campaign, *Geophysical Research Letters*, *22*, 2833–2836, 1995. [Cited on page 108.]

Teitelbaum, H., and F. Vial, On tidal variability induced by nonlinear interaction with planetary waves, *Journal of Geophysical Research: Space Physics*, *96*, 14,169–14,178, 1991. [Cited on page 15.]

Teitelbaum, H., M. Massebeuf, J. Fellous, M. Petitdidier, J. Christophe, and F. Blanco, Simultaneous measurements of meteor winds and green line intensity variations: Gravity waves and planetary waves, *Journal of Geophysical Research: Space Physics*, *86*, 7767–7770, 1981. [Cited on page 108.]

Thompson, D. W., and J. M. Wallace, The arctic oscillation signature in the wintertime geopotential height and temperature fields, *Geophysical research letters*, *25*, 1297–1300, 1998. [Cited on page 57.]

Vadas, S., and H.-l. Liu, Generation of large-scale gravity waves and neutral winds in the thermosphere from the dissipation of convectively generated gravity waves, *Journal of Geophysical Research: Space Physics*, *114*, 2009. [Cited on page 108.]

Vadas, S., and M. Nicolls, The phases and amplitudes of gravity waves propagating and dissipating in the thermosphere: Theory, *Journal of Geophysical Research: Space Physics*, *117*, 2012. [Cited on page 122.]

Vadas, S., J. Yue, C.-Y. She, P. A. Stamus, and A. Z. Liu, A model study of the effects of winds on concentric rings of gravity waves from a convective plume near fort collins on 11 may 2004, *Journal of Geophysical Research: Atmospheres*, *114*, 2009. [Cited on page 108.]

Vadas, S. L., Horizontal and vertical propagation and dissipation of gravity waves in the thermosphere from lower atmospheric and thermospheric sources, *Journal of Geophysical Research: Space Physics*, *112*, 2007. [Cited on page 108.]

Valladares, C., and J. Chau, The low-latitude ionosphere sensor network: Initial results, *Radio Science*, *47*, 1–18, 2012. [Cited on pages 90 and 92.]

VanderPlas, J. T., Understanding the lomb–scargle periodogram, *The Astrophysical Journal Supplement Series*, *236*, 16, 2018. [Cited on page 62.]

Varney, R. H., M. C. Kelley, and E. Kudeki, Observations of electric fields associated with internal gravity waves, *Journal of Geophysical Research: Space Physics*, *114*, 2009. [Cited on page 28.]

Venkatesh, K., P. R. Fagundes, D. S. V. V. D. Prasad, C. M. Denardini, A. J. Abreu, R. Jesus, and M. Gende, Day-to-day variability of equatorial electrojet and its role on the day-to-day characteristics of the equatorial ionization anomaly over the Indian and Brazilian sectors, *Journal of Geophysical Research (Space Physics)*, *120*, 9117–9131, 2015. [Cited on page 28.]

Vial, F., and J. Forbes, Monthly simulations of the lunar semi-diurnal tide, *Journal of Atmospheric and Terrestrial Physics*, *56*, 1591–1607, 1994. [Cited on pages 17 and 18.]

Vineeth, C., T. Pant, K. Kumar, G. Ramkumar, and R. Sridharan, Signatures of low latitude–high latitude coupling in the tropical mlt region during sudden stratospheric warming, *Geophysical Research Letters*, *36*, 2009. [Cited on page 27.]

Waugh, D. W., A. H. Sobel, and L. M. Polvani, What is the polar vortex and how does it influence weather?, *Bulletin of the American Meteorological Society*, *98*, 37–44, 2017. [Cited on page 20.]

Woodman, R. F., Vertical drift velocities and east-west electric fields at the magnetic equator, *Journal of Geophysical Research*, *75*, 6249–6259, 1970. [Cited on page 28.]

Yamazaki, Y., Quasi-6-Day Wave Effects on the Equatorial Ionization Anomaly Over a Solar Cycle, *Journal of Geophysical Research (Space Physics)*, *123*, 9881–9892, 2018. [Cited on page 28.]

Yamazaki, Y., A. Richmond, and K. Yumoto, Stratospheric warmings and the geomagnetic lunar tide: 1958–2007, *Journal of Geophysical Research: Space Physics*, *117*, 2012. [Cited on page 69.]

Yamazaki, Y., B. J. Harding, C. Stolle, and J. Matzka, Neutral wind profiles during periods of eastward and westward equatorial electrojet, *Geophysical Research Letters*, *48*, e2021GL093,567, 2021. [Cited on page 31.]

Yamazaki, Y., et al., Ground magnetic effects of the equatorial electrojet simulated by the tie-gcm driven by timed satellite data, *Journal of Geophysical Research: Space Physics*, *119*, 3150–3161, 2014. [Cited on page 68.]

Yiğit, E., and A. S. Medvedev, Heating and cooling of the thermosphere by internal gravity waves, *Geophysical Research Letters*, *36*, 2009. [Cited on page 108.]

Yiğit, E., and A. S. Medvedev, Role of gravity waves in vertical coupling during sudden stratospheric warmings, *Geoscience Letters*, *3*, 1–13, 2016. [Cited on page 28.]

Zhang, J. T., and J. M. Forbes, Lunar tidal winds between 80 and 110 km from uars/hrdi wind measurements, *Journal of Geophysical Research: Space Physics*, *118*, 5296–5304, 2013. [Cited on page 18.]

Zhang, S. P., and G. G. Shepherd, Solar influence on the O(^{1}D) dayglow emission rate: Global-scale measurements by WINDII on UARS, *Geophys. Res. Lett.*, *31*, L07,804, 2004. [Cited on page 92.]

List of Publications

Publications in Journals

1. **Kumar, S.**, Pallamraju, D., Suryawanshi, P., Vijayalakshmi, T., & Seemala, G. K. (2022). On the latitudinal variation in OI 630.0 nm dayglow emissions in response to the equatorial electrodynamic processes and neutral winds. Advances in Space Research, 69(2), 926-938. https://doi.org/10.1016/j.asr.2021.10.034

2. **Kumar, S.**, Mandal, S., & Pallamraju, D. (2023). Characterization of gravity waves in three dimensions in the daytime thermosphere using combined optical and radio measurements and estimation of horizontal neutral winds. Journal of Geophysical Research: Space Physics, e2022JA030954. https://doi.org/10.1029/2022JA030954

3. **Kumar, S.**, Siddiqui, T.A., Stolle, C., Pedatella, N.M., & Pallamraju, D. Impact of strong and weak stratospheric polar vortices on geomagnetic semidiurnal solar and lunar tides. Earth Planets Space 75, 52 (2023). https://doi.org/10.1186/s40623-023-01810-x

4. Pallamraju, D., Suryawanshi, P., Urmalia, S., **Kumar, S.**, Saha, S., Singh, R. P., Kushwaha, P.K., & Soni, M. (2023). CDAP: A portable CCD-based daytime airglow photometer for investigations of ionosphere-thermosphere phenomena. Journal of Atmospheric and Solar-Terrestrial Physics, 244, 106025. https://doi.org/10.1016/j.jastp.2023.106025 [Not related to this thesis]

5. Saha, S., Pallamraju, D., **Kumar, S.**, Laskar, F.L., & Pedatella, N.M. (2023). OI 630.0 nm post-sunset emission enhancement as an effect of tidal activity over low-latitudes. (Under review)[Not related to this thesis]

Conference Proceedings

1. Pallamraju, D., Mandal, S., Saha, S., **Kumar, S.**, & Pant, T. K. (2022, December). New insights on the precursors to the onset of equatorial plasma irregularity generation. In 2022 URSI Regional Conference on Radio Science (USRI-RCRS) (pp. 1-4). IEEE. https://doi.org/10.23919/URSI-RCRS56822.2022.10118477 [Not related to this thesis]

Presentations at Conferences

1. **Kumar, S.**. Effect of the stratospheric polar vortices on the ionosphere-thermosphere system, presented at 2nd Indian Space Weather Conference at PRL during 19-20 October 2023. [Oral by SK]

2. Pallamraju, D., Saha, S., **Kumar, S.**, Mandal, S., & Pant, T.K. (2023). Recent developments on the precursors to plasma bubbles, presented at 3rd International Workshop on Equatorial Plasma Bubble (EPB-3) at IIG Mumbai during 13-15 September 2023. [Oral by DP]

3. **Kumar, S.**, Siddiqui, T.A., Stolle, C., Pedatella, N.M., & Pallamraju, D. Impact of strong and weak stratospheric polar vortices on the semidiurnal solar and lunar tides of the Equatorial Electrojet, presented at IUGG 2033 during 11-20 July 2023. [oral by TAS]

4. Pallamraju, D., Mandal, S., Saha, S., & **Kumar, S.** (2023). On the daytime precursors of the equatorial spread F, presented at PRESTO Workshop & School during 29 May - 2 June 2023. [oral by DP]

5. **Kumar, S.**, Pallamraju, D., Suryawanshi, P., & Seemala, G. K. (2022). Latitudinal Variability in OI 630.0 nm Dayglow Emissions due to Equatorial Electrodynamics and Meridional Winds over Low Latitudes, presented at AGU fall meeting 2022 held in Chicago during 12-16 December 2022. [oral by SK]

6. Pallamraju, D., Mandal, S., Saha, S., **Kumar, S.**, & Pant, T.K. (2022). New insights on the precursors to the onset of equatorial plasma irregularity generation, presented at URSI-RCRS hosted by IIT Indore during 1-4 December 2022. [oral by DP]

7. **Kumar, S.**, Mandal, S., & Pallamraju, D. (2022). A New Approach to Obtain the Daytime Gravity Wave Characteristics in Three-Dimensions, presented at ISEA-16 held at Kyoto University, Japan during 12-16 September 2022. [poster by SK]

8. **Kumar, S.**, Pallamraju, D., Suryawanshi, P., & Seemala, G. K. (2022). Variation in OI 630.0 nm Dayglow Emission at Different latitudes due to Equatorial Electrodynamics and Meridional Winds Over Low Latitudes, presented at ISEA-16 hosted by Kyoto University, Japan during 12-16 September 2022. [oral by SK]

9. Pallamraju, D., **Kumar, S.**, & Suryawanshi, P. (2022). Recent Results Obtained on the Equatorial Dynamical Processes Using OI 630.0 nm Dayglow Emission Variability and Key Insights Obtained on the Production Mechanisms, presented at AOGS during 1-5 August 2022. [oral by DP]

10. Pallamraju, D., **Kumar, S.**, & Mandal, S. (2022). New results on the low- latitudinal gravity wave behavior obtained through innovative optical and radio techniques, presented at 44th COSPAR Scientific Assembly 2022 held in Athens, Greece during 16-24 July 2022. [oral by DP]

11. Pallamraju, D., Saha, S., **Kumar, S.** (2022). Variations in OI 630.0 nm dayglow and nightglow emissions over low- / equatorial latitudes and their dependence on neutral winds and equatorial electric fields, presented at 44th COSPAR Scientific Assembly 2022 held in Athens, Greece during 16-24 July 2022. [oral by DP]

12. **Kumar, S.**, Pallamraju, D., Suryawanshi, P., Vijayalakshmi, T., & Seemala, G. K. (2022). Effect of equatorial electrodynamic processes and meridional winds on the OI 630.0 nm dayglow emission variability over low latitudes, presented at the 15th Solar Terrestrial Symposium (STP-15) hosted by the Indian Institute of Geomagnetism, Navi Mumbai, India during 21 – 25 February 2022. [oral by SK]

13. **Kumar, S.**, Pallamraju, D., Suryawanshi, P., Vijayalakshmi, T., & Seemala, G. K. (2022). Variation in OI 630 nm dayglow emission due to the equatorial electrodynamics and meridional winds, presented at the 21st National Space Science Symposium (NSSS) hosted by IISER, Kolkata, India during 31 Jan – 4 Feb 2022. [poster by SK]

14. **Kumar, S.**, Mandal, S., & Pallamraju, D. (2022). 3-D characterization of daytime gravity waves obtained using optical and radio measurements, presented at the 21st National Space Science Symposium (NSSS) hosted by IISER, Kolkata, India during 31 Jan – 4 Feb 2022. [oral by SK]

15. Pallamraju, D., **Kumar, S.**, Suryawanshi, P., Viajayalakshmi, T., & Seemala, G.K. (2021). New results on the latitudinal variations in equatorial phenomena over Indian longitudes as obtained using night and daytime optical airglow emissions, presented at AOGS during 1-6 August 2021. [oral by SK]

16. **Kumar, S.,** & Pallamraju, D. (2021). Investigations of oxygen dayglow emission variability over low latitudes under the influence of equatorial electrodynamic processes, presented at CEDAR workshop held during 20-25 June 2021. [poster by SK]

Recognition

SCOSTEP Visiting Scholar at Leibniz Institute of Atmospheric Physics, Germany from 1 Sept - 1 Dec 2022.

Publications attached with the thesis

1. **Kumar, S.**, Pallamraju, D., Suryawanshi, P., Vijayalakshmi, T., & Seemala, G. K. (2022). On the latitudinal variation in OI 630.0 nm dayglow emissions in response to the equatorial electrodynamic processes and neutral winds. Advances in Space Research, 69(2), 926-938. https://doi.org/10.1016/j.asr.2021.10.034.

2. **Kumar, S.**, Mandal, S., & Pallamraju, D. (2023). Characterization of gravity waves in three dimensions in the daytime thermosphere using combined optical and radio measurements and estimation of horizontal neutral winds. Journal of Geophysical Research: Space Physics, e2022JA030954. https://doi.org/10.1029/2022JA030954

3. **Kumar, S.**, Siddiqui, T.A., Stolle, C., Pedatella, N.M., & Pallamraju, D. Impact of strong and weak stratospheric polar vortices on geomagnetic semidiurnal solar and lunar tides. Earth Planets Space 75, 52 (2023). https://doi.org/10.1186/s40623-023-01810-x

Available online at www.sciencedirect.com

ScienceDirect

Advances in Space Research 69 (2022) 926–938

ADVANCES IN SPACE RESEARCH
(a COSPAR publication)

www.elsevier.com/locate/asr

On the latitudinal variation in OI 630.0 nm dayglow emissions in response to the equatorial electrodynamic processes and neutral winds

Sunil Kumar [a,b], Duggirala Pallamraju [a,*], Pradip Suryawanshi [a], Tatiparti Vijayalakshmi [c]
Gopi K. Seemala [d]

[a] *Space and Atmospheric Sciences Division, Physical Research Laboratory, Navrangpura, Ahmedabad 380009, India*
[b] *Indian Institute of Technology, Gandhinagar 382355, India*
[c] *Jawaharlal Nehru Technological University, Kukatpally, Hyderabad, India*
[d] *Indian Institute of Geomagnetism, Navi Mumbai, India*

Received 13 April 2021; received in revised form 17 October 2021; accepted 20 October 2021
Available online 27 October 2021

Abstract

Earth's upper atmosphere over low latitudes is influenced by the equatorial electrodynamics. Its influence can also be modulated by the thermospheric winds. The effect of these two forces on the thermospheric neutral behaviour in the daytime can be investigated by measuring the variations in the OI 630.0 nm dayglow emission rates as these serve as effective tracers of the altitude region of their origin. The capability to measure dayglow emissions over a large field-of-view presents a unique opportunity to investigate the upper atmospheric behaviour over large spatial extents. Diurnal measurements of OI 630.0 nm dayglow emission rates have been carried out from two different locations in India using multi-wavelength imaging echelle spectrographs, MISE, which, together cover a spatial range from 5°-18° magnetic latitude. These investigations have been carried out during January-February 2020 (winter season) when solar flux variation was nearly negligible (varied only by 4 solar flux unit from 68–72 solar flux unit). Therefore, latitudinal variations in the daily averaged oxygen dayglow emission intensities have been analyzed to assess their response to the variations in the strength of the equatorial electrodynamics and the meridional winds. The results reveal that these forces show varying effects with the poleward meridional wind contributing to an enhancement in the OI 630.0 nm dayglow emission rates closer to the magnetic equator and a decrement as one moves away from the equator. The equatorial electric field effect, however, continues to be equally effective in the low-latitudes region under consideration.

Keywords: OI 630.0 nm dayglow; Equatorial electrojet; Equatorial ionization anomaly; Neutral Winds; High-resolution spectrograph; Upper atmospheric dynamics

1. Introduction

Upper atmospheric dynamics is governed by many energy inputs, such as, solar radiation, particle precipitation, ionospheric electrodynamics, and lower atmospheric disturbances by gravity waves. Over high-latitudes, the energy inputs are essentially due to solar radiation and particle precipitation. During geomagnetic disturbances, the

* Corresponding author.
E-mail addresses: sunilk@prl.res.in (S. Kumar), raju@prl.res.in (D. Pallamraju), pradip@prl.res.in (P. Suryawanshi), tatiparti@yahoo.com (T. Vijayalakshmi), gopi.seemala@iigm.res.in (G.K. Seemala).

https://doi.org/10.1016/j.asr.2021.10.034

effect of particle precipitation can also equal to that of the Solar EUV radiation over low-latitudes (Mayr et al., 1978). Auroral electrojet current is generated in the aftermath of particle precipitation that gives rise to Joule heating. This heat over high-latitudes sets up pressure gradient forces which generate equatorward neutral winds. Further, travelling atmospheric disturbances (TADs) and travelling ionospheric disturbances (TIDs) are generated that can influence the dynamics of the upper atmosphere over low-latitudes as they propagate equatorward. Over the equatorial regions, during the daytime, several coupled phenomena are generated e.g., the equatorial electrojet (EEJ), the equatorial plasma fountain effect or the equatorial ionization anomaly (EIA), the equatorial temperature and wind anomaly (ETWA), etc. These phenomena in the daytime are caused due to the eastward electric field over the magnetic equatorial region as confirmed by the Jicamarca incoherent scatter radar measurements (Fejer, 1981; Fejer, 1997). In the dynamo region, this primary eastward electric field in combination with the zonal winds give rise to dynamo action resulting in a strong eastward electrojet that is confined to around $\pm 3^{\circ}$ magnetic latitude (MLAT). It has been shown by radar and modelling studies that the EEJ strength is proportional to the zonal electric field (Hysell and Burcham, 2000; Hysell et al., 2002; Anandarao and Raghavarao, 1987) and so, the pre-noon integrated (7–12 IST) EEJ strength has been used as a proxy to the zonal electric field. Further, as the zonal electric field gives rise to the vertical drift, several studies using ground-based magnetic measurements, modelling and satellite-based ion-drift measurements showed that the EEJ strength is proportional to the magnitudes of the vertical drifts (Anderson et al., 2004; Kumar et al., 2016).

The EIA is a resultant of two processes, namely, the equatorial vertical drift that is caused by the primary eastward electric field and the plasma diffusion along the geomagnetic field lines. The altitude to which plasma can reach by the vertical drift over the equator and the latitudes until which they can extend up to vary with solar activity, seasons, day-to-day, and the time of the day. The strength of the EIA (Rush and Richmond, 1973) has been shown to be directly proportional to the pre-noon integrated strength of the EEJ (Raghavarao et al., 1978). The EIA plays an important role in bringing about latitudinal changes in the electron densities as shown in earlier studies (e.g. Raghavarao et al., 1988; Raju et al., 1996). The strength of the EIA can be modulated by the neutral winds (Anderson, 1973). Occurence of post-sunset enhancements in the OI 630.0 nm nightglow over low-latitudes has been shown recently to be due to the effect of meridional poleward winds (Saha et al., 2021). The inter-hemispheric winds generate asymmetricity in the EIA strength (e.g. Huang et al., 2018; Khadka et al., 2018) and significantly affect the plasma densities in the upper atmosphere. Also, the strength of the EIA and its latitudinal extent is altered by magnitudes of vertical drift (Woodman, 1970; Fejer, 1981), solar activity (Sastri, 1990), and compositional variation brought in during geomagnetic storms (Prölss, 1993). Recently, it was reported that the storm influence over the low-latitudinal region, as seen by compositional changes, can be greater as compared to that of the equatorial electrodynamics during geomagnetic storms (Karan and Pallamraju, 2018).

Investigations on the equatorial upper atmospheric dynamic processes in the daytime carried out using thermospheric dayglow emissions as tracers showed both latitudinal and longitudinal variabilities (e.g., Raju et al., 1996; Sridharan et al., 1999; Chakrabarty et al., 2004; Pallamraju et al., 2010; Karan and Pallamraju, 2017; Karan and Pallamraju, 2018). As the solar flux did not show any significant variation during January-February 2020 (range of variation is only 68–72 solar flux unit (sfu)) and as there were no geomagnetic storms (maximum daily average value of Ap is 15) in this duration, it presents a unique opportunity to investigate the latitudinal extent of equatorial electrodynamical processes and meridional winds. Therefore, in this work, investigations have been carried out using the OI 630.0 dayglow data from two large field-of-view (FOV) imaging spectrographs from Indian longitudes, which collectively cover a large latitudinal extent from 5°-18° MLAT, to assess the relative effect of the equatorial electrodynamics and meridional winds on the upper atmospheric variability as a function of latitude.

2. Data sets

For the results presented in this work, neutral OI 630.0 nm dayglow emissions are used along with other independent data sets, such as, the EEJ current strengths, meridional wind, and *hmF*2 during January-February 2020. These data sets are explained below.

2.1. Dayglow

In the presence of solar radiation, atoms and molecules in the upper atmosphere emit photons due to different photochemical reactions which are referred to as the dayglow. These dayglow emission rates vary with the variations in the densities of the reactants. The reactants, in turn, vary in response to the atmospheric dynamics. Therefore, dayglow emission variability serves as a tracer to study the dynamics of the upper atmosphere and ionosphere-thermosphere coupling that exist at the altitudes from where these emissions emanate. In the presence of a large solar background continuum, observations of dayglow emissions is a challenging task. However, some approaches have been reported in the literature which have succeeded in providing information of the dayglow emissions emanate at different wavelengths (e.g., Narayanan et al., 1989; Sridharan et al., 1993; Sridharan et al., 1998; Pallamraju et al., 2002; Pallamraju et al., 2013; Chakrabarti et al., 2012). In this work, a multi-wavelength imaging spectrograph using echelle grating (MISE) is used to obtain the dayglow emissions at

630.0 nm wavelength over a wide range of latitudes as its FOV is around 140°. Two MISEs are commissioned in the Indian longitudes at: (i) Hyderabad (HYD, 17.4° N, 78.5° E; 9° N MLAT), and (ii) Ahmedabad (AHD, 23° N, 72.6° E; 15° N MLAT). In this study, the OI 630.0 nm emissions which originate from altitudes centered around 230 km are presented. As these slit spectrographs are oriented along the meridional direction, in combination, these yield information over a large spatial extent from 5°-18° MLAT.

MISE provides a sky spectrum which can be different from the solar spectrum in three ways, namely, absorption, emission, and scattering. To obtain dayglow emissions, the high spectral resolution sky spectrum for a given time is matched with the solar spectrum. At the spectral region around OI 630.0 nm (± 0.05 nm), there are no absorptions due to the Earth's atmosphere and, therefore, the scaled sky spectrum when subtracted from the solar spectrum yields information corresponding to the OI 630.0 nm emissions in the upper atmosphere and scattering. In an earlier study (Pallamraju et al., 2000), it has been demonstrated that the scattering contribution in a Fraunhofer absorption line is dependent on its equivalent width. Therefore, by appropriately taking such contribution into account, the dayglow emission magnitudes are obtained. This process is described in detail in our earlier studies (e.g., Pallamraju et al., 2002; Pallamraju et al., 2013) and so, is not repeated here. The spectral images are added for a 5 min duration to increase the signal to noise ratio (which varies from 5–28 during the course of the day), and this process is repeated at a cadence of 5 min to obtain the diurnal behaviour of dayglow emission rates.

The Fig. 1 shows the schematic of the observational locations, wherein the x-axis and the y-axis depict MLAT and the altitude. Red coloured region centered at 230 km corresponds to the OI 630.0 nm dayglow emission with the emission width of 100 km. Black dotted lines represent the magnetic field lines which are plotted using the dipole magnetic field equation. Using the combined FOV of MISE operations from HYD and AHD, one can study the dynamics of the ionosphere-thermosphere over spatial regions from 5° to 18° MLAT. For the current study, the FOV of each of the spectrographs is partitioned into 5 independent segments as shown in black straight lines, and so a total of 10 viewing directions for OI 630.0 nm dayglow emission exist.

2.2. EEJ

The EEJ refers to an equatorial current which is generated by the dynamo action in the E region of the ionosphere over the magnetic equator. The EEJ strength over Indian longitudes are obtained by the ground-based magnetometric measurements of the horizontal component of the magnetic field from an equatorial location, Tirunelveli (TIR, 8.7° N, 77.8° E; 0.43° N MLAT), and an off-equatorial location, Alibag (ABG, 18.6° N, 72.9° E; 10.65° N MLAT) as shown in Fig. 1. The off-equatorial magnetic field strengths are not expected to be affected by the induced EEJ currents as the EEJ is confined to within ±3° MLAT. The respective night-time values of the horizontal magnetic field strengths are subtracted from each of the data to remove the local geomagnetic contribution. Off-equatorial values are subtracted from equatorial data to remove the effect of magnetospheric currents to get the resultant values which are due to the EEJ currents (Chandra and Rastogi, 1974).

2.3. Neutral Winds

The Ionospheric Connection Explorer (ICON) satellite is orbiting at 575 km altitude at an inclination of 27°

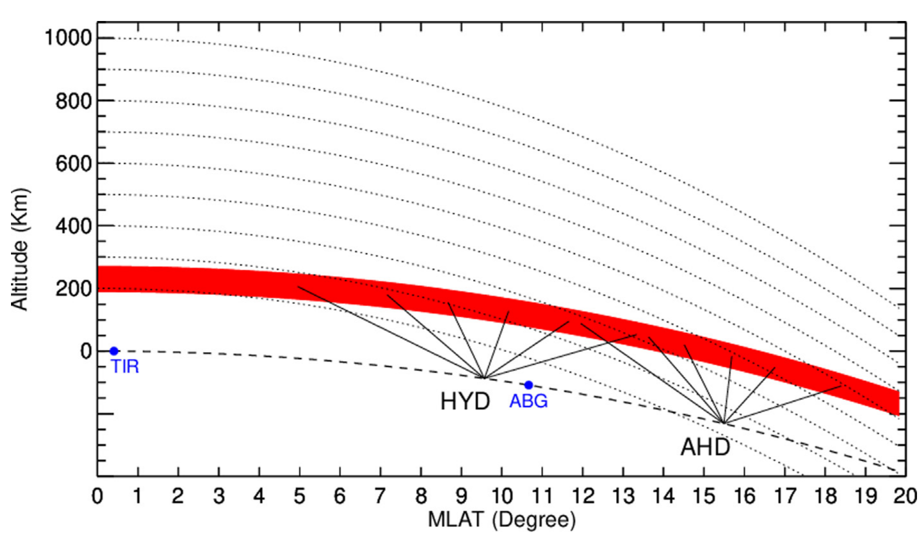

Fig. 1. Schematic showing the regions of OI 630.0 nm dayglow emissions over different MLAT in red colour. The field-of-view of MISE is shown by black solid lines from HYD and AHD. The geomagnetic field line s are represented by dotted black line. TIR and ABG indicate the locations of geomagnetic measurements.

(Immel et al., 2018). The Michelson Interferometer for Global High-Resolution Thermospheric Imaging (MIGHTI) on-board ICON (Englert et al., 2017) is used to estimate neutral winds from 90 km to 300 km from the measurements of Doppler shifts in naturally occurring atomic oxygen airglow emissions at 557.7 and 630.0 nm wavelengths (Harding et al., 2017). In the present study, the MIGHTI cardinal winds obtained by OI 630.0 nm emissions (level 2.2, version 4) are used. The quality factor of data which are used is 1, wherein the uncertainty in the wind varies from 3 -10 ms^{-1}.

ICON satellite has 15 passes for a particular longitudinal location in a day in which it cover different latitudes. The Fig. 2 shows data from 7 passes on a sample day 29 Jan 2020. The black dots in panels a and b of Fig. 2 represent the locations of MIGHTI observations which vary from 12°S to 42°N geographic latitudes for the longitude range of 73°±5°. The corresponding MLAT are also shown on the right side y-axis. Neutral wind shows slight variation in magnitudes with latitude. Therefore, to obtain information on the diurnal variation of meridional winds corresponding to the view directions as seen by the ground-based optical spectrographs, the measured winds by MIGHTI are used along with the HWM-14 (Drob et al., 2015) winds. Figure 2a depicts the meridional wind variation (dotted black line) observed by MIGHTI along the track (black dots) corresponding to the longitude of AHD (73°±5°). HWM -14 diurnal variations of meridional wind corresponding to the locations of MIGHTI observation and the latitude of AHD are shown in magenta and blue coloured lines in Fig. 2b. Therefore, the difference between MIGHTI winds and the HWM -14 winds corresponding to the latitude of MIGHTI observation are applied to the HWM -14 meridional winds at AHD. In this way, the corrected HWM-14 meridional winds over AHD are obtained for all the times of the existence of MIGHTI wind data. It is assumed that the difference between meridional winds at these two latitudes follow the variations as described by the HWM -14 which helps in adjusting the observed meridional winds of MIGHTI at a given latitude to those of our latitude of interest. The diurnal variation in meridional winds over AHD as obtained by this process is shown in Fig. 2b (dashed purple line). Similarly, we have obtained the meridional winds corresponding to the latitude and longitude of all 10 view directions. In the present work, 200 to 260 km averaged meridional wind is used.

2.4. hmF2 Data

The *hmF*2 data are obtained from the ICON EUV spectrograph on-board the ICON satellite. The ICON EUV spectrograph (Sirk et al., 2017) measures the OII 83.4 nm and 61.7 nm EUV emissions which are used to obtain the altitudinal profile of O^+ density. The OII 83.4 nm emissions originate from the lower thermosphere by photoionization of atomic oxygen by solar EUV photons or photoelectrons but pass off by resonant scattering with O^+. Therefore, the OII 83.4 nm emissions reflect the O^+ density which is the dominant species at higher thermospheric altitudes. To remove the contribution from lower thermosphere to avoid ambiguity, the OII 61.7 nm emission is used as it also originates from lower altitudes of thermosphere by similar a mechanism to the production of the OII 83.4 nm emission but the ionosphere is transparent to 61.6 nm photons. The altitudinal coverage of O^+ density is 150–450 km which is used to obtain the *hmF*2 values (Stephan et al., 2017) by making use of International Reference Ionosphere-2007 (Bilitza and Reinisch, 2008). In this work, the *hmF*2 data has been used when the quality flag is 0 (no issue with data) and 1 (moderate issues and can be used with caution). The median deviation of the *hmF*2 in this duration is around 8.5 km.

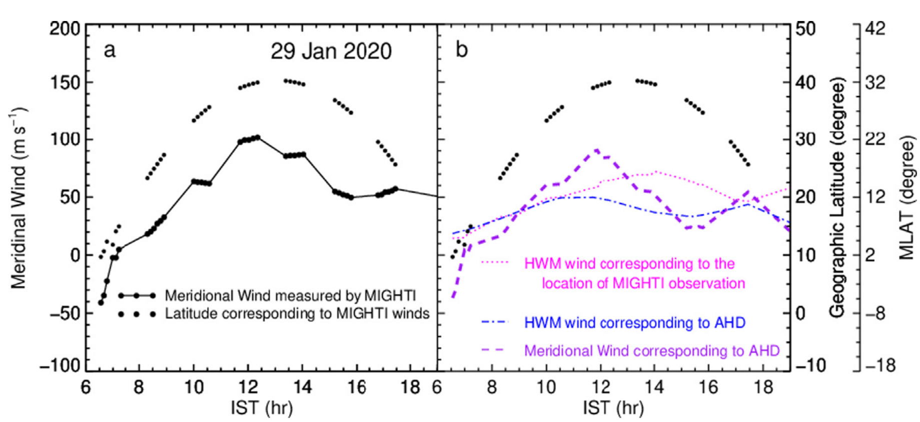

Fig. 2. (a) A sample plot of the meridional wind variation (solid black line) observed from MIGHTI along with the latitudes (black dots) corresponding to the locations of MIGHTI observation. (b) The HWM -14 meridional wind (dotted magenta coloured line) at the locations of MIGHTI observation, HWM -14 meridional wind (blue coloured dot-dashed line) at latitude of AHD are shown. The diurnal variation of the corrected HWM-14 meridional winds (purple coloured dashed line) for the location of AHD as obtained after appropriately applying the observed MIGHTI winds. The right side y-axis show the geographic latitude and MLAT.

3. Observation and Results

Dayglow emission rates vary with solar flux, solar zenith angle (SZA), and contribution from transport. The main production mechanisms for the OI 630.0 nm dayglow emissions are photo-electron impact excitation of ambient atomic oxygen (O), photodissociation of molecular oxygen (O_2), and dissociative recombination of molecular oxygen ions (O_2^+) (Solomon and Abreu, 1989). The first two mechanisms depend on the magnitudes of the solar flux and the SZA, but the third, namely the dissociative recombination is also affected by transportation of plasma caused due to electrodynamics, waves, and neutral winds. Contribution of all these mechanisms are altitude dependent with the dissociative recombination mechanism being at the highest altitude of $\sim$ 250 km among them (Solomon and Abreu, 1989). It has been shown in earlier studies that the dayglow emissions over low-latitudes vary due to the electrodynamics that transports plasma from the equator (e.g., Raju et al., 1996; Chakrabarty et al., 2002; Pallamraju et al., 2010; Karan et al., 2016). Further, the meridional wind plays an important role in the modulation of the EIA strength and generates an asymmetric distribution of the plasma density in both hemispheres dependent on the seasons (Saha et al., 2021). Generally, wind flows from the summer hemisphere to the winter hemisphere on quiet days. In the winter hemisphere, the poleward meridional wind brings the plasma density to lower altitudes due to ion-neutral collision, consequently, the *hmF*2 (peak height of F-layer) is reduced. Contrasting features are seen in the summer hemisphere (Rishbeth, 1977).

Firstly, to investigate the day-to-day effect of the equatorial electrodynamics and meridional winds in the OI 630.0 nm dayglow emission variations in the months of January and February 2020, daily averaged (9–16 IST) OI 630.0 nm dayglow emission intensity over the zenith of HYD and AHD, pre-noon (7–12 IST) integrated EEJ strengths, and daily averaged (9–16 IST) meridional wind are calculated. These are shown in Fig. 3a for HYD and Fig. 3b for AHD as a function of the day of the year (DOY) in red, blue, and, purple coloured lines, respectively. The missing values of the dayglow emission rates around the noon-time are linearly interpolated. The number of clear sky days data available over HYD and AHD are 16 and 32. In the duration of the observation, the solar flux varied slightly from 68 to 72 sfu. Therefore, it is expected that the variation in the dayglow emissions due to variation in the solar flux will be small in this duration. So, the transport effect in terms of equatorial electrodynamics, neutral winds, and waves are the main causes for the day-to-day variations observed in the OI 630.0 nm dayglow emissions. All the days are geomagnetically quiet (maximum daily average value of Ap is 15) and, therefore, modulations in the dynamics from high-latitudes in terms of compositional changes are not expected on the OI 630.0 nm dayglow variations over low-latitudes (e.g., Pallamraju et al., 2004; Karan and Pallamraju, 2018).

It can be noted that the daily averaged dayglow emission intensities vary with the strength of the equatorial electrodynamics. Pre-noon integrated EEJ strength is taken as a proxy of the equatorial electric fields as it has been shown to be proportional with the strength of the equatorial ion-

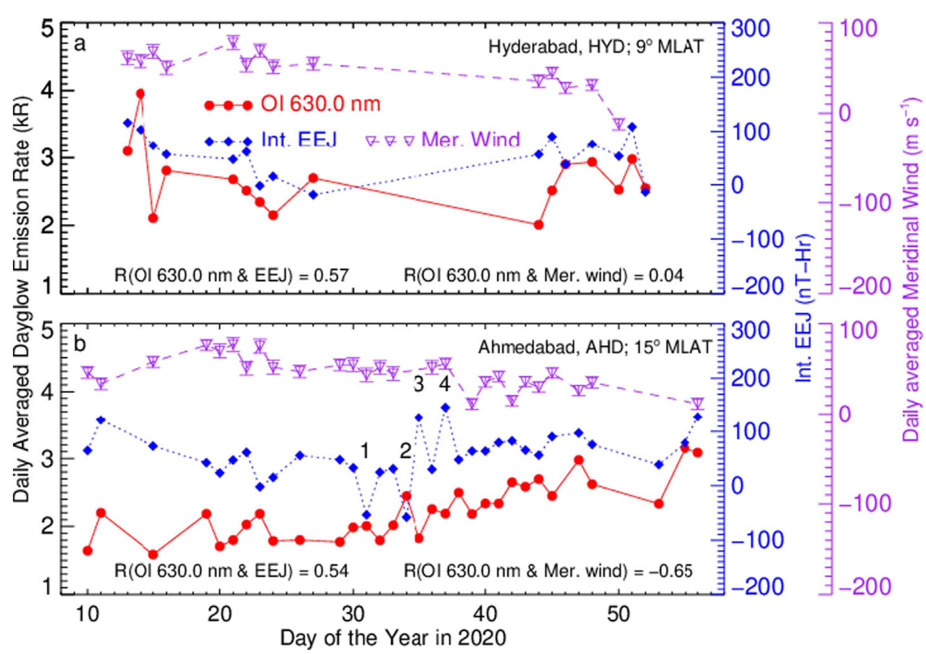

Fig. 3. The daily averaged OI 630.0 nm dayglow emissions (solid red line), pre-noon integrated EEJ (dotted blue line) and daily averaged meridional wind (dashed purple coloured line) as obtained for the corresponding latitude (HYD/AHD) are shown. Panel a and Panel b correspond to the zenith of HYD and AHD. Each panel also shows the R values between these parameters.

ization anomaly (e.g. Raghavarao et al., 1978; Rush and Richmond, 1973). In the following text of this work, the phrase EEJ strength is used to refer to the pre-noon integrated EEJ strength. The EEJ strength shows a moderate correlation (0.57) with the dayglow emissions over zenith location of HYD as shown in Fig. 3. In the estimation of this correlation, the counter electrojet days are not considered. Therefore, it is clear that there are other factors that affect the observed variability in the daily averaged dayglow emission intensities. The value of correlation between dayglow emission intensities and meridional wind for HYD is 0 but for AHD it is found to be −0.65. The OI 630.0 nm daily averaged dayglow emission intensities over AHD (panel b) are also found to be influenced by the equatorial electrodynamics to a similar extent as over HYD (R value 0.53). There are two days wherein counter electrojet occurred (small values) and two days with large values between DOY 30–40 as shown in Fig. 3 (marked by numbers 1 to 4) but the daily averaged dayglow emission intensities do not show much variation on these days. These days are not considered in the linear regression analysis and are dealt with separately below. From these R values, it can be inferred that over HYD, the effect of the equatorial electrodynamics is significant than that of the meridional wind. But, for AHD, meridional wind plays a more important role in the observed variability of the daily averaged dayglow emission intensities than the equatorial electrodynamics.

So far, the variations in the dayglow emission intensities over two zenith directions (HYD and AHD) have been presented which showed varying impact of the equatorial electrodynamics and meridional wind on the variation of the upper atmospheric behaviour over two low-latitude locations. To investigate this effect on different days, a comparison is made for neighbouring days but with differing electrodynamics and neutral dynamic conditions: Case (I) when magnitude of meridional winds is similar, but the EEJ strengths are different; Case (II) EEJ strength is similar, but meridional wind magnitudes are different; Case (III) EEJ strength and meridional wind magnitude are larger compared to the other day; and Case (IV) days when counter electrojet and strong EEJ occurred (number 1 and 4). These different cases are shown in Figs. 4–7, respectively, which yield a greater understanding of the relative behaviour of these two parameters on the observed OI 630.0 nm dayglow emission variability.

Case (I): As shown in Fig. 4, panels a and d show the diurnal variation of the EEJ where pre-noon integrated EEJ values are depicted in nT-hr for 22 & 24 Jan 2020. In panels b and e, variations in diurnal meridional wind magnitudes are shown where daily averaged meridional wind values (in ms^{-1}) are presented. Diurnal dayglow emission rates are presented in panels c and f corresponding to the zenith of the HYD and AHD in red and black coloured lines. The daily averaged dayglow emission intensity (in Rayleigh) are also shown in respective colours. On these days, Ap values (1 & 3) are very small and the magnitudes of meridional wind (47 & 46 ms^{-1}) are similar, however the EEJ strength is quite different (61 & 15 nT-hr). Therefore, it is expected that the contribution from wind and compositional changes will be similar on both days and, mainly, the difference in the dayglow emissions on these days will be due to the equatorial electrodynamics. It can be seen that the values of daily averaged dayglow emission inten-

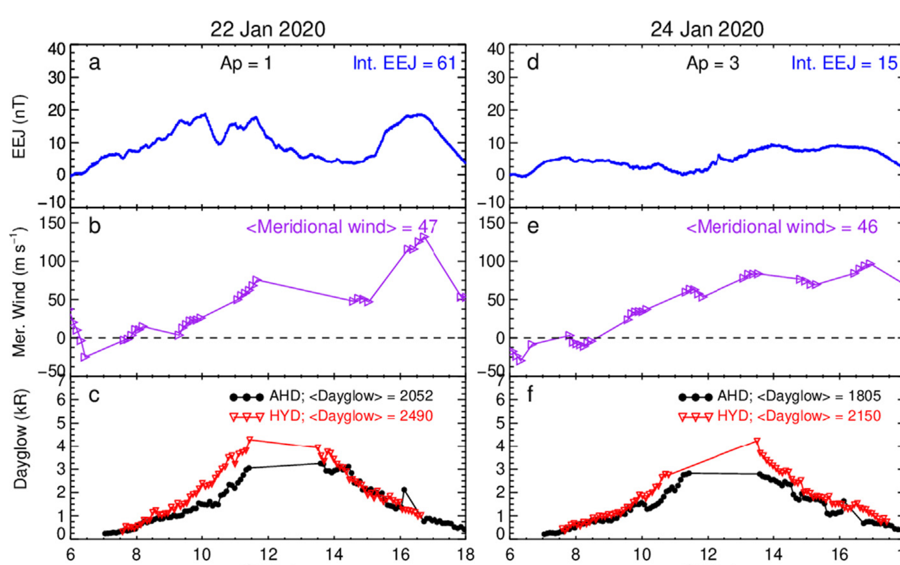

Fig. 4. The diurnal EEJ, meridional wind, and OI 630.0 nm dayglow emission (over zenith at HYD and AHD) for 22 Jan (panel a,b,c) and 24 Jan 2020 (panels d,e,f) corresponding to Case (I), when magnitudes of meridional winds are similar, but pre-noon integrated EEJ strengths are different, are shown. Pre-noon integrated EEJ strengths, averaged meridional wind (<Mer. wind>), and averaged OI 630.0 dayglow emission intensities (<Dayglow>) are also shown in the relevant panels.

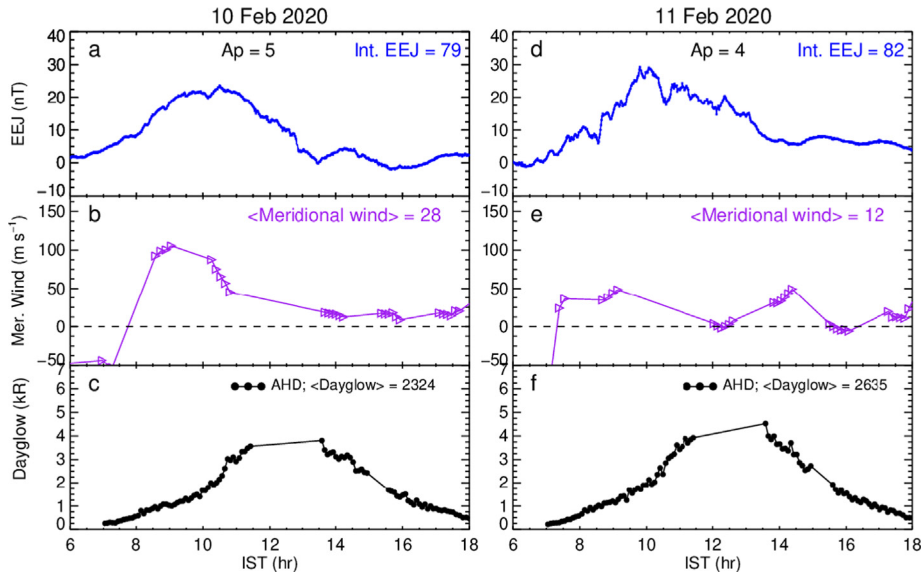

Fig. 5. Similar to Fig. 4 but for 10 and 11 Feb 2020 corresponding to Case (II), when EEJ strengths are similar, but magnitudes of meridional winds are different.

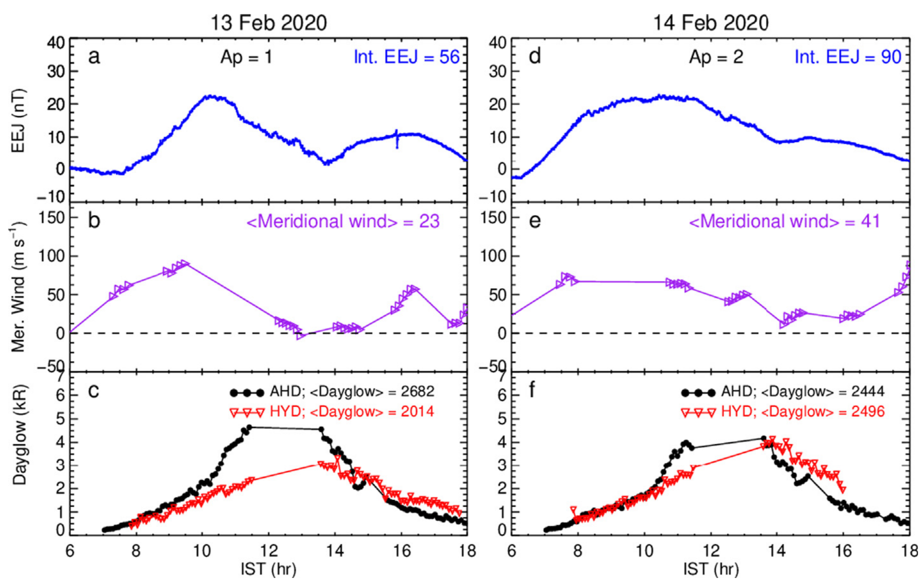

Fig. 6. Similar to Fig. 4 but for 13 and 14 Feb 2020 corresponding to Case (III), when magnitudes of both meridional winds and EEJ strengths are different.

sity over zenith at HYD and AHD are larger on 22 Jan (as compared to 24 Jan), essentially due to the effect of strong equatorial electrodynamics.

Case (II): Fig. 5 shows the data corresponding to 10 and 11 Feb 2020 where all panels are arranged in a manner similar to that described in the Fig. 4. The Ap values (5 & 4) are similar. Over these two days, the equatorial electrodynamics effect is similar (EEJ strengths are 79 and 82 nT-hr) but the poleward meridional winds were larger on the 10th (28 ms^{-1}) as compared to 11th (12 ms^{-1}). Interestingly, the daily averaged dayglow emission intensity over AHD are smaller on 10th Feb when meridional wind magnitude is larger. On these two days, the dayglow data from HYD is not available.

Case (III): Two other sample days are shown when one day (13 Feb) the EEJ strength is 56 nT-hr and meridional wind is 23 ms^{-1}, and on 14th Feb EEJ strength was 90 nT-hr and meridional wind magnitude was 41 ms^{-1} (Fig. 6). Ap values on these two days were 1 and 2. Interestingly, although the dayglow intensity over HYD responds to the increase in the equatorial electrodynamic strength on 14th Feb, the averaged dayglow emission intensity over AHD is larger on the 13th even though the electrodynamic strength was smaller by around 34 nT-hr. This enhancement in emissions over AHD on the 13th Feb can most likely be attributed to smaller poleward meridional wind on this day. This indicates that the dayglow emissions over AHD are more critically dependent

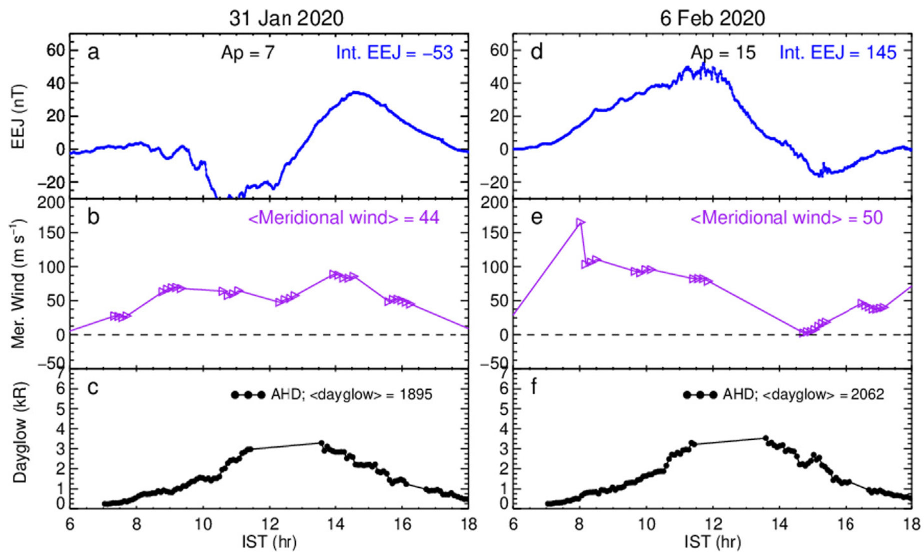

Fig. 7. Similar to Fig. 4 but for 31 Jan 2020 and 6 Feb 2020 corresponding to Case (IV), in which days with counter electrojet and strong EEJ strengths (number 1 and 4 in Fig. 3.b) are compared.

on the meridional winds. Thus, it is clear that the effect of the electrodynamics on the OI 630.0 dayglow emissions dominates that of the meridional winds at HYD but at AHD, the influence of meridional wind is stronger.

Case (IV): Out of the four days of data over AHD wherein two days were counter electrojet and two days with large EEJ strengths (marked as 1, 2, 3, 4 in panel b of Fig. 3) on two days 31 Jan & 6 Feb (corresponding to 1 & 4 in the Fig. 3) wind data are available (Fig. 7), so, these days are considered for discussion. On these days, the Ap values were 7 and 15. On 31 Jan, EEJ strength (-53 nT-hr) is much weaker than on the 6 Feb (145 nT-hr). In spite of the comparatively large equatorial electrodynamic effect on 6 Feb, dayglow emission intensity over AHD shows only marginal enhancement compared to that on 31 Jan, presumably due to larger meridional wind magnitude on the 6th Feb. OI 630.0 nm dayglow data are not available for these days from HYD, but based on the discussion so far and data shown in Fig. 4–6, it is expected that if the dayglow data over HYD were present on 6th Feb, it would have shown large magnitudes in emissions as compared to these on 31 Jan.

As discussed in detail above and shown in figures 3–7, It is clear that the effects of equatorial electrodynamics and meridional winds are different at different latitudes. Hence, as described above, we have organized the total available optical data into 10 different spatial regions spanning 5° - 18° MLAT. Column integrated dayglow emission intensities measured in each of the 10 directions are considered separately. The contribution to the dayglow emissions due to the ionization brought in from the magnetic equatorial region will be different at different view directions at any given time. To gain a comprehensive understanding of the systemic nature of these variations as a function of latitude, equatorial electrodynamic strength is compared with the daily averaged OI 630.0 nm dayglow emission intensity at each of the latitudes (viewing directions). As shown in Fig. 8a, the OI 630.0 nm daily averaged dayglow emission intensity obtained along each of the view directions is plotted corresponding to the integrated EEJ strength on that day and linear regression analyses have been obtained. Each of the plots correspond to different MLAT which progressively increase as we move from top to bottom. Similarly, the linear regression analyses have been carried out between OI 630.0 nm dayglow emission intensities and meridional winds for each of the view directions and are shown in Fig. 8b.

It is seen that the effect of equatorial electrodynamics on the OI 630.0 nm dayglow emission is nearly similar in all latitudes as shown in Fig. 8a, however, the effects of meridional winds on the OI dayglow emission rates gradually change from the favourable to adverse as one moves away from dip equator (Fig. 8b). These correlation values are summarized in Fig. 9. Here, the x-axis represents the MLAT and y-axis represents the R values, where, blue and purple coloured lines show the R values between dayglow emission intensities and EEJ strength, and dayglow emission intensities and meridional wind at different MLAT. It can be noted that the equatorial electric field effect on the OI 630.0 nm dayglow emissions over large MLAT is nearly similar with correlation coefficient varying from 0.62 to 0.4 (except 17.5° MLAT where it is 0.3).

The R values between dayglow emission intensities and meridional winds vary from the 0.42 to −0.67 (Fig. 9) in the given latitudinal range. This means that closer to the dip equator the poleward meridional wind assists the OI 630.0 nm dayglow emission rates, while at latitudes further away, they contributes to a reduction in the OI 630.0 nm emission rates. There are a few excursions in the correlation coefficients at 9°, 14°, and 17.5° MLAT. As the main

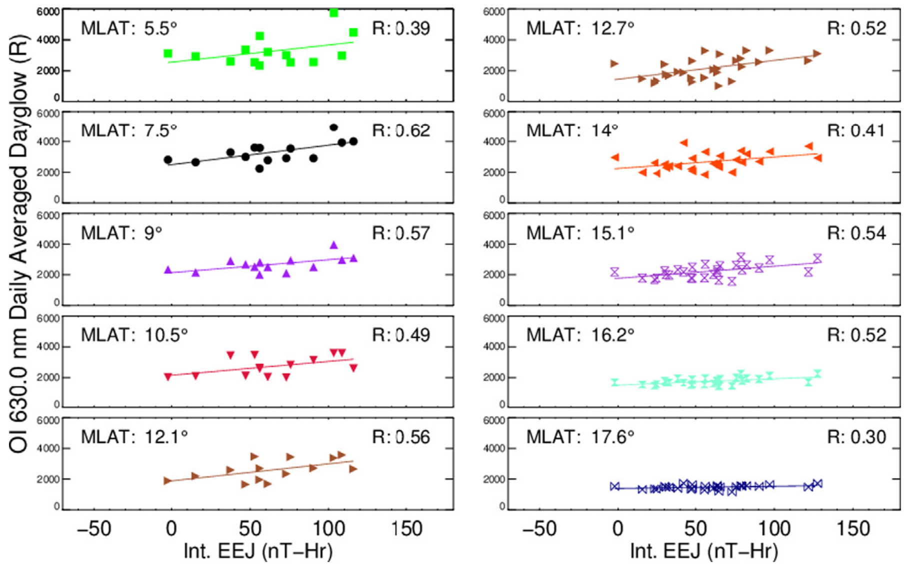

Fig. 8a. OI 630.0 nm daily averaged dayglow emission intensities with pre-noon integrated EEJ strengths along with linear fits corresponding to different view directions (MLAT).

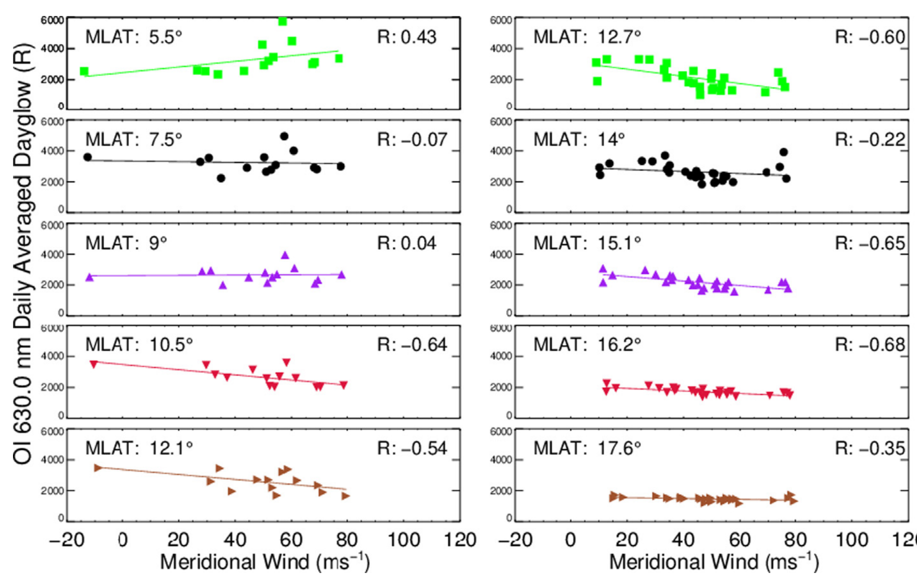

Fig. 8b. OI 630.0 nm daily averaged dayglow emission intensities as a function of averaged meridional winds along with linear fits corresponding to different view directions (MLAT).

objective here is to study the systemic nature of variation in the OI 630.0 nm dayglow emissions due to different forcing factors, a linear fit is drawn to these variations in the R values for the correlation of meridional winds with the OI 630.0 nm dayglow emission intensities. From this fitted line it can be noted that near the equator, the meridional wind assists in enhancing the dayglow emission rates, but, as one moves further away from the dip equator, meridional wind contributes to the reduction in the dayglow emission rates.

4. Discussion

Earlier studies have shown that solar flux plays an important role in the magnitude of dayglow emissions (e.g., Solomon and Abreu, 1989; Pallamraju et al., 2010; Pallamraju et al., 2020; Shepherd and Cho, 2021). The variation in solar flux in this observational duration has been insignificant (only a small variation from 68–72 sfu) and so it is expected that it does not contribute significantly to the variation in the dayglow emissions that are observed from one day to another. It is known that the electron density depends on *in situ* production by solar EUV flux and its transport by fountain effect over low-latitudes. The electron density can also be modulated by the neutral winds. It is also seen that magnitudes of electron densities play an important role in the OI 630.0 nm dayglow emission rates. The dependence of OI 630.0 nm dayglow emissions on the equatorial electrodynamics over HYD with the strength of

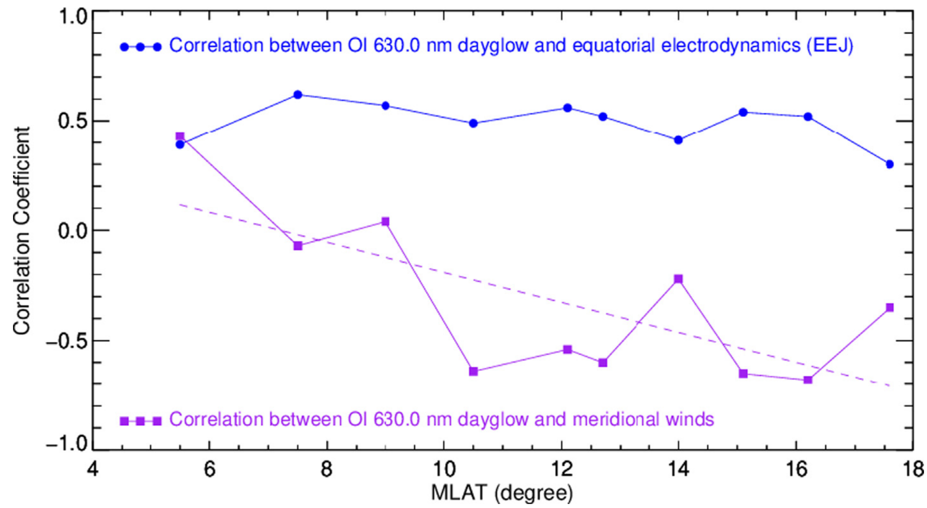

Fig. 9. Correlation coefficient values as in Fig. 8a and 8b are shown along with MLAT. The linear fit between the correlation coefficients of the OI 630.0 nm averaged dayglow emission intensities with meridional wind and MLAT is shown in dashed purple colour.

the EEJ is consistent with our earlier findings as well (Karan et al., 2016). This was later shown to be useful in estimating the daily strength of the equatorial vertical drift (Karan and Pallamraju, 2020).

In this work, the relative contributions of the equatorial electrodynamics and meridional wind as a function of MLAT (in the range of 5°-18°) on the OI 630.0 nm dayglow emissions are investigated. For doing so, OI 630.0 nm dayglow data from two locations HYD & AHD are considered. These two locations are separated in longitude by around 6°. It has been shown in earlier studies that longitudinal differences can exist at such distances (Karan and Pallamraju, 2017). However, such longitudinal differences in equatorial electrodynamic processes are not expected to significantly alter the results arrived at in this study, as, (i) a systemic nature of variation is being investigated here for which the daily averaged values are being considered and hence, any longitudinal variations within a day will be averaged out, and (ii) the correlation coefficient between the equatorial electrodynamic variation and dayglow emission for segments 1–5 and 6–10 shown in Fig. 8a are all similar and the view directions of all these segments are within the crest of the EIA.

To understand the cause of such varying effects of the meridional wind on the dayglow emissions, the production mechanism and ionospheric state as a function of latitude is looked into. It is known that production due to dissociative recombination in the OI 630.0 nm dayglow emission peaks at an altitude around 250 km (Solomon and Abreu, 1989). Fig. 10 shows the *hmF*2 in the daytime as a function of latitude as obtained by ICON EUV spectrograph on-board ICON for the days of the dayglow data considered in this study. It is noted that the *hmF*2 decreases as one moves away from the dip equator. The quality flag of the *hmF*2 data is 1 (which can be used with caution), nevertheless, this data can be used to understand the systemic nature of ionospheric variations across latitudes. It is known that the equatorial electrodynamics drift contributes to the upliftment of the ionosphere to high altitudes over the dip equator, while, at latitudes away from the dip equator, other effects along with the equatorial electrodynamics get convolved resulting in the observed *hmF*2 values. The effect of poleward meridional wind in the northern hemisphere contributes to a downward motion of the ionospheric F-layer with heights proportional to $U\cos I\sin I$, where U is the meridional wind and I is the dip angle at a given latitude. Consequently, the *hmF*2 decreases. Similarly, for an equatorward wind, the ionospheric layer is lifted upwards. Therefore, contribution by the dissociative recombination mechanism in the OI 630.0 nm dayglow emissions is positive or negative depending on whether the plasma density increases or decreases as it is brought in or taken away by the meridional winds around the peak emission altitude region of dissociative recombination. In the current solar epoch and winter season, from the altitudes of *hmF*2 (Fig. 10), it can be understood that whenever the height of *hmF*2 is greater than the peak emission altitude of dissociative recombination, a poleward wind assists in the enhancement of the dayglow emission rates as plasma is brought into the region of greater production of excited atomic state ($O(^1D)$) via the dissociative recombination mechanism. When *hmF*2 is lower than the peak emission altitude of dissociative recombination, a meridional wind brings the plasma down to altitudes lower than the region where the production by the dissociative recombination is most effective. This feature is clearly reflected in the correlation analysis between the variation in the meridional wind magnitudes and the dayglow emission rates as seen in Fig. 8b, it can be seen in this figure that the positive correlation closer to the dip equator between these parameters systematically changes to negative as one moves away from the dip equator.

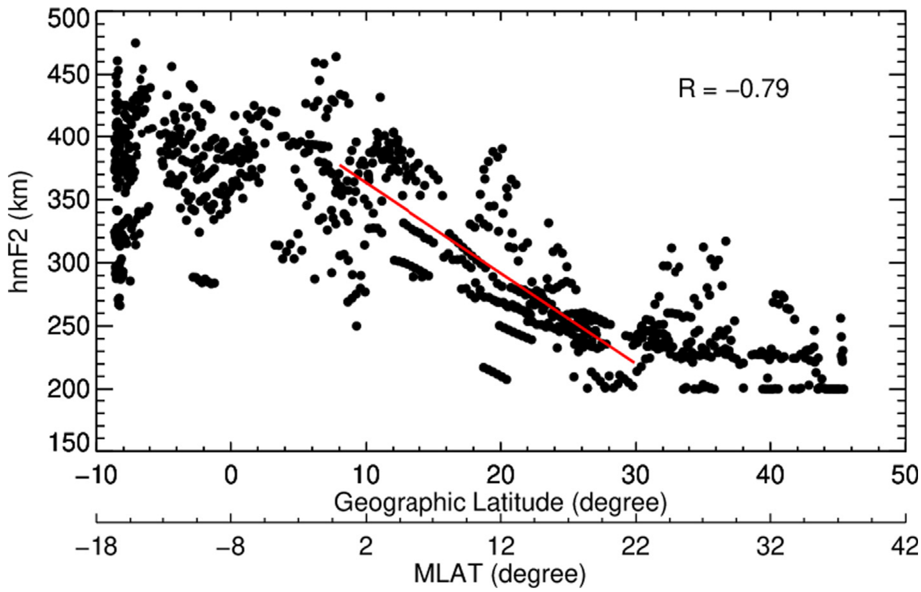

Fig. 10. The *hmF*2 values are shown with geographic and geomagnetic latitude as obtained from ICON EUV spectrograph on-board the ICON satellite. The linear fit between the *hmF*2 and MLAT for the northern hemisphere up to 22° MLAT, until which location a significant variation is seen with latitudes, is shown in red solid line. (For interpretation of the references to colour in this figure legend, the reader is referred to the web version of this article.)

Further, from Fig. 4, it is seen that around 75% decrease in the EEJ strength due to equatorial electrodynamics results in around 14% and 12% decrease in the daily integrated OI dayglow emission rates over HYD and AHD. From Fig. 5, it is seen that about 57% decrease in the meridional winds contributes to a 13% enhancement in the daily averaged dayglow emission intensity over AHD. While competing effects due to enhancements in EEJ strength (by 61%) and meridional wind (by 78%) resulted in a decreased dayglow emission intensity over AHD by $\sim 9\%$ (Fig. 6). However, from the same figure, it can be noted that over HYD it resulted in an enhancement of dayglow emission intensity by 24%. Therefore, it can be surmised that the relative contributions of equatorial electrodynamics and meridional winds to the OI 630.0 nm dayglow emission rates are non-linear and vary as a function of latitude. The linear fit shown in Fig. 9, therefore, can, at best, be described as a zeroth order estimate wherein only one parameter is considered. This result also opens up further possibilities in characterizing the OI 630.0 nm dayglow emissions as a function of equatorial electrodynamics and meridional winds in addition to the known variables.

To the best of our knowledge, the effect of the equatorial electrodynamics and meridional winds on the latitudinal variations in the dayglow emissions is being reported for the first time. Such characterization will not only help in improving our understanding of the ionosphere-thermosphere system but also help in modeling the influence of the equatorial electrodynamics and meridional winds on the low-latitude upper atmosphere.

5. Summary

The variations in the OI 630.0 nm dayglow emission rates which originate from thermospheric altitudes can represent the dynamics of the upper atmosphere at those altitude regions. The dynamics of the upper atmosphere can vary on short scales in latitudes and in longitudes. In the observational duration considered in this study (Jan-Feb 2020), the variation in the solar flux was little, and so it provided an opportunity to investigate the variation in the OI 630.0 nm dayglow emission rates in response to the equatorial electrodynamics and meridional winds. To investigate the latitudinal variation of these effects, linear regression analyses have been carried out for the optical data corresponding to each of the viewing directions with respect to the EEJ and meridional wind and the correlation between them have been obtained. It is shown that for this solar epoch and winter season, the effect of the equatorial electrodynamics in the OI 630.0 nm dayglow emissions shows only a small variation with MLAT, whereas, the effect of the meridional winds has a greater role to play in the OI 630.0 nm dayglow emissions with MLAT. Due to meridional winds, the variation in the OI 630.0 nm dayglow emission intensities over 5°- 18° MLAT were varied from positive ly correlated closer to the dip equator to that of negative as one moves away from the dip equator.

Declaration of Competing Interest

The authors declare that they have no known competing financial interests or personal relationships that could have appeared to influence the work reported in this paper.

Acknowledgements

The authors acknowledge the assistance provided by Mr. Abhilash, and Mr. Sambasivam in the operation of MISE at the Jawaharlal Nehru Technological University in Hyderabad, India. The optical data are maintained by Physical Research Laboratory and can be made available by contacting the corresponding author. Mr. Sunil Kumar thanks Dr. Subir Mandal and Mr. Sovan Saha for discussions with respect to data analysis. The EEJ data are obtained from the Indian Institute of Geomagnetism, Mumbai, India. The neutral winds data are obtained from ICON satellite. ICON is supported by NASA's Explorers Program through contracts NNG12FA45C and NNG12FA42I. ICON data are processed in the ICON Science Data Center at UCB and available at https://icon.ssl.berkeley.edu/Data. The solar flux data are obtained from https://omniweb.gsfc.nasa.gov/form/dx1.html. The authors thank one of the reviewers for providing constructive comments which improved the quality of the result. This work is supported by the Department of Space, Government of India.

References

Anandarao, B., Raghavarao, R., 1987. Structural changes in the currents and fields of the equatorial electrojet due to zonal and meridional winds. Journal of Geophysical Research: Space Physics 92, 2514–2526. https://doi.org/10.1029/JA092iA03p02514.

Anderson, D., 1973. A theoretical study of the ionospheric f region equatorial anomaly-i. theory. Planet. Space Sci. 21, 409–419. https://doi.org/10.1016/0032-0633(73)90040-8.

Anderson, D., Anghel, A., Chau, J., Veliz, O., 2004. Daytime vertical e×b drift velocities inferred from ground-based magnetometer observations at low latitudes. Space Weather 2. https://doi.org/10.1029/2004SW000095.

Bilitza, D., Reinisch, B., 2008. International reference ionosphere 2007: Improvements and new parameters. Adv. Space Res. 42, 599–609. https://doi.org/10.1016/j.asr.2007.07.048.

Chakrabarti, S., Jokiaho, O.-P., Baumgardner, J.L., Cook, T.A., Martel, J., Galand, M., 2012. High-throughput and multislit imaging spectrograph for extended sources. Opt. Eng. 51, 013003. https://doi.org/10.1117/1.OE.51.1.013003.

Chakrabarty, D., Sekar, R., Chandra, H., Narayanan, R., Pathan, B., Subbarao, K., 2002. Characterizations of the diurnal shapes of oi 630.0 nm dayglow intensity variations: inferences. Ann. Geophys. 20, 1851–1855. https://doi.org/10.5194/angeo-20-1851-2002.

Chakrabarty, D., Sekar, R., Narayanan, R., Pant, T.K., Niranjan, K., 2004. Thermospheric gravity wave modes over low and equatorial latitudes during daytime. Journal of Geophysical Research: Space Physics 109. https://doi.org/10.1029/2003JA010169.

Chandra, H., Rastogi, R., 1974. Geomagnetic storm effects on ionospheric drifts and the equatorial es over the magnetic equator. Indian Journal of Radio and Space Physics 3, 332–336, http://nopr.niscair.res.in/handle/123456789/37843.

Drob, D.P., Emmert, J.T., Meriwether, J.W., Makela, J.J., Doornbos, E., Conde, M., Hernandez, G., Noto, J., Zawdie, K.A., McDonald, S.E., et al., 2015. An update to the horizontal wind model (hwm): The quiet time thermosphere. Earth and Space Science 2, 301–319. https://doi.org/10.1002/2014EA000089.

Englert, C.R., Harlander, J.M., Brown, C.M., Marr, K.D., Miller, I.J., Stump, J.E., Hancock, J., Peterson, J.Q., Kumler, J., Morrow, W.H., et al., 2017. Michelson interferometer for global high-resolution thermospheric imaging (mighti): instrument design and calibration. Space science reviews 212, 553–584. https://doi.org/10.1007/s11214-017-0358-4.

Fejer, B., 1997. The electrodynamics of the low-latitude ionosphere: Recent results and future challenges. J. Atmos. Solar Terr. Phys. 59, 1465–1482. https://doi.org/10.1016/S1364-6826(96)00149-6.

Fejer, B.G., 1981. The equatorial ionospheric electric fields. a review. Journal of Atmospheric and terrestrial physics 43, 377–386. https://doi.org/10.1016/0021-9169(81)90101-X.

Harding, B.J., Makela, J.J., Englert, C.R., Marr, K.D., Harlander, J.M., England, S.L., Immel, T.J., 2017. The mighti wind retrieval algorithm: description and verification. Space science reviews 212, 585–600. https://doi.org/10.1007/s11214-017-0359-3.

Huang, H., Lu, X., Liu, L., Wang, W., Li, Q., 2018. Transition of interhemispheric asymmetry of equatorial ionization anomaly during solstices. Journal of Geophysical Research: Space Physics. https://doi.org/10.1029/2018JA026055.

Hysell, D.L., Burcham, J.D., 2000. Ionospheric electric field estimates from radar observations of the equatorial electrojet. Journal of Geophysical Research: Space Physics 105, 2443–2460. https://doi.org/10.1029/1999JA900461.

Hysell, D.L., Chau, J.L., & Fesen, C.G. (2002). Effects of large horizontal winds on the equatorial electrojet. Journal of Geophysical Research: Space Physics, 107, SIA 27–1–SIA 27–12. doi: 10.1029/2001JA000217.

Immel, T.J., England, S., Mende, S., Heelis, R., Englert, C., Edelstein, J., Frey, H., Korpela, E., Taylor, E., Craig, W., et al., 2018. The ionospheric connection explorer mission: mission goals and design. Space Sci. Rev. 214, 1–36. https://doi.org/10.1007/s11214-017-0449-2.

Karan, D.K., Pallamraju, D., 2017. Small-scale longitudinal variations in the daytime equatorial thermospheric wave dynamics as inferred from oxygen dayglow emissions. Journal of Geophysical Research: Space Physics 122, 6528–6542. https://doi.org/10.1002/2017JA023891.

Karan, D.K., Pallamraju, D., 2018. Effect of geomagnetic storms on the daytime low-latitude thermospheric wave dynamics. J. Atmos. Solar Terr. Phys. 170, 35–47. https://doi.org/10.1016/j.jastp.2018.02.003.

Karan, D.K., Pallamraju, D., 2020. On estimation of daytime equatorial vertical (e×b) plasma drifts using optical neutral dayglow emission measurements. Journal of Geophysical Research: Space Physics 125. https://doi.org/10.1029/2019JA026775, e2019JA026775.

Karan, D.K., Pallamraju, D., Phadke, K.A., Vijayalakshmi, T., Pant, T. K., Mukherjee, S., 2016. Electrodynamic influence on the diurnal behaviour of neutral daytime airglow emissions. Ann. Geophys. 34, 1019–1030. https://doi.org/10.5194/angeo-34-1019-2016.

Khadka, S.M., Valladares, C.E., Sheehan, R., Gerrard, A.J., 2018. Effects of electric field and neutral wind on the asymmetry of equatorial ionization anomaly. Radio Science 53, 683–697. https://doi.org/10.1029/2017RS006428.

Kumar, S., Veenadhari, B., Ram, S.T., Su, S.-Y., Kikuchi, T., 2016. Possible relationship between the equatorial electrojet (eej) and daytime vertical e×b drift velocities in f region from rocsat observations. Adv. Space Res. 58, 1168–1176. https://doi.org/10.1016/j.asr.2016.06.009.

Mayr, H., Harris, I., Spencer, N., 1978. Some properties of upper atmosphere dynamics. Rev. Geophys. 16, 539–565. https://doi.org/10.1029/RG016i004p00539.

Narayanan, R., Desai, J., Modi, N., Raghavarao, R., Sridharan, R., 1989. Dayglow photometry: a new approach. Appl. Opt. 28, 2138–2142. https://doi.org/10.1364/AO.28.002138.

Pallam Raju, D., Sridharan, R., Gurubaran, S., & Raghavarao, R. (1996). First results from ground-based daytime optical investigation of the development of the equatorial ionization anomaly. In Annales Geophysicae (p. 238). volume 14. doi: 10.1007/s00585-996-0238-9.

Pallamraju, D., Baumgardner, J., Chakrabarti, S., 2000. A multiwavelength investigation of the ring effect in the day sky spectrum. Geophysical research letters 27, 1875–1878. https://doi.org/10.1029/1999GL010961.

Pallamraju, D., Baumgardner, J., & Chakrabarti, S. (2002). Hirise: A ground-based high-resolution imaging spectrograph using echelle grating for measuring daytime airglow/auroral emissions. doi: 10.1016/S1364-6826(02)00095-0.

Pallamraju, D., Chakrabarti, S., Valladares, C., 2004. Magnetic storm-induced enhancement in neutral composition at low latitudes as inferred by o (1 d) dayglow measurements from chile. Ann. Geophys., volume 22. Copernicus GmbH, pp. 3241–3250. https://doi.org/10.5194/angeo-22-3241-2004.

Pallamraju, D., Das, U., Chakrabarti, S., 2010. Short-and long-timescale thermospheric variability as observed from oi 630.0 nm dayglow emissions from low latitudes. Journal of Geophysical Research: Space Physics 115. https://doi.org/10.1029/2009JA015042.

Pallamraju, D., Karan, D.K., Laskar, F.I., Lakshmi, T.V., Chakrabarti, S., 2020. Effect of solar flux versus compositional variations on the variability of daytime oxygen optical emission rates over low-and mid-latitudes. J. Atmos. Solar Terr. Phys. 205, 105293. https://doi.org/10.1016/j.jastp.2020.105293.

Pallamraju, D., Laskar, F.I., Singh, R.P., Baumgardner, J., Chakrabarti, S., 2013. Mise: A multiwavelength imaging spectrograph using echelle grating for daytime optical aeronomy investigations. J. Atmos. Solar Terr. Phys. 103, 176–183. https://doi.org/10.1016/j.jastp.2012.12.003.

Prölss, G., 1993. Common origin of positive ionospheric storms at middle latitudes and the geomagnetic activity effect at low latitudes. Journal of Geophysical Research: Space Physics 98, 5981–5991. https://doi.org/10.1029/92JA02777.

Raghavarao, R., Nageswararao, M., Sastri, J.H., Vyas, G.D., Sriramarao, M., 1988. Role of equatorial ionization anomaly in the initiation of equatorial spread f. Journal of Geophysical Research: Space Physics 93, 5959–5964. https://doi.org/10.1029/JA093iA06p05959.

Raghavarao, R., Sharma, P., & Sivaraman, M. (1978). Correlation of the ionisation anomaly with the intensity of the electrojet,. URL https://ui.adsabs.harvard.edu/abs/1978spre.conf..277R/abstract.

Rishbeth, H., 1977. Dynamics of the equatorial f-region. J. Atmos. Terr. Phys. 39, 1159–1168. https://doi.org/10.1016/0021-9169(77)90024-1.

Rush, C., Richmond, A., 1973. The relationship between the structure of the equatorial anomaly and the strength of the equatorial electrojet. J. Atmos. Terr. Phys. 35, 1171–1180. https://doi.org/10.1016/0021-9169(73)90013-5.

Saha, S., Pallamraju, D., Pant, T., Chakrabarti, S., 2021. On the cause of nocturnal oi 630nm airglow variability over low-latitude thermosphere. Journal of Geophysical Research: Space Physics 126. https://doi.org/10.1029/2021JA029146.

Sastri, J., 1990. Equatorial anomaly in f-region - a review. Indian Journal of Radio and Space Physics 19, 225–240, http://nopr.niscair.res.in/handle/123456789/36285.

Shepherd, G.G., Cho, Y.-M., 2021. On the relationship of the o (1d) 630.0 nm dayglow emission to the f10. 7 cm solar flux and the solar zenith angle. Journal of Geophysical Research: Space Physics. https://doi.org/10.1029/2020JA028715 (p. e2020JA028715).

Sirk, M.M., Korpela, E.J., Ishikawa, Y., Edelstein, J., Wishnow, E.H., Smith, C., McCauley, J., McPhate, J.B., Curtis, J., Curtis, T., et al., 2017. Design and performance of the icon euv spectrograph. Space science reviews 212, 631–643. https://doi.org/10.1007/s11214-017-0384-2.

Solomon, S.C., Abreu, V.J., 1989. The 630 nm dayglow. Journal of Geophysical Research: Space Physics 94, 6817–6824. https://doi.org/10.1029/JA094iA06p06817.

Sridharan, R., Modi, N., Raju, D.P., Narayanan, R., Pant, T.K., Taori, A., Chakrabarty, D., 1998. A multiwavelength daytime photometer-a new tool for the investigation of atmospheric processes. Meas. Sci. Technol. 9, 585. https://doi.org/10.1088/0957-0233/9/4/005.

Sridharan, R., Narayanan, R., Modi, N., Raju, D.P., 1993. Novel mask design for multiwavelength dayglow photometry. Applied optics 32, 4178–4180. https://doi.org/10.1364/AO.32.004178.

Sridharan, R., Raju, D.P., Somayajulu, V., Taori, A., Chakrabarty, D., Raghavarao, R., 1999. Imprint of equatorial electrodynamical processes in the oi 630.0 nm dayglow. J. Atmos. Solar Terr. Phys. 61, 1143–1155. https://doi.org/10.1016/S1364-6826(99)00064-4.

Stephan, A.W., Korpela, E.J., Sirk, M.M., England, S.L., Immel, T.J., 2017. Daytime ionosphere retrieval algorithm for the ionospheric connection explorer (icon). Space science reviews 212, 645–654. https://doi.org/10.1007/s11214-017-0385-1.

Woodman, R.F., 1970. Vertical drift velocities and east-west electric fields at the magnetic equator. J. Geophys. Res. 75, 6249–6259. https://doi.org/10.1029/JA075i031p06249.

AGU ADVANCING EARTH AND SPACE SCIENCE

JGR Space Physics

RESEARCH ARTICLE
10.1029/2022JA030954

Key Points:

- Three-dimensional characterization of daytime thermospheric gravity waves has been made using collocated optical and radio measurements
- Estimated vertical wavelengths of gravity waves from their horizontal characteristics reasonably match with those measured from digisonde
- Thermospheric neutral winds estimated using measured 3-D gravity wave information show a good match with those measured by MIGHTI

Supporting Information:

Supporting Information may be found in the online version of this article.

Correspondence to:

D. Pallamraju,
raju@prl.res.in

Citation:

Kumar, S., Mandal, S., & Pallamraju, D. (2023). Characterization of gravity waves in three dimensions in the daytime thermosphere using combined optical and radio measurements and estimation of horizontal neutral winds. *Journal of Geophysical Research: Space Physics*, *128*, e2022JA030954. https://doi.org/10.1029/2022JA030954

Received 26 AUG 2022
Accepted 14 FEB 2023

Author Contributions:

Conceptualization: Duggirala Pallamraju
Formal analysis: Sunil Kumar, Subir Mandal
Funding acquisition: Duggirala Pallamraju
Investigation: Sunil Kumar, Subir Mandal
Project Administration: Duggirala Pallamraju
Supervision: Duggirala Pallamraju
Writing – review & editing: Sunil Kumar, Subir Mandal, Duggirala Pallamraju

Characterization of Gravity Waves in Three Dimensions in the Daytime Thermosphere Using Combined Optical and Radio Measurements and Estimation of Horizontal Neutral Winds

Sunil Kumar[1,2], Subir Mandal[1,3], and Duggirala Pallamraju[1]

[1]Space and Atmospheric Sciences Division, Physical Research Laboratory, Ahmedabad, India, [2]Indian Institute of Technology, Gandhinagar, India, [3]Now at British Antarctic Survey, Cambridge, UK

Abstract Gravity waves, which are considered omnipresent in the Earth's upper atmosphere, are generally investigated by monitoring the fluctuations in different atmospheric parameters. Here, we report the propagation characteristics of thermospheric gravity waves both in horizontal and vertical directions obtained using collocated optical and radio measurements from Ahmedabad, India for February 2021. The measurements of OI 630.0 nm dayglow emission rates over zenith are used to derive time periods of gravity waves. Wave number analyses of variations in the emission over a large field-of-view have been performed to derive gravity wave scale sizes and propagation characteristics in the horizontal direction. Time periods, horizontal scale sizes, and propagation directions are found to be in the range of 31–125 min, 78–243 km, and 203°–248° from east, respectively. Vertical wavelengths of the gravity waves are obtained from radio measurements and are in the range of 26–247 km. As the gravity wave characteristics are influenced by the ambient neutral winds, the measured gravity wave propagation characteristics in three dimensions have been used as inputs into the gravity wave dispersion relation to estimate the magnitudes of thermospheric horizontal neutral winds. These estimated daytime winds in the direction of wave propagation are found to be in the range of 1–105 ms^{-1}, and they compare well with those measured independently from MIGHTI added HWM14 model-derived winds. The daytime winds estimated by this approach are possibly the first of their kind as obtained from ground-based measurements.

Plain Language Summary Atmospheric gravity waves are mostly generated in the lower atmosphere due to different processes, and they carry energy away from their source regions. Therefore, these waves play a crucial role in the coupling and energetics of the atmosphere. As the neutral density decreases exponentially with height, amplitudes of these waves grow in order to conserve energy. At high altitudes, when the amplitudes become very large, these waves break due to non-linear wave-wave interactions and deposit their energy. Such energy deposition can further give rise to secondary and tertiary gravity waves. In favorable background conditions, these waves can propagate deep into the upper atmosphere and alter the prevailing dynamics. Therefore, the characterization of their spatial and temporal scales in the upper atmosphere is extremely important for a comprehensive understanding of atmospheric dynamics. As neutrals and plasma share the same space in the upper atmosphere, we have used simultaneous observations of both the neutrals and plasma, using ground-based optical and radio measurements, to derive the propagation characteristics of the atmospheric gravity waves in all three dimensions. Further, we have used these parameters to estimate the magnitudes of daytime thermospheric horizontal winds, which are otherwise difficult to obtain from ground-based platforms in daytime.

1. Introduction

Waves of different spatial and temporal scales are known to have a significant influence on the upper atmospheric dynamics as they contribute to the coupling of different regions. Among the different types of waves, the effects of large-scale waves such as planetary waves and tides in the atmosphere are relatively well understood, whereas, the understanding of the dynamics related to the gravity waves is far from complete, more so in the daytime. The gravity waves are mostly generated in the lower atmosphere due to changes in orography (e.g., Alexander, 1996; Smith & Lyjak, 1985), tropospheric convective activities (e.g., Alexander et al., 2000; Sato et al., 1995; Singh & Pallamraju, 2016), and wind shears (e.g., Fritts, 1982, 1984; Pallamraju et al., 2014; Pramitha et al., 2015). Further, these waves can also be generated due to auroral processes over the high-latitudes

(Hocke & Schlegel, 1996; Pallamraju et al., 2001), and equatorial electrojet over the low-latitudes (Pallamraju et al., 2010; Raghavarao et al., 1988), among others. If the background conditions are favorable, these gravity waves can propagate to higher altitudes and significantly contribute to the prevailing dynamics (Fritts & Alexander, 2003). As the wave amplitudes increase with altitude, non-linear wave-wave interactions occur in the mesosphere-lower-thermosphere (MLT), which can lead to the breaking of waves. The deposition of energy resulting from the breaking of these waves accelerates the background mean flow at these altitudes. These can further excite secondary and tertiary waves in the MLT region (e.g., Medvedev & Klaassen, 2000; Vadas et al., 2003; Yigit et al., 2008), which can reach the thermospheric altitudes, where they are potentially dissipated by the molecular viscosity and thermal diffusivity (e.g., Francis, 1973; Pitteway & Hines, 1963; Richmond, 1978; Hickey & Cole, 1988; Vadas, 2007; Vadas & Fritts, 2004). Numerous theoretical simulations and modeling studies on the effects of the lower atmospheric gravity waves on thermospheric dynamics have been reported in the literature (e.g., Vadas, 2007; Vadas & Liu, 2009; Yigit & Medvedev, 2009). Studies have shown that gravity waves effects in the ionosphere-thermosphere are comparable to the ion-drag effects, and they can contribute to the heating or cooling of the thermosphere by up to 170 K-day^{-1} till the peak F-layer altitudes (e.g., Miyoshi et al., 2014; Yiğit & Medvedev, 2009). Hence, a critical knowledge of the temporal and spatial characteristics of these atmospheric gravity waves is essential for a better understanding of the upper atmospheric variability. Propagation features of these atmospheric gravity waves are strongly influenced by background conditions, such as, temperature, neutral density, and winds. The neutral winds control the propagation characteristics of the gravity waves, and as a result, the horizontal/vertical scale sizes of the gravity waves increase/decrease due to the neutral winds flowing in the same direction of gravity wave propagation (e.g., Li & Lu, 2021; Mandal et al., 2019; Mandal & Pallamraju, 2020; Pallamraju et al., 2016; Vadas et al., 2009). Therefore, the horizontal neutral winds and propagation of gravity waves are inter-coupled. Further, these background atmospheric parameters are altered by the variation in the incoming solar radiation in the EUV and X-ray wavelengths. Based on changes in the wave dissipation conditions at thermospheric altitudes, the number of gravity waves in the daytime thermosphere, their vertical propagation speeds, and vertical wavelengths have been shown to increase with an increase in the solar activity (e.g., Laskar et al., 2015; Mandal et al., 2020).

One of the most established methods to characterize these neutral gravity waves in the upper atmosphere is to monitor the fluctuations in the natural airglow emissions. As the propagation of any wave disturbs the density and temperature of the reactants that produce these emissions, they leave their imprint on the variations of these airglow emissions (e.g., Pallamraju et al., 2010; Teitelbaum et al., 1981). Single point photometric measurements of airglow emissions can only provide the information of time periods of these waves, whereas, scale sizes and propagation directions of these waves can be derived using large field-of-view (FOV) imaging measurements (e.g., Lakshmi Narayanan et al., 2010; Shiokawa et al., 2009; Taylor et al., 1995). In the presence of strong solar background brightness in the daytime, observation of these faint dayglow emissions is extremely challenging. However, with the advent of new and innovative optical techniques with a high spectral resolution, such measurements have become possible in the recent past. Some of the results obtained by using high-resolution spectrographs are reviewed by Pallamraju and Chakrabarti (2006). Owing to the large FOV of these spectrographs, it is also possible to obtain gravity wave scale sizes by carrying out wave number analysis (e.g., Karan & Pallamraju, 2017, 2018; Pallamraju et al., 2014, 2016). Combining such analyses in the zonal and meridional directions, horizontal scale sizes of gravity waves can be obtained. Such observations were obtained from three dayglow emissions, namely, OI 557.7, OI 630.0, and OI 777.4 nm that emanate from three different altitudes as reported earlier (Pallamraju et al., 2016).

In the present work, we have derived the horizontal propagation characteristics (time periods, scale sizes, and propagation directions) of thermospheric gravity waves using the large FOV observations of OI 630.0 nm dayglow emission rates from Ahmedabad. Further, we have used the phase delays in the height variations of multiple isoelectron densities, as obtained from a digisonde, to derive the vertical propagation characteristics (time periods, phase speed, and scale sizes) of these waves. In an earlier work, using combined optical and radio measurements, it was shown that the wave features are similar in both these measurements indicating that these are the same waves but observed in different techniques (Mandal et al., 2019). Therefore, in this study, we have used such collocated and simultaneous optical and radio measurements to obtain gravity wave characteristics in three dimensions. Further, as the neutral winds affect the wave propagation, using the measured values of gravity wave parameters in all three dimensions from our study as inputs into the gravity wave dispersion relation, we have estimated the thermospheric neutral wind magnitudes. The estimated winds along the direction of wave

10.1029/2022JA030954

propagation by the present method as reported in this study have been found to compare well with those measured by the Ionospheric Connection Explorer (ICON) satellite.

It is known that the measurements of the daytime thermospheric winds from ground-based instruments are extremely challenging in the presence of background sunlight. Applications of the ground-based Fabry-Perot etalons have been reported in the literature as a means for the measurement of neutral winds (e.g., Burnside et al., 1981; Makela et al., 2013; Meriwether et al., 1986), which are restricted to the nighttime, except the one using a triple etalon system, which is suitable for daytime conditions as well (Gerrard & Meriwether, 2011). Instruments on-board satellites have provided daytime neutral winds measurements (e.g., Englert et al., 2017; Herrero et al., 1988; Shepherd et al., 1993). Thus, to the best of our knowledge, the results obtained on daytime thermospheric winds using three-dimensional gravity wave characteristics obtained from ground-based measurements, as reported in the present study, are the first of their kind.

2. Data Sets

For the present study, we have used (a) the OI 630.0 nm dayglow emissions measured by MISE, (b) ionospheric data from digisonde, (c) thermospheric neutral winds measured by MIGHTI on board the ICON satellite, (d) outputs of winds from the Horizontal Wind Model-14 (HWM14) model, and (e) neutral atmospheric parameters, such as, temperature and mass density from the NRLMSISE model. These data sets used for the duration of 5–19 February 2021 are briefly discussed below.

2.1. OI 630.0 nm Dayglow

Dayglow refers to the naturally occurring atmospheric emissions in the daytime, which are produced from different photochemical reactions that occur in the Earth's upper atmosphere. Temporal variations in their emission rates depend on the temperatures and densities of the reactants, which are affected by wave propagation. Therefore, the fluctuations superposed on the broad variations in these emission rates can be used as a tracer to derive the wave propagation characteristics. In this work, the OI 630.0 nm dayglow emissions, which peak at around 230 km, have been used to study the behavior of the gravity waves. The emission region has a thickness of half-value width of around 100 km. The OI 630.0 nm emission is produced mainly from photoelectron impact excitation of atomic oxygen, photodissociation of molecular oxygen, and dissociative recombination of molecular oxygen ions with ambient electrons (Solomon & Abreu, 1989). We have retrieved the dayglow emission rates at 630.0 nm wavelength using the data obtained from the multi-wavelength imaging spectrograph using echelle grating, MISE (Pallamraju et al., 2013), which is in operation from Ahmedabad, India. MISE is an imaging spectrograph providing high-resolution spectral images over a large FOV (around 140°). To retrieve the dayglow emission rates from the sky images obtained by MISE, we remove the scattering contribution due to the Ring-effect (atmospheric scattering) by considering the scattering in the neighboring Scandium line. Such methodology of extracting dayglow emissions buried in the strong solar background continuum is well-established, details of which have been reported in the literature (Pallamraju et al., 2002, 2013). In this study, we have used dayglow observations within the FOV of 106° (zenith − 57° to zenith + 49°), which corresponds to a spatial distance of around 622 km (355 km away from the zenith in one direction and 267 km in the other). We have restricted ourselves to this FOV to avoid the effects of filling-in due to atmospheric scattering from low-elevation angles. The MISE instrument uses a CCD detector of 1,024 × 1,024 pixels. In order to improve the signal-to-noise ratio (SNR), we apply an 8-pixel on-chip binning along the spatial direction of the spectrograph, resulting in the final image size of 1,024 × 128. The dark count (0.017 electrons s^{-1} pix^{-1} at −75°C) and readout noise (3.3 electrons RMS at the readout frequency of 50 kHz) of this CCD are very small. The readout noise gets reduced further due to the 8-pixel binning in the spatial direction.

2.2. Ionospheric Electron Density

We have used the ionospheric electron density measurements from DPS-4D digisonde located at Ahmedabad. This digisonde is programmed to provide ionograms (frequency vs. height of reflection) in the range of 1–12 MHz at a cadence of 7.5 min. All the ionograms have been manually scaled and the variations in the heights of the isoelectron density contours corresponding to digisonde transmitted frequencies at 5.0, 5.5, and 6.0 MHz have been used collectively to derive the time periods and vertical wavelengths of the gravity waves present in the ionosphere-thermosphere region.

2.3. Neutral Winds

Measured neutral winds from the Michelson Interferometer for Global High-Resolution Thermospheric Imaging, MIGHTI (Englert et al., 2017), on-board ICON (Immel et al., 2018) satellite are used for comparison with our estimated values. MIGHTI makes use of the Doppler shifts in the observed airglow emissions at OI 557.7 and 630.0 nm to provide wind magnitudes between 90 and 300 km. The wind measurements from MIGHTI cover the spatial region of 12°S to 42°N geographic latitudes. Further, we have used MIGHTI added HWM14 winds, an approach described in Kumar et al. (2022) to estimate the diurnal variation in thermospheric winds at a given location. In this approach the MIGHTI winds are used to provide day-to-day corrections to those provided by the HWM14, which is climatological in nature, thereby yielding the diurnal variation of thermospheric wind at a given location, as briefly described in Section 4.4 below.

3. Data Analyses

In this work, we have used collocated digisonde and optical measurements from Ahmedabad, a low-latitude location in the Indian longitudes. The horizontal and vertical propagation characteristics of the thermospheric gravity waves have been derived using OI 630.0 nm dayglow emission observations over a large FOV and radio measurements, respectively. Detailed analysis methodologies are described in the following sections.

3.1. Estimations of Time Period and Horizontal Propagation Characteristics of Gravity Waves

As discussed above, OI 630.0 nm dayglow emission rates can be obtained over a large spatial distance using the observation by MISE. For the present work, we have carried out a special campaign mode observation, wherein, we have rotated the MISE instrument in orthogonal directions—meridional (north-south) and zonal (east-west); in a way such that the slit through which the light enters the instrument, is oriented in each of the directions for 30 min. Such repeated observations along two orthogonal directions enable us to obtain the gravity wave scale sizes in both meridional and zonal directions over a spatial distance of around 622 km (along the FOV of MISE) for the OI 630.0 nm emission altitude as a function of time. The dayglow emission rates at the zenith, which is common in both these orientations, are used to obtain the diurnal variation of dayglow emissions. Further, we have co-added the images obtained for 5 min and over 21 pixels centered around the zenith to improve the SNR. The diurnal variation of OI 630.0 nm dayglow emission rate on a sample day (5 February 2021) is depicted in Figure 1a. It can be noted that in addition to the broad diurnal variations, there are smaller scale fluctuations, which are understood to be caused by the wave activity that exists in those regions. In order to derive more accurate information on the periodic behavior of these fluctuations in the gravity wave regime, residuals (shown as red-dotted line) have been obtained by subtracting 2 hr running-averaged values (black-dashed line) from the actual dayglow values. Thus, the residuals obtained will contain information on the periodicities smaller than the sub-harmonic of the tidal periods (3 hr). The dayglow data used in this work are non-uniformly sampled in the course of observation on a given day. This unequal spacing of data arises due to different exposure times, presence of clouds in the FOV, on occasions, and lack of data around local noon, when the CCD gets saturated by the direct solar glare. Thus, to carry out spectral analysis of the data, we have used the Lomb-Scargle periodogram (Lomb, 1976; Scargle, 1982) technique, which is capable of yielding frequencies present in the non-uniformly sampled data. The Lomb-Scargle periodogram refers to a generalized form of classical periodogram with properties like, (a) it reduces to a classical periodogram for uniformly sampled data, (b) the resultant periodogram is insensitive to time shifts in the data, and (c) it is identical to results obtained by fitting sinusoidal function to the data and constructing a periodogram from the χ^2 goodness of fit at each frequency (VanderPlas, 2018). The results from such analyses of diurnal variation of dayglow emission rates on 5 February 2021 are shown in Figure 1c, wherein, significant time periods (time periods with power spectral density higher than 90% false alarm limit, FAL or statistical significance level) can be seen. It can be noted that gravity waves of time periods around 37, 66, and 101 min are present on this day. Similarly, gravity wave scale sizes are obtained from the variations in dayglow emission rates along the spatial directions. In this case, data obtained for 10–15 min have been co-added and a 11-pixel running average values have been considered to improve the SNR. As an example,

10.1029/2022JA030954

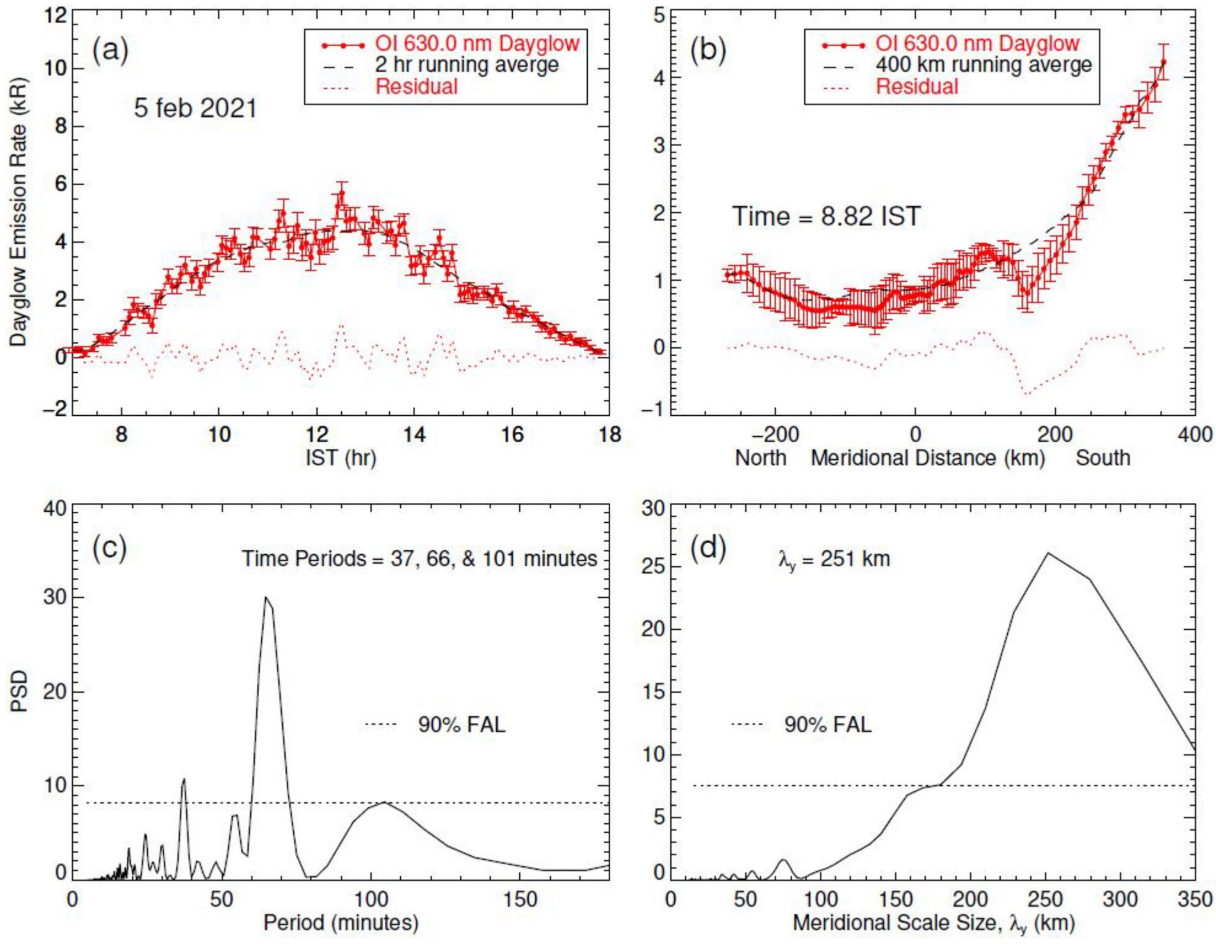

Figure 1. The diurnal variation of the OI 630.0 nm dayglow emissions on a sample day of 5 February 2021 is shown in red-color; black-dashed curve represents 2 hr running averaged values and red-dotted curve is the residual obtained by subtracting the 2 hr running-averaged values from the original values. (b) Variation in the dayglow emission rates at OI 630.0 nm wavelength in the meridional direction corresponding to 8.82 IST; black-dashed line represents 400 km running average dayglow and the residual (obtained by subtracting the running averaged values from original data) is shown by red-dotted line. (c) The Lomb-Scargle periodogram of the residual obtained from the diurnal profile of dayglow is shown in (a), wherein time periods of 37, 66, and 101 min are found to be significant. The black dash-dotted line represents the statistical significance level of 90%. (d) The results from spectral analysis of the residual from meridional dayglow data as presented in (b) are shown here. Presence of a dominant scale size of around 250 km can be seen.

the variations in the dayglow emission rates along the meridional direction at a given time are shown in Figure 1b. The spatial region covered by each pixel is different at different angles, as they vary non-linearly. Over zenith, it is 4 km pixel^{-1} and at the farthest view direction, it is 12 km pixel^{-1}. Thus, considering a 2-pixel separation for estimating the spatial resolution, the maximum uncertainty turns out to be 24 km. Wave number analyses have been carried out on the residual of the spatially varying dayglow emission rates to find the statistically significant scale sizes. The residual is obtained by subtracting 400 km running averaged values from the original data. These residuals are shown by red-dotted line in Figure 1b. Thus, meridional scale sizes (λ_y) of the gravity waves are obtained by performing wave number analysis on data shown in Figure 1b. From Figure 1d, one can see the presence of a meridional scale size of around 251 km on this day at around 8.82 IST. Similarly, we have obtained the zonal scale sizes (λ_x) of gravity waves using the dayglow intensity variation across the zonal direction. In this way, we have obtained the gravity wave scale sizes in the zonal and meridional directions throughout the day. As discussed earlier, the duration of observations in zonal and meridional directions is 30 min each.

Observational evidences have been shown earlier that gravity waves in the thermosphere exist in the form of monochromatic wave packets, that is, they are coherent waves or have similar characteristics throughout the day (e.g., Djuth et al., 2004; Oliver et al., 1994). Further, one wave packet typically lasts around 1–2 hr and has a separation of 20–60 min from another wave packet. In this background, we can safely assume that the gravity

10.1029/2022JA030954

waves observed within 30 min are the same (as the time periods of these gravity waves are 37, 66, and 101 min as shown in Figure 1c). Hence, we have combined the λ_x and λ_y information obtained over 30 min to estimate the horizontal scale sizes (λ_H) of these gravity waves as per the following relation,

$$k_H^2 = k_x^2 + k_y^2 \text{ or } \lambda_H = (\lambda_x \times \lambda_y)/\left(\lambda_x^2 + \lambda_Y^2\right)^{1/2} \tag{1}$$

where k_H, k_x, and k_y are the wave numbers in horizontal, zonal, and meridional directions, respectively.

The derived values of λ_H thus correspond to the time, which is the average of the duration of λ_x and λ_y. We have calculated these values of horizontal scale sizes of gravity waves for all 10 days on which bi-directional observations of OI 630.0 nm dayglow emission are available. Table 1 lists all the time periods of gravity waves obtained from the analyses of dayglow emission rates, and it can be noted that they are greater than 30 min. Therefore, our assumption of considering the scale sizes obtained in orthogonal directions within 30 min to be of the same gravity wave to calculate λ_H is valid for all these days. The diurnal variation of λ_H is shown in Figure 2 for 10 days. In this figure, λ_H is only shown when both λ_x and λ_y are significant (above 90% FAL) in the wave number spectral analysis. Around the local noon, to prevent the saturation of the detector due to direct solar glare, the instrument has been kept in the east-west direction from 12 to 13.5 IST (UT + 5.5 hr). Therefore, for this period, we only have the values of λ_x. The values of λ_y for these times are interpolated by considering the values of λ_y around 12 and 13.5 hr IST (pre- and post-noon time). They have been considered together to estimate the values of λ_H, and are shown by black-dotted lines in Figure 2 to separate them from the other values.

Further, the phase propagation angles (θ_H) of these waves are calculated using the measured λ_x and λ_y since they are related as $\theta_H = \tan^{-1}(\lambda_x/\lambda_y)$. These values of θ_H have a degeneracy of 180°. In order to estimate the propagation direction unambiguously, we have used the methodology described in an earlier study (Pallamraju et al., 2016). In this method, to obtain the spatial location of a dominant scale size at a given time, inverse Fourier transforms have been performed by retaining only the power spectral signal of a given dominant scale size (in the frequency domain) at a time. In doing so the spectral power corresponding to the dominant scale size with a bandwidth of 24 km (which is the uncertainty in the scale sizes as discussed above) is retained and the power of the rest of the scale sizes have been equated to zero. This process is repeated throughout the day for both directions and the results from such an exercise for a representative day (5 February 2021) are shown in Figure 3, wherein, the locations of the wave crests and troughs as a function of time become clearly visible. The *y*-axis of the left panel shows the wave characteristics in the meridional direction, whereas, the *x*-axis shows the time in IST. In the right panel, the waves in the zonal direction are shown along the *x*-axis, and time along the *y*-axis. One can note the crests and troughs of the gravity wave scale sizes oriented in orthogonal directions in both these panels. The black lines are drawn to trace the crests and troughs of the gravity wave at different times. Thus, they indicate the movement of phase fronts with time which are southward as seen in the left panel, and westward as seen in the right panel. Based on this combined information, it can be inferred that the gravity waves are broadly propagating in the south-west direction on this day. Such analyses have been carried out for all the days and we found that the observed gravity waves are propagating in the south-west directions in this duration. The propagation directions of these waves as described in this method are presented with time in Figure 4 as red-colored dashed arrows for all the 10 days of available bi-directional data that are shown in Figure 2 (the solid black lines are the direction of neutral winds as described below in Section 4.4). Here, the values on the *y*-axis correspond to the day of the month of February 2021. Such methods have been shown (Hocke & Kampfer, 2009; Pallamraju et al., 2016) to bring out accurate information on the spatio-temporal variations of a given periodic fluctuations. In an earlier work (Mandal & Pallamraju, 2020), by comparing the variations in the vertical speeds of gravity waves as obtained from analyses of digisonde measurements with the variation in the HWM14 model-derived winds, it was inferred that the gravity waves mostly show south-westward propagation in the daytime thermosphere over Ahmedabad. Hence, the horizontal wavelengths and propagation directions of atmospheric gravity waves obtained in the present work in the daytime thermosphere over Ahmedabad are consistent with the earlier findings as well. The horizontal characteristics (time period, λ_x, λ_y, λ_H, and θ_H) of gravity waves on all these 10 days are found to be in the range of 31–138 min, 88–344 km, 123–344 km, 78–243 km, and 203°–248° from the east direction, respectively, and are listed in Table 1.

3.2. Vertical Propagation Characteristics of Gravity Waves

Digisonde-derived height variations of isoelectron densities have been used to obtain the vertical wavelengths of the atmospheric gravity waves present in the thermosphere. The details of deriving vertical scale sizes have

10.1029/2022JA030954

Table 1

Gravity Wave Parameters, Such as, Time Periods in Optical Data, Time Periods in Radio Data, λ_x, λ_y, λ_H, θ_H, Estimated λ_z From Gravity Wave Dispersion Relation Using Horizontal Characteristics of Gravity Waves as Obtained by Optical Measurement, and Measured λ_z From Digisonde are Shown for all the Days.

A	B	C	D	E	F	G	H	I	J
S.No.	Date (in the month of February 2021)	Optical period (minutes)	Radio period (minutes)	Zonal scale size, λ_x (km) from optical data	Meridional scale size, λ_y (km) from optical data	Horizontal scale size, λ_H (km) from optical data	Phase propagation angle, θ_H from optical data	Estimated vertical scale size, λ_Z (km) from Hines, (1960) GW dispersion relation	Measured vertical scale size λ_Z (km) from radio data
1	5 February	37, 66, **101**	**94**	182–281	182–344	128–199	207–232	40–61	65–90
								19–36	
								9–25	
2	6 February	33, 53, 65, 126	NVP	206–344	123–344	140–243	208–239	36–109	-
								15–74	
								9–64	
								1–44	
3	7 February	**41**, 55, 66, 99	**41**	88–281	162–344	78–199	207–243	18–72,	71–81
								13–57,	
								11–51,	
								4–40	
4	8 February	**49**, 63, 79, 135	37, **52**, 109	162–344	162–344	115–243	222–237	30–51	51–75
								21–39	69–82
									149–247
								15–31	
								6–23	
5	12 February	**40**, 54, 67, 116	**37**	162–344	182–344	128–199	211–242	34–53	28–36
								22–39	
								16–32	
								3–19	
6	13 February	**31**, 63, **94**, 126	**37**, **104**	147–281	162–344	112–199	203–237	28–72	56–83
								8–40	85–167
								2–32	
								1–28	
7	14 February	**37**, 56, 65, 138	**37**	147–344	134–281	113–199	221–248	30–56	26–41
								3–38	
								1-30	
								1–26	
8	16 February	37, 90	NVP	123–281	123–281	87–199	214–239	5–59	-
								6–31	
9	18 February	**45**, **90**	**44**, **95**, 143	147–344	147–344	104–243	219–233	17–59	63–76
								2–38	108–160
									84–96
10	19 February	33, 49, 65, 90	NVP	147–344	147–344	109–243	203–246	14–79	-
								2–53	
								0–43	
								2–36	

Note. No vertical propagations (NVPs) of gravity waves are found on 6, 16, and 19 February 2021. The time periods in bold fonts correspond to those with a match between the optical and the radio measurements within the temporal window of the Brunt-Väisälä period.

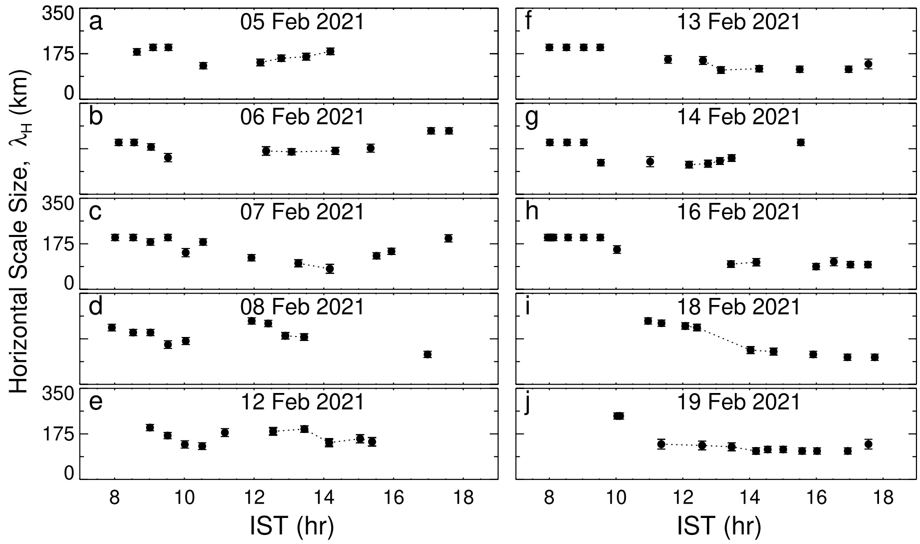

Figure 2. Diurnal variation of horizontal scale sizes of gravity waves for all the 10 days of bi-directional observation of dayglow emissions at OI 630.0 nm during 5–19 February 2021 are shown. The points joined by black-dotted line during noon-time correspond to those obtained by interpolating the values of λ_y before and after noon.

been described in an earlier study (Mandal et al., 2019). Several insightful results obtained with regard to gravity wave dynamics as a function of the seasons, solar flux variations, geomagnetic conditions, and day-to-day behavior have been reported in the literature (Mandal et al., 2020, 2022; Mandal & Pallamraju, 2020). In the present study, we have monitored the true height variations of constant electron densities corresponding to 5.0, 5.5, and 6.0 MHz transmission frequencies of digisonde, which has been shown in Figure 5a for a sample day of 5 February 2021. The phases can be seen to appear first in the higher heights, that is, in the variation of 6.0 MHz isoelectron density contours (red color) and they appear later in time in the case of 5.0 MHz contour (orange color). To aid the eye, black-dashed lines have been drawn for identification of downward phase movement. This kind of downward phase propagation is a characteristic property of upward propagating atmospheric gravity waves (Hines, 1960). Further, to ascertain that these phase offsets were indeed caused by an upward propagating gravity wave, time series analyses as described above are carried out for each of these isoelectron density contours for all the days of available data and are shown in Figure 5b. The Lomb-Scargle periodogram analysis shows the presence of multiple periods (66 and 94 min) in all three isoelectron density contours that are significant as can be

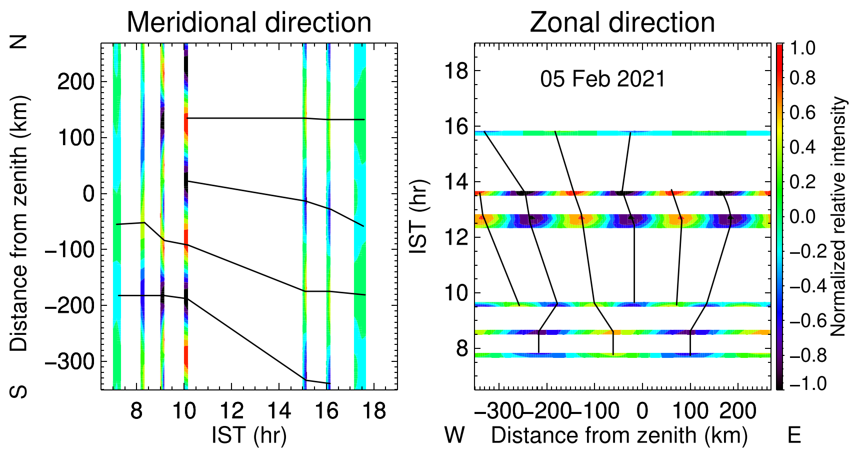

Figure 3. The normalized relative dayglow intensity variations obtained through inverse Fourier transform of a band centered on the dominant scale size are shown for a given day 5 February 2021. The left/right panels correspond to meridional/zonal directions. Black solid lines connect the crest/trough at one time to the other and aid the eye in the visualization of the movement of crests and troughs with time.

seen in Figure 5b. As fluctuations of different temporal scales are superposed in the height variations of these isoelectron density contours, we filtered each of these contours for the particular gravity wave of time period of around 94 min. In this, the spectral power for this particular time period ±10 min window (corresponding to the Brunt-Väisälä period) is retained. For the rest of the frequencies, it is made zero. Then, the inverse Fourier transform is performed to obtain height variations in the isoelectron density contours only for that chosen common time period of the gravity waves. Figure 5c shows filtered variations in the heights of isoelectron density contours for a gravity wave of period 94 min on 5 February 2021. The downward phase propagation becomes more apparent in these filtered contours (as can be seen in Figure 5c). For time period of 66 min, such downward phase propagation was not seen in the filtered height variation in all the frequencies. We then use the height and time differences between crests and troughs of successive isoelectron density contours to calculate vertical propagation speeds of these gravity waves and vertical scale sizes (λ_z) by taking a product of the time periods and propagation speeds. On 5 February 2021, the λ_z of the gravity wave of time period 94 min is found to be varying in the range of 65–90 km. It is important and pertinent to note that this period of 94 min seen in the digisonde (Figure 5) data analysis is very close within the limit of the Brunt-Väisälä period (10 min) of the 101 min periodicity obtained from the optical data (Figure 1). This clearly strengthens the conjecture that the λ_x and λ_y obtained from optical data and the λ_z obtained from the digisonde data combinedly describe the three-dimensional behavior of the same gravity wave in the daytime. In this study, digisonde data have been analyzed for all

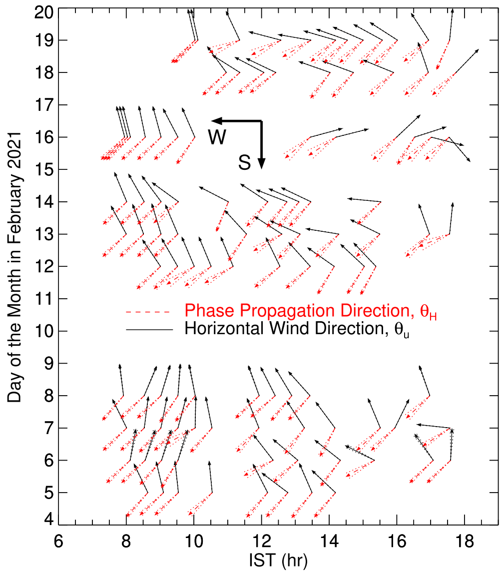

Figure 4. The time variation in propagation directions of the gravity waves for all the 10 days considered in this study are shown by red-dashed arrows and those for observed thermospheric winds by MIGHTI are presented in black-colored arrows.

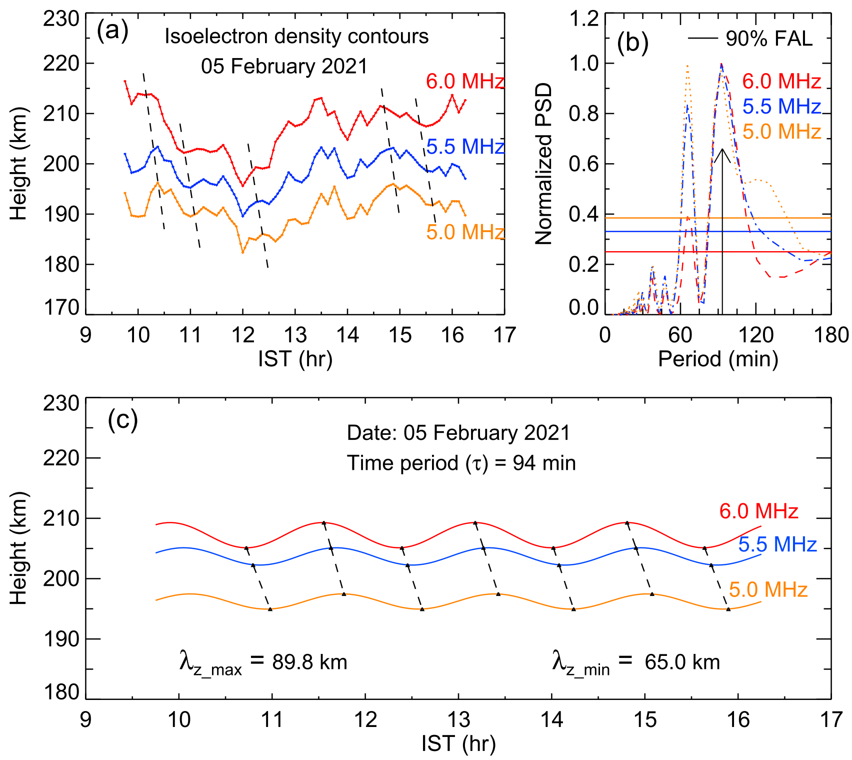

Figure 5. (a) Height variations of isoelectron densities corresponding to digisonde transmission frequencies of 5.0 (orange), 5.5 (blue), and 6.0 MHz (red). (b) The Lomb-Scargle periodogram of the isoelectron density height variations presented in (a), wherein a time period of 66 and 94 min are found to be significant and present in all of them. (c) Height variations of isoelectron density contours filtered for the gravity wave of time period of 94 min.

10 days of bi-directional mode of operation of optical data. Among the 10 days of data vertical propagation is seen to be existing on 7 days. In an earlier study (Mandal & Pallamraju, 2020), based on the analyses of 2 years of data, it has been shown that the vertical propagation of gravity waves is present on only around 40% of the days. This study revealed that although gravity waves are omnipresent, not on all days they propagate upwards as also seen from the results of the present study. In these seven days, the time periods and vertical wavelengths are found to be in the range of 37–143 min and 26–247 km, respectively (listed in Table 1). For a given day, only the time periods of gravity waves which showed vertical propagation are listed in the Table. The time periods in bold fonts correspond to those with a match between the optical and the radio measurements within the temporal window of the Brunt-Väisälä period. Thus, they combinedly are considered to represent the characteristics of the three-dimensional gravity wave on that day. Therefore, collocated and simultaneous optical and radio measurements, enable obtaining unique information on the horizontal and vertical propagation characteristics of the daytime thermospheric gravity wave.

4. Results

We have used the horizontal characteristics to estimate the vertical scale sizes of gravity waves. All the three-dimensional characteristics have been used to estimate horizontal winds. These estimates have been compared with the measured values and they are described in the sections below.

4.1. Estimation of Vertical Scale Sizes Using Gravity Wave Dispersion Relation

We used the gravity wave dispersion relation to estimate the gravity wave vertical scale sizes from the measured horizontal wave propagation characteristics as obtained by optical measurement. In the thermosphere, the strength of the wave dissipating factors such as molecular viscosity, thermal diffusivity, and ion-drag increase and cause dissipation of the upward propagating gravity waves. These forces are more prominent in the upper thermosphere above 300 km as shown in earlier studies (Fukao et al., 1993; Nicolls et al., 2012; Oliver et al., 1997; Vadas & Nicolls, 2012). Oliver et al. (1997) have shown that the thermospheric gravity wave characteristics obtained by the MU radar match with those of the non-dissipative gravity waves. They found that at around 500 km there are no downward phase propagations of gravity waves. Further, Nicolls et al. (2012) reported growth in amplitudes of the gravity waves with height in the altitude range of 200–300 km, which suggest that these gravity waves are not dissipating at these altitudes. In this work, we have used the OI 630.0 nm dayglow emission to study the horizontal propagation of thermospheric gravity waves and the peak emission altitude of this dayglow is around 230 km, which is in the non-dissipative region of gravity waves. Therefore, we have used the Hines' dispersion relation (Hines, 1960) of non-dissipating gravity waves for the estimation of vertical scale sizes of these observed gravity waves.

$$\omega_I^2 = k_H^2 \, * \, N^2/\left(k_H^2 + k_z^2 + 1/4H^2\right) \tag{2}$$

where, ω_I = intrinsic frequency, k_z = vertical wave number, and k_H = horizontal wave number of the gravity wave; H = scale height (=kT/mg, where k is the Boltzmann constant, T is neutral temperature, and m is the atomic mass); and N = Brunt-Väisälä frequency (=[$2g^*/5H$]1/2, where g* is the gravitational acceleration at observation altitude).

The intrinsic and observed frequencies of the observed gravity waves are related as,

$$\omega_I = \omega - k_H \,.U \cos(\Delta\theta) \tag{3}$$

where ω = observed angular frequency; U = horizontal neutral wind; and $\Delta\theta$ = angle between the propagation directions of gravity waves and horizontal winds.

Here, we have used the values of ω, k_H, and θ_H obtained from the analyses of OI 630.0 nm dayglow data (refer to Figures 1, 2, and 4). The NRLMSISE-00 model-derived values corresponding to an altitude of 230 km over Ahmedabad have been used to calculate N and H. In addition to these, HWM14 model-derived (Drob et al., 2015) horizontal wind profiles (directions and magnitudes) corresponding to an altitude of 230 km over Ahmedabad, have been used as inputs in the dispersion relation (Equation 2). In this way, we have estimated the gravity wave vertical scale sizes throughout the day, whenever λ_H measurements are available. For comparison, such

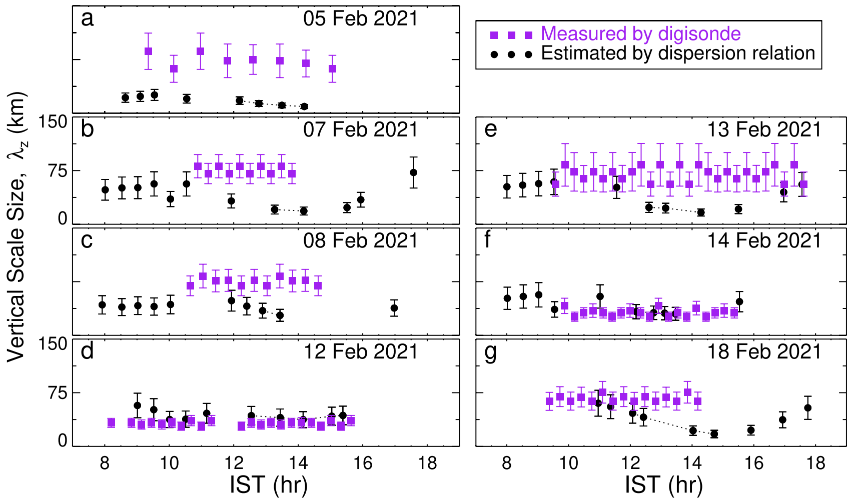

Figure 6. (a) Estimated values of λ_z from the dispersion relation are shown in black-circles and violet-squares are the measured values of λ_z from digisonde data for 5 February 2021. Panels (b–g) show the results as shown in Panel (a), but for 7, 8, 12, 13, 14, and 15 February 2021, respectively. The values connected by black-dotted lines represent those which have used interpolated λ_y values as described in the text.

estimations have been carried out for all 7 days, when measured values of λ_z are also available from collocated digisonde measurements. Also, these calculations have been carried out only for the common time periods, as observed in both optical and radio measurements (listed in Table 1 in bold fonts). These are presented in different panels in Figure 6 by black circles.

4.2. Comparison of Estimated Vertical Scale Sizes With Those Obtained From Digisonde Measurements

In Section 3.2, we have discussed the details of the digisonde data analyses to obtain vertical scale sizes (λ_z) of the upward propagating gravity waves. Thus, we have carried out a comparison of the estimated λ_z from the dispersion relation (as described in Section 4.1) with the measured values of λ_z as obtained from digisonde for all 7 days (Figure 6). Here, the violet-colored squares represent the measured values of λ_z resulted from the analyses of digisonde-derived isoelectron density contours (as discussed in Section 3.2). From this figure, one can appreciate the fact that the estimated λ_z values match reasonably well on some days with those measured independently from digisonde. However, there are days (5, 7, and 8 February) when the matching is not encouraging. One of the reasons could be that the model-derived winds and neutral atmospheric parameters may not accurately represent the upper atmospheric behavior on those days. Out of these two, the model-derived winds have a higher uncertainty in their values compared to the neutral atmospheric parameters. In a recent study, it has been shown that the optical dayglow emissions are influenced by the meridional (poleward) winds as they transport the constituents spatially (Kumar et al., 2022). Thus, this comparison serves as a motivation to explore the possibility of obtaining values of thermospheric neutral winds using the measured characteristics of gravity waves, information on which is very limited in the daytime. Such an effort has been carried out as described below and shown in the supplementary data.

4.3. Estimation of Thermospheric Neutral Winds

So far, we have seen that the vertical scale sizes estimated from gravity wave dispersion relation, match reasonably well on many occasions with those measured independently by radio technique. For the estimation of vertical scale sizes using the dispersion relation, we have used the HWM14 model-derived neutral winds which, being climatological in nature, is not expected to represent the true behavior of the atmosphere on a given day, especially, if there are some developments away from the normal. Nevertheless, in the present work, as we have with us the measured values of gravity wave parameters in all three dimensions, this presents a unique possibility of obtaining information on the ambient neutral winds. Thus, we have made such an attempt, wherein, the measured

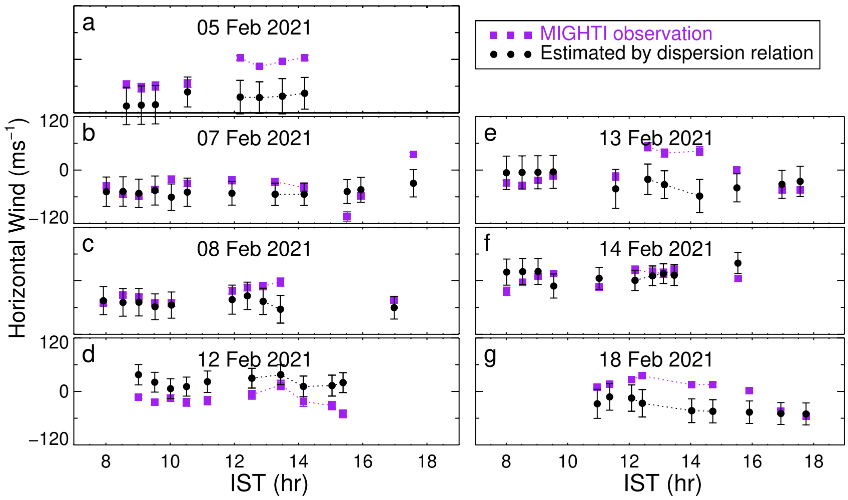

Figure 7. (a) Estimated horizontal wind magnitudes along the direction of wave propagation are shown by black-dotted line for 5 February 2021. Violet-colored squares represent the measured wind magnitudes along the wave propagation direction as obtained from the MIGHTI on-board ICON satellite. Panels (b–g) show the results as shown in Panel (a) but for 7, 8, 12, 13, 14, and 18 February 2021, respectively. The values joined by dotted lines correspond to those where λ_y values are interpolated as described in text.

values have been used, as inputs, into the gravity wave dispersion relation to obtain the thermospheric neutral winds. The results so obtained are discussed below.

All the measured horizontal and vertical propagation characteristics of gravity waves obtained by the collocated optical and radio observations are used as inputs in Equations 2 and 3 along with the NRLMSISE-00 model-derived neutral atmospheric parameters. Then these equations are solved for the wind values along the direction of wave propagations. Since the times corresponding to the measured values of λ_z from digisonde are different from those obtained for λ_H from optical data (as can be seen in Figure 6), the nearest measured λ_z value(s) have been considered for a given time in this calculation. The estimated wind magnitudes as a function of time for each of these days are shown in different panels as black-circles in Figures 7a–7g. Thus, by using this method, neutral winds in the direction of gravity propagation have been estimated.

4.4. Comparison of Neutral Wind Derived by the 3-D Gravity Waves With Measured MIGHTI Winds Onboard ICON

Recently, with the launch of the ICON satellite, thermospheric wind measurements became available through MIGHTI. This provides us with an opportunity to compare the estimated winds by the present method with those measured by MIGHTI. However, these measured winds cannot be readily used for comparison, as MIGHTI winds are not available for all times at a given location. Therefore, to obtain the diurnal variation of these measured neutral winds over our observational location, Ahmedabad, we have used a methodology described in one of our earlier works (Kumar et al., 2022). In this method, we use the HWM14 (Drob et al., 2015) model-derived winds to describe the climatological variations between the latitude of interest and the latitude of MIGHTI observations in a longitude region at a given time. We use the MIGHTI winds to provide the corrections to the HWM14 winds at the location of our interest. Thus, the difference between the HWM14 model winds and the observed MIGHTI winds for a given latitude of MIGHTI observation has been added to the HWM14 model-derived winds for a latitude of our interest.

In the present case, a ±5° longitudinal region centered at Ahmedabad is considered and the latitudes at which MIGHTI winds are available at different times in that longitude region are noted. As mentioned above, the difference between the HWM14 and MIGHTI measured winds at that location is added to the HWM14 winds over Ahmedabad at a given time and thereby we obtain the diurnal variation in winds over Ahmedabad. This 'MIGHTI added HWM14 winds' method was successfully applied in the earlier study (Kumar et al., 2022) to obtain neutral winds over Ahmedabad, and interesting dynamics of meridional winds versus OI 630.0 nm dayglow emissions intensity variation were obtained. While this method provides neutral winds over Ahmedabad, for it to be compared with the estimated winds in the present study, measured winds along the direction of wave propagation are required to be considered. For this, the cosine components of these winds are calculated along the direction of wave propagation using the measured angle between the wind and wave propagation directions as shown in Figure 4. Here, the wind propagation directions are calculated using the magnitude of zonal and meridional winds and are shown as black-colored arrows in Figure 4. In this way, the magnitude of measured thermospheric winds by MIGHTI on-board ICON satellite are calculated along the wave propagation directions and they are shown by violet-colored lines in Figures 7a–7g. It can be appreciated that these winds, derived through independent measurements: one estimated using the measured gravity wave parameters in three dimensions from collocated ground-based optical and radio measurements; and the other measured from the ICON satellite, show a very good match. Therefore, the characterization of gravity waves in three dimensions from ground-based measurements can be used to obtain a very good estimate of daytime thermospheric winds at a very high temporal resolution.

5. Discussion

We have presented a new approach and a new possibility of obtaining (a) vertical scale sizes of gravity waves in the daytime by using only the optical measurements (Section 4.1), and (b) thermospheric neutral winds by using coupled optical and radio measurements (Section 4.3). All these measurements and model outputs are independent of one another. The match in the parameters derived in the present study, namely, (a) estimated λ_z from the optical technique with the measured λ_z by radio technique (Section 4.2), and (b) estimated horizontal winds by the combined optical and radio measurements with the MIGHTI observed horizontal winds (Section 4.4), are remarkable. However, there are deviations in such comparison between the estimated and measured values of λ_z as noted on 5, 7, and 8 February 2021 (Figures 6a–6g) along with a few times on other days. It is well-known that the upper atmosphere is a highly dynamic and coupled system, with winds controlling the horizontal and vertical scale sizes of gravity waves. The neutral winds in the same/opposite direction of gravity wave propagation increase/decrease the horizontal scale sizes. Accordingly, the magnitude of vertical scale sizes decreases/increases (e.g., Mandal et al., 2019; Mandal & Pallamraju, 2020; Pallamraju et al., 2016; Vadas et al., 2009). Thus, horizontal propagation characteristics, which are used as inputs in gravity wave dispersion relation, are sensitive to surrounding wind fields. In this background, the differences between the estimated and measured values of λ_z on 5, 7, and 8 February 2021 could be understood as the estimated winds on 7 and 8 February, show a good match with measured winds from MIGHTI throughout the day. On 5 February, winds obtained by the two techniques match reasonably well except around noon-time. On some of the days (5, 13, and 18 February 2021), the values of estimated and measured winds around noon time as shown in Figure 7 do not match with each other. The possible reason of this difference could be that the λ_H and θ_H values in this duration were interpolated and not measured as discussed in Section 3.1. Nevertheless, by reducing the duration of optical observation in the zonal direction and carefully allowing a few meridional observations, this time gap can be reduced, which will be attempted in the future.

We further carried out an exercise to estimate λ_z using these measured winds instead of HWM14 model-derived winds. In that case, the estimated λ_z values have been found to show a good agreement with the measured ones (as shown in Figure S1). This further strengthens the discussion carried out in Section 4.2 that the locally varying neutral dynamics, do not get accurately described by the outputs of climatological models (HWM14 and NRLMSISE-00) at all times. This could be the probable source of deviations between the measured and estimated values of λ_z and winds on some occasions (Figures 6 and 7).

Here, one should note that it is not possible to estimate the neutral winds only by using optical measurements as there are two unknown parameters in the dispersion relation, namely, λ_z and time period, which need to be ascertained first. While various gravity wave parameters can be derived from the optical data and digisonde data independently, the key is to track the time period of gravity waves that are common in both optical and radio measurements. Attention is drawn to Table 1, wherein, the nearly similar values of time periods in the optical and radio measurements are listed in bold fonts, which are attributed to corresponding to the same wave. Thus, the gravity wave information obtained by the combined optical and radio measurements complement each other in describing the three-dimensional characteristics of gravity waves in the daytime from the ground-based measurements at an unprecedented temporal resolution. These describe the three-dimensional structure of the gravity wave characteristics accurately, which are also confirmed by the encouraging comparison between the horizontal winds derived by our measurements and those measured independently on-board ICON satellite. Results such as these provide new directions for the investigation of the upper atmospheric neutral dynamics from ground-based measurements. These results and approach described assume a greater significance, as it is now possible to derive thermospheric neutral winds from ground-based techniques as this is a very challenging task, especially in daytime conditions. This result, to the best of our knowledge, is first of its kind, wherein the intriguing nature of interaction between the thermospheric neutral winds and gravity waves in the daytime has been demonstrated experimentally using high cadence ground-based experiments.

6. Summary

Detailed analyses of daytime airglow emission variations and digisonde-derived height profiles of electron densities have been carried out to characterize the thermospheric gravity waves in three dimensions in the daytime. Different parameters that characterize the atmospheric gravity waves are obtained/derived by using measurements, such as, time periods observed in the optical data, time periods observed in the radio data, λ_x, λ_y, λ_H, phase propagation angle from the east, estimated and measured λ_z are listed in Table 1. Out of the 10 days of bi-directional mode of operation of MISE, the vertical propagations of gravity wave are found to exist on 7 days. In this period, gravity wave parameters, such as, time period, θ_H, λ_x, λ_y, λ_H, and λ_z obtained from optical and radio measurements are found to be varying in the range of 31–138 min, 203°–248° from east, 88–344, 123–344, 78–243, and 26–247 km, respectively. Further, we have used these horizontal propagation characteristics of gravity waves obtained from large FOV optical measurements of OI 630.0 nm dayglow along with the model-derived winds and neutral atmospheric parameters to estimate the vertical scale sizes of these waves. The estimated vertical scale sizes show a reasonable match with those obtained from the analyses of digisonde-derived isoelectron density height variations. As the combined measurements describe the gravity wave in three-dimension very well, we have used all the measured wave parameters in the gravity wave dispersion relation to estimate the thermospheric neutral winds along the wave propagation direction. These estimated wind magnitudes show a reasonable match with those measured by MIGHTI added HWM14 model-derived winds. These results make the present work very unique, and it is expected that such findings on the daytime thermospheric neutral gravity waves and wind dynamics provide new directions and insights into the investigation of the upper atmospheric research.

Data Availability Statement

ICON data are processed in the ICON Science Data Center at UCB and available at https://icon.ssl.berkeley.edu/Data. The NRLMSISE-00 model-data are available at http://ccmc.gsfc.nasa.gov/modelweb/models/nrlmsise00.php. Text files needed to reproduce the figures presented in this paper can be accessed from: https://osf.io/rg3xs/.

Acknowledgments

The optical and digisonde experiments are conducted and maintained by the Physical Research Laboratory, Ahmedabad, India. The data can be made available by contacting the corresponding author. The neutral winds data are obtained from the ICON satellite, which is supported by NASA's Explorers Program through contracts NNG12FA45C and NNG12FA42I. The authors sincerely acknowledge the help of Pradip Suryawanshi, Kshitiz Upadhyay, and Mohit Soni during the field campaigns. This work is supported by the Department of Space, Government of India.

References

Alexander, M. J. (1996). A simulated spectrum of convectively generated gravity waves: Propagation from the tropopause to the mesopause and effects on the middle atmosphere. *Journal of Geophysical Research*, *101*(D1), 1571–1588. https://doi.org/10.1029/95JD02046

Alexander, M. J., Beres, J. H., & Pfister, L. (2000). Tropical stratospheric gravity wave activity and relationships to clouds. *Journal of Geophysical Research: Atmosphere*, *105*(D17), 22299–22309. https://doi.org/10.1029/2000JD900326

Burnside, R., Herrero, F., Meriwether, J., Jr., & Walker, J. (1981). Optical observations of thermospheric dynamics at Arecibo. *Journal of Geophysical Research*, *86*(A7), 5532–5540. https://doi.org/10.1029/JA086iA07p05532

Djuth, F., Sulzer, M., Gonzales, S., Mathews, J., Elder, J., & Walterscheid, R. (2004). A continuum of gravity waves in the Arecibo thermosphere? *Geophysical Research Letters*, *31*(16), L16801. https://doi.org/10.1029/2003GL019376

Drob, D. P., Emmert, J. T., Meriwether, J. W., Makela, J. J., Doornbos, E., Conde, M., et al. (2015). An update to the horizontal wind model (HWM): The quiet time thermosphere. *Earth and Space Science*, *2*(7), 301–319. https://doi.org/10.1002/2014EA000089

Englert, C. R., Harlander, J. M., Brown, C. M., Marr, K. D., Miller, I. J., Stump, J. E., et al. (2017). Michelson interferometer for global high-resolution thermospheric imaging (MIGHTI): Instrument design and calibration. *Space Science Reviews*, *212*(1), 553–584. https://doi.org/10.1007/s11214-017-0358-4

Francis, S. H. (1973). Acoustic-gravity modes and large-scale traveling ionospheric disturbances of a realistic, disturbances of a realistic, dissipative atmosphere. *Journal of Geophysical Research*, *78*(13), 2278–2301. https://doi.org/10.1029/JA078i013p02278

Fritts, D. C. (1982). Shear excitation of atmospheric gravity waves. *Journal of the Atmospheric Sciences*, *39*(9), 1936–1952. https://doi.org/10.1175/1520-0469

Fritts, D. C. (1984). Shear excitation of atmospheric gravity waves. Part I: Non-linear radiation from a free shear layer. *Journal of the Atmospheric Sciences*, *41*(4), 524–537. https://doi.org/10.1175/1520-0469

Fritts, D. C., & Alexander, M. J. (2003). Gravity wave dynamics and effects in the middle atmosphere. *Review of Geophysics*, *41*(1), 1003. https://doi.org/10.1029/2001RG000106

Fukao, S., Yamamoto, Y., Oliver, W., Takami, T., Yamanaka, M., Yamamoto, M., et al. (1993). Middle and upper atmosphere radar observations of ionospheric horizontal gradients produced by gravity waves. *Journal of Geophysical Research*, *98*(A6), 9443–9451. https://doi.org/10.1029/92JA02846

Gerrard, A. J., & Meriwether, J. W. (2011). Initial daytime and nighttime SOFDI observations of thermospheric winds from Fabry-Perot Doppler shift measurements of the 630-nm OI line-shape profile. *Annales Geophysicae*, *29*(9), 1529–1536. https://doi.org/10.5194/angeo-29-1529-2011

Herrero, F., Mayr, H., & Spencer, N. (1988). Low latitude thermospheric meridional winds between 250 and 450 km altitude: AE-E satellite data. *Journal of Atmospheric and Terrestrial Physics*, *50*(10–11), 1001–1006. https://doi.org/10.1016/0021-9169(88)90087-6

Hickey, M., & Cole, K. (1988). A numerical model for gravity wave dissipation in the thermosphere. *Journal of Atmospheric and Terrestrial Physics*, *50*(8), 689–697. https://doi.org/10.1016/0021-9169(88)90032-3

Hines, C. O. (1960). Internal atmospheric gravity waves at ionospheric heights. *Canadian Journal of Physics*, *38*(11), 1441–1481. https://doi.org/10.1139/p60-150

Hocke, K., & K˙ampfer, N. (2009). Gap filling and noise reduction of unevenly sampled data by means of the Lomb-Scargle periodogram. *Atmospheric Chemistry and Physics*, *9*(12), 4197–4206. https://doi.org/10.5194/acp-9-4197-2009.,

Hocke, K., & Schlegel, K. (1996). A review of atmospheric gravity waves and travelling ionospheric disturbances: 1982-1995. *Annales Geophysicae*, *14*(9), 917–940. https://doi.org/10.1007/s00585-996-0917-6.,

Immel, T. J., England, S., Mende, S., Heelis, R., Englert, C., Edelstein, J., et al. (2018). The ionospheric connection explorer mission: Mission goals and design, design. *Space Science Reviews*, *214*(1), 1–36. https://doi.org/10.1007/s11214-017-0449-2

Karan, D. K., & Pallamraju, D. (2017). Small-scale longitudinal variations in the daytime equatorial thermospheric wave dynamics as inferred from oxygen dayglow emissions. *Journal of Geophysical Research: Space Physics*, *122*(6), 6528–6542. https://doi.org/10.1002/2017JA023891

Karan, D. K., & Pallamraju, D. (2018). Effect of geomagnetic storms on the day-time low-latitude thermospheric wave dynamics. *Journal of Atmospheric and Solar-Terrestrial Physics*, *170*, 35–47. https://doi.org/10.1016/j.jastp.2018.02.003.,

Kumar, S., Pallamraju, D., Suryawanshi, P., Vijayalakshmi, T., & Seemala, G. K. (2022). On the latitudinal variation in oi 630.0 nm dayglow emissions in response to the equatorial electrodynamic processes and neutral winds. *Advances in Space Research*, *69*(2), 926–938. https://doi.org/10.1016/j.asr.2021.10.034

Lakshmi Narayanan, V., Gurubaran, S., & Emperumal, K. (2010). Airglow imaging observations of small-scale structures driven by convective instability in the upper mesosphere over Tirunelveli (8.7°N). *Journal of Geophysical Research: Atmospheres*, *115*(D19), D19119. https://doi.org/10.1029/2009JD012937

Laskar, F. I., Pallamraju, D., Veenadhari, B., Lakshmi, T. V., Reddy, M. A., & Chakrabarti, S. (2015). Gravity waves in the thermosphere: Solar activity dependence. *Advances in Space Research*, *55*(6), 1651–1659. https://doi.org/10.1016/j.asr.2014.12.040

Li, J., & Lu, X. (2021). Global responses of gravity waves and zonal mean winds to the madden-julian oscillation and the latitudinal dependence of their relations using MERRA-2. *Geophysical Research Letters*, *48*(20), e2021GL094717. https://doi.org/10.1029/2021GL094717

Lomb, N. R. (1976). Least-squares frequency analysis of unequally spaced data. *Astrophysics and Space Science*, *39*(2), 447–462. https://doi.org/10.1007/BF00648343

Makela, J. J., Fisher, D. J., Meriwether, J. W., Buriti, R. A., & Medeiros, A. F. (2013). Near-continual ground-based nighttime observations of thermospheric neutral winds and temperatures over equatorial Brazil from 2009 to 2012. *Journal of Atmospheric and Solar-Terrestrial Physics*, *103*, 94–102. https://doi.org/10.1016/j.jastp.2012.11.019

Mandal, S., & Pallamraju, D. (2020). Thermospheric gravity wave characteristics in the daytime over low-latitudes during geomagnetic quiet and disturbed conditions. *Journal of Atmospheric and Solar-Terrestrial Physics*, *211*, 105470. https://doi.org/10.1016/j.jastp.2020.105470

Mandal, S., Pallamraju, D., Karan, D., Phadke, K., Singh, R., & Suryawanshi, P. (2019). On deriving gravity wave characteristics in the daytime upper atmosphere using radio technique. *Journal of Geophysical Research: Space Physics*, *124*(8), 6985–6997. https://doi.org/10.1029/2019JA026723

Mandal, S., Pallamraju, D., & Pant, T. (2022). Vertical propagation speeds of gravity waves in the daytime as a precursor to the onset of the equatorial spread-f. *Journal of Geophysical Research: Space Physics*, *127*(8). https://doi.org/10.1029/2022JA030401

Mandal, S., Pallamraju, D., & Suryawanshi, P. (2020). Changes in the daytime thermospheric gravity wave propagation characteristics over low-latitudes in response to the variation in solar flux. *Journal of Atmospheric and Solar: Terrestrial Physics*, *209*, 105414. https://doi.org/10.1016/j.jastp.2020.105414

Medvedev, A., & Klaassen, G. (2000). Parameterization of gravity wave momentum deposition based on nonlinear wave interactions: Basic formulation and sensitivity tests. *Journal of Atmospheric and Solar-Terrestrial Physics*, *62*(11), 1015–1033. https://doi.org/10.1016/S1364-6826(00)00067-5

Meriwether, J., Jr., Moody, J., Biondi, M., & Roble, R. (1986). Optical interferometric measurements of nighttime equatorial thermospheric winds at Arequipa, Peru. *Journal of Geophysical Research*, *91*(A5), 5557–5566. https://doi.org/10.1029/JA091iA05p05557

Miyoshi, Y., Fujiwara, H., Jin, H., & Shinagawa, H. (2014). A global view of gravity waves in the thermosphere simulated by a general circulation model. *Journal of Geophysical Research: Space Physics*, *119*(7), 5807–5820. https://doi.org/10.1002/2014JA019848

Nicolls, M., Vadas, S., Meriwether, J., Conde, M., & Hampton, D. (2012). The phases and amplitudes of gravity waves propagating and dissipating in the thermosphere, thermosphere: Application to measurements over Alaska. *Journal of Geophysical Research: Space Physics*, *117*(A5). https://doi.org/10.1029/2012JA017542

Oliver, W. L., Fukao, S., Yamamoto, Y., Takami, T., Yamanaka, M. D., Yamamoto, M., et al. (1994). Middle and upper atmosphere radar observations of ionospheric density gradients produced by gravity wave packets. *Journal of Geophysical Research*, *99*(A4), 6321–6329. https://doi.org/10.1029/94JA00171

Oliver, W. L., Otsuka, Y., Sato, M., Takami, T., & Fukao, S. (1997). A climatology of F region gravity wave propagation over the middle and upper atmosphere radar, radar. *Journal of Geophysical Research*, *102*(A7), 14499–14512. https://doi.org/10.1029/97JA00491

Pallamraju, D., Baumgardner, J., & Chakrabarti, S. (2002). Hirise: A ground-based high-resolution imaging spectrograph using echelle grating for measuring daytime airglow/auroral emissions (Vol. *64*). https://doi.org/10.1016/S1364-6826(02)00095-0

Pallamraju, D., Baumgardner, J., Chakrabarti, S., & Pedersen, T. R. (2001). Simultaneous ground based observations of an auroral arc in daytime/twilighttime OI, OI 630.0 nm emission and by incoherent scatter radar. *Journal of Geophysical Research*, *106*(A4), 5543–5549. https://doi.org/10.1029/2000JA000244

Pallamraju, D., Baumgardner, J., Singh, R. P., Laskar, F. I., Mendillo, C., Cook, T., et al. (2014). Daytime wave characteristics in the mesosphere lower thermosphere region: Results from the balloon-borne investigations of regional-atmospheric dynamics experiment. *Journal of Geophysical Research: Space Physics*, *119*(3), 2229–2242. https://doi.org/10.1002/2013JA019368

Pallamraju, D., & Chakrabarti, S. (2006). Contributions of imaging echelle spectrographs to daytime optical aeronomy. *Journal of Atmospheric and Solar-Terrestrial Physics*, *68*(13), 1459–1471. https://doi.org/10.1016/j.jastp.2005.05.013

Pallamraju, D., Das, U., & Chakrabarti, S. (2010). Short-and long-timescale thermospheric variability as observed from oi 630.0 nm dayglow emissions from low latitudes. *Journal of Geophysical Research*, *115*(A6). https://doi.org/10.1029/2009JA015042

Pallamraju, D., Karan, D. K., & Phadke, K. A. (2016). First three dimensional wave characteristics in the daytime upper atmosphere derived from ground-based multiwavelength oxygen dayglow emission measurements. *Geophysical Research Letters*, *43*(11), 5545–5553. https://doi.org/10.1002/2016GL069074

Pallamraju, D., Laskar, F. I., Singh, R. P., Baumgardner, J., & Chakrabarti, S. (2013). MISE: A multiwavelength imaging spectrograph using echelle grating for daytime optical aeronomy investigations. *Journal of Atmospheric and Solar-Terrestrial Physics*, *103*, 176–183. https://doi.org/10.1016/j.jastp.2012.12.003

Pitteway, M. L. V., & Hines, C. O. (1963). The viscous damping of atmospheric gravity waves. *Canadian Journal of Physics*, *41*(12), 1935–1948. https://doi.org/10.1139/p63-194

Pramitha, M., Venkat Ratnam, M., Taori, A., Krishna Murthy, B., Pallamraju, D., & Vijaya Bhaskar Rao, S. (2015). Evidence for tropospheric wind shear ex-citation of high-phase-speed gravity waves reaching the mesosphere using the ray-tracing technique. *Atmospheric Chemistry and Physics*, *15*(5), 2709–2721. https://doi.org/10.5194/acp-15-2709-2015

Raghavarao, R., Sridharan, R., Sastri, J. H., Agashe, V. V., Rao, B. C. N., Rao, P. B., & Somayajulu, V. V. (1988). *The equatorial ionosphere; wits handbook world ionosphere/thermosphere study* (Vol. 1). SCOSTEP Secretariat, University of Illinois,

Richmond, A. (1978). Gravity wave generation, propagation, and dissipation in the thermosphere. *Journal of Geophysical Research*, *83*(A9), 4131–4145. https://doi.org/10.1029/ja083ia09p04131

Sato, K., Hashiguchi, H., & Fukao, S. (1995). Gravity waves and turbulence associated with cumulus convection observed with the uhf/vhf clear-air Doppler radars. *Journal of Geophysical Research*, *100* (D4), 7111–7119. https://doi.org/10.1029/95JD00198

Scargle, J. D. (1982). Studies in astronomical time series analysis. II-Statistical aspects of spectral analysis of unevenly spaced data. *The Astrophysical Journal*, *263*, 835–853. https://doi.org/10.1086/160554

Shepherd, G. G., Thuillier, G., Gault, W., Solheim, B., Hersom, C., Alunni, J., et al. (1993). Windii, the wind imaging interferometer on the upper atmosphere research satellite. *Journal of Geophysical Research*, *98*(D6), 10725–10750. https://doi.org/10.1029/93JD00227

Shiokawa, K., Otsuka, Y., & Ogawa, T. (2009). Propagation characteristics of night-time mesospheric and thermospheric waves observed by optical mesosphere thermosphere imagers at middle and low latitudes. *Earth Planets and Space*, *61*, 479–491. https://doi.org/10.1186/bf03353165

Singh, R. P., & Pallamraju, D. (2016). Effect of cyclone Nilofar on mesospheric wave dynamics as inferred from optical nightglow observations from Mount Abu, India. *Journal of Geophysical Research*, *121*(6), 5856–5867. https://doi.org/10.1002/2016JA022412

Smith, A. K., & Lyjak, L. V. (1985). An observational estimate of gravity wave drag from the momentum balance in the middle atmosphere. *Journal of Geophysical Research*, *90*(D1), 2233–2241. https://doi.org/10.1029/JD090iD01p02233

Solomon, S. C., & Abreu, V. J. (1989). The 630 nm dayglow. *Journal of Geophysical Research: Space Physics*, *94*(A6), 6817–6824. https://doi.org/10.1029/JA094iA06p06817

Taylor, M. J., Bishop, M. B., & Taylor, V. (1995). All-sky measurements of short period waves imaged in the OI(557.7 nm), Na(589.2 nm) and near infrared OH and O_2(0, 1) nightglow emissions during the aloha-93 campaign. *Geophysical Research Letters*, *22*(20), 2833–2836. https://doi.org/10.1029/95GL02946

Teitelbaum, H., Massebeuf, M., Fellous, J., Petitdidier, M., Christophe, J., & Blanco, F. (1981). Simultaneous measurements of meteor winds and green line intensity variations: Gravity waves and planetary waves. *Journal of Geophysical Research: Space Physics*, *86* (A9), 7767–7770. https://doi.org/10.1029/JA086iA09p07767

Vadas, S. (2007). Horizontal and vertical propagation and dissipation of gravity waves in the thermosphere from lower atmospheric and thermospheric sources. *Journal of Geophysical Research*, *112*(A6). https://doi.org/10.1029/2006JA011845.,

Vadas, S., & Fritts, D. C. (2004). Thermospheric responses to gravity waves arising from mesoscale convective complexes. *Journal of Atmospheric and Solar-Terrestrial Physics*, *66*(6–9), 781–804. https://doi.org/10.1016/j.jastp.2004.01.025

Vadas, S., Fritts, D. C., & Alexander, M. J. (2003). Mechanism for the generation of secondary waves in wave breaking regions. *Journal of the Atmospheric Sciences*, *60*(1), 194–214. https://doi.org/10.1175/1520-0469

Vadas, S., & Liu, H.-l. (2009). Generation of large-scale gravity waves and neutral winds in the thermosphere from the dissipation of convectively generated gravity waves. *Journal of Geophysical Research*, *114*(A10). https://doi.org/10.1029/2009JA014108

Vadas, S., & Nicolls, M. (2012). The phases and amplitudes of gravity waves propagating and dissipating in the thermosphere: Theory. *Journal of Geophysical Research*, *117*(A5). https://doi.org/10.1029/2011JA017426

Vadas, S., Yue, J., She, C.Y., Stamus, P. A., Liu, A. Z., Liu, H. L., et al. (2009). A model study of the effects of winds on concentric rings of gravity waves from a convective plume near Fort Collins on 11 May 2004. *Journal of Geophysical Research*, *114*(D6), D06104. https://doi.org/10.1029/2008JD011244

VanderPlas, J. T. (2018). Understanding the lomb–scargle periodogram. *The Astrophysical Journal - Supplement Series*, *236*(1), 16. https://doi.org/10.3847/1538-4365/aab76

Yiğit, E., Aylward, A. D., & Medvedev, A. S. (2008). Parameterization of the effects of vertically propagating gravity waves for thermosphere general circulation models: Sensitivity study. *Journal of Geophysical Research*, *113*(D19), D19106. https://doi.org/10.1029/2008JD010135

Yiğit, E., & Medvedev, A. S. (2009). Heating and cooling of the thermosphere by internal gravity waves. *Geophysical Research Letters*, *36*(14), L14807. https://doi.org/10.1029/2009GL038507

Earth, Planets and Space

EXPRESS LETTER

Open Access

Impact of strong and weak stratospheric polar vortices on geomagnetic semidiurnal solar and lunar tides

Sunil Kumar[1,2], Tarique A. Siddiqui[3*], Claudia Stolle[3], Nicholas M. Pedatella[4,5] and Duggirala Pallamraju[1]

Abstract

The impact of strong and weak stratospheric polar vortices on geomagnetic semidiurnal solar and lunar tides is investigated during Northern Hemisphere (NH) winters using ground-based magnetic field observations at the Huancayo (12.05° S, 284.67° E; magnetic latitude: 0.6° S) equatorial observatory. We analyze the periods between December 15 and March 1 for 34 NH winters between 1980 and 2020 and find that the response of semidiurnal solar and lunar tides as seen in geomagnetic field depends on the strength of the stratospheric polar vortex. During weak polar vortex events, geomagnetic semidiurnal solar and lunar tidal amplitudes show an average enhancement by ~ 25% and ~ 50%, respectively, which is consistent with the known results during sudden stratospheric warmings. When the stratospheric polar vortex is strong, geomagnetic semidiurnal solar and lunar tidal amplitudes decline on an average by ~ 15% and ~ 25%, respectively, during weak polar vortex events. Our results also reveal that the response of the geomagnetic semidiurnal solar tidal variations to strong and weak polar vortex conditions is delayed by approximately 10 days while the response of geomagnetic semidiurnal lunar tidal variations do not show a time delay. These results provide observational evidence that along with weak polar vortices in the Northern Hemisphere, the strong stratospheric polar vortices also have pronounced effects on the equatorial ionosphere.

Keywords Strong polar vortex, Weak polar vortex, Stratospheric Sudden Warming, Solar semidiurnal tide, Lunar semidiurnal tide, Equatorial electrojet, Northern Annular Mode, Ionosphere, MLT

*Correspondence:
Tarique A. Siddiqui
siddiqui@iap-kborn.de
Full list of author information is available at the end of the article

Graphical Abstract

Plots of geomagnetic semidiurnal solar and lunar tides responding to variability in the stratospheric polar vortex

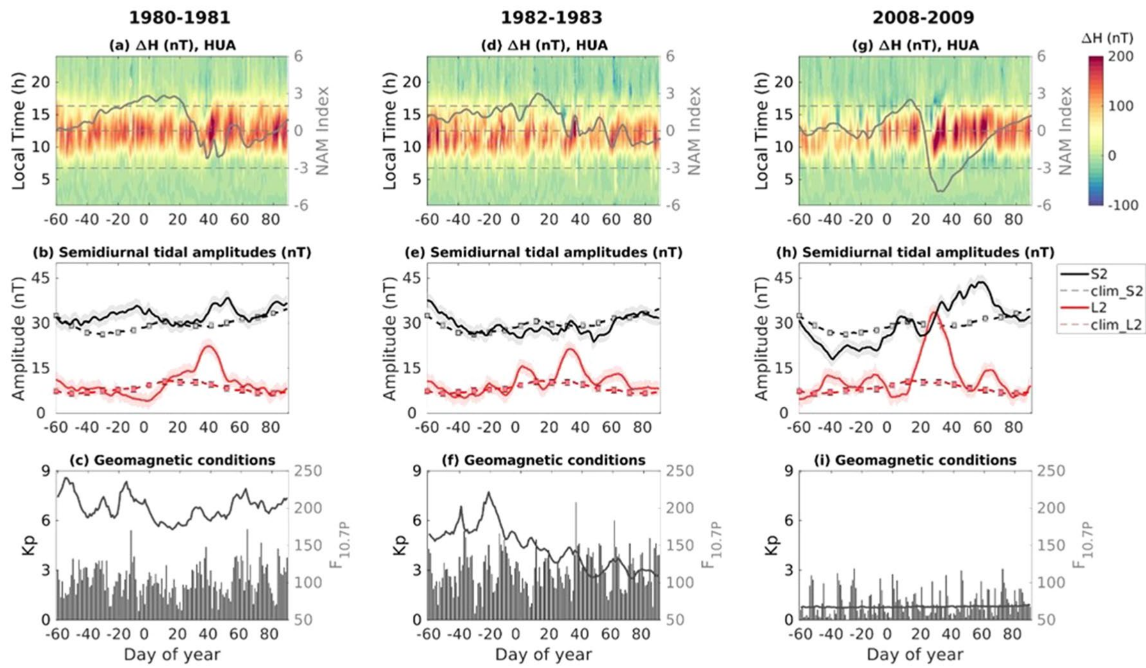

Introduction

During winter, the latitudinal variation in insolation causes a large-scale temperature gradient between mid-latitudes and the pole, which results in the formation of the polar vortex in the stratosphere (Baldwin et al. 2021). The stratospheric polar vortex (SPV) is characterized by a band of strong eastward winds that encircle the mid- to high- latitude polar region and span from about 100 hPa to above 1 hPa in altitude. The polar vortex extends well into the mesosphere (Harvey et al. 2018) but the strength of the mesospheric polar vortex is not considered in this study. The SPV experiences large inter-annual variability due to interaction with upward propagating planetary-scale waves that are forced from the troposphere (e.g., Charney and Drazin 1961; Matsuno 1971). These planetary waves (PWs) can propagate vertically and break in the polar stratosphere resulting in the deposition of westward momentum (McIntyre and Palmer 1983), which decelerates the eastward winds of the SPV. Air converges and descends at high-latitudes resulting in warming of the polar stratosphere. Owing to larger topographic and land-sea contrasts, the PWs in the Northern Hemisphere (NH) have larger amplitudes than in the Southern Hemisphere (SH) (e.g., Waugh 2017), which results in the NH SPV being weaker and more prone to distortion than the SH SPV (e.g., Waugh and Randel 1999). In the NH, a complete breakdown of SPV due to the disruption by PWs is relatively common and happens approximately every 2 years during extreme meteorological events called sudden stratospheric warmings (SSWs) (Charlton and Polvani 2007; Butler et al. 2015). In contrast, SSWs in the SH are rare and have so far only been observed in 2002 and 2019 during the month of September (e.g., Charlton et al. 2005; Yamazaki et al. 2020). During SSWs, a rapid rise in the polar stratospheric temperature by several tens of degrees is often accompanied by a breakdown of the SPV. SSWs are therefore associated with weak polar vortex conditions. Conversely, the development of a strong polar vortex takes place in the absence of strong tropospheric PW activity, which allows for uninterrupted radiative cooling and thereby strengthening of the SPV (e.g, Lawrence et al. 2020). In comparison to SSWs, extended periods of strong polar vortex conditions are relatively rare in the NH mainly because of the short-time scales on which PW forcing can act and rapidly change the state of the SPV (e.g., Lawrence and Manney 2018).

The weak and strong states of SPV play an important role in atmospheric coupling processes and thus have a wide range of impacts in different layers of the atmosphere (e.g., Baldwin et al. 2021; Pedatella and Harvey

2022). In recent decades, the impact of weak SPV conditions on the middle and upper atmospheres in the context of SSWs have been extensively investigated and it is now well-recognized that SSW associated effects can significantly change the dynamics and chemistry of mesosphere, thermosphere and ionosphere (e.g., Goncharenko et al. 2021; Laskar and Pallamraju 2015; Singh and Pallamraju 2015). The SSW-driven variability in the mesosphere and lower thermosphere (MLT) are primarily due to modified gravity wave (GW) forcing that results from the deceleration and reversal of eastward winds of SPV during SSWs (e.g., Holton 1983; Liu and Roble 2002). Additionally, the variability in the ionosphere and thermosphere during SSWs are primarily driven by changes in upward propagating migrating and nonmigrating solar and lunar tides, which result due to a combination of changes in background winds and tidal forcing conditions (e.g., Jin et al. 2012; Forbes and Zhang 2012). Here, tides refer to global-scale oscillations of the atmosphere that have harmonic periods of a solar or a lunar day (Lindzen and Chapman 1969). The upward propagating solar tides are thermally forced and are generated through periodic absorption of solar radiation by water vapour in the troposphere and ozone in the stratosphere whereas the upward propagating lunar tide is primarily forced in the lower atmosphere by the gravitational effects of the moon. For a detailed overview of the impacts of SSWs on the middle and upper atmospheres, the readers may refer to the following reviews by Chau et al., (2012), Baldwin et al., (2021) and Goncharenko et al., (2021). In contrast to the well-studied SSW effects, the impact of strong polar vortex events has only been considerably investigated in the troposphere (e.g., Baldwin and Dunkerton 2001) and is still relatively unknown in the middle and upper atmospheres.

In a recent work by Pedatella and Harvey (2022; hereafter PH22), the impact of strong and weak NH SPV on the MLT has been examined using the Specified Dynamics version of the Whole Atmosphere Community Climate Model with thermosphere-ionosphere eXtension (SD-WACCM-X) simulations. This was the first such study that compared the anomalies in tides, zonal-mean temperature and zonal-mean winds in the MLT during periods of strong and weak NH SPV. From their results, it was found that the response of zonal mean and tidal anomalies during strong SPV are generally opposite in comparison to those that occur during weak SPV periods. The authors further investigated the anomalies in selected atmospheric tides during strong and weak NH SPV time periods and found, in particular, that the migrating semidiurnal solar tide (SW2) shows the most notable change in the MLT with a 25–35% reduction in amplitudes at NH mid-latitudes during strong SPV time periods. During periods of weak SPV, an even stronger enhancement in SW2 tides was also identified from their results. In comparison, migrating diurnal solar tide (DW1) and non-migrating semidiurnal solar tides (SW1 and SW3) showed smaller changes during strong and weak NH SPV conditions. The work by PH22 did not consider the changes in migrating semidiurnal lunar tide (M2) during periods of either strong or weak SPV as the lunar tidal forcing was not explicitly included in the SD-WACCM-X simulations.

The changes seen in migrating and non-migrating solar tides from the results of PH22 during periods of strong NH SPV could potentially also lead to variability in the ionosphere as it is well-established that the upward propagating tides upon reaching the E-region dynamo heights contribute to the generation of ionospheric currents (e.g., Baker and Martyn 1953). One such current that results due to this ionospheric E-region wind dynamo phenomenon is the equatorial electrojet (EEJ), which is a narrow ribbon of intense current that flows during daytime above the magnetic dip equator. About one-half of the current intensity of the EEJ is driven by the upward-propagating tides (Yamazaki et al. 2014). The EEJ is confined to a latitudinal width of about ±3 deg and its high current density is primarily due to the horizontal geometry of the magnetic field lines, which in the presence of large-scale polarisation electric fields enable strongly enhanced (Cowling) conductivity in the ionospheric E-region. The EEJ causes significant magnetic field deflection at ground-based observatories that are located below the magnetic dip equator and therefore magnetic field recordings have been extensively utilized to investigate its various characteristics.

The results of PH22 in the MLT motivate us to compare the ionospheric variability of the semidiurnal solar and lunar tides during periods of strong and weak NH SPV. For this purpose, we use the magnetic field recordings at the Huancayo (HUA, 12.05° S, 284.67° E; magnetic latitude: 0.6° S) observatory to derive the geomagnetic semidiurnal solar and lunar tides. We find that in addition to the known enhancement in geomagnetic semidiurnal solar and lunar tides during periods of SSWs (weak SPV), these tides show a reduction during strong SPV but this decline is not as large as the enhancement during weak SPV conditions. These results demonstrate that in addition to SSWs, periods of strong SPV also lead to considerable impacts in the equatorial ionosphere.

Data set and analysis methods

Northern annular mode

The Northern Annular Mode (NAM) accounts for the dominant fraction of extratropical atmospheric circulation variability (e.g., Thompson and Wallace, 1998). In the troposphere, the NAM characterizes the meridional shifts in the tropical jet streams with its positive phase indicating an increase in the pressure gradient between the mid-latitudes and pole and a poleward displacement of the extratropical jet stream. In the stratosphere, the NAM characterizes the variability in the strength of stratospheric polar vortex (Baldwin and Dunkerton 2001). A positive NAM indicates a stronger than average stratospheric polar vortex and vice versa. In this study, we use the same time-series of NAM index that was used for analysis by PH22. Following the procedure of Gerber and Martineau (2018), the NAM index was calculated based on the average geopotential height anomalies poleward of 65°N at 10 hPa using the National Aeronautics and Space Administration (NASA) Modern-Era Retrospective analysis for Research and Applications version 2 (MERRA-2) reanalysis (e.g., Gelaro et al. 2017). The state of SPV is considered to be strong if the daily NAM at 10 hPa is >2.0 and weak if the daily NAM is <−3.0.

Geomagnetic semidiurnal solar and lunar tides

Hourly mean values of the horizontal component, H, of the geomagnetic field observed by the ground-based magnetometer at HUA have been used in this study to estimate the geomagnetic semidiurnal solar and lunar tides for the periods 1980–1991 and 1997–2020. For this purpose, we use a similar technique that has been applied to investigate the geomagnetic lunar tidal modulation in relation to SSWs in earlier studies by Yamazaki et al., (2012) and Siddiqui et al., (2015). The time period of our analysis is similar to the interval that was covered by PH22. The HUA data are available at the website of the World Data Centre (WDC) for Geomagnetism, Edinburgh and have been downloaded for the abovementioned periods. The data for the years 1991-1996 for HUA remain unavailable.

At the dip equator, the primary sources of the variations in the horizontal component of the geomagnetic field, H, include contributions from the Earth's main magnetic field (H_{MF}), the magnetospheric ring current (H_{MP}), and the induced magnetic field due to the large-scale solar quiet (Sq) currents (H_{Sq}) and the EEJ (H_{EEJ}).

$$H = H_{MF} + H_{MP} + H_{EEJ} + H_{Sq} \tag{1}$$

As Sq and EEJ currents effectively flow only during the daytime and disappear during the night (Malin and Gupta 1977), the quiet night-time values of H can be used to approximate H_{MF}. For this purpose, the mean of the night-time values between 23:30 and 02:30 LT for the five monthly International Quiet Days (IQDs) are used. The IQDs are the days where the geomagnetic variations are at a minimum in each month. These night-time values are subtracted from the daily recorded H data to remove the effects of the Earth's main magnetic field. During geomagnetically disturbed periods, notable reduction is seen in H due to the development of a westward ring current in the magnetosphere (e.g., Kamide and Maltsev 2007). To minimize this magnetospheric ring current effect, the Dst index is used. The contribution of the ring current (H_{MP}) is then removed from H by subtracting the Disturbance Storm Time (Dst) index.

$$\Delta H = H - H_{MF} - Dst \tag{2}$$

In equation 2, the daily variation ΔH represents the deviation from the quiet-night time levels. The variations in ΔH show a dependence on solar activity (Alken and Maus 2007) and in order to consider this dependence we use the solar flux values, $F_{10.7}$ (in solar flux unit (s.f.u) : $10^{-22}\text{Wm}^{-2}\text{Hz}^{-1}$). We calculate the index $F_{10.7P}$ using the observed value of $F_{10.7}$ for each day and its 81-day-centered average, $F_{10.7A}$, with the following relation:

$$F_{10.7P} = (F_{10.7} + F_{10.7A})/2 \tag{3}$$

and use it to normalize ΔH to a solar flux level of 150 s.f.u with the method described in Park et al., (2012) (see equation 1). We use the index $F_{10.7P}$ for normalizing ΔH since it is known that this index provides a better representation of the solar cycle variations of the solar extreme ultraviolet (EUV) radiation in comparison to $F_{10.7}$ alone (e.g., Richards et al. 1994).

The geomagnetic solar (S) tides control much of the daily variation in ΔH and its diurnal (S_1) and semidiurnal (S_2) components dominate the spectral components of ΔH. The geomagnetic solar tides in ΔH result due to the contribution of both upward propagating solar tides and in situ generated solar tides in the thermosphere (e.g., Forbes 1982a, 1982b). Additionally, there exist tidal components in ΔH that are dependent on the phase of the moon, which are called geomagnetic lunar (L) tides. As the atmospheric lunar tides are dominated by its semidiurnal component ($M2$; 12.421 h), the geomagnetic lunar semidiurnal (L_2) component dominates in L. The amplitude of L in ΔH is typically much smaller than the amplitude of S, owing to weaker tidal winds. However, on certain so-called 'big-L' days that usually occur during NH winters, the amplitude of L can become comparable or even larger than that of S (Bartels and Johnston 1940). Recent studies have pointed out that these 'big-L' days of enhanced lunar amplitudes are associated with the occurrence of SSWs (e.g., Fejer et al. 2010).

In this study, the S and L variations of ΔH are determined using the Chapman-Miller method that has been summarized in Malin and Chapman (1970). The components of S and L can be mathematically expressed as following:

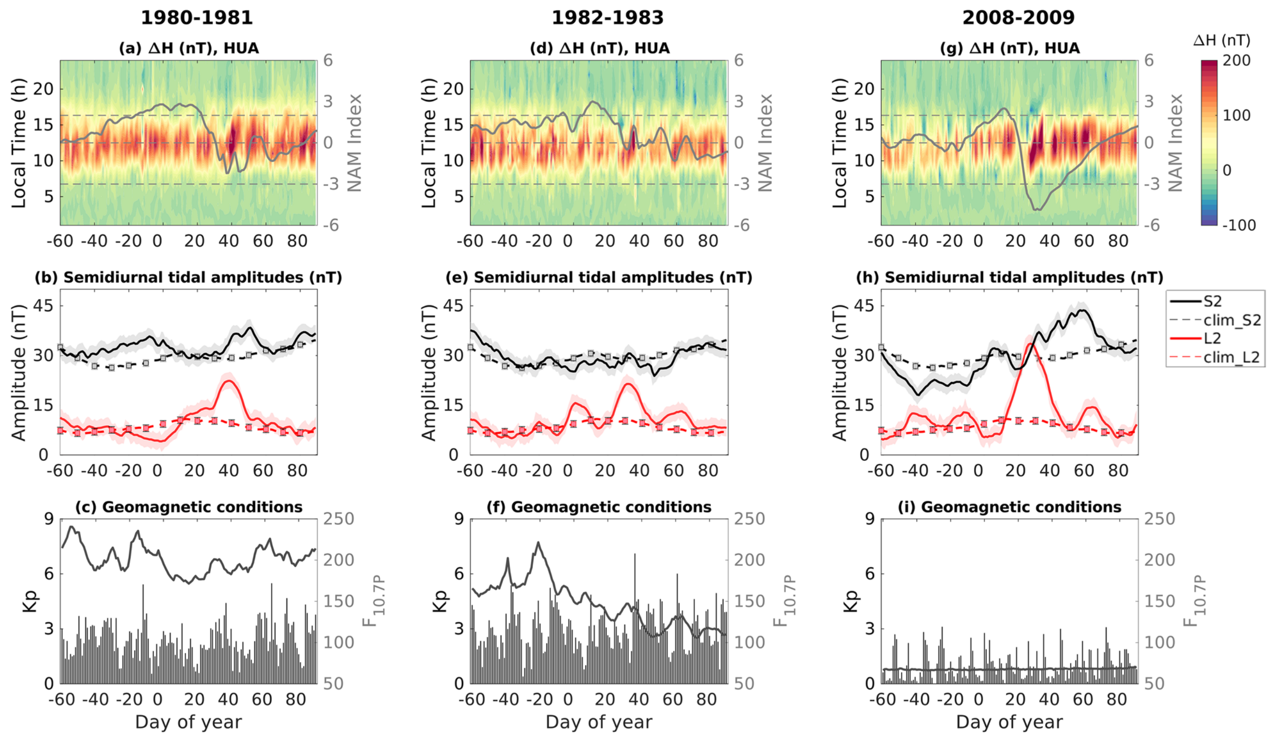

Fig. 1 Panels **a**, **d** and **g** show the local time variation of *ΔH* from 1st November to 31st March for the winters of years 1980–1981, 1982–1983 and 2008–2009, respectively. The solid gray lines in the top panels represent the NAM values, while dashed gray lines correspond to the NAM value of 2 and -3 associated with the reference values for strong and weak SPV, respectively. In panels **b**, **e** and **h**, the amplitudes of semidiurnal solar (solid black line) tide and its climatology (dashed black line) are shown for the same years as mentioned above. In a similar way, the amplitudes of semidiurnal lunar (solid red line) tide and its climatology (dashed red line) are shown in these figures. The gray and red shadings in these panels indicate the 95% confidence intervals of semidiurnal solar and lunar tides, respectively. The error bars indicate the 95% confidence intervals of the climatological tidal amplitudes. Panels **c**, **f** and **i** show the averaged daily Kp values in black bars and daily $F_{10.7P}$ levels in solid gray lines

$$S_n = s_n sin\left(\frac{2\pi}{24}nt + \sigma_n\right) \tag{4}$$

$$L_n = l_n sin\left(\frac{2\pi}{24}nt - \frac{2\pi}{24}(2\nu) + \lambda_n\right) \tag{5}$$

Here, S_n and L_n denote the nth component of S and L, respectively, with corresponding s_n and l_n amplitudes. The phases σ_n and λ_n denote the phase angle of the nth component of S and L, respectively. The lunar age in hours is denoted by ν and the solar local time in hours is denoted by t. The S and L variations are simultaneously determined by fitting their four respective Fourier coefficients to ΔH over a 21-day moving window through an ordinary least-squares (OLS) approach by using equations 4 and 5. The 21-day moving window has been chosen because it allows the separation of solar and lunar semidiurnal tides without generating any major artifacts and has been utilized in similar studies by Chau et al., (2015) and Conte et al., (2017).

Based on the common OLS approach, we employ the classical Gauss-Markov assumptions to estimate the standard errors (SE) of regression coefficients by taking the square root of the diagonal elements of the variance-covariance matrix of the OLS estimator (e.g., Greene 2018; see Chapter 4). Further, the s_n and l_n amplitudes are functions of OLS regression coefficients and error propagation formula (e.g., Taylor 1982; Montgomery, 2012; see Chapter 3) is applied to compute the standard errors of tidal amplitudes (SE_tidal). The 95% confidence interval of the estimated s_n and l_n amplitudes are then constructed using SE_tidal estimates (see Additional file 1 for complete mathematical derivations). The climatological amplitudes of s_n and l_n are obtained by computing the mean of the amplitudes over the 34 analyzed winter periods and its associated standard error (SE_clim) is estimated by SE_tidal/$\sqrt{34}$, which is then used to construct its 95% confidence interval. It is important to note that the amplitudes of S and L that are determined using this method include contributions from migrating and non-migrating semidiurnal solar and lunar tides, respectively.

For a more complete description of the efficacy of this method, the readers are referred to Siddiqui et al., (2018).

Results

Between 1980 and 2020, there are 24 winters with strong SPV, 12 winters with weak SPV and 4 winters with both strong and weak SPV (see the complete list of dates in the supplemental data of PH22). In Fig. 1, we present the S_2 and L_2 variations in ΔH during individual NH winters with both a strong and weak SPV. We select the winters in 1980–1981, 1982–1983 and 2008–2009 for this purpose. These time periods were also analyzed by PH22 (see their Fig. 3). In Figure 1a, the daily ΔH values that have been normalized to 150 s.f.u are presented between November 01, 1980 and March 31, 1981. In this figure, the daily diurnal variation of ΔH with a maxima during the local noontime can be easily identified. The variations in ΔH show a day-to-day variability that are almost entirely confined to daytime hours and these variations are caused by eastward-directed EEJ currents. In Fig. 1a, negative deflections in ΔH can also be seen during morning and evening hours, which are related to westward flow of current at these times and are referred to as counter-electrojets (e.g., Yamazaki and Maute 2017). The day-to-day variability of the NAM index is shown in bold gray line in this figure, the values of which are shown in the right y-axis. The dashed gray lines correspond to the NAM value of 2 and −3 associated with the reference values for strong and weak SPV, respectively. The amplitudes of S_2 (black line) and L_2 (red line) tides that are estimated from ΔH are presented along with their error estimates in Fig. 1b. The gray and red shadings indicate the 95% confidence intervals of S_2 and L_2 tidal amplitudes, respectively. The dashed black and red lines denote the climatological S_2 and L_2 tidal amplitudes, respectively, with the error bars indicating the 95% confidence intervals of these mean tidal amplitudes. In Fig. 1c, the bar plot presents the daily averaged Kp levels (black bars) and the gray lines correspond to the daily $F_{10.7P}$ levels during this time interval, the values of which are shown on the right y-axis. From Fig. 1c, we note that this time period was marked by high $F_{10.7P}$ levels and was also geomagnetically active on days -12 and 64 as the averaged daily Kp values remained high. As we account for variability due to geomagnetic activity and solar flux levels in ΔH and use a 21-day window for the estimation of tidal amplitudes, we think that any abrupt influence of geomagnetic effects on tides would be smoothed out. As it can be seen in Fig. 1a, the period between mid-December (day -15) and late January (day 23) was characterized by strong SPV conditions as the NAM index remained above 2 during this time. In response to strong SPV conditions, S_2 amplitudes in Fig. 1b decline from ~36 nT on day − 8 to below its climatological levels to ~30 nT by day 8 and remain at these levels until day 35. A more discernible decline is seen in L_2 with its amplitude showing a reduction from ~7 nT on day -30, which is close to its climatological levels, to ~4 nT by day 0. Compared to the slightly lagged response of S_2 to strong SPV conditions, the decline in L_2 amplitudes begin soon after the initial NAM increase from day -35 onward. After day 21, the SPV conditions begin to weaken and NAM starts to decline sharply and eventually reaches − 2 by day 37. It remains around this value until mid-February before recovering and rising to 0 in the beginning of March. During this weakening of SPV, a semidiurnal structure with its peak shifting to later local times on succeeding days is seen in ΔH appears around day 40 in Fig. 1a, which is associated with L_2 enhancement during SSWs (e.g., Chau et al. 2009; Fejer et al. 2010). Corresponding to this weakened state of SPV, we notice an enhancement in S_2 amplitudes in Fig. 1b as it rises above its climatological levels to ~36 nT by day 42 and peaks at ~39 nT on day 52. The response of L_2 to weakening SPV is slightly earlier than S_2 and its peak enhancement is seen on day 40 with an amplitude of ~22 nT, which is almost two times its climatological levels. As the SPV begins to recover in early March and NAM values increase from their minima, S_2 and L_2 amplitudes decline sharply. The L_2 amplitudes return back to their climatological levels by day 60 but S_2 amplitudes decline below their climatological levels for a few days in early March and gradually begin to return towards this level by the end of March. For this winter, the results of PH22 showed a decline in MLT SW2 amplitudes with a minima centered around day 10 and an enhancement with a maxima centered around day 40. We find that our observation of S_2 in ΔH is generally consistent with their findings for this event.

Similar to Fig. 1a, the daily normalized ΔH values are presented between November 01, 1982 and March 31, 1983 in Fig. 1d. From the NAM index, it can be seen that strong SPV conditions existed between late December and mid-January for this winter. The SPV weakens first in late January and early February and then again towards the end of February and from mid-March onward. However, it can be seen that based on the NAM index, the extent of weakening of the SPV is slightly reduced in comparison to the 1980-1981 winter. Fig. 1e shows that S_2 amplitudes respond to strong SPV conditions with a decline from ~30 nT on day -15 to below their climatological levels by day -8 and reach their minima of ~25 nT by day 2. The S_2 amplitudes show a small enhancement in response to declining NAM, which happens around day 0 to record a maxima of ~28 nT by day 8. As the NAM values rise again and reach a peak value of ~3 on day 11, S_2 amplitudes respond with a decline and reach their minima of ~26 nT by day 21. With a decline in NAM values in late January to levels below 0, S_2 amplitudes show an enhancement and rise above their climatological levels to ~31 nT on day 32 before falling back when NAM values increase after this day. Another enhancement in S_2 amplitudes happen towards the end of February when NAM values decline and SPV weakens, which result in S_2 amplitudes reaching above their climatological levels to ~33 nT after day 60.

Compared to S_2, the response of L_2 to the variability of NAM index is more easily recognizable for this winter in Fig. 1e as the minima and maxima in L_2 amplitudes are seen to occur concurrently with increasing and decreasing NAM values, respectively. With a local minima in NAM values around day −20, an enhancement can be seen in L_2 with its amplitude rising just above its climatological levels to ~10 nT. Thereafter, as NAM values increase and relatively stronger SPV conditions exist until day −5, L_2 amplitudes decline below their climatological levels to ~6 nT. Another local minima in NAM ensues around day 0 and L_2 amplitudes enhance to a local maxima of ~15 nT on day 1. As NAM rises above 2 between day 0 and 20, L_2 amplitudes fall below their climatological amplitudes under this strong SPV conditions. Once NAM begins its sharp decline in late January, L_2 amplitudes rise to a maxima of ~22 nT on day 31. Associated with this L_2 tidal enhancement, the local time shifting semidiurnal structure in ΔH again appears between days 30 and 40 in Fig. 1d. In association with declining NAM, the appearance of afternoon depression in ΔH around 15 LT on day 30 can be noticed in Fig. 1d. These depressions are caused by westward counter-electorjet currents that have been reported to be associated with weak SPV conditions (e.g., Fejer et al. 2010). In Fig. 1e, a decline is seen in L_2 amplitudes again as they fall back close to their climatological levels by day 50 when NAM values increase above 0 after day 46 and peak around day 50. Another enhancement in L_2 is also seen when NAM values decline below 0 around day 60. We note from Fig. 1f that this time period was marked by moderate-to-high $F_{10.7P}$ levels and was also geomagnetically active especially on day 61 as the averaged daily Kp values reached above 6 on this day.

The daily normalized ΔH values are presented between November 01, 2008 and March 31, 2009 in Fig. 1g. From Fig. 1i, we note that this time period was marked by low $F_{10.7P}$ levels and was also geomagnetically quiet as the averaged daily Kp values remained low. In Fig. 1g, the NAM values remain around 0 in November and mid-December before gradually rising to levels above 2 between late December and mid-January. Higher NAM values correspond to strong SPV conditions during these times. In late January, the NAM values decline sharply to levels below −3 and remain there until mid-February before gradually rising and returning to 0 by mid-March. The period between late January and mid-February correspond to weak SPV conditions, which resulted in the strong 2009 SSW event. Corresponding to strong SPV conditions, L_2 amplitudes in Fig. 1h decline from ~13 nT in late December to reach below their climatological levels to ~5 nT in mid-January. When SPV conditions become weak in late January, L_2 amplitudes increase to more than 3 times their climatological levels and reach ~33 nT by day 28. With the increase in L_2 amplitudes, strong depressions in ΔH associated with counter-electrojets is seen around day 26 between 12 and 15 LT in Fig. 1g. Additionally, the development of a multi-day semidiurnal pattern with enhancement of ΔH in morning hours and weakening in the afternoon hours that shifts in time on succeeding days can be seen between days 27 and 35 in this figure. This feature in ΔH is characteristic of enhanced lunar effects during SSWs and it has also been observed in equatorial F region vertical plasma drifts (e.g., Chau et al. 2009). With the subsequent recovery of the SPV in February, L_2 amplitudes decline to their climatological levels. As seen earlier for the 1980-1981 and 1982-1983 winters, S_2 amplitudes in Fig. 1h also show a slightly delayed response to both strong and weak SPV conditions during the 2008–2009 winter. With strengthening SPV, S_2 amplitudes decline from ~31 nT in early January to reach below their climatological levels to ~26 nT around day 20. With the weakening of the SPV between late January and mid-February and thereafter its subsequent recovery, S_2 amplitudes gradually increase past their climatological levels by day 24 and eventually reach up to ~42 nT on day 50. As the SPV recovers by early March, S_2 amplitudes begin to decline back to their climatological levels.

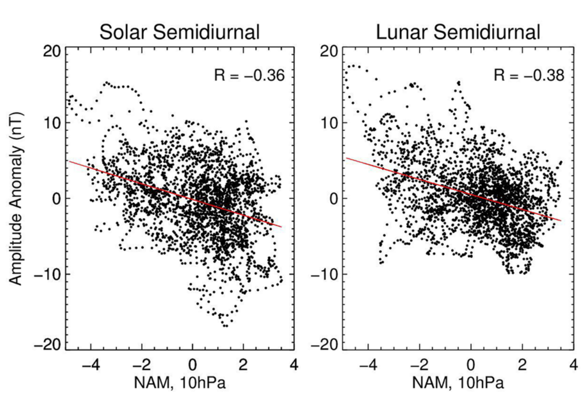

Fig. 2 Scatter plot between the anomalies in S_2 and L_2 geomagnetic tides versus the Northern Annular Mode (NAM) at 10 hPa. Results are restricted to the period of 15 December to 1 March for all the available data between 1980 and 2020. The S_2 and L_2 tidal anomalies are plotted against NAM with a lag of 10 and 0 days, respectively

Discussion

From the above results, it can be clearly inferred that geomagnetic semidiurnal solar and lunar tides typically decline in response to strong SPV conditions but with a slightly weaker sensitivity when compared to its enhancement during weak SPV conditions. Thus, S_2 and L_2 tidal amplitudes seem to be anti-correlated to the NAM index especially during strong and weak SPV conditions as larger semidiurnal tidal amplitudes are seen during weak state of SPV and vice-versa. In order to further quantify the relationship between geomagnetic semidiurnal tides and the states of SPV, we plot the S_2 and L_2 tidal anomalies against the NAM at 10 hPa for all available data between December 15 and March 1 for the years 1980-2020 in Fig. 2. Contrary to L_2 tides, S_2 tides generally respond with a time lag to the state of the SPV. While the enhancement and reduction of L_2 amplitudes generally coincide with the fall and rise of NAM index, the S_2 amplitudes do not show enhancement or reduction immediately but with a time lag of several days. To account for this lag, we calculated a median response time of S_2 tides to SPV based on a cross-correlation analysis between S_2 tidal amplitudes and NAM by using discrete lag interval of 0-20 days for each of the winters during the years of 1980-2020 and found it to be around 10 days. Thus, the S_2 and L_2 tidal anomalies are plotted between December 15 and March 1 against NAM with a lag of 10 and 0 days, respectively. The results show that there is a clear linear relationship between S_2 and L_2 tides throughout the different range of states of the SPV. The linear correlation coefficient for S_2 is -0.36 and for L_2 is -0.38, indicating that ~15% of the variability in S_2 and L_2 tides during NH winter can be explained by the state of the SPV. Based on this plot, the average enhancement in geomagnetic solar and lunar tidal amplitudes during weak SPV (NAM < -3.0) comes to be ~25% and ~50%, respectively. During strong SPV (NAM > 2.0), the geomagnetic solar and lunar tidal amplitudes decline on an average by ~15% and ~25%, respectively. It is also important to note that these correlation coefficient values may be longitude dependent and in case if a similar analysis is performed with magnetic-field recordings at a different equatorial station, the results may differ because longitudinal variability of geomagnetic tidal amplitudes during weak SPV conditions have been found in earlier studies (e.g., Siddiqui et al. 2017).

Although our results are based on observations and not on controlled simulations, they compare well with those of PH22 despite focusing on the effects in the ionosphere rather than on the neutral atmosphere. However, we find that the absolute value of linear correlation coefficient between S_2 and NAM is lower and almost half of their reported value for SW2 and NAM. There could be various reasons for this difference between the responses of S_2 and SW2 tides to NAM. For example, S_2 tides in ΔH comprise of different migrating and non-migrating semidiurnal components that have the following main sources: (1) in situ thermal forcing in the thermosphere, and (2) upward-propagating tides that are generated in the lower atmosphere. Since it is not possible to separate the migrating and non-migrating semidiurnal components from single-station observations, the contributions from non-migrating semidiurnal tides are also included in our calculation of S_2 amplitudes. The contributions from non-migrating semidiurnal tides can certainly be non-negligible during SSWs as it has been reported that they can be generated by nonlinear interaction between tides and PWs (e.g., Pedatella and Forbes 2010) and possibly by longitudinal changes in stratospheric ozone distributions (Goncharenko et al. 2012). Additionally, the contributions of in situ generated thermospheric semidiurnal tides, though small (e.g., Forbes and Garrett 1979), are also included in our calculated S_2 amplitudes. Also, it was found by PH22 that the relationship between non-migrating semidurnal tides (SW1 & SW3) and NAM (see their Additional file 1) is considerably weaker in comparison to SW2. Based on these factors, we presume that the contributions of non-migrating semidiurnal tides and in situ generated semidiurnal tides in S_2 amplitudes may be a reason for the lower correlation coefficient seen between S_2 and NAM in our results in comparison to the results of PH22.

From our results, it was also observed that L_2 tidal variations respond with almost no time lag to the strong and weak states of SPV while S_2 tidal variations responded with a median time lag of around 10 days. It is plausible that the difference in the timing of L_2 and S_2 tidal responses could be due to the mechanisms that drive these tidal variations and further analysis and more research is certainly needed to understand the role of these different processes.

Conclusions

In this study, we have used the horizontal magnetic field recordings from the Huancayo equatorial observatory to study the variations of geomagnetic semidiurnal solar and lunar tides during periods of strong and weak SPV. Based on the analysis of 34 NH winters between 1980 and 2020, we find that the response of the geomagnetic semidiurnal solar and lunar tides is dependent on the state of the NH SPV. These tides typically show an average enhancement (~25% for S_2, ~50% for L_2) during times of weak SPV and an average reduction (~15% for S_2, ~25% for L_2) during times of strong SPV. The decline in tides, however, occurs with a weaker sensitivity during strong

SPV conditions when compared to its enhancement during weak SPV conditions. Our results also reveal that the geomagnetic semidiurnal solar tidal response to strong and weak SPV conditions is delayed by approximately 10 days while the response of geomagnetic semidiurnal lunar tide is almost immediate without any time lag. This suggests that there are different sources of semidiurnal solar and lunar tidal variations that are driving these tidal changes during strong and weak SPV conditions. Further, these results confirm the simulation results of PH22 and provide observational evidence that in addition to weak NH polar vortices, strong NH polar vortices also have a pronounced short-term effect on the semidiurnal solar and lunar tides in the ionosphere.

Abbreviations

Dst	Disturbance storm time
DW1	Migrating solar diurnal tide
EEJ	Equatorial electrojet
GFZ	German Research Centre for Geosciences
GW	Gravity wave
HUA	Huancayo
IQD	International quiet day
L2	Geomagnetic semidiurnal lunar tides
M2	Migrating lunar semidiurnal tide
MERRA	Modern era retrospective analysis for research and applications
MLT	Mesosphere lower thermosphere
NAM	Northern annular mode
NH	Northern hemisphere
PW	Planetary wave
S2	Geomagnetic semidiurnal solar tides
SD	Specified dynamics
SH	Southern hemisphere
SPV	Stratospheric polar vortex
SSW	Sudden stratospheric warming
SW1	Nonmigrating solar semidiurnal westward wave-1
SW2	Migrating solar semidiurnal tide
SW3	Migrating solar semidiurnal westward wave-3
Sq	Solar quiet
WACCM-X	Whole atmosphere community climate model with thermosphere and ionosphere extension
WDC	World data centre

Supplementary Information

The online version contains supplementary material available at https://doi.org/10.1186/s40623-023-01810-x.

Additional file 1. Error analysis of tides obtained by least-squares fitting.

Acknowledgements
The work at PRL is supported by the Department of Space, Government of India. SK acknowledges support from Leibniz Institute of Atmospheric Physics, Kühlungsborn, Germany during his visit under the SCOSTEP visiting scholar program. This material is based upon work supported by the National Center for Atmospheric Research, which is a major facility sponsored by the U.S. National Science Foundation under Cooperative Agreement 1852977.

Author contributions
All the authors contributed to the design, implementation of the result, and writing the manuscript. All authors read and approved the final manuscript.

Funding
SK obtain the financial support from Leibniz-IAP, Kühlungsborn, Germany and SCOSTEP under the SCOSTEP visiting scholar program.

Availability of data and materials
The results presented in this paper rely on the data collected at Huancayo that have been downloaded using the website of WDC, Edinburgh (https://wdc.bgs.ac.uk/catalog/master.html). We thank the INTERMAGNET for promoting high standards of magnetic observatory practice and the Instituto Geofisico del Peru for supporting geomagnetic observatory operations at Huancayo. We are very thankful to WDC for Geomagnetism, Kyoto, for making available the *Dst* indices, which are available at https://wdc.kugi.kyoto-u.ac.jp/. The data for *F*10.7 and Kp were obtained from the GSFC/SPDF OMNIWeb interface at http://omniweb.gsfc.nasa.gov. The MERRA-2 data used for calculation of NAM is available via https://gmao.gsfc.nasa.gov/reanalysis/MERRA-2/. The International Quiet Days have been downloaded from the website of GFZ Potsdam via the following link https://www.gfz-potsdam.de/sektion/geomagnetismus/daten-produkte-dienste/geomagnetischer-kp-index.

Declarations

Competing interests
The authors declare that they have no competing interests.

Author details
[1]Physical Research Laboratory, Space and Atmospheric Sciences Division, Ahmedabad, India. [2]Indian Institute of Technology, Gandhinagar, India. [3]Leibniz Institute of Atmospheric Physics at the University of Rostock, Kühlungsborn, Germany. [4]High Altitude Observatory, National Center for Atmospheric Research, Boulder, CO, USA. [5]COSMIC Program Office, University Corporation for Atmospheric Research, Boulder, CO, USA.

Received: 20 January 2023 Accepted: 21 March 2023
Published online: 10 April 2023

References

Alken P, Maus S (2007) Spatio-temporal characterization of the equatorial electrojet from CHAMP, Ørsted, and SAC-C satellite magnetic measurements. J Geophys Res Space 112:A09305. https://doi.org/10.1029/2007JA012524

Baker W, Martyn DF (1953) Electric currents in the ionosphere-the conductivity. Philos t r Soc Lond S-A 246:281–294

Baldwin MP, Dunkerton TJ (2001) Stratospheric harbingers of anomalous weather regimes. Science 294:581–584. https://doi.org/10.1126/science.1063315

Baldwin MP, Ayarzagüena B, Birner T, Butchart N, Butler AH, Charlton-Perez AJ et al (2021) Sudden stratospheric warmings. Rev Geophys 59:e2020RG000708. https://doi.org/10.1029/2020RG000708

Bartels J, Johnston H (1940) Geomagnetic tides in horizontal intensity at Huancayo. Terr Magn Atmos Electr 45:269–308. https://doi.org/10.1029/TE045i003p00269

Butler AH, Seidel DJ, Hardiman SC, Butchart N, Birner T, Match A (2015) Defining sudden stratospheric warmings. Bull Am Meteorol Soc 96(11):1913–1928. https://doi.org/10.1175/BAMS-D-13-00173.1

Charlton AJ, Polvani LM (2007) A new look at stratospheric sudden warmings. Part I: Climatology and modeling benchmarks. J Clim 20(3):449–469. https://doi.org/10.1175/JCLI3996.1

Charlton AJ, O'Neill A, Lahoz WA, Berrisford P (2005) The splitting of the stratospheric polar vortex in the Southern Hemisphere, September 2002: dynamical evolution. J Atmos Sci 62:590–602. https://doi.org/10.1175/JAS-3318.1

Charney JG, Drazin PG (1961) Propagation of planetary-scale disturbances from the lower into the upper atmosphere. J Geophys Res 66(1):83–109. https://doi.org/10.1029/JZ066i001p00083

Chau JL, Fejer BG, Goncharenko LP (2009) Quiet variability of equatorial E x B drifts during a sudden stratospheric warming event. Geophys Res Lett 36:L05101. https://doi.org/10.1029/2008GL036785

Chau JL, Goncharenko LP, Fejer BG, Liu H-L (2012) Equatorial and low latitude ionospheric effects during sudden stratospheric warming events. Space Sci Rev 168:385–417. https://doi.org/10.1007/s11214-011-9797-5
Chau JL, Hoffmann P, Pedatella NM, Matthias V, Stober G (2015) Uppermesospheric lunar tides over middle and high latitudes during sudden stratospheric warming events. J Geophys Res Space 120:3084–3096. https://doi.org/10.1002/2015JA020998
Conte JF, Chau JL, Stober G, Pedatella N, Maute A, Hoffmann P, Janches D, Fritts D, Murphy DJ (2017) Climatology of semidiurnal lunar and solar tides at middle and high latitudes: Interhemispheric comparison. J Geophys Res Space 122:7750–7760. https://doi.org/10.1002/2017JA024396
Fejer BG, Olson ME, Chau JL, Stolle C, Lühr H, Goncharenko LP, Nagatsuma T (2010) Lunar-dependent equatorial ionospheric electrodynamic effects during sudden stratospheric warmings. J Geophys Res 115:A00G03. https://doi.org/10.1029/2010JA015273
Forbes JM (1982a) Atmospheric tides, 1, model description and results for the solar diurnal component. J Geophys Res 87:5222–5240
Forbes JM (1982b) Atmospheric tides, 2, the solar and lunar semidiurnal component. J Geophys Res 87:5222–5240
Forbes JM, Garrett HB (1979) Theoretical studies of atmospheric tides. Rev Geophys 17(8):1951–1981. https://doi.org/10.1029/RG017i008p01951
Forbes JM, Zhang X (2012) Lunar tide amplification during the January 2009 stratosphere warming event: Observations and theory. J Geophys Res 117:A12312. https://doi.org/10.1029/2012JA017963
Gelaro R, McCarty W, Suárez MJ, Todling R, Molod A, Takacs L, Randles CA, Darmenov A, Bosilovich MG, Reichle R, Wargan K, Coy L, Cullather R, Draper C, Akella S, Buchard V, Conaty A, da Silva AM, Gu W, Kim G, Koster R, Lucchesi R, Merkova D, Nielsen JE, Partyka G, Pawson S, Putman W, Rienecker M, Schubert SD, Sienkiewicz M, Zhao B (2017) The modern-era retrospective analysis for research and applications, Version 2 (MERRA-2). J Clim 30(14):5419–5454. https://doi.org/10.1175/JCLI-D-16-0758.1
Gerber EP, Martineau P (2018) Quantifying the variability of the annular modes: Reanalysis uncertainty vs. sampling uncertainty. Atmospheric Chem Phys 18(23):17099–17117. https://doi.org/10.5194/acp-18-17099-2018
Goncharenko LP, Coster AJ, Plumb RA, Domeisen DIV (2012) The potential role of stratospheric ozone in the stratosphere-ionosphere coupling during stratospheric warmings. Geophys Res Lett 39:L08101. https://doi.org/10.1029/2012GL051261
Goncharenko LP, Harvey VL, Liu H, Pedatella NM (2021) Sudden stratospheric warming impacts on the ionosphere–thermosphere system. In: Huang C, Lu G, Zhang Y, Paxton LJ (eds) Ionosphere dynamics and applications. American Geophysical Union, Washington, DC, pp 369–400
Greene W (2018) Econometric analysis, 8th edn. Pearson Education Limited, London
Harvey VL, Randall CE, Goncharenko LP, Becker E, France JA (2018) On the upward extension of the polar vortices into the mesosphere. J Geophys Res Atmos. https://doi.org/10.1020/2018JD028815
Holton JR (1983) The influence of gravity wave breaking on the general circulation of the middle atmosphere. J Atmos Sci 40:2497–2507. https://doi.org/10.1175/1520-0469(1983)040%3c2497:TIOGWB%3e2.0.CO;2
Jin H, Miyoshi Y, Pancheva D, Mukhtarov P, Fujiwara H, Shinagawa H (2012) Response of migrating tides to the stratospheric sudden warming in 2009 and their effects on the ionosphere studied by a whole atmosphere-ionosphere model GAIA with COSMIC and TIMED/SABER observations. J Geophys Res 117:A10323. https://doi.org/10.1029/2012JA017650
Kamide Y, Maltsev YP (2007) Geomagnetic storms. In: Kamide Y, Chian A (eds) Handbook of the Solar-Terrestrial Environment. Springer, Berlin, pp 355–374
Laskar FI, Pallamraju D (2015) Does sudden stratospheric warming induce meridional circulation in the mesosphere thermosphere system? J Geophys Res Space Phys 119:10133–10143. https://doi.org/10.1002/2014JA020086
Lawrence ZD, Manney GL (2018) Characterizing stratospheric polar vortex variability with computer vision techniques. J Geophys Res Atmospheres 123:1510–1535. https://doi.org/10.1002/2017JD027556
Lawrence ZD, Perlwitz J, Butler AH, Manney GL, Newman PA, Lee SH, Nash ER (2020) The remarkably strong arctic stratosspheric polar vortex of winter 2020: Links to record-breaking arctic oscillation and ozone loss. J Geophys Res Atmospheres 125(22):2020033271. https://doi.org/10.1029/2020JD033271
Lindzen RS, Chapman S (1969) Atmospheric tides. Space Sci Rev 10(1):3–188
Liu H-L, Roble RG (2002) A study of a self-generated stratospheric sudden warming and its mesospheric-lower thermospheric impacts using the coupled TIME-GCM/CCM3. J Geophys Res Atmos 107:4695. https://doi.org/10.1029/2001JD001533
Malin SRC, Chapman S (1970) The determination of lunar daily geophysical variations by the Chapman-Miller method. Geophys J Int 19:15–35
Malin SRC, Gupta JC (1977) The Sq current system during the international geophysical year. Geophys J R Astron Soc 49:515–529
Matsuno T (1971) A dynamical model of the stratospheric sudden warming. J Atmos Sci 28(8):1479–1494. https://doi.org/10.1175/15200469(1971)028%3c1479:ADMOTS%3e2.0.CO;2
McIntyre M, Palmer T (1983) Breaking planetary waves in the stratosphere. Nature 305:593–600. https://doi.org/10.1038/305593a0
Montgomery DC, Peck EA, Vining GG (2012) Introduction to linear regression analysis. John Wiley & Sons, Hoboken
Park J, Lühr H, Kunze M, Fejer BG, Min KW (2012) Effect of sudden stratospheric warming on lunar tidal modulation of the equatorial electrojet. J Geophys Res Space 117:A03306. https://doi.org/10.1029/2011JA017351
Pedatella NM, Forbes JM (2010) Evidence for stratosphere sudden warming-ionosphere coupling due to vertically propagating tides. Geophys Res Lett 37:L11104. https://doi.org/10.1029/2010GL043560
Pedatella NM, Harvey VL (2022) Impact of strong and weak stratospheric polar vortices on the mesosphere and lower thermosphere. Geophys Res Lett 49:e2022GL098877. https://doi.org/10.1029/2022GL098877
Richards PG, Fennelly JA, Torr DG (1994) EUVAC: A solar EUV flux model for aeronomic calculations. J Geophys Res 99:8981–8992. https://doi.org/10.1029/94JA00518
Siddiqui TA, Stolle C, Lühr H, Matzka J (2015) On the relationship between weakening of the northern polar vortex and the lunar tidal amplification in the equatorial electrojet. J Geophys Res Space Phys 120:10006–10019. https://doi.org/10.1002/2015JA021683
Siddiqui TA, Stolle C, Lühr H (2017) Longitude-dependent lunar tidal modulation of the equatorial electrojet during stratospheric sudden warmings. J Geophys Res Space Phys 122:3760–3776. https://doi.org/10.1002/2016JA023609
Siddiqui TA, Maute A, Pedatella N, Yamazaki Y, Lühr H, Stolle C (2018) On the variability of the semidiurnal solar and lunar tides of the equatorial electrojet during sudden stratospheric warmings. Ann Geophys 36:1545–1562. https://doi.org/10.5194/angeo-36-1545-2018
Singh RP, Pallamraju D (2015) On the latitudinal distribution of mesospheric temperatures during sudden stratospheric warming events. J Geophys Res Space Phys. https://doi.org/10.1002/2014JA020355
Taylor JR (1982) An introduction to error analysis. University Science Books, Sausalito, p 270
Thompson DWJ, Wallace JM (1998) The arctic oscillation signature in the wintertime geopotential height and temperature fields. Geophys Res Lett 25:1297–1300. https://doi.org/10.1029/98GL00950
Waugh DW, Randel WJ (1999) Climatology of arctic and Antarctic polar vortices using elliptical diagnostics. J Atmos Sci 56(11):1594–1613. https://doi.org/10.1175/1520-0469(1999)056%3c1594:COAAAP%3e2.0.CO;2
Waugh DW, Sobel AH, Polvani LM (2017) What is the polar vortex and how does it influence weather? Bull Am Meteor Soc 98(1):37–44. https://doi.org/10.1175/BAMS-D-15-00212.1
Yamazaki Y, Maute A (2017) Sq and EEJ—a review on the daily variation of the geomagnetic field caused by ionospheric dynamo currents. Space Sci Rev 206:299–405. https://doi.org/10.1007/s11214-016-0282-z
Yamazaki Y, Richmond A, Yumoto K (2012) Stratospheric warmings and the geomagnetic lunar tide: 1958–2007. J Geophys Res Space 117:A04301. https://doi.org/10.1029/2012JA017514
Yamazaki Y, Richmond AD, Maute A, Wu Q, Ortland DA, Yoshikawa A, Adimula IA, Rabiu B, Kunitake M, Tsugawa T (2014) Ground magnetic effects of the equatorial electrojet simulated by the TIE-GCM driven by TIMED satellite data. J Geophys Res Space Phys 119:3150–3161. https://doi.org/10.1002/2013JA019487
Yamazaki Y, Matthias V, Miyoshi Y, Stolle C, Siddiqui T, Kervalishvili G, Alken P (2020) September 2019 antarctic sudden stratospheric warming: Quasi-6-day wave burst and ionospheric effects. Geophys Res Lett 47(1):e2019GL086577. https://doi.org/10.1029/2019GL086577

Publisher's Note